

REPORT DOCUMENTATION PAGE				Form Approved OMB No. 0704-0188	
<p>The public reporting burden for this collection of information is estimated to average 1 hour per response, including the time for reviewing instructions, searching existing data sources, gathering and maintaining the data needed, and completing and reviewing the collection of information. Send comments regarding this burden estimate or any other aspect of this collection of information, including suggestions for reducing the burden, to the Department of Defense, Executive Service Directorate (0704-0188). Respondents should be aware that notwithstanding any other provision of law, no person shall be subject to any penalty for failing to comply with a collection of information if it does not display a currently valid OMB control number.</p> <p>PLEASE DO NOT RETURN YOUR FORM TO THE ABOVE ORGANIZATION.</p>					
1. REPORT DATE (DD-MM-YYYY) 12/14/2009		2. REPORT TYPE Final Performance Report		3. DATES COVERED (From - To) 05/01/2006 - 12/31/2009	
4. TITLE AND SUBTITLE Strain and Polarization Studies of InGaN for Optoelectronic, Electronic, and Photovoltaic Applications				5a. CONTRACT NUMBER NA	
				5b. GRANT NUMBER FA9550-06-1-0317	
				5c. PROGRAM ELEMENT NUMBER NA	
				5d. PROJECT NUMBER NA	
6. AUTHOR(S) Pan, Ernie Albrecht, John				5e. TASK NUMBER NA	
				5f. WORK UNIT NUMBER NA	
7. PERFORMING ORGANIZATION NAME(S) AND ADDRESS(ES) The University of Akron 302 Buchtel Common Akron, OH 44325				8. PERFORMING ORGANIZATION REPORT NUMBER	
9. SPONSORING/MONITORING AGENCY NAME(S) AND ADDRESS(ES) USAF, AFRL AF Office of Scientific Research 875 N. Randolph St. Room 3112 Arlington, VA 22203				10. SPONSOR/MONITOR'S ACRONYM(S)	
				11. SPONSOR/MONITOR'S REPORT NUMBER(S)	
12. DISTRIBUTION/AVAILABILITY STATEMENT No limitation on public distribution					
13. SUPPLEMENTARY NOTES					
14. ABSTRACT <p>This final report summarizes the investigation conducted at the University of Akron by Prof. Ernie Pan's group in close collaboration with AFRL Sensors Directorate (Dr. John Albrecht AFRL/RDXX). Through this work, we have co-developed electro-mechanical simulations that take into account material polarization and piezoelectric properties that cannot be suppressed in many group III-V semiconductor nanostructures. This work addresses key physics issues in these polarized semiconductors and also provides laboratory researchers with access to design and analysis specifics that are not accessible by or do not exist in the limited physical models available in commercial semiconductor modeling software. The specifics of these models and related publications are provided in the chapters of the report. Another important contribution is on the magnetoelectric (ME) effect of multiferroic composites. We found that while any imperfect interface would reduce the ME effect in multiferroic composites, suitably designed graded composites can substantially enhance the ME effect.</p>					
15. SUBJECT TERMS <p>Quantum-dot nanostructure, Strain, Polarization, Green's functions, boundary integral equation, multiferroic composite, magnetoelectric effect, functionally graded materials.</p>					
16. SECURITY CLASSIFICATION OF:			17. LIMITATION OF ABSTRACT		18. NUMBER OF PAGES
a. REPORT U	b. ABSTRACT U	c. THIS PAGE U			198
19a. NAME OF RESPONSIBLE PERSON <i>[Signature]</i>					19b. TELEPHONE NUMBER (Include area code) 330-972-8311

FINAL TECHNICAL PROGRESS REPORT

(2006–2009)

Project Title

**Strain and Polarization Studies of InGaN for Optoelectronic, Electronic, and
Photovoltaic Applications**

AFOSR FA9550-06-1-0317

Program Manager: Dr. Donald Silversmith

Prepared by Ernie Pan
Dept. of Civil Engineering/Applied Mathematics
University of Akron

On December 14, 2009

In Collaboration with
Dr. John Albrecht of AFRL and Dr. C.C. Yang of National Taiwan University

Executive Summary

This report gives a detailed description of investigations conducted at the University of Akron by Prof. Ernie Pan's group in close collaboration with AFRL Sensors Directorate (Dr. John Albrecht AFRL/RYDX). Through this work, we have co-developed electro-mechanical simulations that take into account material polarization and piezoelectric properties that cannot be suppressed in many group III–V semiconductor nanostructures. This work addresses key physics issues in these polarized semiconductors and also provides laboratory researchers with access to design and analysis specifics that are not accessible by or do not exist in the limited physical models available in commercial semiconductor modeling software. The specifics of these models and related publications are provided in the chapters of this report.

A crucial development in these investigations is the simultaneous multi-physics treatment of lattice polarization coupled to both electronic and mechanical properties. In particular, we would like to point out that the fully-coupled piezoelectric model developed jointly with AFRL/SN is now attracting worldwide attention in the wurtzite semiconductor community (seen through numerous recent citations and contacts made by the broader academic community) where the electro-mechanical coupling can be a dominant, if often overlooked, physical feature. In addition to the program developed at AFRL to model strongly polarized layered semiconductor well structures, the program developed at Akron will be continuously tested during the new phase to insure transition to the laboratory. To help with this transition, we plan to add a user-friendly interface so that in the near future, scientists at AFRL and students/faculties at Akron can easily use the program for designing strained semiconductor structures with tailored piezoelectric interactions.

Furthermore, the transition of this work for attacking important problems for AFRL researchers is seen in Chapter 5 on nanocolumn structures. In the joint laboratory work between AFRL/RY and AFRL/RX, the strain profile is sought in epitaxial nanocolumn structures of GaN for development of near defect-free template critical for device and circuit technologies of interest to the Air Force. We have shown in collaboration with Dr. Albrecht that the strain profile in small 100 nm columns has a decay length far shorter than the typical column height used in experiments (microns). This strain profile calculation will allow AFRL to interpret and verify spectroscopic and microstructural experimental data which seemed to indicate certain critical strain properties. This theoretical work is also sufficiently general to be applied to a broader category of problems, including hollow cylindrical nanocolumns of piezoelectric materials and columns with direct electrical contacts by metals.

Also in this work, we have co-derived, by virtue of the unified Stroh formalism, the ex-

tremely concise and elegant solutions for two-dimensional and (quasi-static) time-dependent Green's functions in anisotropic magnetoelectroelastic multiferroic bimaterials with a viscous interface subjected to an extended line force and an extended line dislocation located in the upper half-plane. It is found *for the first time* that, in the multiferroic bimaterial Green's functions, there are *twenty five* static image singularities and *fifty moving image* singularities in the form of the extended line force and extended line dislocation in the upper or lower half-plane. It is further observed that, as time evolves, the moving image singularities, which originate from the locations of the static image singularities, will move further away from the viscous interface with explicit time-dependent locations. Moreover, explicit expression of the time-dependent image force on the extended line dislocation due to its interaction with the viscous interface is derived, which is also valid for mathematically degenerate materials. These Green's functions can not only be directly applied to the study of dislocation mobility in the novel multiferroic bimaterials, they can also be utilized as kernel functions in a boundary integral formulation to investigate more complicated boundary value problems where multiferroic materials/composites are involved.

It was recently discovered that inclusions, fatigue damage and other types of material imperfections and defects in metals can be nondestructively detected by noncontacting magnetic measurements that sense the thermoelectric currents produced by directional heating and cooling. Since detection of small defects in thermoelectric materials is ultimately limited by intrinsic thermoelectric anisotropy and inhomogeneity of the material to be inspected, a thorough study is required on their impact to the nondestructive capability. Therefore, in this new joint investigation the induced electric current densities and thermal fluxes are first derived for a steady line heat source in an inhomogeneous and anisotropic thermoelectric material. The exact closed-form solutions are obtained by converting the original problem into two inhomogeneous Helmholtz equations via eigenvalue/eigenvector separation. The material properties are assumed to vary exponentially in the same manner in an arbitrary direction. For the corresponding homogeneous but anisotropic material case, we also present an elegant formulation based on the complex variable method. It is shown that the induced magnetic fields can be expressed in a concise and exact closed form for a line heat source in an infinite homogeneous anisotropic material and in one of the two bonded anisotropic half-planes. Our numerical results demonstrate clearly that both property anisotropy and gradient in thermoelectric materials can significantly influence the induced thermoelectric currents and magnetic fields.

Contents

1	Strain and piezoelectric fields in embedded quantum wire arrays	14
1.1	Introduction	14
1.2	Problem description	15
1.3	Results and analysis	16
1.3.1	QWR array in infinite substrate GaAs	16
1.3.2	QWR array in half-space substrate GaAs	17
1.4	Conclusions	22
2	Elastic and piezoelectric fields in quantum wire semiconductor structures—a boundary integral equation analysis	27
2.1	Introduction	27
2.2	Problem description and basic equations	28
2.3	Boundary integral equations and constant-element discretization	30
2.4	Numerical examples	34
2.4.1	Circular and elliptic QWRs	34
2.4.2	Square QWR in GaAs and hexagon QWR in AlN	36
2.4.3	QWRs of different polygonal shapes	39
2.5	Concluding remarks	43
3	Exact closed-form electromagnetic Green’s functions for graded uniaxial multiferroic materials	45
3.1	Introduction	45
3.2	Green’s functions for a functionally graded multiferroic material	46
3.3	Conclusions	57
3.4	Appendices	57
3.4.1	Derivatives of the Green’s functions	57
3.4.2	Boundary integral equation formulation for an FGM multiferroic	58
4	Anisotropic elasticity of multilayered crystals deformed by a biperiodic network of misfit dislocations	61
4.1	Introduction	61
4.2	Specification of the problem	62
4.3	Stroh formalism for biperiodic problems	64
4.4	Transfer matrix for the $(N - 1)$ thin bonded layers	67
4.5	The general solution for the two semi-infinite media	69

4.6	Solution of the total structure	69
4.7	Main features of the methodology	71
4.8	Application	72
4.9	Conclusions	77
5	Decay rates for a transversely isotropic piezoelectric hollow circular nanocolumn	78
5.1	Introduction	78
5.2	General Solutions of Transversely Isotropic Piezoelectric Solids	79
5.3	Decay rates of the transversely isotropic piezoelectric nanocolumn	82
5.3.1	Torsional Case	82
5.3.2	Torsionless Case	83
5.4	Results and Discussions	85
5.5	Conclusions	90
6	Electromagnetic Fields Induced by a Concentrated Heat Source in Multiferroic Materials	91
6.1	Introduction	91
6.2	A steady point heat source in a homogeneous uniaxial multiferroic material	92
6.2.1	The nondegenerate case: $\lambda_1 \neq \lambda_2 \neq \lambda_0$	95
6.2.2	The degenerate case: $\lambda_1 = \lambda_0$ ($\lambda_1 \neq \lambda_2$)	97
6.3	A steady point heat source in a homogeneous uniaxial multiferroic bimaterial	98
6.4	Conclusions	100
7	Effective Properties of Multilayered Functionally Graded Multiferroic Composites	102
7.1	Introduction	102
7.2	Effective Properties of Multilayered Multiferroic Composites	103
7.3	Applications	106
7.3.1	Effective properties of a multiferroic composite composed of an orthotropic piezoelectric phase and an orthotropic magnetostrictive phase	106
7.3.2	Effective properties of a multiferroic composite composed of an orthotropic piezoelectric phase, an orthotropic magnetostrictive phase, and an orthotropic elastic substrate	111
7.3.3	Effective properties of a multiferroic composite composed of an orthotropic FGM piezoelectric phase and an orthotropic FGM magnetostrictive phase	112
7.4	Conclusion	116
8	Two-Dimensional Green's Functions in Anisotropic Multiferroic Bimaterials with a Viscous Interface	119
8.1	Introduction	119
8.2	Basic Formulations	120
8.3	General Solution for the Green's Functions	122

8.4	Image Singularities	126
8.5	Time-Dependent Image Force on an Extended Line Dislocation	130
8.5.1	Isotropic elastic bimaterials	130
8.5.2	Transversely isotropic multiferroic bimaterials	132
8.5.3	Relaxation time	132
8.5.4	Image force for a perfect interface at the initial moment	133
8.5.5	Image force for a free-sliding interface when time approaches infinity	133
8.5.6	A comparison of image force $F_2(0)$ with $F_2(\infty)$	134
8.6	Conclusions	135
8.7	An appendix: Proof that p cannot be real in Eq. (8.3)	136
9	Role of Material Property Gradient and Anisotropy in Thermoelectric Materials	137
9.1	Introduction	137
9.2	A Line Heat Source in an Infinite Exponentially Gradient Anisotropic Thermoelectric Material	138
9.3	Complex Variable Formulation for Homogeneous Anisotropic Thermoelectric Materials and its Applications	143
9.3.1	Complex Variable Formulation	144
9.3.2	Applications	145
9.4	Numerical Examples	147
9.5	Conclusion	148
10	Elastic And Electric Fields Induced By QWR In Bimaterial Plane	150
10.1	Bimaterial Green's Functions	151
10.1.1	Integration of Bimaterial Green's Functions	153
10.1.2	Derivatives of Bimaterial Green's Functions	155
10.2	Numerical Examples	155
10.2.1	Definition of the Relative Strain Energy	155
10.2.2	Variation of Relative Strain Energy with QWR Depth	156
10.2.3	Effect of QWR Shape on Relative Strain Energy and Distribution of Strain Energy Density	157
10.3	Conclusions	162
11	Strain Energy On The Surface Of Half-Plane Substrate Induced By An Isolated QD	163
11.1	Problem description for QD Embedded in Anisotropic Half-space Substrate	163
11.2	Integration of Half-space Green's Functions over QD Surfaces	164
11.3	Numerical Examples	166
11.4	Conclusions	168
12	Elastic And Electric Fields Distribution In AlN QDs Structures	174

13 Ab initio calculation on magnetic and magnetoelectric coupling effect on a series of perovskite compounds	177
---	------------

List of Tables

2.1	Material properties & misfit strains in InAs(001)/GaAs(001) [1, 2]	33
2.2	Material properties & misfit strains in InN(0001)/AlN (0001) [1, 2]	33
2.3	Strains in inclusion GaAs (001) and inhomogeneity InAs(001)/GaAs (001) .	34
2.4	Strains in inclusion GaAs (111) and inhomogeneity InAs(111)/GaAs (111) .	35
2.5	Strains in inclusion AlN(0001) and inhomogeneity InN(0001)/AlN(0001) .	35
2.6	Strains in inclusion AlN(1000) and inhomogeneity InN(1000)/AlN(1000) .	35
2.7	Electric fields ($\times 10^6$ V/m) at the center of a polygonal InAs QWR with n sides in GaAs(111)	42
2.8	Electric fields ($\times 10^7$ V/m) at the center of a polygonal InN QWR with n sides in AlN	43
4.1	Values of σ_{11} on the two sides of each interface of the multilayer GaAs/Si/GaAs/Si/GaAs/Si with $N = 5$. The interface locations are denoted by x_3 . Two material cases are studied: elastically isotropic (assumed for demonstration purposes) and elastically cubic (true). The values in the parentheses in the second row are the results of Bonnet [3].	72
5.1	Material properties of GaN [4, 5]	86
10.1	Variation of relative strain energy with base angle of the isosceles triangle of InAs (111) QWR, which is free-standing on the GaAs (111) substrate. . .	158
11.1	Maximum strain energy E_{max} on the surface of the substrate GaAs for different QD shapes with different depths (unit of energy = 118.8×10^{15} N · m).169	

List of Figures

1.1	Variation of the hydrostatic strain for QWR arrays buried in (a) (001)-oriented and (b) (111)-oriented GaAs substrates. Panel (c) gives the geometric layout of the QWR arrays in an infinite space and the dashed line indicates the location of the cut line $z = 0$ for the field calculations of Figures 1.1 and 1.3.	18
1.2	Contour plots of total hydrostatic strain for QWR arrays buried in infinite spaces. (a) 1×1 and (b) 3×3 arrays in (001)-oriented GaAs substrates; (c) 1×1 and (d) 3×3 arrays in (111)-oriented substrates.	19
1.3	Variation of electric field components (a) E_x and (b) E_z along the x -axis (that is, $z = 0$ as shown in Figure 1.1(c)) for the case of QWR arrays buried in infinite space (111)-oriented substrates.	20
1.4	Variation of the hydrostatic strain for QWR arrays buried in half space (001)-oriented substrates. Hydrostatic strain is plotted for cut lines (a) along the z -axis, that is, $x = 0$, (b) along the horizontal line $z = -4$ nm, and (c) along the free surface $z = 0$. Panel (d) gives the geometric layout of the QWR arrays in a half space and the dashed lines indicate the locations for the field calculations of Figures 1.4–1.8.	21
1.5	Variation of the hydrostatic strain for QWR arrays buried in half space (001)-oriented substrates. Hydrostatic strain is plotted for cut lines (a) along the z -axis, that is, $x = 0$, (b) along the horizontal line $z = -4$ nm, and (c) along the free surface $z = 0$. The cut lines are shown schematically in Figure 1.4(d).	23
1.6	Contour plots of total hydrostatic strain for QWR arrays buried in half-spaces. (a) 1×1 and (b) 3×3 arrays in (001)-oriented GaAs substrates; (c) 1×1 and (d) 3×3 arrays in (111)-oriented substrates.	24
1.7	Variation of electric field components (a) E_x and (b) E_z along the free surface (that is, $z = 0$ as shown in Figure 1.4(d)) for the case of QWR arrays buried in half-space (111)-oriented substrates.	25
1.8	Variation of electric field components (a) E_x and (b) E_z along the z -axis (that is, $x = 0$ as shown in Figure 1.4(d)) for the case of QWR arrays buried in half-space (111)-oriented substrates.	26
2.1	(a) A circular QWR of radius $r = 10$ nm in an infinite substrate, and (b) an elliptical QWR with length of the semi-major axis $a = 20$ nm in horizontal x -direction and the semi-minor axis $b = 5$ nm in vertical z -direction in an infinite substrate in (b).	34

2.2	A square QWR in GaAs (a) and a hexagon QWR in AlN (b). The dashed lines show where the responses are calculated.	36
2.3	Hydrostatic strains ($\gamma_{xx} + \gamma_{zz}$) in a square QWR InAs/GaAs (001) along the horizontal (a) and diagonal (b) lines as defined in Figure 2.2(a).	37
2.4	Hydrostatic strains ($\gamma_{xx} + \gamma_{zz}$) in a square QWR InAs/GaAs (111) along the (a) horizontal and (b) diagonal dashed lines shown in Figure 2.2(a).	37
2.5	(a) E_x and (b) E_z along the horizontal dashed line shown in Figure 2.2(a), and (c) E_x and (d) E_z along the diagonal dashed line of the same figure, in a square QWR InAs/GaAs(111).	38
2.6	Hydrostatic strains ($\gamma_{xx} + \gamma_{zz}$) in a hexagonal QWR InN/AlN (0001) along the (a) horizontal and (b) inclined dashed lines shown in Figure 2.2(b).	39
2.7	(a) E_x in InN/AlN(1000) and (b) E_z in InN/AlN(0001) along the horizontal line shown in Figure 2.2(b).	40
2.8	(a) E_x and (b) E_z in InN/AlN (0001) along the inclined line shown in Figure 2.2(b).	40
2.9	(a) E_x and (b) E_z in InN/AlN (1000) along the inclined line shown in Figure 2.2(b).	41
2.10	The polygons with number of sides $n = 3, 4, 5, 6, 10$, and ∞ , where a polygon with an infinite number of sides is a circle.	41
2.11	(a) E_x and (b) E_z in InAs/GaAs(111) along the x -axis for $n = 3, 4, 5, 6, 10$, and ∞ , where a polygon with an infinite number of sides is a circle.	42
2.12	(a) E_x in InN/AlN(1000) and (b) E_z in InN/AlN(0001) along the x -axis for $n = 3, 4, 5, 6, 10$, and ∞ , where a polygon with an infinite number of sides is a circle.	43
3.1	Distribution of the electromagnetic Green's function $G_{\phi P}$ along x_3 -axis for different gradient parameter $\beta_3 (= -10, -3, -1, 0, 1, 3, 10 \text{ m}^{-1})$ with $\beta_1 = \beta_2 = 0$	52
3.2	Distribution of the electromagnetic Green's function $G_{\phi M}$ along x_3 -axis for different gradient parameter $\beta_3 (= -10, -3, -1, 0, 1, 3, 10 \text{ m}^{-1})$ with $\beta_1 = \beta_2 = 0$	53
3.3	Distribution of the electromagnetic Green's function $G_{\psi P}$ along x_3 -axis for different gradient parameter $\beta_3 (= -10, -3, -1, 0, 1, 3, 10 \text{ m}^{-1})$ with $\beta_1 = \beta_2 = 0$	54
3.4	Distribution of the electromagnetic Green's function $G_{\psi M}$ along x_3 -axis for different gradient parameter $\beta_3 (= -10, -3, -1, 0, 1, 3, 10 \text{ m}^{-1})$ with $\beta_1 = \beta_2 = 0$	55
3.5	Distribution of the magnetic potential along x_3 -axis induced by a unit electric dipole ($p = 1$) at origin and along the uniaxial x_3 -direction for different gradient parameter $\beta_3 (= -3, -1, 0, 1, 3 \text{ m}^{-1})$ with $\beta_1 = \beta_2 = 0$	56
4.1	Cross section of a multilayered system with N interfaces and $N + 1$ anisotropic elastic media. A biperiodic, hexagonal, misfit dislocation network that accommodates a misfit dislocation between layer n and layer $n + 1$ lies on the interface $x_3 = z_n =$ of the multilayered structure.	63

4.2	Distribution of the in-plane stress σ_{11} along the x_3 -axis ($x_1 = 0$) for a $N = 5$ multilayered structure formed by alternating GaAs and Si. The misfit dislocation array lies at the interface $x_3 = 4$ nm and is infinitely long in the x_2 -direction. The dark solid lines are the results when GaAs and Si are taken to be cubic and the pink dashed lines are the corresponding results when GaAs and Si are assumed to be isotropic.	73
4.3	Distribution of the in-plane stress σ_{33} along the x_3 -axis ($x_1 = 0$) for a $N = 5$ multilayered structure formed by alternating GaAs and Si. The misfit dislocation array lies at the interface $x_3 = 4$ nm and is infinitely long in the x_2 -direction. The dark solid lines are the results when GaAs and Si are taken to be cubic and the pink dashed lines are the corresponding results when GaAs and Si are assumed to be isotropic.	74
4.4	Periodic distribution of the horizontal displacement u_1 along the traction-free surface of the InAs thin film bonded to GaAs substrate. The misfit dislocation array lies at the InAs/GaAs interface. The dark solid line is the result when both the InAs thin film and GaAs substrate are taken to be cubic, whereas the pink dashed line is the corresponding result when both InAs and GaAs are assumed to be isotropic.	75
4.5	Periodic distribution of the horizontal displacement u_3 along the traction-free surface of the InAs thin film bonded to GaAs substrate. The misfit dislocation array lies at the InAs/GaAs interface. The dark solid line is the result when both the InAs thin film and GaAs substrate are taken to be cubic, whereas the pink dashed line is the corresponding result when both InAs and GaAs are assumed to be isotropic.	76
5.1	A simplified free-standing transversely isotropic piezoelectric nanocolumn over a substrate.	80
5.2	Dimensionless complex decay roots ρb under axisymmetric torsionless deformation for an isotropic elastic hollow nanocolumn with Poisson's ratio $\nu = 0.25$. Only real parts of the roots are shown.	86
5.3	Dimensionless complex decay roots ρb under axisymmetric torsionless deformation for a transversely isotropic piezoelectric hollow GaN nanocolumn with boundary condition $D_r = 0$ on $r = a$ and $r = b$. Only real parts of the roots are shown.	87
5.4	Dimensionless complex decay roots ρb under axisymmetric torsionless deformation for a transversely isotropic piezoelectric hollow GaN nanocolumn with boundary condition $\phi = 0$ on $r = a$ and $r = b$. Only real parts of the roots are shown.	88
5.5	Dimensionless complex decay roots ρb under axisymmetric torsionless deformation for a decoupled purely elastic and purely electric hollow GaN nanocolumn. The smallest decay model loci of the corresponding fully coupled piezoelectric case are also shown for comparison (the dashed line is for insulating and dash-dotted line for conducting boundary conditions on the two surface). Only real parts of the roots are shown.	89

7.1	Multilayered multiferroic (2-2) composites. h_k is the thickness of the k^{th} layer, and h is the total thickness of the composite.	103
7.2	A multiferroic composite composed of an orthotropic piezoelectric phase and an orthotropic magnetostrictive phase.	107
7.3	A multiferroic composite composed of an orthotropic piezoelectric phase, an orthotropic magnetostrictive phase and an orthotropic elastic substrate.	111
7.4	Variation of the ME coefficient $\bar{\alpha}_{11}$ vs. the BaTiO ₃ volume fraction for a series of the substrate volume fraction \bar{v}_s . The multiferroic composite is composed of a CoFe ₂ O ₄ –BaTiO ₃ bilayer on an elastic substrate.	113
7.5	Variation of the ME coefficient $\bar{\alpha}_{33}$ vs. the BaTiO ₃ volume fraction for a series of the substrate volume fraction \bar{v}_s . The multiferroic composite is composed of a CoFe ₂ O ₄ –BaTiO ₃ bilayer on an elastic substrate.	114
7.6	A multiferroic composite composed of a functionally graded orthotropic piezoelectric phase and a functionally graded orthotropic magnetostrictive phase.	115
7.7	Variation of the ME coefficient $\bar{\alpha}_{11}$ vs. the FGM BaTiO ₃ volume fraction v_p for a series gradient parameter λ_p with a linearly varied FGM BaTiO ₃ bonded to a homogeneous CoFe ₂ O ₄ layer.	117
7.8	Variation of the ME coefficient $\bar{\alpha}_{11}$ vs. the FGM BaTiO ₃ volume fraction v_p for a series gradient parameter λ_p with an exponentially varied FGM BaTiO ₃ bonded to a homogeneous CoFe ₂ O ₄ layer.	118
9.1	Distributions of the thermoelectric current density component j_1 along the x -axis ($y = 0$) induced by a line heat source of unit strength ($Q = 1$) located at origin for different values of the gradient parameter $\beta_1 = -5, -1, 0, 1, 5 \text{ m}^{-1}$ with $\beta_2 = 0$. The result for the homogeneous material case ($\beta_1 = \beta_2 = 0$) is the same as that based on the complex variable method (Eqs. (9.32) and (9.36)) as shown in open circles.	148
9.2	Distribution of the thermoelectric current density component j_1 along the x -axis ($y = 0$) induced by a line heat source of unit strength ($Q = 1$) located at origin for different combinations of the material property ratios σ , κ and ϵ with $\beta_1 = 1 \text{ m}^{-1}$ and $\beta_2 = 0$	149
10.1	A general QWR within a bimaterial substrate: An eigenstrain γ_{ij}^* is applied to the QWR which is an arbitrarily shaped polygon.	151
10.2	Geometry of a square InAs QWR on or inside the GaAs substrate. Shown in (a) to (c) are the three special cases: Namely, totally free-standing (a), half free-standing (half-in and half-out in (b)), and fully embedded (c).	157
10.3	Variation of relative strain energy with depth of a square QWR.	158
10.4	Variation of relative strain energy with base angle of isosceles triangle of InAs (111) QWR, which is free-standing on the GaAs (111) substrate.	159
10.5	Contours of strain energy density (10^9 kg/ms^2) in isosceles triangle of InAs (111) QWR with base angle 30° (a) or 45° (b)	160
10.6	Contours of strain energy density (10^9 kg/ms^2) in isosceles triangle of InAs (111) QWR with base angle 60° (a) or 75° (b).	161

11.1	Geometry of the flat triangle Δ (with corners 1,2,3), and transformation from the global (x_1, x_2, x_3) to local (ξ_1, ξ_2, ξ_3) coordinates where ξ_3 is along the outward normal direction of the flat triangle.	167
11.2	Geometry for (a) a cubic QD, (b) a truncated pyramid QD, (c) a pyramid QD, and (d) a point QD. Top row is the 3D view and bottom row is the vertical x - z plan view. All these QDs have the same volume.	168
11.3	Normalized strain energy on the surface of the half-space substrate of GaAs (001) (top row) and GaAs (111) (bottom row) induced by (a) a cubic, (b) a truncated pyramid, (c) a pyramid, and (d) a point QD, where the heavy blue, red and black lines correspond to normalized strain energy of 0.3, 0.6 and 0.9 respectively. The QD is embedded within the substrate with its top side at a depth $d = 2$ nm from the surface.	169
11.4	Geometry of a cubic QD within a half-space substrate with different depth d : the vertical x - z plan view (top row), and the strain energy induced by the cubic QD in substrate GaAs(001) (middle row) and GaAs (111) (bottom row): (a) $d = 1$, (b) $d = 2$, and (c) $d = 3$. The heavy blue, red and black lines correspond to normalized strain energy of 0.3, 0.6 and 0.9 respectively.	170
11.5	Geometry of a truncated pyramid QD within a half-space substrate with different depth d : the vertical x - z plan view (top row), and the strain energy induced by the truncated pyramid QD in substrate GaAs(001) (middle row) and GaAs (111) (bottom row): (a) $d = 1$, (b) $d = 2$, and (c) $d = 3$. The heavy blue, red and black lines correspond to normalized strain energy of 0.3, 0.6 and 0.9 respectively.	171
11.6	Geometry of a pyramid QD within a half-space substrate with different depth d : the vertical x - z plan view (top row), and the strain energy induced by the pyramid QD in substrate GaAs(001) (middle row) and GaAs (111) (bottom row): (a) $d = 1$, (b) $d = 2$, and (c) $d = 3$. The heavy blue, red and black lines correspond to normalized strain energy of 0.3, 0.6 and 0.9 respectively.	172
12.1	Schematic diagrams of hexagonal truncated-pyramidal QD showing dot shape and geometrical parameters. (a) 3D view of a single QD buried under half space substrate. Line A is parallel to the z -axis; (b) View of the QD structure in x - y plane; (c) View of two QDs in x - z plane.	175
12.2	(a) Contours of the electric potential Φ on the surface of AlN (0001) due to a hexagonal truncated-pyramidal QD. (b) Contours of the electric potential Φ on the surface of AlN (1000) due to a hexagonal truncated-pyramidal QD.	175
12.3	Strain distributions along line A of the QD embedded in a matrix of (a) AlN (0001) or (b) AlN (1000). The dashed line denotes γ_{xx} , the dot-dashed line γ_{zz} , and the solid line hydrostatic strain $\gamma_{xx} + \gamma_{yy} + \gamma_{zz}$	176
12.4	(a) Contours of the electric potential Φ on the surface of AlN (0001) due to two hexagonal truncated-pyramidal QDs. (b) Contours of the electric potential Φ on the surface of AlN (1000) due to two hexagonal truncated-pyramidal QDs. The distance D_x between the two QDs is 25 nm.	176

13.1	The GGA predicted ground state magnetic configuration- AF2 . (The arrow directions represent the spin arrangement)	178
13.2	Total density of states (TDOS) along with partial density of states (PDOS) of 4 <i>f</i> orbitals calculated for TbCu ₃ Mn ₄ O ₁₂ in the AF2 magnetic state using different methods. (a) GGA, (b) GGA+U with U_f 6.0 eV, (c) GGA+SOC [111], and (e) GGA+ U_f [111] with $U_f = 6.0$ eV at lower symmetry. The Fermi energy is indicated by the dotted line. The positive and negative values indicate spin up and spin down, respectively.	179
13.3	(a) Density of states (DOS) versus electronic energy for electrons of orbitals Tb-4 <i>f</i> , O-2 <i>p</i> , Cu-3 <i>d</i> , and Mn-3 <i>d</i> . (b) Electronic density distributions for electrons with energies in the range of -2.0 to -1.5 eV. Distributions colored red are for electrons with spin down (\downarrow), and distributions colored blue are for electrons with spin up (\uparrow).	180
13.4	Crystal structures and the coordination environment of Fe ions of CaFe ₃ Ti ₄ O ₁₂ in the left and CaFeTi ₂ O ₆ in the right.	180
13.5	Electron density plots around Fermi level for (a) AFM CaFe ₃ Ti ₄ O ₁₂ (d_{xy} , d_{xz} and d_{yz} orbitals are the same due to its m-3 point group symmetry in this perovskite) and (b) FM CaFeTi ₂ O ₆ (isosurface at 0.1 $e/\text{\AA}^3$ produced using XCRYSDEN).	181
13.6	GGA calculated total density of states for (a) CaFe ₃ Ti ₄ O ₁₂ in AFM and (b) CaFeTi ₂ O ₆ in FM; and GGA+ U_{eff} ($U_{eff} = 4.0$ eV) calculated results for (c) CaFe ₃ Ti ₄ O ₁₂ in AFM and (d) CaFeTi ₂ O ₆ in FM.	182

Chapter 1

Strain and piezoelectric fields in embedded quantum wire arrays

1.1 Introduction

Embedded quantum wires (QWRs) are semiconductor structures with electron confinement in two dimensions achieved using materials of different band gaps. The structures are either fabricated or directly grown such that long (on the order of 1 μm) and narrow (less than tens of nanometers) sections of semiconductor are surrounded by a cladding of a larger band gap material. The embedded situation is in contrast to free-standing or etched QWRs which are nanostructures surrounded at least partially by vacuum in order to achieve confinement, resulting in several key differences in physical behavior. The embedded wires almost always exhibit large strain fields owing to the inevitable lattice mismatch between the crystalline structure of the wire material and that of its surroundings. Another key difference is that the embedded wires can be electronically coupled at larger inter-wire spacing because the typical electron confinement is far weaker than that provided by the semiconductor-vacuum interface.

Embedded wire arrays can be separated into two main categories of infinite-space and half-space substrates that have distinct experimental realizations and theoretical treatments [6–8]. The infinite-space substrate case corresponds to the physical situation where a self-organization process results in embedded vertical wires orthogonal to the growth surface. Recently, vertical arrays have been proposed for a device structure to provide efficient carrier extraction mechanism in QWR solar cells [9]. The half-space substrate or ‘buried wire’ case corresponds to the situation where wires are defined lithographically from epitaxial films and overgrown to result in embedded wires oriented in the plane of the surface.

Strain and electric fields in nanoscale semiconductor structures induced by QWRs have been extensively investigated because the presence and magnitude of these fields are crucial for understanding the electronic and optical performance [10]. However, analytical studies are mostly restricted to a single QWR with the substrate being further limited to the purely elastic solid only [11–13], with some recent advances on size-dependent strain [14] and on nonuniform misfit eigenstrain [15]. As QWR arrays can be self-organized layer-by-layer and also can be grown in different orientations, a more realistic QWR semiconductor

model should include the electromechanical coupling present with closely spaced QWRs [1, 2, 16–22].

In this paper, a recently reported exact closed-form solution for a single QWR within a piezoelectric substrate [23] is extended to the QWR array case with multiple QWRs. While the QWR geometry can be arbitrary, the square shape is assumed in the analysis of the induced elastic and electric fields and of the interaction due to multiple QWRs. Both infinite and half-space GaAs substrates are considered with growth orientations of (001) and (111). The size of the individual square QWR is $4 \times 4 \text{ nm}^2$, and the number of QWR array is 1×1 , 3×3 , 5×5 , 7×7 for the full-space substrate and 1×1 , 2×3 , 3×5 , 4×7 for the half-space substrate. We remark that in this paper the simple inclusion model is followed as the difference between inclusion and inhomogeneity models is only about 10% within or close to the QWR region [24]. In what follows, we will first describe the problem in more detail with a brief review of the necessary equations for the induced strain and electric fields. Then numerical examples will be carried out and presented in terms of curves and contours. Finally, conclusions will be drawn on the QWR array induced elastic and piezoelectric features.

1.2 Problem description

We assume for the present discussion that simple arrays of QWRs with square cross-section are embedded in either GaAs(001) or GaAs(111) substrates. Each QWR has dimensions of $4 \text{ nm} \times 4 \text{ nm}$ and the center-to-center wire distance is 8 nm as in Figure 1.1(c). The half-space substrate case is distinguished from the infinite one by the presence of a free surface 2 nm from the top row of the array as in Figure 1.4(d). The lattice misfit strain within the wire is hydrostatic, i.e., $\gamma_{xx}^* = \gamma_{yy}^* = \gamma_{zz}^* = 0.07 = (a - a_o)/a_o$, where a and a_o are the lattice constants in the QWR and surrounding material, respectively. This approximation gives an upper bound on the strain present in the QWR. These strains would in reality be decreased by the presence of any dislocations or other lattice defects often present in overgrown cladding layers.

The elastic properties for modeling GaAs (001) are $C_{11} = 118 \times 10^9 \text{ N/m}^2$, $C_{12} = 54 \times 10^9 \text{ N/m}^2$, and $C_{44} = 59 \times 10^9 \text{ N/m}^2$. The piezoelectric constant and permeability for GaAs(001) are, respectively, $e_{14} = -0.16 \text{ C/m}^2$ and $\epsilon_{11} = 0.11 \times 10^{-9} \text{ C/V} \cdot \text{m}$. For (001)-oriented structures, the global coordinates x , y , and z are coincident with the crystalline axes, and for (111)-oriented structures the x -axis is along $[11\bar{2}]$, the y -axis along $[\bar{1}10]$, and the z -axis along the $[111]$ direction of the GaAs crystal structure [2]. The boundary condition on the surface for the half-space case is assumed to be traction-free and insulating [25]. The specific QWR arrays are 1×1 , 3×3 , 5×5 , 7×7 wires for full-space substrate and 1×1 , 2×3 , 3×5 , 4×7 wires for the half-space substrate as shown in Figures 1.1(c) and 1.4(d). The dashed lines in these figures indicate the locations at which the induced fields will subsequently be plotted and analyzed in detail.

For a QWR of polygonal shape within either an infinite or half-space substrate, the lattice misfit induced strain and electric fields can be expressed in exact closed form as in Ref. 23. While we briefly list these induced fields below, the complete derivation can be found in Ref. 23.

For an arbitrary side (line segment) of the polygon starting from point 1 (x_1, z_1) and ending at point 2 (x_2, z_2), the outward normal components $n_i(\mathbf{x})$ are constants, given by

$$n_1 = (z_2 - z_1)/l \quad n_2 = -(x_2 - x_1)/l \quad (1.1)$$

where $l = \sqrt{(x_2 - x_1)^2 + (z_2 - z_1)^2}$ is the length of the line segment (or the side of the polygon).

The strain and electric fields due to this side of the QWR polygon were found to be [23]

$$\begin{aligned} \gamma_{\beta\alpha}(\mathbf{X}) = & 0.5n_i C_{iJLm} \gamma_{Lm}^* \frac{l}{\pi} \text{Im} \left\{ A_{JR} h_{R,\alpha}(X, Z) A_{\beta R} + \sum_{v=1}^4 A_{JR} g_{R,\alpha}^v(X, Z) Q_{R\beta}^v \right\} \\ & + 0.5n_i C_{iJLm} \gamma_{Lm}^* \frac{l}{\pi} \text{Im} \left\{ A_{JR} h_{R,\beta}(X, Z) A_{\alpha R} + \sum_{v=1}^4 A_{JR} g_{R,\beta}^v(X, Z) Q_{R\alpha}^v \right\} \end{aligned} \quad (1.2)$$

$$\gamma_{2\alpha}(\mathbf{X}) = 0.5n_i C_{iJLm} \gamma_{Lm}^* \frac{l}{\pi} \text{Im} \left\{ A_{JR} h_{R,\alpha}(X, Z) A_{2R} + \sum_{v=1}^4 A_{JR} g_{R,\alpha}^v(X, Z) Q_{R2}^v \right\} \quad (1.3)$$

$$E_{\alpha}(\mathbf{X}) = -n_i C_{iJLm} \gamma_{Lm}^* \frac{l}{\pi} \text{Im} \left\{ A_{JR} h_{R,\alpha}(X, Z) A_{4R} + \sum_{v=1}^4 A_{JR} g_{R,\alpha}^v(X, Z) Q_{R4}^v \right\} \quad (1.4)$$

where the summation convention is applied to repeated indices. Lowercase indices range from 1 to 3, and upper case indices range from 1 to 4. Greek indices, e.g. α and β , only take on the values 1 or 3. $\text{Im}(z)$ is the imaginary part of the complex number z . C_{iJLm} are the extended material coefficients (elastic, piezoelectric, and permeability), and the matrices \mathbf{A} and \mathbf{Q} in Eqs. (1.2)–(1.4) are functions of these coefficients. Finally matrices \mathbf{h} and \mathbf{g} are functions of the arbitrary field point $\mathbf{X} = (X, Z)$, which are given in Ref. 23. We point out that these expressions of the strain and electric fields are for the half-space substrate case with the first terms (that is, the ones proportional to the matrix \mathbf{h}) being simply the results for the corresponding infinite substrate case.

We finally remark that Eqs. (1.2)–(1.4) are the strain and electric fields induced by one side of the QWR polygon. In order to find the induced fields due to the whole QWR polygon, we simply add the results from all sides of the polygon together. Similarly, for the multiple QWR case (or QWR array), we add the contributions from all the QWR polygons.

1.3 Results and analysis

1.3.1 QWR array in infinite substrate GaAs

Figures 1.1(a) and (b) show the variation of the hydrostatic strain along the positive x -axis for QWR arrays 1×1 to 7×7 in infinite-space GaAs (001) and (111) substrates, respectively. The corresponding geometry and coordinates are sketched in Figure 1.1(c). It is clearly shown in Figures 1.1(a) and (b) that the hydrostatic strains inside each QWR are nearly the same for different QWR array sizes, while the strains outside the QWRs are slightly different. We further remark that the induced hydrostatic strain inside the QWR is large, dominated by the misfit strain and therefore relatively insensitive to the number of

wires in a particular array. On the other hand, the calculated strain fields in the cladding outside of the QWR regions are more strongly influenced by the number of wires in the array. It is also observed that the distribution of the hydrostatic strain inside the QWR is different for the two substrate cases. While the strain curve inside the QWR is curved down for the (001) case, it is curved up for the (111) substrate case; the magnitude inside the QWR of (001) is slightly larger than that inside the QWR of (111). The induced hydrostatic strain inside the QWR is smaller than the preexisting misfit strain (0.14 for the misfit hydrostatic strain) due to the strain relaxation of the substrate.

The hydrostatic strain contours induced by QWR arrays within an infinite cladding are plotted in Figure 1.2. Panels (a) and (b) show the results for a single QWR (that is, a 1×1 QWR array) and a 3×3 array for the (001) substrate. Panels (c) and (d) are for the corresponding results for the (111)-oriented substrate. We observe again that the hydrostatic strain distributions for the two orientations are different, with even a logarithmic singularity existing at the corners of the GaAs (111) QWR [23].

As was observed recently, for QWR with GaAs (111) orientation, a large electric field could be also induced [2]. However, there is no literature report on the interaction of the induced electric field in a QWR array. Figure 1.3 presents the distribution of the electric field components E_x and E_z along the positive x -axis in an infinite substrate of GaAs (111) due to QWR arrays ranging in size from 1×1 to 7×7 . It is extremely interesting that while the component E_x within the QWR is relatively independent of the number of QWRs (Figure 1.3(a)), just like the strain distribution within the QWR, component E_z is completely different for different numbers of QWRs (Figure 1.3(b)).

1.3.2 QWR array in half-space substrate GaAs

Having studied the elastic and electric fields in infinite substrates GaAs(001) and GaAs(111), we now look at the case where the QWR arrays are within the half-space substrate. For this case, the surface boundary condition is assumed to be traction-free and electrically insulating [25] and the distance of the first row of the QWR array to the surface is $d = 2$ nm as shown in Figure 1.4(d). The distance among neighboring QWRs is the same as for the infinite substrate case, that is, the QWRs are separated by a distance of 8 nm (Figure 1.4(d)).

The first three subfigures of Figure 1.4 display hydrostatic strain variations along three different lines in the half-space GaAs (001) substrate. The QWR arrays studied are 1×1 , 2×3 , 3×5 , and 4×7 . While Figure 1.4(a) shows the variation of the hydrostatic strain along the z -axis, Figures 1.4(b) and (c) show the variation along the horizontal line at $z = -4$ nm (which is along the center of the first row of the QWR array) and along the free surface, respectively. It is apparent that the elastic fields both inside and outside the QWR have been greatly enhanced by the free surface condition, combined with the interaction among QWRs. This feature is particularly clear for the elastic strain close to the free surface where, for instance, the hydrostatic strains inside the QWR can be larger than the hydrostatic misfit strain (0.14) (array 4×7 in subfigures (a) and (b) of Figure 1.4). Furthermore, due to the existence of the free surface, the strain fields inside and outside the QWR are now clearly different for different numbers of QWRs (Figure 1.4(a)–(c)). The corresponding hydrostatic strain distributions within the (111) half-space substrate are shown in Figure 1.5. Again, similar features can be observed whilst the strain distribution

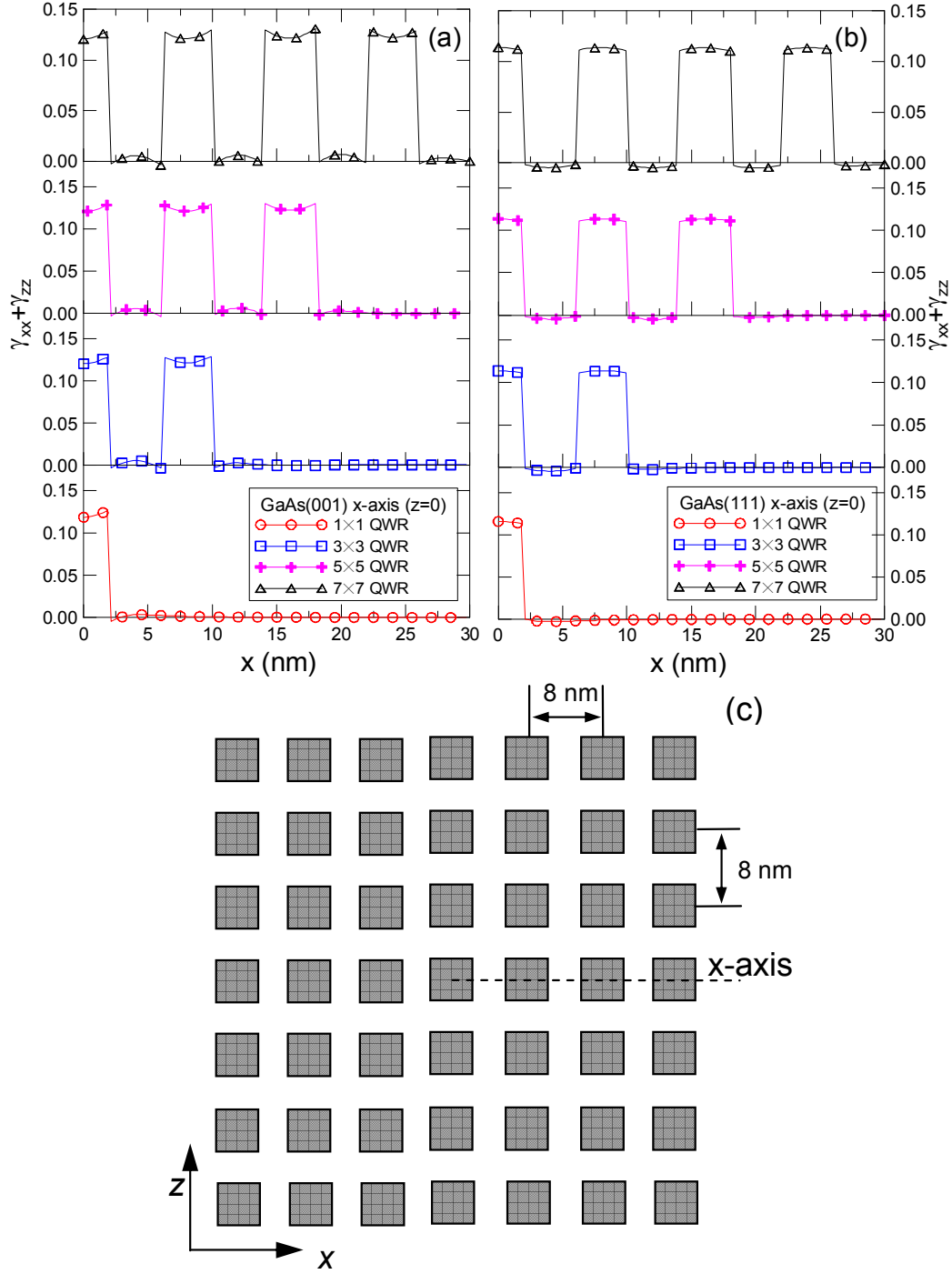


Figure 1.1: Variation of the hydrostatic strain for QWR arrays buried in (a) (001)-oriented and (b) (111)-oriented GaAs substrates. Panel (c) gives the geometric layout of the QWR arrays in an infinite space and the dashed line indicates the location of the cut line $z = 0$ for the field calculations of Figures 1.1 and 1.3.

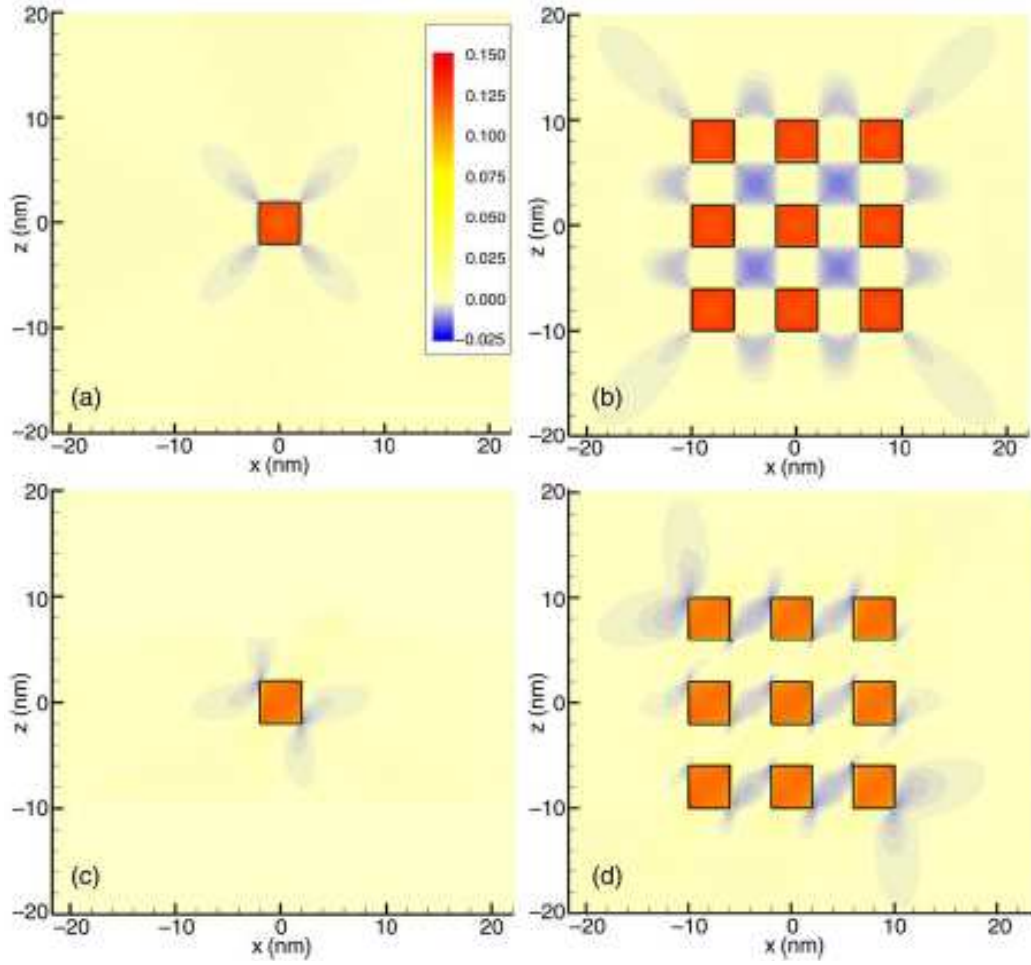


Figure 1.2: Contour plots of total hydrostatic strain for QWR arrays buried in infinite spaces. (a) 1×1 and (b) 3×3 arrays in (001)-oriented GaAs substrates; (c) 1×1 and (d) 3×3 arrays in (111)-oriented substrates.

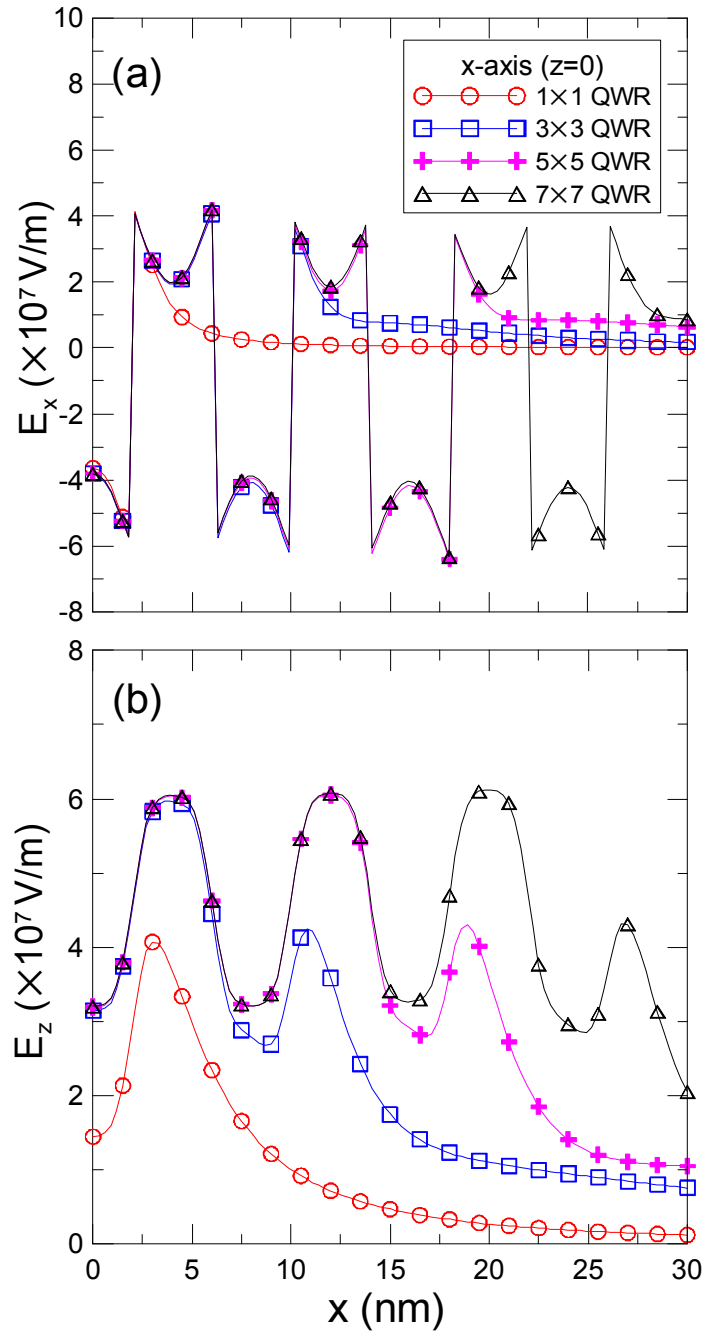


Figure 1.3: Variation of electric field components (a) E_x and (b) E_z along the x -axis (that is, $z = 0$ as shown in Figure 1.1(c)) for the case of QWR arrays buried in infinite space (111)-oriented substrates.

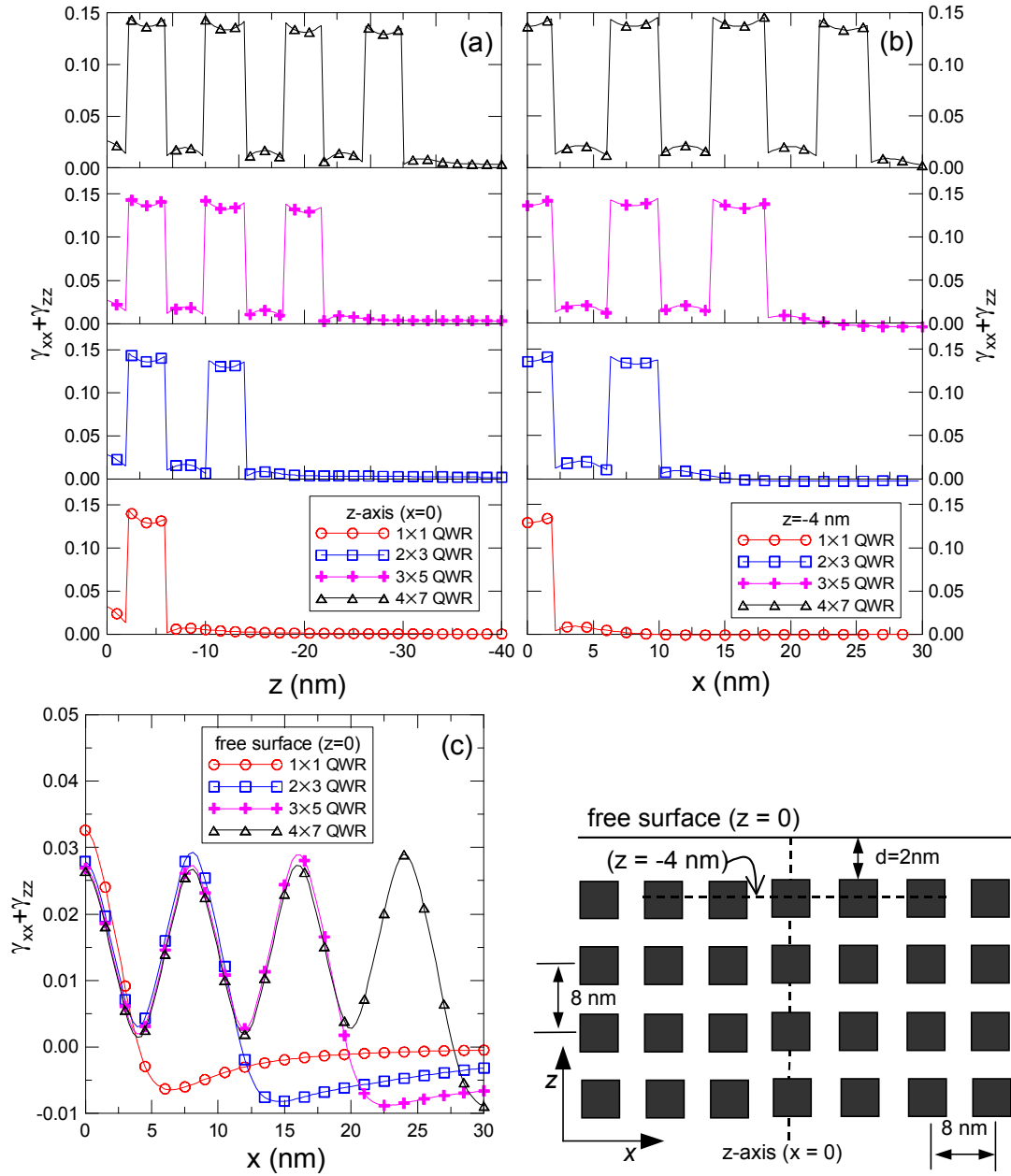


Figure 1.4: Variation of the hydrostatic strain for QWR arrays buried in half space (001)-oriented substrates. Hydrostatic strain is plotted for cut lines (a) along the z -axis, that is, $x = 0$, (b) along the horizontal line $z = -4$ nm, and (c) along the free surface $z = 0$. Panel (d) gives the geometric layout of the QWR arrays in a half space and the dashed lines indicate the locations for the field calculations of Figures 1.4–1.8.

is no longer symmetric as for the (001) case.

Figure 1.6 shows the contour of the hydrostatic strain in the half-space substrate GaAs, with QWR array 1×1 in (a) and 3×3 in (b) of GaAs(001), and QWR array 1×1 in (c) and 3×3 in (d) of GaAs(111). Comparing these contours to those in the corresponding infinite substrate (subfigures (a)-(d) of Figure 1.2), we observed that the free surface enhances the magnitude and alters the distribution of the strain fields. The effect of the substrate orientation on the strain distribution is also apparent by comparing the symmetry of the contours in Figures 1.6(a) and (b) with the asymmetric contours in Figures 1.6(c) and (d).

Figure 1.7 shows the distribution of the electric field components E_x and E_z along the free surface of the half-space substrate GaAs(111) for QWR arrays 1×1 to 4×7 . It is obvious that the electric field distribution is closely dependent on the size of the arrays, and the difference can be clearly identified for the field outside the QWRs (e.g. Figure 1.7(b)).

Finally, Figure 1.8 shows the variation of the electric field components E_x and E_z along the z -axis in the half-space GaAs (111) substrates. Again, the QWR array sizes range from 1×1 to 4×7 . The figure shows clearly the correlation between the number of QWRs and the electric field distribution, and this result could be useful to QWR-related device design.

1.4 Conclusions

A recent exact closed-form solution for a single QWR is extended to the QWR array case where each QWR is of a square shape. The QWR array can be within an infinite substrate or a half-space substrate. The induced elastic and electric fields are calculated for the substrate made of GaAs(001) and GaAs(111). The arrangement of QWR arrays is 1×1 , 3×3 , 5×5 , or 7×7 for the infinite-space substrate, and 1×1 , 2×3 , 3×5 , or 4×7 for the half-space substrate. Comparing the induced field within the infinite substrate to that in the half-space substrate, we observed that the existence of the free surface can greatly enhance the magnitude of the induced elastic and electric fields. It is particularly interesting that different number of QWRs has only slight influence on the elastic field inside the QWR. While different number of QWRs can affect the elastic field outside, this field is usually much smaller in magnitude than that inside. For the electric field, however, different number of QWRs can produce totally different field distributions both inside and outside the QWRs, in sharp contrast to the insensitivity of the elastic field inside the QWR to the number of QWRs.

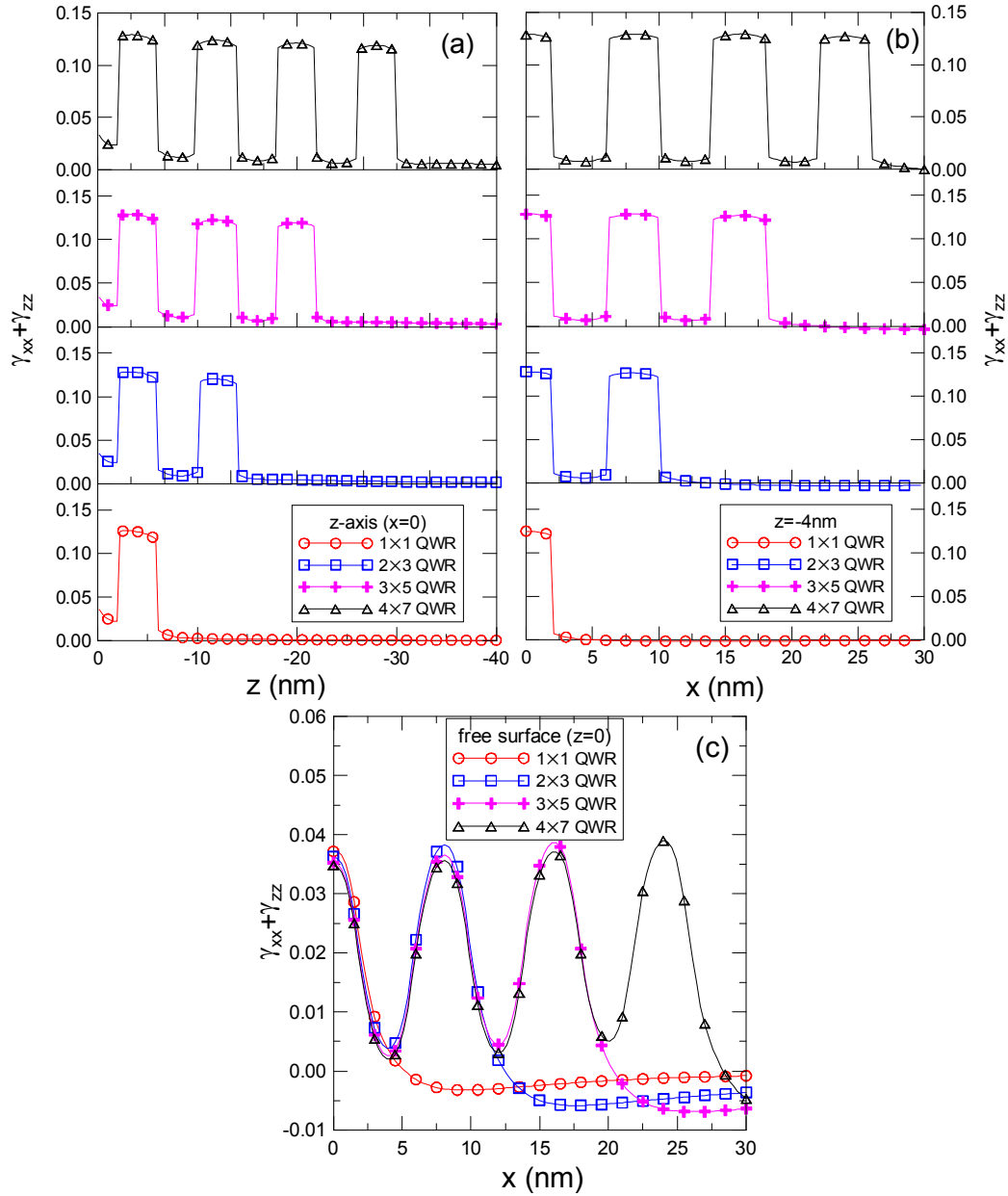


Figure 1.5: Variation of the hydrostatic strain for QWR arrays buried in half space (001)-oriented substrates. Hydrostatic strain is plotted for cut lines (a) along the z -axis, that is, $x = 0$, (b) along the horizontal line $z = -4$ nm, and (c) along the free surface $z = 0$. The cut lines are shown schematically in Figure 1.4(d).

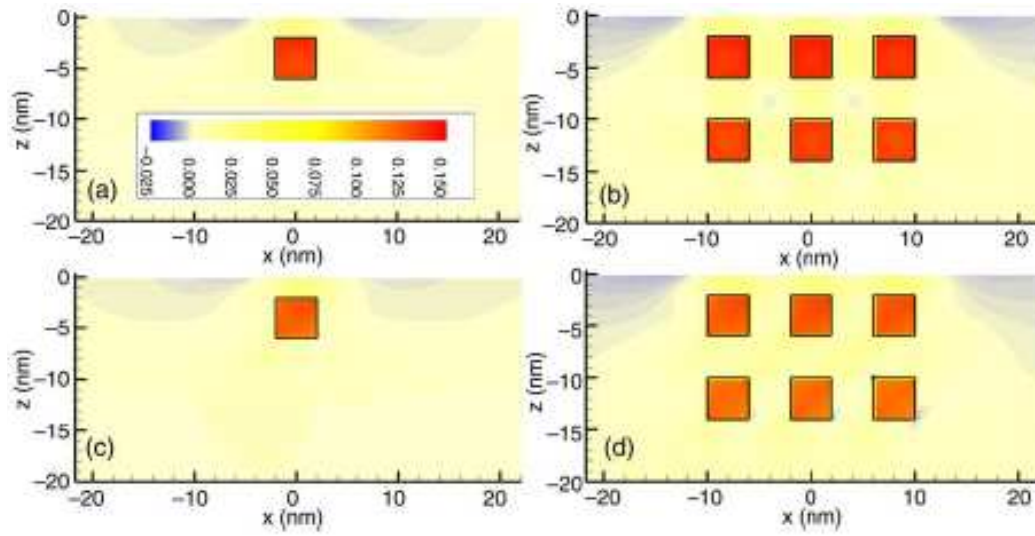


Figure 1.6: Contour plots of total hydrostatic strain for QWR arrays buried in half-spaces. (a) 1×1 and (b) 3×3 arrays in (001)-oriented GaAs substrates; (c) 1×1 and (d) 3×3 arrays in (111)-oriented substrates.

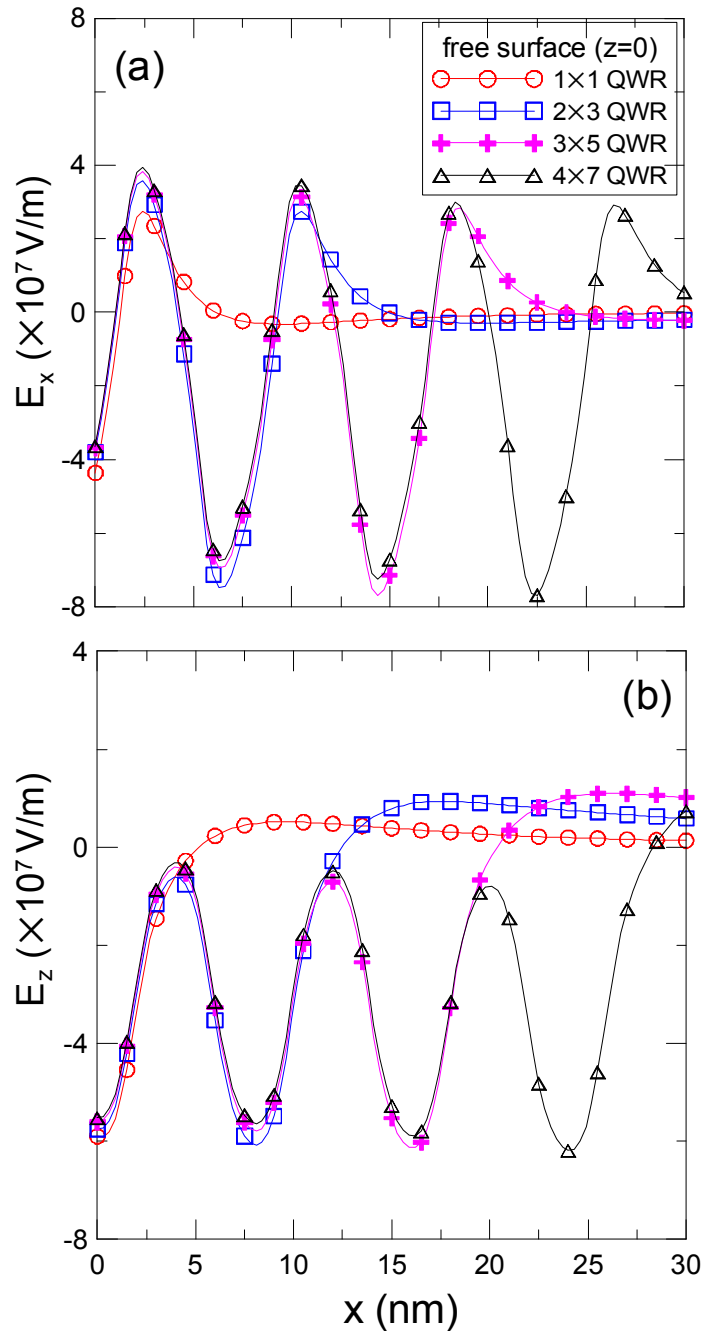


Figure 1.7: Variation of electric field components (a) E_x and (b) E_z along the free surface (that is, $z = 0$ as shown in Figure 1.4(d)) for the case of QWR arrays buried in half-space (111)-oriented substrates.

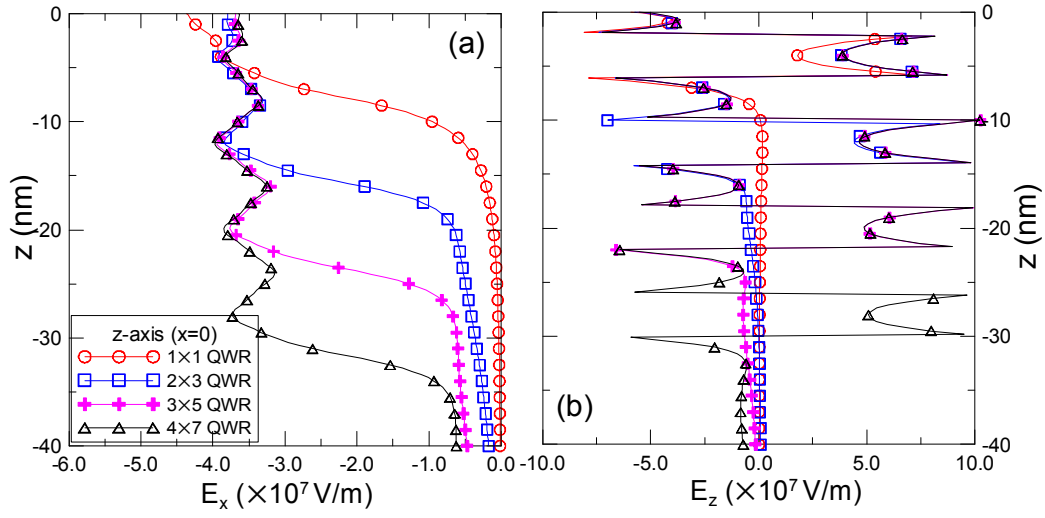


Figure 1.8: Variation of electric field components (a) E_x and (b) E_z along the z -axis (that is, $x = 0$ as shown in Figure 1.4(d)) for the case of QWR arrays buried in half-space (111)-oriented substrates.

Chapter 2

Elastic and piezoelectric fields in quantum wire semiconductor structures—a boundary integral equation analysis

2.1 Introduction

Quantum well (QW), quantum wire (QWR), and quantum dot (QD) semiconductor nanostructures with their associated degrees of quantum carrier confinement can be tailored to address the electron energy state requirements of future electronic and optoelectronic devices [26]. Frequently, the nanostructures under consideration are formed through heteroepitaxy. Therefore the lattice misfit conditions, or pseudomorphically induced strain fields, are central to determining and engineering the electronic states of the quantum mechanical system through modifications to the electronic structure (changes in band gap and effective mass) of the constituent materials and direct modifications to the confining potential (changes in lattice polarization). It is crucial from a device modeling perspective that the induced strain and electric fields in the nanostructure be modeled accurately and efficiently.

This study is focused on the elastic and piezoelectric field prediction in strained QWR structures. From the field of continuum mechanics, we have a first approximation, the well-known Eshelby inclusion method [27–29], which has been successfully applied to study the induced strain/electric fields in many structures. In the Eshelby treatment, the lattice misfit between the QWR and substrate (or matrix) is imposed but the QWR material is assumed to be the same as its substrate [10, 18, 23, 30–32]. The advantage of the Eshelby inclusion method is its simplicity and the induced elastic and electric fields can be found analytically for both 2D QWR and 3D QD cases.

Recently, the relative accuracy and underlying assumptions of the inclusion model have come under scrutiny. A structural inhomogeneity model which considers the relevant and different elastic material properties present in realistic QWR/QD structures was developed [24, 33] and compared with the inclusion method. In our previous work [24], the issue of the homogeneous inclusion vs. structural inhomogeneity in the context of strained QWRs

was studied in detail for purely elastic zincblende semiconductors using the boundary integral equation method (BEM). Numerical examples were given for InAs/GaAs QWRs in both (001) and (111) growth directions for square and trapezoidal QWR cross-sections. Several results were obtained:

1. As expected, the strain fields predicted in the substrate but far away from the QWR were very similar for both models because the internal details of the wire composition are irrelevant to the far-field response.
2. For points within or near to the QWR, the variation in predicted field strengths between the models can be as high as 10% for these materials and geometries.
3. Although the singular behavior present near the sharp corners of the QWR looks similar in form for both models, the amplitudes of the singularity are significantly different in some cases.

A more complete picture of the strain effects on quantum heterostructures is gained by extending the calculations to include any spontaneous and piezoelectric polarizations which will directly change the local electrostatic potential. So far, the differences present in the induced polarization electric fields as obtained by both the homogeneous inclusion and structural inhomogeneity models have not been reported in the literature, which is the main motivation of this study. In this paper we therefore develop a simple BEM formulation to investigate the elastic and electric fields present in QWR semiconductor structures. Our BEM algorithm is based on constant-element discretization with analytical kernel function integration. The corresponding BEM routine is then applied to systems composed of InAs QWRs in (001)- and (111)-orientated GaAs and of InN QWRs in (0001)- and (1000)-oriented wurtzite AlN ((1000) means along the polar direction, i.e., a direction normal to the (0001)-axis). The QWRs considered are polygonal and the formalism is sufficiently general to include the possibility of irregular shapes. While our BEM program includes the simple homogeneous inclusion as a limiting case, the Eshelby inclusion solution developed before [24] is also applied to check the accuracy of our BEM program. Though the elastic strain features from both the inclusion and inhomogeneity models are consistent with previous reports [24, 33], we will show that the induced electric fields can be very different. The main conclusion is that the inhomogeneous material properties need to be taken into account to reliably predict the induced electric fields in strained QWRs.

2.2 Problem description and basic equations

A general QWR problem is illustrated by Figure 2.1, where, to facilitate our discussion, we have defined the following extended strain:

$$\gamma_j = \begin{cases} \gamma_j & I = i = 1, 2, 3 \\ -E_j & I = 4 \end{cases} \quad (2.1)$$

In Eq. (2.1), γ_{ij} is the total elastic strain tensor and E_i the i^{th} Cartesian component of the total electric field, which are related to the total elastic displacement u_i and total electric

potential ϕ in the usual way by

$$\begin{aligned}\gamma_{ij} &= \frac{1}{2} \left(\frac{\partial u_i}{\partial x_j} + \frac{\partial u_j}{\partial x_i} \right) \\ E_j &= -\frac{\partial \phi}{\partial x_j}\end{aligned}\tag{2.2}$$

The total extended strain is the sum

$$\gamma_{ij} = \gamma_{ij}^e + \gamma_{ij}^*\tag{2.3}$$

where γ_{ij}^* is the extended eigenstrain in the QWR, and γ_{ij}^e the extended strain that appears in the generalized constitutive relation [24] as

$$\sigma_{iJ} = C_{iJKl} \gamma_{Kl}^e\tag{2.4a}$$

or

$$\sigma_{iJ} = C_{iJKl} (\gamma_{Kl} - \chi \gamma_{Kl}^*)\tag{2.4b}$$

where summation over repeated indices K, l is implied and χ is equal to one if the observation point is within the QWR domain V and zero outside. It is clear that, in this paper, the contribution from the spontaneous polarization is not considered. Furthermore, the corresponding material properties belong to the QWR and substrate should be used in Eq. (2.4) when calculating the induced extended stress, which is defined as

$$\sigma_{iJ} = \begin{cases} \sigma_{ij} & J = j = 1, 2, 3 \\ D_i & J = 4 \end{cases}\tag{2.5}$$

where σ_{ij} and D_i are the stress and electric displacement, respectively. In Eq. (2.4), the general moduli are defined as

$$C_{iJKl} = \begin{cases} C_{ijkl} & J, K = j, k = 1, 2, 3 \\ e_{lij} & J = j = 1, 2, 3; K = 4 \\ e_{ikl} & J = 4; K = k = 1, 2, 3 \\ -\epsilon_{il} & J = K = 4 \end{cases}\tag{2.6}$$

with C_{ijkl} , e_{ijk} and ϵ_{ij} being the elastic moduli, piezoelectric coefficients, and dielectric constants, respectively. For completeness, we further define the extended displacement as

$$u_I = \begin{cases} u_i & I = i = 1, 2, 3 \\ \phi & I = 4 \end{cases}\tag{2.7}$$

Let us assume that the general misfit strain γ_{ij}^* is uniform within the QWR domain and is zero outside. The interface between the QWR and matrix is labeled S . We also denote C_{iJKl}^w and C_{iJKl}^m as the general moduli of the QWR and matrix materials, respectively. For

the homogeneous inclusion problem, $C_{iJKl}^w = C_{iJKl}^m$. If there is no body force and no electric charge within the QWR system, one can easily show that, for the matrix domain,

$$C_{iJKl}^m u_{K,li}^m = 0 \quad (2.8)$$

and for the QWR domain,

$$C_{iJKl}^w u_{K,li}^w = C_{iJKl}^w \gamma_{Kl,i}^* \quad (2.9)$$

It is clear that the right hand side of Eq. (2.9) is equivalent to a body force defined as

$$f_J^{(w)} = -C_{iJKl}^w \gamma_{Kl,i}^* \quad (2.10)$$

which is also called the equivalent body force of the eigenstrain [23, 29]. This equivalent body force will be employed in the next section to convert the contribution of the eigenstrain to a boundary integral along the interface of the QWR and its substrate. Again, the superscripts m and w denote quantities associated with the matrix and QWR, respectively.

2.3 Boundary integral equations and constant-element discretization

To solve the problem shown in Figure 2.1, we apply the BEM to both the QWR and its matrix/substrate. The boundary integral formulation can be expressed as [24, 33]

$$b_{IJ}(\mathbf{X}) u_J^m(\mathbf{X}) = \int_S [U_{IJ}^m(\mathbf{X}, \mathbf{x}) t_J^m(\mathbf{x}) - T_{IJ}^m(\mathbf{X}, \mathbf{x}) u_J^m(\mathbf{x})] ds(\mathbf{x}) \quad (2.11)$$

for the matrix, and

$$b_{IJ}(\mathbf{X}) u_J^w(\mathbf{X}) = \int_S [U_{IJ}^w(\mathbf{X}, \mathbf{x}) (t_J^w(\mathbf{x}) + f_J^w(\mathbf{x})) - T_{IJ}^w(\mathbf{X}, \mathbf{x}) u_J^w(\mathbf{x})] ds(\mathbf{x}) \quad (2.12)$$

for the QWR.

In Eqs. (2.11) and (2.12) t_J and u_J are the traction and displacement components, and \mathbf{x} and \mathbf{X} are the coordinates of the field and source points, respectively. The coefficients b_{IJ} equal δ_{IJ} if \mathbf{X} is an interior point and $\delta_{IJ}/2$ at a smooth boundary point. For points at complicated geometry locations, these coefficients can be determined by the rigid-body motion method [34]. Furthermore, in Eq. (2.12), f_J^w is the traction induced by the misfit eigenstrain inside the QWR, which is given by Eq. (2.10).

The Green's functions U_{IJ} and T_{IJ} in Eqs. (2.11) and (2.12) are taken to be the special 2D Green's functions for the full plane [25, 35]. The indices I and J indicate the J^{th} Green's (general) displacement/traction (at \mathbf{x}) in response to a (general) line force in the I^{th} direction (applied at \mathbf{X}). Note that the Green's functions are in exact closed form, and thus their integration over constant elements can be carried out exactly as discussed below. This is computationally desirable as it is very efficient and accurate for the calculation.

Employing constant-value elements, we divide the boundary (that is, the interface) into N segments with the n^{th} element being labeled as s_n . The constant values u_{Jn} and t_{Jn} on the n^{th} element are equal to the displacement and traction values at the center of the

element. Under this assumption, the boundary integral equations (2.11) and (2.12) for the surrounding matrix and QWR domains are reduced to the following algebraic equations

$$b_{IJ}u_J^m + \sum_{n=1}^N \left(\int_{s_n} T_{IJ}^m ds \right) u_{Jn}^m = \sum_{n=1}^N \left(\int_{s_n} U_{IJ}^m ds \right) t_{Jn}^m \quad (2.13)$$

and

$$b_{IJ}u_J^w + \sum_{n=1}^N \left(\int_{s_n} T_{IJ}^w ds \right) u_{Jn}^w = \sum_{n=1}^N \left(\int_{s_n} U_{IJ}^w ds \right) (t_{Jn}^w + C_{pJKl}^w \gamma_{Kl}^* n_p) \quad (2.14)$$

The difference between Eqs. (2.13) and (2.14) is the traction induced by the misfit eigen-strain inside the QWR in Eq. (2.14). The remaining problem is to find suitable Green's functions U_{IJ} and T_{IJ} , as well as their integrals over each element s_n , which are the kernel functions in these equations. Next we will present the analytical integration of these Green's functions over an arbitrary constant element.

To carry out the line integration of the Green's functions over a constant element, we first look at the Green's functions in Eqs. (2.13) and (2.14). They can be expressed as [23, 25, 35]

$$U_{IJ}(\mathbf{x}, \mathbf{X}) = \frac{1}{\pi} \text{Im} \{ A_{JR} \ln(z_R - s_R) A_{IR} \} \quad (2.15)$$

$$T_{IJ}(\mathbf{x}, \mathbf{X}) = \frac{1}{\pi} \text{Im} \left\{ B_{JR} \frac{p_R n_1 - n_3}{z_R - s_R} A_{IR} \right\} \quad (2.16)$$

where Im stands for the imaginary part of the complex value, A_{IJ} and B_{IJ} are two constant matrices related only to the material properties [35], n_1 and n_3 are the unit outward normal components projected along the x - and z -directions, p_R ($R = 1, 2, 3, 4$) are the Stroh eigenvalues, and $z_R = x + p_R z$ and $s_R = X + p_R Z$ are the field and source points, respectively.

To form an arbitrary element, we define a generic line segment representing any constant element along the interface in the xz -plane, starting from point 1, (x_1, z_1) and ending at point 2, (x_2, z_2) . In terms of the parameter t (where $0 \leq t \leq 1$), any constant line element can be parameterized as

$$\begin{aligned} x &= x_1 + (x_2 - x_1)t \\ z &= z_1 + (z_2 - z_1)t \end{aligned} \quad (2.17)$$

The outward normal components along the line segment are constant, given by

$$n_1 = (z_2 - z_1)/l \quad n_3 = -(x_2 - x_1)/l \quad (2.18)$$

where l is the length of the line segment and the elemental length is $ds = l dt$.

It is observed that Eqs. (2.11) and (2.12) consist of only two different integrals possessing the following analytic results. The first integral is a function of the source point $\mathbf{X} = (X, Z)$ and is expressed in parameterized form by

$$h_R(X, Z) \equiv \int_0^1 \ln(z_R - s_R) dt \quad (2.19)$$

which can be expanded as

$$h_R(X, Z) = \int_0^1 \ln\{[(x_2 - x_1) + p_R(z_2 - z_1)]t + [(x_1 + p_R z_1) - s_R]\} dt \quad (2.20)$$

and can immediately be evaluated to the following closed form:

$$h_R(X, Z) = \frac{(x_1 + p_R z_1) - s_R}{(x_2 - x_1) + p_R(z_2 - z_1)} \ln \left[\frac{x_2 + p_R z_2 - s_R}{x_1 + p_R z_1 - s_R} \right] + \ln[x_2 + p_R z_2 - s_R] - 1 \quad (2.21)$$

Similarly, we take the second integral as

$$g_R(X, Z) \equiv \int_0^1 \frac{dt}{z_R - s_R} \quad (2.22)$$

which upon evaluation leads to

$$g_R(X, Z) = \frac{1}{(x_2 - x_1) + p_R(z_2 - z_1)} \ln \left[\frac{x_2 + p_R z_2 - s_R}{x_1 + p_R z_1 - s_R} \right] \quad (2.23)$$

Therefore, based on the constant-element discretization, the two boundary integral equations (2.11) and (2.12) for the QWR and matrix/substrate can be cast into a system of algebraic equations for the interface points. In matrix form, they can be expressed as

$$\mathbf{U}^w \mathbf{t}^w - \mathbf{T}^w \mathbf{u}^w = \mathbf{f}^w \quad (2.24)$$

$$\mathbf{U}^m \mathbf{t}^m - \mathbf{T}^m \mathbf{u}^m = 0 \quad (2.25)$$

where the coefficient matrices \mathbf{U} and \mathbf{T} are the exact integrals of Green's functions on each constant element given in Eqs. (2.21) and (2.23), and \mathbf{u} and \mathbf{t} are the general displacement and traction vectors at the center of each element. The right-hand side term \mathbf{f}^w in Eq. (2.24) is the general equivalent force corresponding to the misfit eigenstrain within the QWR.

We assume that the matrix and QWR are perfectly bonded along the interface S , that is, the continuity conditions $\mathbf{u}^m = \mathbf{u}^w$ and $\mathbf{t}^m = -\mathbf{t}^w$ hold. Then the number of unknowns is identical to the number of equations and all the nodal (general) displacements and tractions can be determined. Furthermore, making use of the Somigliana identity, the displacement at any location within the QWR can be easily obtained in general as

$$b_{IJ} u_J^w + \sum_{n=1}^N \left(\int_{s_n} T_{IJ}^w d\Gamma \right) u_{Jn}^w = \sum_{n=1}^N \left(\int_{s_n} U_{IJ}^w d\Gamma \right) (t_{Jn}^w + C_{pJKl}^w \gamma_{Kl}^* n_p) \quad (2.26)$$

where the last force term exists exclusively for the QWR domain. Furthermore, using Eqs. (2.1)–(2.5), we can calculate the induced elastic and electric fields at any point within the matrix or QWR.

In summary, we have derived exact boundary integral equations for the QWR and matrix domains by constant-element discretization along their interface. These equations can be used to find the elastic and piezoelectric responses along the interface and at any location within the QWR and its surrounding matrix. Applications of these solutions to QWR systems are discussed in the next section.

	InAs	GaAs
$C_{11} = C_{22} = C_{33}$ (GPa)	83.29	118.8
$C_{12} = C_{13} = C_{23}$	45.26	53.8
$C_{44} = C_{55} = C_{66}$	39.59	59.4
$e_{14} = e_{25} = e_{36}$ (C/m ²)	-0.0456	-0.16
$\epsilon_{11} = \epsilon_{22} = \epsilon_{33}$ ($10^{-9}\text{C}^2/(\text{N} \cdot \text{m}^2)$)	0.1345808	0.110675
$\gamma_{11}^* = \gamma_{22}^* = \gamma_{33}^*$	0.07	

Table 2.1: Material properties & misfit strains in InAs(001)/GaAs(001) [1, 2]

	InN	AlN
$C_{11} = C_{22}$ (GPa)	223.0	396.0
C_{33}	224.0	373.0
C_{12}	115.0	137.0
$C_{13} = C_{23}$	92.0	108.0
$C_{44} = C_{55}$	48.0	116.0
C_{66}	54.0	129.5
$e_{15} = e_{24}$ (C/m ²)	-0.22	-0.48
$e_{31} = e_{32}$	-0.57	-0.58
e_{33}	0.97	1.55
$\epsilon_{11} = \epsilon_{22}$ ($10^{-9}\text{C}^2/(\text{N} \cdot \text{m}^2)$)	132.81	79.686
ϵ_{33}	132.81	97.372
$\gamma_{11}^* = \gamma_{22}^*$	0.1357	
γ_{33}^*	0.1267	

Table 2.2: Material properties & misfit strains in InN(0001)/AlN (0001) [1, 2]

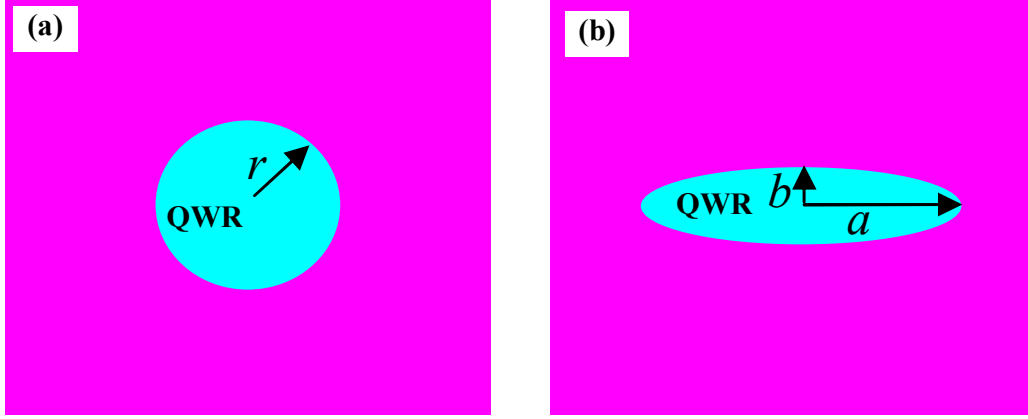


Figure 2.1: (a) A circular QWR of radius $r = 10$ nm in an infinite substrate, and (b) an elliptical QWR with length of the semi-major axis $a = 20$ nm in horizontal x -direction and the semi-minor axis $b = 5$ nm in vertical z -direction in an infinite substrate in (b).

		Inclusion	Inhomogeneity	Relative Error (%)
Circle	$\gamma_{xx} = \gamma_{zz}$	0.0612	0.0566	9
Ellipse	γ_{xx}	0.0208	0.0134	55
	γ_{zz}	0.1058	0.1133	7

Table 2.3: Strains in inclusion GaAs (001) and inhomogeneity InAs(001)/GaAs (001)

2.4 Numerical examples

Numerical examples are developed in this section for two QWR material systems. One is the case of InAs wires in GaAs with (001)- and (111)-oriented substrates, and the other case is for InN wires buried in AlN with (1000)- and (0001)-orientations. Both the inclusion and inhomogeneity models are studied. For the corresponding inclusion model, the QWR materials take the material constants of their surrounding matrix but retain their misfit strain conditions. The material properties and eigenstrains within the QWR in the material coordinates are listed in Tables 2.1 and 2.2 [1, 2].

For InAs (111) and GaAs (111), the coordinate x -axis is along $[11\bar{2}]$, y -axis along $[\bar{1}10]$, and z -axis along $[111]$ directions of the crystal [2]. Their material properties can be obtained by coordinate rotations [2]. For InN(1000) and AlN(1000), the material properties can be obtained by simply switching the coordinate directions (between x and z).

2.4.1 Circular and elliptic QWRs

The first example is for circular and elliptic QWRs in an infinite substrate (Figure 2.1). For this case, exact solutions can be obtained for both the inclusion and inhomogeneity models.

Tables 2.3 through 2.6 compare the strain and electric fields inside both the circular and elliptic QWRs treated as inclusions and inhomogeneities (Figure 2.1), using the material properties and eigenstrains listed in Tables 2.1 and 2.2. We point out that for these QWR

		Inclusion	Inhomogeneity	Relative Error (%)
Circle	γ_{xx}	0.0596	0.0551	8
	γ_{zz}	0.0543	0.5000	9
	$2\gamma_{xz}$	-0.0149	-0.0145	2
	$E_x (\times 10^7 \text{ V/m})$	4.020	0.2738	1368
	$E_z (\times 10^7 \text{ V/m})$	-2.843	-0.1936	1368
Ellipse	γ_{xx}	0.0260	0.0196	33
	γ_{zz}	0.0829	0.0861	4
	$2\gamma_{xz}$	-0.0081	-0.0075	9
	$E_x (\times 10^7 \text{ V/m})$	1.235	0.4773	176
	$E_z (\times 10^7 \text{ V/m})$	-9.770	2.074	571

Table 2.4: Strains in inclusion GaAs (111) and inhomogeneity InAs(111)/GaAs (111)

		Inclusion	Inhomogeneity	Relative Error (%)
Circle	γ_{xx}	0.1184	0.1063	11
	γ_{zz}	0.0984	0.0876	12
	$E_z (\times 10^7 \text{ V/m})$	-47.05	-42.65	10
Ellipse	γ_{xx}	0.0515	0.0310	66
	γ_{zz}	0.1555	0.1746	11
	$E_z (\times 10^7 \text{ V/m})$	-159.0	-130.1	22

Table 2.5: Strains in inclusion AlN(0001) and inhomogeneity InN(0001)/AlN(0001)

		Inclusion	Inhomogeneity	Relative Error (%)
Circle	γ_{xx}	0.0984	0.0876	12
	γ_{zz}	0.1184	0.1063	11
	$E_x (\times 10^7 \text{ V/m})$	-47.05	-42.65	10
Ellipse	γ_{xx}	0.0403	0.0223	81
	γ_{zz}	0.1797	0.2008	11
	$E_x (\times 10^7 \text{ V/m})$	2.436	2.780	12

Table 2.6: Strains in inclusion AlN(1000) and inhomogeneity InN(1000)/AlN(1000)

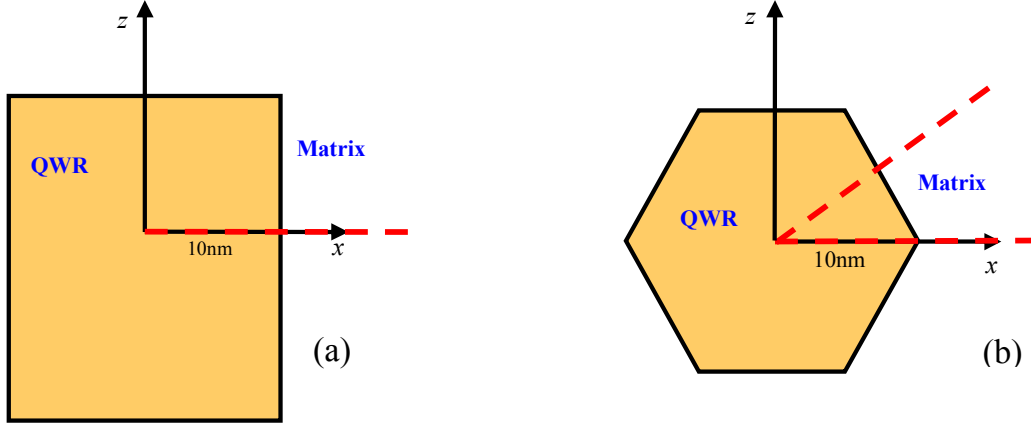


Figure 2.2: A square QWR in GaAs (a) and a hexagon QWR in AlN (b). The dashed lines show where the responses are calculated.

shapes, the induced fields inside the QWR are uniform for both models. These results can be obtained using the analytical solution for the QWR inclusion problem [23], combined with the Eshelby inhomogeneity method [27–29]. Furthermore, we have also used our BEM formulation presented above for these models. In doing so, we have mutually checked our analytical and numerical solutions.

It is observed from Tables 2.3 through 2.6 that the relative error, defined as (inclusion solution – inhomogeneity solution)/(inhomogeneity solution), for the strain (the large z -component γ_{zz} in the ellipse case) between the inclusion and inhomogeneity models is generally around 10%, which is consistent with the recent prediction for the purely elastic QWR case [24, 33]. We also note that for the elliptical QWR case, the horizontal strain γ_{xx} (the small x -component) based on the inhomogeneity model can be much different from that based on the inclusion model. Perhaps the most important feature is on the difference of the electric fields (in units of 10^7 V/m) in the InAs/GaAs (111) system. It is observed that the electric field difference based on the inclusion and inhomogeneity models can be more than one order of the magnitude (Table 2.4). This special feature has not been reported in any previous investigation and will be discussed again in the following two examples.

2.4.2 Square QWR in GaAs and hexagon QWR in AlN

The second example is for a square QWR in GaAs and a hexagonal QWR in AlN, shown in Figure 2.2, where the induced strain and electric fields are presented along the horizontal and diagonal dashed lines in the figure.

Shown in Figures 2.3 and 2.4 are the hydrostatic strains ($\gamma_{xx} + \gamma_{zz}$) along both horizontal and diagonal lines in both InAs/GaAs (001) and InAs/GaAs (111). These results are similar to those for the InAs/GaAs QWR with trapezoidal cross-section [24]. In general, the elastic strain fields inside the QWR are much larger than those in the substrate and the difference in the strain fields based on the inhomogeneity and inclusion models is apparent, particularly within the QWR.

While there is no induced electric field in the InAs/GaAs (001) system, large electric

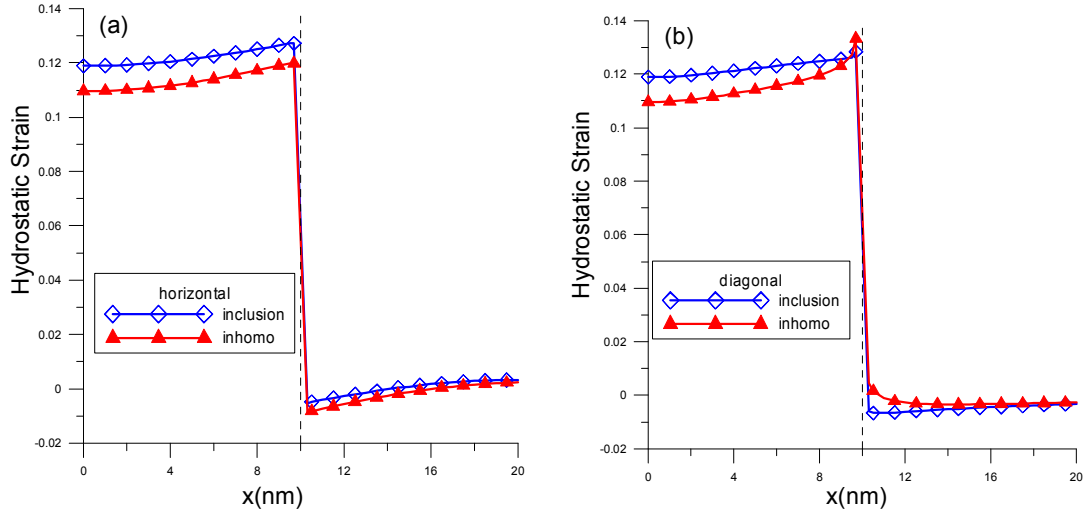


Figure 2.3: Hydrostatic strains ($\gamma_{xx} + \gamma_{zz}$) in a square QWR InAs/GaAs (001) along the horizontal (a) and diagonal (b) lines as defined in Figure 2.2(a).

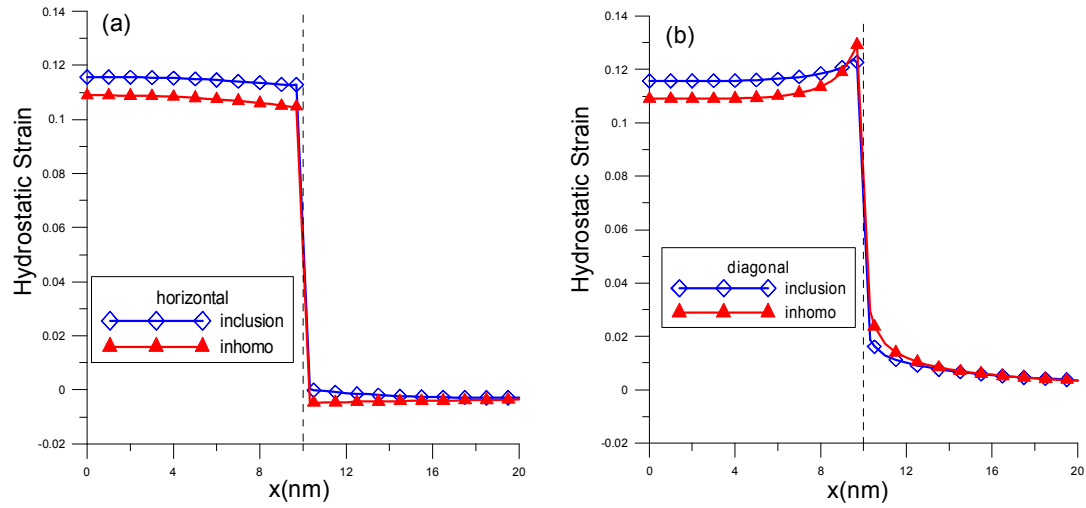


Figure 2.4: Hydrostatic strains ($\gamma_{xx} + \gamma_{zz}$) in a square QWR InAs/GaAs (111) along the (a) horizontal and (b) diagonal dashed lines shown in Figure 2.2(a).

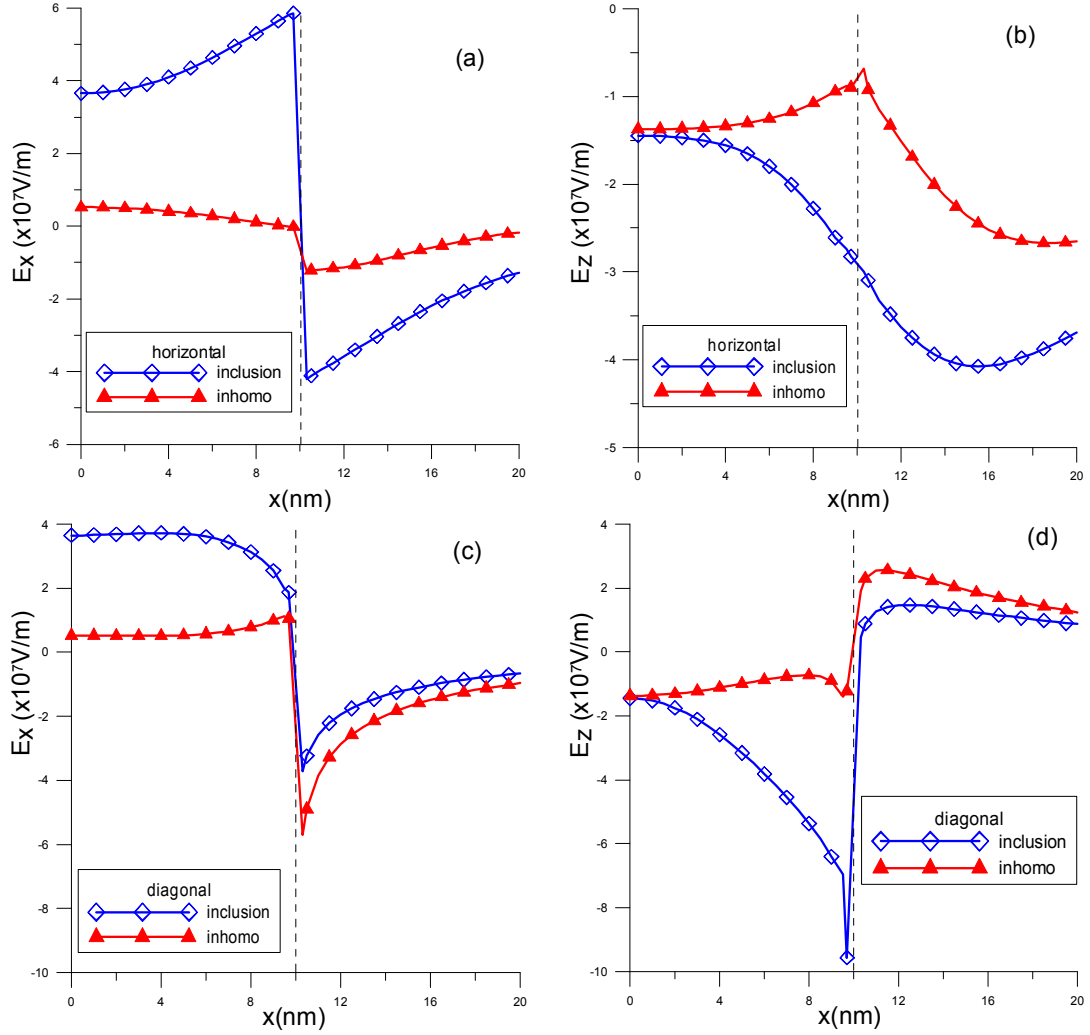


Figure 2.5: (a) E_x and (b) E_z along the horizontal dashed line shown in Figure 2.2(a), and (c) E_x and (d) E_z along the diagonal dashed line of the same figure, in a square QWR InAs/GaAs(111).

fields can be observed in QWs, QWRs, and QDs (111) systems [2, 16]. Here in Figure 2.5, we show for the first time that the induced electric fields along the horizontal and diagonal lines in InAs/GaAs (111) of a square QWR can be large and that the difference between the electric fields based on the inclusion and inhomogeneity models can be significant, especially within the QWR. In other words, electric fields in the InAs/GaAs (111) orientation should not be neglected, and should be considered using the inhomogeneity model as the simple inclusion model could be completely wrong. Furthermore, for the induced electric field, its magnitude both inside and outside the QWR are comparable, in contrast to the corresponding strain field featured in Figures 2.3 and 2.4.

Figure 2.6 shows the hydrostatic strain in InN/AlN(0001) along the horizontal and inclined lines. Similar to the hydrostatic strain in the InAs/GaAs system, we observed that outside the QWR, both the inclusion and inhomogeneity models predict similar results,

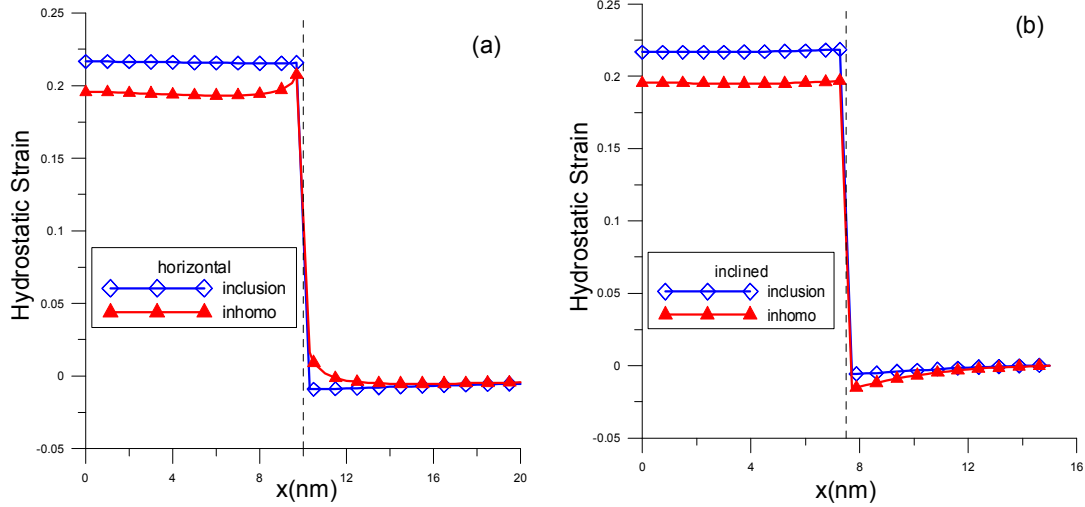


Figure 2.6: Hydrostatic strains ($\gamma_{xx} + \gamma_{zz}$) in a hexagonal QWR InN/AlN (0001) along the (a) horizontal and (b) inclined dashed lines shown in Figure 2.2(b).

with their magnitudes outside being also much smaller than those inside the QWRs. However, near the interface between the QWR and substrate, apparent differences can be observed. Furthermore, for the hydrostatic strain inside the QWR, the inclusion model predicts a higher value than the inhomogeneity model does (about 11%). For the InN/AlN (1000) QWR, the hydrostatic strain distribution is similar.

Figure 2.7 shows the electric field distribution along the horizontal line for both the InN/AlN (0001) and (1000) QWRs. For orientation (0001), the only non-zero electric field component is E_x while for (1000), it is E_z . It is observed from the figure that the inclusion model predicts very close results as compared to those based on the inhomogeneity model, particularly for E_x , except for the points close to the interface where the electric field experiences a shape change, resulting in different values based on different models.

Shown in Figures 2.8 and 2.9 are the electric field components E_x and E_z along the inclined line shown in Figure 2.2(b) for both InN/AlN (0001) and (1000) systems. It is noted that whereas along the horizontal, one of these field components is always zero, along the inclined line, both E_x and E_z are in general nonzero. Again, outside the QWR, the inclusion and inhomogeneity models predict similar results, while near the interface or inside the QWR, their predictions differ more markedly.

2.4.3 QWRs of different polygonal shapes

In this example, we study the induced electric fields inside and outside a polygonal QWR with n sides where $n = 3, 4, 5, 6, 10$, and ∞ , shown in Figure 2.10, where a polygon with an infinite number of (infinitesimal) sides is a circle. This model was used before for the corresponding corner singularity study [36]. Only the results from the inhomogeneity models InAs (111)/GaAs(111), InN (0001)/AlN(0001), and InN(1000)/AlN(1000) are presented, and the electric field components are shown only for points along the x -axis.

Figure 2.11 shows that inside and outside the QWR of InAs/GaAs(111), both electric

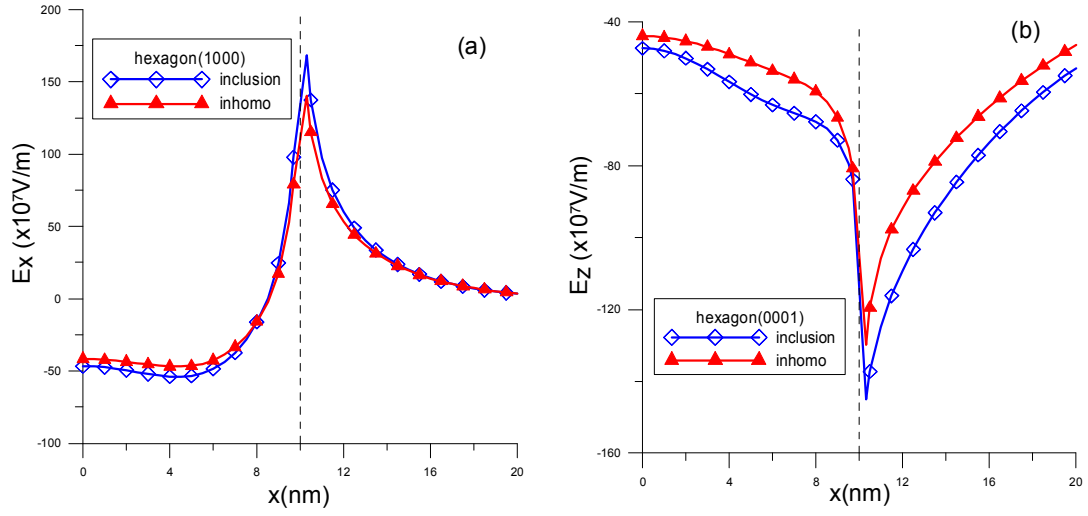


Figure 2.7: (a) E_x in InN/AlN(1000) and (b) E_z in InN/AlN(0001) along the horizontal line shown in Figure 2.2(b).

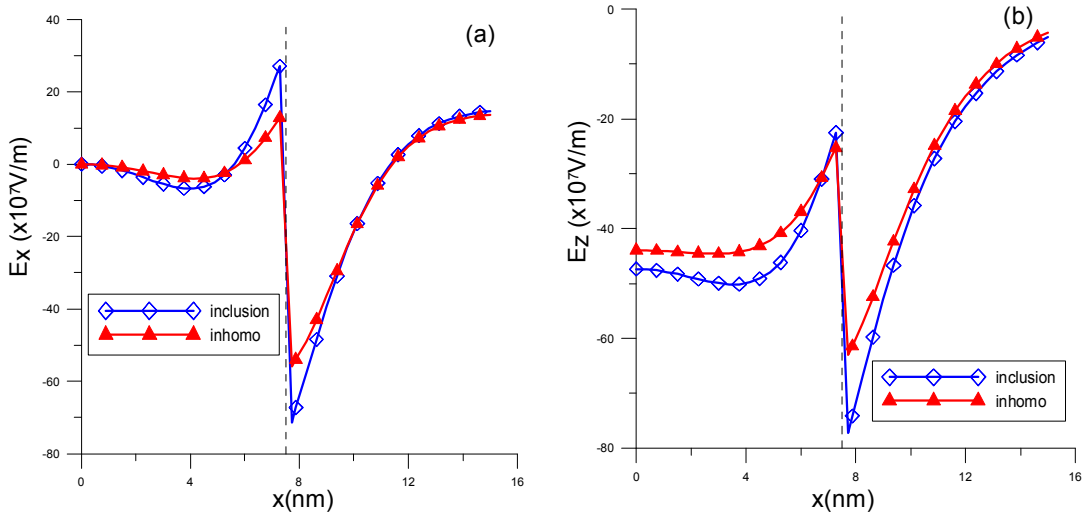


Figure 2.8: (a) E_x and (b) E_z in InN/AlN (0001) along the inclined line shown in Figure 2.2(b).

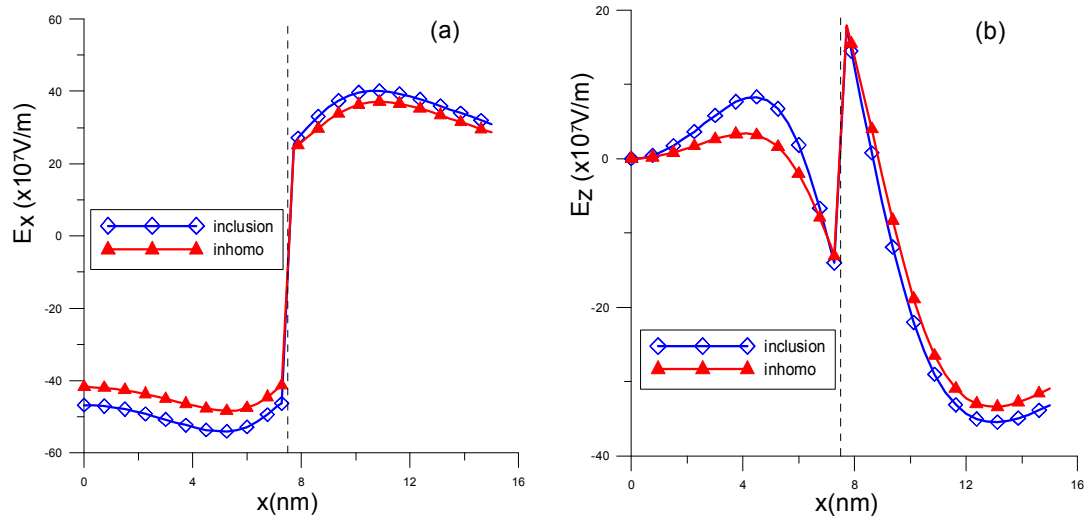


Figure 2.9: (a) E_x and (b) E_z in InN/AlN (1000) along the inclined line shown in Figure 2.2(b).

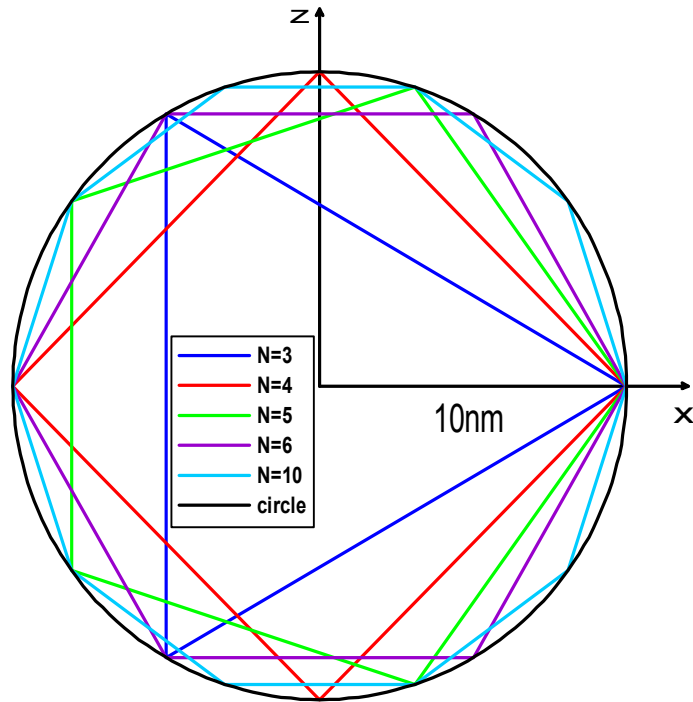


Figure 2.10: The polygons with number of sides $n = 3, 4, 5, 6, 10$, and ∞ , where a polygon with an infinite number of sides is a circle.

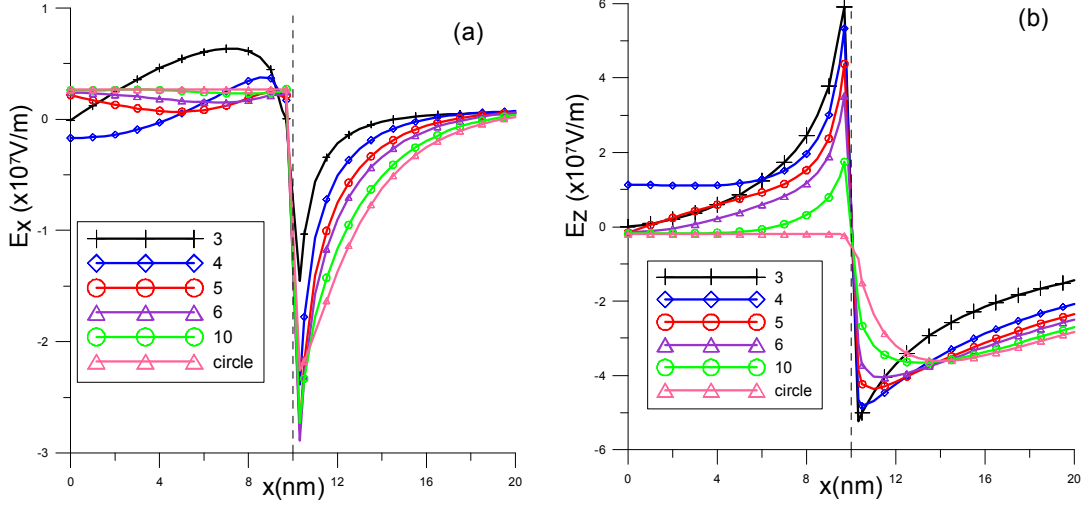


Figure 2.11: (a) E_x and (b) E_z in InAs/GaAs(111) along the x -axis for $n = 3, 4, 5, 6, 10$, and ∞ , where a polygon with an infinite number of sides is a circle.

n	E_x	E_z
3	-0.0071	0.0012
4	-0.1701	1.1285
5	0.2182	-0.1546
6	0.2396	-0.1430
10	0.2613	-0.1851
∞	0.2689	-0.1902

Table 2.7: Electric fields ($\times 10^6$ V/m) at the center of a polygonal InAs QWR with n sides in GaAs(111)

field components are generally nonzero along the x -axis and that just as for the second example, the magnitudes of these fields are comparable both inside and outside the QWR. We also observe that the results from the regular triangle and square QWRs are completely different from the other polygonal QWRs. This can be seen more clearly from Table 2.7 where the electric fields at the center of the polygons are listed. It is obvious that the signs of E_x and E_z are respectively the same for both triangle and square QWRs, which, however, have opposite signs as compared to those in other polygons. Furthermore, while the central values of the electric fields are very small for the triangle QWR, the E_z component in the square QWR is much larger than that of other polygons (about 50–100% larger). These distinguished features are directly associated with the geometric shape. While the triangle and square are very different from each other, a polygon with a number of sides $n \geq 5$ is closer to a circular shape than either a triangle or a square (Figure 2.10).

Figure 2.12 shows the electric field along the x -axis in InN/AlN(1000) and (0001). Due to the symmetric property of the problem the only nonzero component is E_x in (1000) orientation and E_z in (0001) orientation. It is noted that

1. there is a sharp change in the electric field at the geometric corner point ($x = 10$ nm);

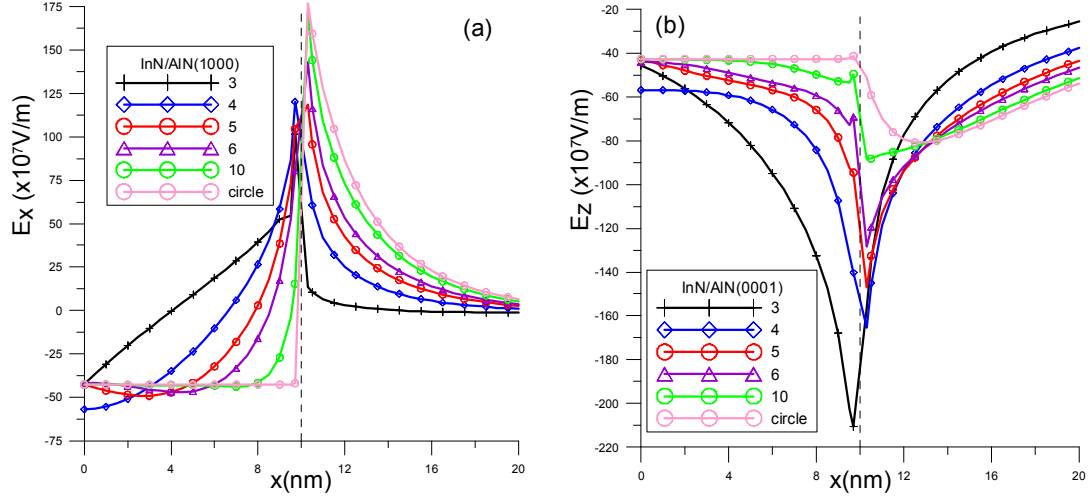


Figure 2.12: (a) E_x in InN/AlN(1000) and (b) E_z in InN/AlN(0001) along the x -axis for $n = 3, 4, 5, 6, 10$, and ∞ , where a polygon with an infinite number of sides is a circle.

n	E_x in (1000)	E_z in (0001)
3	-42.33	-45.74
4	-56.89	-56.89
5	-42.86	-43.00
6	-41.73	-43.96
10	-42.63	-42.76
∞	-42.66	-42.66

Table 2.8: Electric fields ($\times 10^7$ V/m) at the center of a polygonal InN QWR with n sides in AlN

- the trend of the field variation in triangle QWR is completely different from those in other polygons; and
- at the center of the polygons, the electric field of the square is much larger than those in other polygons where the results are very close to each other (Table 2.8) except for the square QWR. The difference of the electric field magnitude at the center between square and other polygons is about 25%.

2.5 Concluding remarks

In the paper, an accurate BEM modeling is proposed for the strain and electric field analysis in QWR structures. Constant elements are employed to discretize the interface between the QWR and substrate with the integral being analytically determined using closed-form Green's functions for anisotropic piezoelectric solids. The elastic and piezoelectric response at any location can be predicted based on the inclusion and inhomogeneity models.

From our study, some important features are observed, with those for the strain field being consistent to recent published results:

1. In the substrate and far away from the QWR, both the inclusion and inhomogeneity models predict nearly the same strain field. In other words, the simple inclusion model can be safely applied if one would like to have a quick estimation of the far-field strain.
2. For points inside or close to the QWR, the strain difference between the two models can be as high as 10% for the test structures, which can result in strong variations of the confined electronic states.
3. While the magnitude of strain inside the QWR is much larger than that outside, the electric fields have the same magnitudes both inside and outside the QWR.
4. While the relative difference in the electric fields based on both inclusion and inhomogeneity models can be large in the InAs/GaAs(111) system, that for the InN/AlN is relatively small. In other words, for InN/AlN where the electric field is large, the simple inclusion model could be employed for the calculation of the induced electric field. This is particularly true as the difference in the electric field based on both models could be small compared to the difference that arises due to the uncertainty in the material constants used [37].
5. It is also observed that the electric fields in the QWR depend strongly on the QWR geometry shape; the electric field in triangular and square QWRs is different from those in the polygons made of more than 4 sides.

Chapter 3

Exact closed-form electromagnetic Green's functions for graded uniaxial multiferroic materials

3.1 Introduction

Multiferroic materials that combine a spontaneous magnetization with a ferroelectric polarization are of great theoretical and practical interest [38–40]. Strong coupling between the polarization and magnetization in multiferroic materials would allow ferroelectric data storage combined with a magnetic read. The ability to tune or switch the magnetic properties with an electric field and vice versa could lead to unexpected developments in conventional devices such as transducers. Various models in the framework of micromechanics have been proposed for multiferroic materials [41–48].

The Green's function-based methods are mathematically elegant and computational powerful [35, 49]. Green's functions in multiferroic materials can be utilized to predict the magnetoelectric effect and to investigate inclusion problems [41–48], to name a few. It is observed that so far the derived Green's functions for multiferroic materials are restricted to homogeneous or piecewise homogeneous materials [45–48, 50]. The graded spatial compositions associated with functionally graded materials (FGMs) provide additional freedom to optimize the design and fabrication of novel structures for interface modulation and also for exploiting other unique features of these systems [51, 52]. Very recently, multiferroic FGMs based on piezoelectric BaTiO_3 and magnetostrictive CoFe_2O_4 , on PbTiO_3 - CoFe_2O_4 , and on BiMnO_3 and Mn_3O_4 have been successfully fabricated using different approaches for better dielectric and magnetic properties [53–55]. Furthermore, an interesting theoretical analysis on the behavior of piezoelectric FGMs was also carried out, which showed the flexibility of FGMs for modulating and adjusting the structure response [56]. To the best of the authors' knowledge, however, Green's functions in FGMs are currently limited to heat conduction [57], elastostatics [58, 59], and piezoelectricity [60].

Therefore, in the paper, we derive three-dimensional (3D) electromagnetic Green's functions for a uniaxial multiferroic FGM which is exponentially graded in an arbitrary

direction. Upon introduction of two new functions [47, 48], the set of coupled governing partial differential equations can be decoupled into two independent inhomogeneous partial differential equations. It is observed that the original problem can be reduced to the determination of Green's functions for two independent 3D Helmholtz equations. Explicit expressions of the Green's functions and their derivatives are thus derived, along with the corresponding boundary integral equations. Numerical examples (of the Green's functions and electric-dipole solutions) are also presented for different exponential factors in the FGMs, and it is found that, along the compositional gradient direction, amplitudes of the field response in a FGM multiferroic space can be either reduced or kept in the same values as those in the corresponding homogeneous material (for the Green's function solutions).

3.2 Green's functions for a functionally graded multiferroic material

The constitutive equations for a uniaxial multiferroic material with its unique axis along the x_3 -direction can be written as [46, 50]

$$\begin{bmatrix} D_1 \\ B_1 \end{bmatrix} = \begin{bmatrix} \kappa_{11} & \alpha_{11} \\ \alpha_{11} & \mu_{11} \end{bmatrix} \begin{bmatrix} E_1 \\ H_1 \end{bmatrix}, \quad \begin{bmatrix} D_2 \\ B_2 \end{bmatrix} = \begin{bmatrix} \kappa_{11} & \alpha_{11} \\ \alpha_{11} & \mu_{11} \end{bmatrix} \begin{bmatrix} E_2 \\ H_2 \end{bmatrix}, \quad \begin{bmatrix} D_3 \\ B_3 \end{bmatrix} = \begin{bmatrix} \kappa_{33} & \alpha_{33} \\ \alpha_{33} & \mu_{33} \end{bmatrix} \begin{bmatrix} E_3 \\ H_3 \end{bmatrix} \quad (3.1)$$

where D_i and B_i ($i = 1, 2, 3$) are the electric displacement and magnetic flux components (in the x_1 -, x_2 -, and x_3 -directions); E_i and H_i are the electric field and magnetic field components; κ_{11} and κ_{33} are the two dielectric permittivity coefficients in the x_1 - and x_3 -directions, respectively; α_{11} and α_{33} are the two magnetoelectric coefficients (in the x_1 - and x_3 -directions); and μ_{11} and μ_{33} are the two magnetic permeability coefficients (in the x_1 - and x_3 -directions).

For a FGM uniaxial multiferroic material with exponential variation in an arbitrary direction, the material coefficients in Eq. (3.1) can be described by (assuming a uniform variation in space for all the material coefficients [57–60].)

$$\begin{bmatrix} \kappa_{ii}(x) & \alpha_{ii}(x) & \mu_{ii}(x) \end{bmatrix} = \begin{bmatrix} \kappa_{ii}^0 & \alpha_{ii}^0 & \mu_{ii}^0 \end{bmatrix} \exp(2\beta_1 x_1 + 2\beta_2 x_2 + 2\beta_3 x_3) \quad i = 1, 3 \quad (3.2)$$

where β_1 , β_2 , and β_3 are three exponential factors characterizing the degree of material gradient in the x_1 -, x_2 -, and x_3 -directions, respectively. The superscript “0” indicates the coordinate-independent factor in the material coefficient, and the factor of 2 in the exponential is introduced to simplify the derivation of Green's function expressions. It is obvious that $\beta_1 = \beta_2 = \beta_3 = 0$ corresponds to the homogeneous multiferroic material case investigated previously [35, 46–50]. We further point out that the special exponential variation is assumed so that exact-closed form Green's functions can be derived, and that the assumed exponential function can be used to piecewise approximate any smooth variation of the FGM in a small space domain.

The electric and magnetic fields are related to the electric potential ϕ and magnetic potential ψ through the following 2×1 column matrix relation

$$\begin{bmatrix} E_i \\ H_i \end{bmatrix} = - \begin{bmatrix} \phi_{,i} \\ \psi_{,i} \end{bmatrix} \quad (3.3)$$

where the subscript comma “,” followed by the index i ($i = 1, 2, 3$) denotes the derivative of the potential with respect to the coordinate x_i .

For the FGM uniaxial multiferroic free-space, we assume, without loss of generality, that there is a point electric charge P and a point magnetic charge M both located at the origin (See section 3.4.1 for the case where the source is not at the origin). Thus the electric displacement D_i and magnetic flux B_i satisfy the following equations [47, 48]

$$\begin{aligned}\frac{\partial D_1}{\partial x_1} + \frac{\partial D_2}{\partial x_2} + \frac{\partial D_3}{\partial x_3} &= P\delta(x_1)\delta(x_2)\delta(x_3) \\ \frac{\partial B_1}{\partial x_1} + \frac{\partial B_2}{\partial x_2} + \frac{\partial B_3}{\partial x_3} &= M\delta(x_1)\delta(x_2)\delta(x_3)\end{aligned}\quad (3.4)$$

where δ is the Dirac delta function.

Substituting Eqs. (3.2) and (3.3) into Eq. (3.1), and then the results into Eq. (3.4), we arrive at the following set of inhomogeneous partial differential equations for ϕ and ψ :

$$\begin{aligned}\begin{bmatrix} \kappa_{11}^0 & \alpha_{11}^0 \\ \alpha_{11}^0 & \mu_{11}^0 \end{bmatrix} \begin{bmatrix} \left(\frac{\partial^2}{\partial x_1^2} + \frac{\partial^2}{\partial x_2^2}\right) \phi \\ \left(\frac{\partial^2}{\partial x_1^2} + \frac{\partial^2}{\partial x_2^2}\right) \psi \end{bmatrix} + \begin{bmatrix} \kappa_{33}^0 & \alpha_{33}^0 \\ \alpha_{33}^0 & \mu_{33}^0 \end{bmatrix} \begin{bmatrix} \frac{\partial^2 \phi}{\partial x_3^2} \\ \frac{\partial^2 \psi}{\partial x_3^2} \end{bmatrix} \\ + 2 \begin{bmatrix} \kappa_{11}^0 & \alpha_{11}^0 \\ \alpha_{11}^0 & \mu_{11}^0 \end{bmatrix} \begin{bmatrix} \beta_1 \frac{\partial \phi}{\partial x_1} + \beta_2 \frac{\partial \phi}{\partial x_2} \\ \beta_1 \frac{\partial \psi}{\partial x_1} + \beta_2 \frac{\partial \psi}{\partial x_2} \end{bmatrix} + 2\beta_3 \begin{bmatrix} \kappa_{33}^0 & \alpha_{33}^0 \\ \alpha_{33}^0 & \mu_{33}^0 \end{bmatrix} \begin{bmatrix} \frac{\partial \phi}{\partial x_3} \\ \frac{\partial \psi}{\partial x_3} \end{bmatrix} = \\ - \begin{bmatrix} P \\ M \end{bmatrix} \delta(x_1)\delta(x_2)\delta(x_3) \quad (3.5)\end{aligned}$$

where the well-known properties of the delta function have been employed.

In order to solve the above set of coupled differential equations, we first consider the following eigenvalue problem [47, 48]

$$\left(\begin{bmatrix} \kappa_{11}^0 & \alpha_{11}^0 \\ \alpha_{11}^0 & \mu_{11}^0 \end{bmatrix} - \lambda \begin{bmatrix} \kappa_{33}^0 & \alpha_{33}^0 \\ \alpha_{33}^0 & \mu_{33}^0 \end{bmatrix} \right) \mathbf{v} = \begin{bmatrix} 0 \\ 0 \end{bmatrix} \quad (3.6)$$

The two eigenvalues λ_1 and λ_2 are given by

$$\begin{aligned}\lambda_1 &= \frac{\mu_{33}^0 \kappa_{11}^0 + \mu_{11}^0 \kappa_{33}^0 - 2\alpha_{11}^0 \alpha_{33}^0}{2[\mu_{33}^0 \kappa_{33}^0 - (\alpha_{33}^0)^2]} \\ &+ \frac{\sqrt{(\mu_{11}^0 \kappa_{33}^0 - \mu_{33}^0 \kappa_{11}^0)^2 + 4(\alpha_{11}^0 \mu_{33}^0 - \alpha_{33}^0 \mu_{11}^0)(\alpha_{11}^0 \kappa_{33}^0 - \alpha_{33}^0 \kappa_{11}^0)}}{2[\mu_{33}^0 \kappa_{33}^0 - (\alpha_{33}^0)^2]} \\ \lambda_2 &= \frac{\mu_{33}^0 \kappa_{11}^0 + \mu_{11}^0 \kappa_{33}^0 - 2\alpha_{11}^0 \alpha_{33}^0}{2[\mu_{33}^0 \kappa_{33}^0 - (\alpha_{33}^0)^2]} \\ &- \frac{\sqrt{(\mu_{11}^0 \kappa_{33}^0 - \mu_{33}^0 \kappa_{11}^0)^2 + 4(\alpha_{11}^0 \mu_{33}^0 - \alpha_{33}^0 \mu_{11}^0)(\alpha_{11}^0 \kappa_{33}^0 - \alpha_{33}^0 \kappa_{11}^0)}}{2[\mu_{33}^0 \kappa_{33}^0 - (\alpha_{33}^0)^2]}\end{aligned}\quad (3.7)$$

and the corresponding eigenvectors associated with λ_1 and λ_2 are

$$\mathbf{v}_1 = \begin{bmatrix} -\alpha_{11}^0 + \lambda_1 \alpha_{33}^0 \\ \kappa_{11}^0 - \lambda_1 \kappa_{33}^0 \end{bmatrix}, \quad \mathbf{v}_2 = \begin{bmatrix} -\alpha_{11}^0 + \lambda_2 \alpha_{33}^0 \\ \kappa_{11}^0 - \lambda_2 \kappa_{33}^0 \end{bmatrix} \quad (3.8)$$

Since the two matrices on the left-hand side of Eq. (3.6) are real and symmetric, it can be easily verified that the orthogonality conditions

$$\begin{aligned} \begin{bmatrix} \mathbf{v}_1^T \\ \mathbf{v}_2^T \end{bmatrix} \begin{bmatrix} \kappa_{33}^0 & \alpha_{33}^0 \\ \alpha_{33}^0 & \mu_{33}^0 \end{bmatrix} \begin{bmatrix} \mathbf{v}_1 & \mathbf{v}_2 \end{bmatrix} &= \begin{bmatrix} \delta_1 & 0 \\ 0 & \delta_2 \end{bmatrix} \\ \begin{bmatrix} \mathbf{v}_1^T \\ \mathbf{v}_2^T \end{bmatrix} \begin{bmatrix} \kappa_{11}^0 & \alpha_{11}^0 \\ \alpha_{11}^0 & \mu_{11}^0 \end{bmatrix} \begin{bmatrix} \mathbf{v}_1 & \mathbf{v}_2 \end{bmatrix} &= \begin{bmatrix} \lambda_1 \delta_1 & 0 \\ 0 & \lambda_2 \delta_2 \end{bmatrix} \end{aligned} \quad (3.9)$$

are satisfied. In Eq. (3.9), the superscript T denotes matrix transpose, and

$$\begin{aligned} \delta_1 &= \alpha_{11}^{02} \kappa_{33}^0 + \kappa_{11}^{02} \mu_{33}^0 - 2\alpha_{11}^0 \alpha_{33}^0 \kappa_{11}^0 + (\mu_{33}^0 \kappa_{33}^0 - \alpha_{33}^{02})(\lambda_1^2 \kappa_{33}^0 - 2\lambda_1 \kappa_{11}^0) \\ \delta_2 &= \alpha_{11}^{02} \kappa_{33}^0 + \kappa_{11}^{02} \mu_{33}^0 - 2\alpha_{11}^0 \alpha_{33}^0 \kappa_{11}^0 + (\mu_{33}^0 \kappa_{33}^0 - \alpha_{33}^{02})(\lambda_2^2 \kappa_{33}^0 - 2\lambda_2 \kappa_{11}^0) \end{aligned} \quad (3.10)$$

We now introduce two new functions f and g , which are related to ϕ and ψ through

$$\begin{bmatrix} \phi \\ \psi \end{bmatrix} = \underline{\Phi} \begin{bmatrix} f \\ g \end{bmatrix} \quad (3.11)$$

where $\underline{\Phi} = [\mathbf{v}_1 \ \mathbf{v}_2]$.

In view of Eqs. (3.5), (3.9) and (3.11), the two new functions f and g are required to satisfy the following two independent, inhomogeneous, and partial differential equations

$$\begin{aligned} \left(\frac{\partial^2}{\partial x_1^2} + \frac{\partial^2}{\partial x_2^2} + \frac{1}{\lambda_1} \frac{\partial^2}{\partial x_3^2} + 2\beta_1 \frac{\partial}{\partial x_1} + 2\beta_2 \frac{\partial}{\partial x_2} + \frac{2\beta_3}{\lambda_1} \frac{\partial}{\partial x_3} \right) f \\ = - \frac{(-\alpha_{11}^0 + \lambda_1 \alpha_{33}^0)P + (\kappa_{11}^0 - \lambda_1 \kappa_{33}^0)M}{\delta_1 \lambda_1} \delta(x_1) \delta(x_2) \delta(x_3) \end{aligned} \quad (3.12)$$

$$\begin{aligned} \left(\frac{\partial^2}{\partial x_1^2} + \frac{\partial^2}{\partial x_2^2} + \frac{1}{\lambda_2} \frac{\partial^2}{\partial x_3^2} + 2\beta_1 \frac{\partial}{\partial x_1} + 2\beta_2 \frac{\partial}{\partial x_2} + \frac{2\beta_3}{\lambda_2} \frac{\partial}{\partial x_3} \right) g \\ = - \frac{(-\alpha_{11}^0 + \lambda_2 \alpha_{33}^0)P + (\kappa_{11}^0 - \lambda_2 \kappa_{33}^0)M}{\delta_2 \lambda_2} \delta(x_1) \delta(x_2) \delta(x_3) \end{aligned} \quad (3.13)$$

Equations (3.12) and (3.13) can be equivalently expressed as

$$\begin{aligned} \left(\frac{\partial^2}{\partial x_1^2} + \frac{\partial^2}{\partial x_2^2} + \frac{\partial^2}{\partial (\sqrt{\lambda_1} x_3)^2} + 2\beta_1 \frac{\partial}{\partial x_1} + 2\beta_2 \frac{\partial}{\partial x_2} + \frac{2\beta_3}{\sqrt{\lambda_1}} \frac{\partial}{\partial (\sqrt{\lambda_1} x_3)} \right) f = \\ - 4\pi K_1 \delta(x_1) \delta(x_2) \delta(\sqrt{\lambda_1} x_3) \end{aligned} \quad (3.14)$$

$$\begin{aligned} \left(\frac{\partial^2}{\partial x_1^2} + \frac{\partial^2}{\partial x_2^2} + \frac{\partial^2}{\partial (\sqrt{\lambda_2} x_3)^2} + 2\beta_1 \frac{\partial}{\partial x_1} + 2\beta_2 \frac{\partial}{\partial x_2} + \frac{2\beta_3}{\sqrt{\lambda_2}} \frac{\partial}{\partial (\sqrt{\lambda_2} x_3)} \right) g = \\ - 4\pi K_2 \delta(x_1) \delta(x_2) \delta(\sqrt{\lambda_2} x_3) \end{aligned} \quad (3.15)$$

where the two constants K_1 and K_2 are defined as

$$\begin{aligned} K_1 &= \frac{(-\alpha_{11}^0 + \lambda_1 \alpha_{33}^0)P + (\kappa_{11}^0 - \lambda_1 \kappa_{33}^0)M}{4\pi\delta_1\sqrt{\lambda_1}} \\ K_2 &= \frac{(-\alpha_{11}^0 + \lambda_2 \alpha_{33}^0)P + (\kappa_{11}^0 - \lambda_2 \kappa_{33}^0)M}{4\pi\delta_2\sqrt{\lambda_2}} \end{aligned} \quad (3.16)$$

Next we introduce another two new functions F and G defined by

$$f = \exp(-\beta_1 x_1 - \beta_2 x_2 - \beta_3 x_3)F \quad g = \exp(-\beta_1 x_1 - \beta_2 x_2 - \beta_3 x_3)G \quad (3.17)$$

Consequently, Eqs. (3.14) and (3.15) can now be changed into the following two independent inhomogeneous 3D Helmholtz equations

$$\left(\frac{\partial^2}{\partial x_1^2} + \frac{\partial^2}{\partial x_2^2} + \frac{\partial^2}{\partial (\sqrt{\lambda_1} x_3)^2} - \eta_1^2 \right) F = -4\pi K_1 \delta(x_1) \delta(x_2) \delta(\sqrt{\lambda_1} x_3) \quad (3.18)$$

$$\left(\frac{\partial^2}{\partial x_1^2} + \frac{\partial^2}{\partial x_2^2} + \frac{\partial^2}{\partial (\sqrt{\lambda_2} x_3)^2} - \eta_2^2 \right) G = -4\pi K_2 \delta(x_1) \delta(x_2) \delta(\sqrt{\lambda_2} x_3) \quad (3.19)$$

where

$$\eta_1 = \sqrt{\beta_1^2 + \beta_2^2 + \frac{\beta_3^2}{\lambda_1}} \quad \eta_2 = \sqrt{\beta_1^2 + \beta_2^2 + \frac{\beta_3^2}{\lambda_2}} \quad (3.20)$$

The solutions to Eqs. (3.18) and (3.19) can be expediently given by

$$F = K_1 \frac{\exp(-\eta_1 r_1)}{r_1} \quad G = K_2 \frac{\exp(-\eta_2 r_2)}{r_2} \quad (3.21)$$

where $r_1 = \sqrt{x_1^2 + x_2^2 + \lambda_1 x_3^2}$ and $r_2 = \sqrt{x_1^2 + x_2^2 + \lambda_2 x_3^2}$.

In view of Eq. (3.17), the expressions of the two functions f and g are given by

$$\begin{aligned} f &= K_1 \frac{\exp(-\beta_1 x_1 - \beta_2 x_2 - \beta_3 x_3 - \eta_1 r_1)}{r_1} \\ g &= K_2 \frac{\exp(-\beta_1 x_1 - \beta_2 x_2 - \beta_3 x_3 - \eta_2 r_2)}{r_2} \end{aligned} \quad (3.22)$$

It follows from Eq. (3.11) that the electric and magnetic potentials can be now obtained as

$$\begin{bmatrix} \phi \\ \psi \end{bmatrix} = \underline{\Phi} \begin{bmatrix} K_1 \exp(-\beta_1 x_1 - \beta_2 x_2 - \beta_3 x_3 - \eta_1 r_1)/r_1 \\ K_2 \exp(-\beta_1 x_1 - \beta_2 x_2 - \beta_3 x_3 - \eta_2 r_2)/r_2 \end{bmatrix} \quad (3.23)$$

Based on Eq. (3.23), the multiferroic Green's functions $G_{\alpha\beta}$ are then found to be

$$4\pi G_{\phi P} = \frac{(\alpha_{11}^0 - \lambda_1 \alpha_{33}^0)^2 \exp(-\beta_1 x_1 - \beta_2 x_2 - \beta_3 x_3 - \eta_1 r_1)}{\delta_1 \sqrt{\lambda_1} r_1} + \frac{(\alpha_{11}^0 - \lambda_2 \alpha_{33}^0)^2 \exp(-\beta_1 x_1 - \beta_2 x_2 - \beta_3 x_3 - \eta_2 r_2)}{\delta_2 \sqrt{\lambda_2} r_2} \quad (3.24a)$$

$$4\pi G_{\phi M} = 4\pi G_{\psi P} = \frac{(\lambda_1 \alpha_{33}^0 - \alpha_{11}^0)(\kappa_{11}^0 - \lambda_1 \kappa_{33}^0) \exp(-\beta_1 x_1 - \beta_2 x_2 - \beta_3 x_3 - \eta_1 r_1)}{\delta_1 \sqrt{\lambda_1} r_1} + \frac{(\lambda_2 \alpha_{33}^0 - \alpha_{11}^0)(\kappa_{11}^0 - \lambda_2 \kappa_{33}^0) \exp(-\beta_1 x_1 - \beta_2 x_2 - \beta_3 x_3 - \eta_2 r_2)}{\delta_2 \sqrt{\lambda_2} r_2} \quad (3.24b)$$

$$4\pi G_{\psi M} = \frac{(\kappa_{11}^0 - \lambda_1 \kappa_{33}^0)^2 \exp(-\beta_1 x_1 - \beta_2 x_2 - \beta_3 x_3 - \eta_1 r_1)}{\delta_1 \sqrt{\lambda_1} r_1} + \frac{(\kappa_{11}^0 - \lambda_2 \kappa_{33}^0)^2 \exp(-\beta_1 x_1 - \beta_2 x_2 - \beta_3 x_3 - \eta_2 r_2)}{\delta_2 \sqrt{\lambda_2} r_2} \quad (3.24c)$$

In Eqs. (3.24), the definitions of the Green's functions are: $G_{\phi P}(x_i)$ is the electric potential ϕ at x_i due to a unit point electric charge ($P = 1$) at $x_i = 0$. $G_{\phi M}(x_i)$ is the electric potential ϕ at x_i due to a unit point magnetic charge ($M = 1$) at $x_i = 0$. $G_{\psi P}(x_i)$ is the magnetic potential ψ at x_i due to a unit point electric charge ($P = 1$) at $x_i = 0$, and $G_{\psi M}(x_i)$ is the magnetic potential ψ at x_i due to a unit point magnetic charge ($M = 1$) at $x_i = 0$. If one is interested in the electric and magnetic fields or the electric displacement and magnetic flux components induced by the point source, the derivatives of these Green's functions are essential as in the boundary integral equation formulation [57]. These derivatives of the Green's functions and the corresponding boundary integral equation formulation for the FGM multiferroic are presented, respectively, in sections 3.4.1 and 3.4.2.

Some interesting features can be observed from the Green's function expression in Eqs. (3.24).

1. When $\beta_1 = \beta_2 = \beta_3 = 0$, Eqs. (3.24) reduce to the Green's functions for a homogeneous multiferroic material [46–48, 50], as expected.
2. The magnitudes of the FGM multiferroic Green's functions $G_{\alpha\beta}$ decay to zero faster than their counterparts for the homogeneous multiferroic material when the field point is away from the origin ($r = \sqrt{x_1^2 + x_2^2 + x_3^2} \rightarrow \infty$). This is due to the appearance of the decaying exponential terms in these FGM Green's functions.
3. Just like the Green's functions in the corresponding homogeneous space, the FGM Green's functions in Eqs. (3.24) are also *symmetric* in their indices. In other words, the electric potential at x_i due to a unit point magnetic charge at the origin equals the magnetic potential at x_i due to a unit point electric charge at the origin. However, unlike the homogeneous Green's functions, the source and field points in the FGM Green's functions are *asymmetric*. Namely, the source and fields points cannot be exchanged.

4. Although the exact-closed form Green's functions are based on the special exponential variation, any smooth variation of the FGM in a small space domain can be piecewise approximated by the exponential function. In other words, the application of the present Green's function is not limited to the exponential variation, particularly when it is implemented into the corresponding boundary integral formulation. (See section 3.4.2.)

We illustrate in Figures 3.1–3.4 the distribution of the electromagnetic Green's functions $G_{\alpha\beta}$ along the x_3 -axis for different gradient parameter $\beta_3 (= -10, -3, -1, 0, 1, 3, 10 \text{ m}^{-1})$ with $\beta_1 = \beta_2 = 0$. This situation implies that the material is graded in the uniaxial x_3 -direction [53–56]. The coordinate-independent factors in the material coefficients are chosen to be (for a typical multiferroic composite) [46, 50]

$$\begin{aligned}\alpha_{11}^0 &= 5 \times 10^{-12} \text{ N} \cdot \text{s/V} \cdot \text{C} & \alpha_{33}^0 &= 3 \times 10^{-12} \text{ N} \cdot \text{s/V} \cdot \text{C} \\ \kappa_{11}^0 &= 8 \times 10^{-11} \text{ C}^2/(\text{N} \cdot \text{m}^2) & \kappa_{33}^0 &= 9.3 \times 10^{-11} \text{ C}^2/(\text{N} \cdot \text{m}^2) \\ \mu_{11}^0 &= 5.9 \times 10^{-4} \text{ N} \cdot \text{s}^2/\text{C}^2 & \mu_{33}^0 &= 1.57 \times 10^{-4} \text{ N} \cdot \text{s}^2/\text{C}^2\end{aligned}$$

As expected, the figures show that the gradient parameter β_3 has a significant influence on the distribution of the Green's functions along the x_3 -axis. In particular, the magnitudes of these Green's functions decrease with increasing magnitude of β_3 . It is striking that for the special case where $\beta_1 = \beta_2 = 0$ and $x_1 = x_2 = 0$, the distribution of the Green's functions in Eq. (3.24) along the negative x_3 -axis is the same as that in the corresponding homogeneous multiferroic material ($\beta_1 = \beta_2 = \beta_3 = 0$), independent of the positive values of β_3 . On the other hand, the distribution of the Green's functions in Eq. (3.24) along the positive x_3 -axis is also the same as that in the corresponding homogeneous multiferroic material, independent of the negative values of β_3 . These interesting behaviors of field responses can be also observed along the x_1 -axis for positive and negative β_1 (with $\beta_2 = \beta_3 = 0$), and along the x_2 -axis for positive and negative β_2 (with $\beta_1 = \beta_3 = 0$).

Finally, as an interesting application of the derived Green's function solutions, we study the electric and magnetic potentials induced by an electric dipole at the origin and along the uniaxial x_3 -direction with the electric moment (or dipole moment) p . This is very important because charge pairs of opposite sign are the model for polarized and magnetized atoms and molecules [61–63]. By employing the Green's function solutions, Eqs. (3.24), and making use of the limiting process, the expressions of the electric and magnetic potentials induced by the electric dipole of moment p can be given by

$$\begin{aligned}\phi &= \frac{p\sqrt{\lambda_1}(\lambda_1\alpha_{33}^0 - \alpha_{11}^0)^2 e^{-\eta_1 r_1 - \sum_{m=1}^3 \beta_m x_m}}{4\pi\delta_1} \left(\frac{x_3}{r_1^3} + \frac{\eta_1 x_3}{r_1^2} - \frac{\beta_3}{\lambda_1 r_1} \right) \\ &+ \frac{p\sqrt{\lambda_2}(\lambda_2\alpha_{33}^0 - \alpha_{11}^0)^2 e^{-\eta_2 r_2 - \sum_{m=1}^3 \beta_m x_m}}{4\pi\delta_2} \left(\frac{x_3}{r_2^3} + \frac{\eta_2 x_3}{r_2^2} - \frac{\beta_3}{\lambda_2 r_2} \right) \\ \psi &= \frac{p\sqrt{\lambda_1}(\kappa_{11}^0 - \lambda_1\kappa_{33}^0)(\lambda_1\alpha_{33}^0 - \alpha_{11}^0) e^{-\eta_1 r_1 - \sum_{m=1}^3 \beta_m x_m}}{4\pi\delta_1} \left(\frac{x_3}{r_1^3} + \frac{\eta_1 x_3}{r_1^2} - \frac{\beta_3}{\lambda_1 r_1} \right) \\ &+ \frac{p\sqrt{\lambda_2}(\kappa_{11}^0 - \lambda_2\kappa_{33}^0)(\lambda_2\alpha_{33}^0 - \alpha_{11}^0) e^{-\eta_2 r_2 - \sum_{m=1}^3 \beta_m x_m}}{4\pi\delta_2} \left(\frac{x_3}{r_2^3} + \frac{\eta_2 x_3}{r_2^2} - \frac{\beta_3}{\lambda_2 r_2} \right)\end{aligned}\tag{3.25}$$

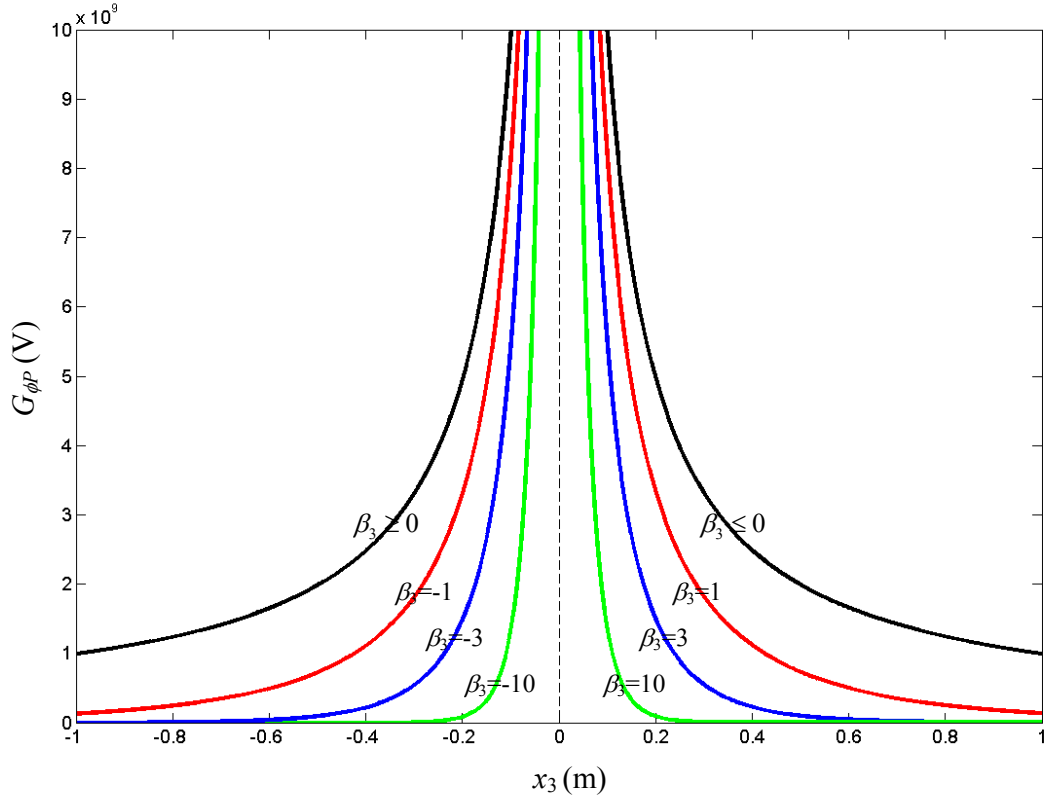


Figure 3.1: Distribution of the electromagnetic Green's function $G_{\phi P}$ along x_3 -axis for different gradient parameter $\beta_3 (= -10, -3, -1, 0, 1, 3, 10 \text{ m}^{-1})$ with $\beta_1 = \beta_2 = 0$.

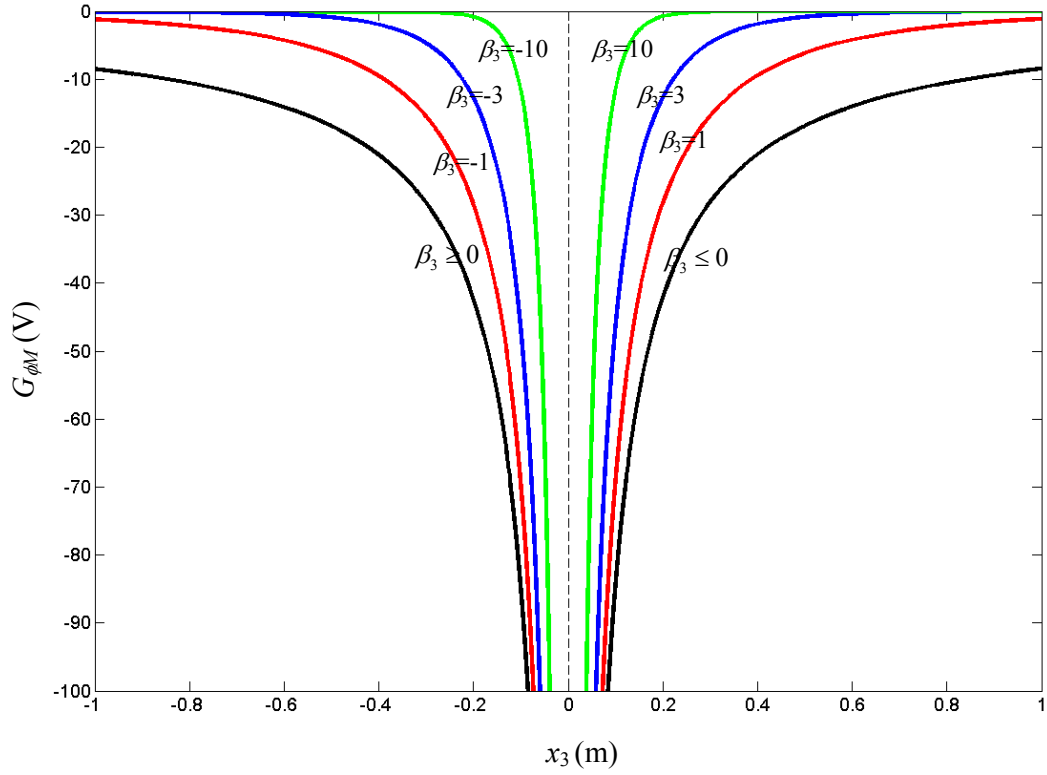


Figure 3.2: Distribution of the electromagnetic Green's function $G_{\phi M}$ along x_3 -axis for different gradient parameter $\beta_3 (= -10, -3, -1, 0, 1, 3, 10 \text{ m}^{-1})$ with $\beta_1 = \beta_2 = 0$.

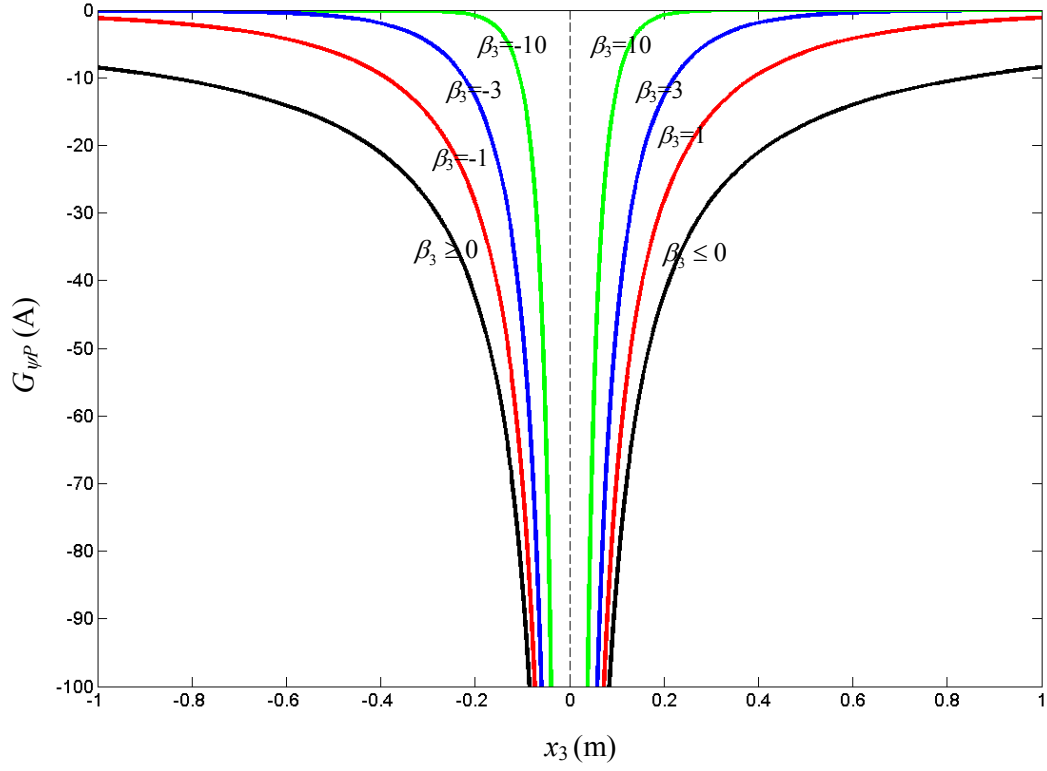


Figure 3.3: Distribution of the electromagnetic Green's function $G_{\psi P}$ along x_3 -axis for different gradient parameter $\beta_3 (= -10, -3, -1, 0, 1, 3, 10 \text{ m}^{-1})$ with $\beta_1 = \beta_2 = 0$.

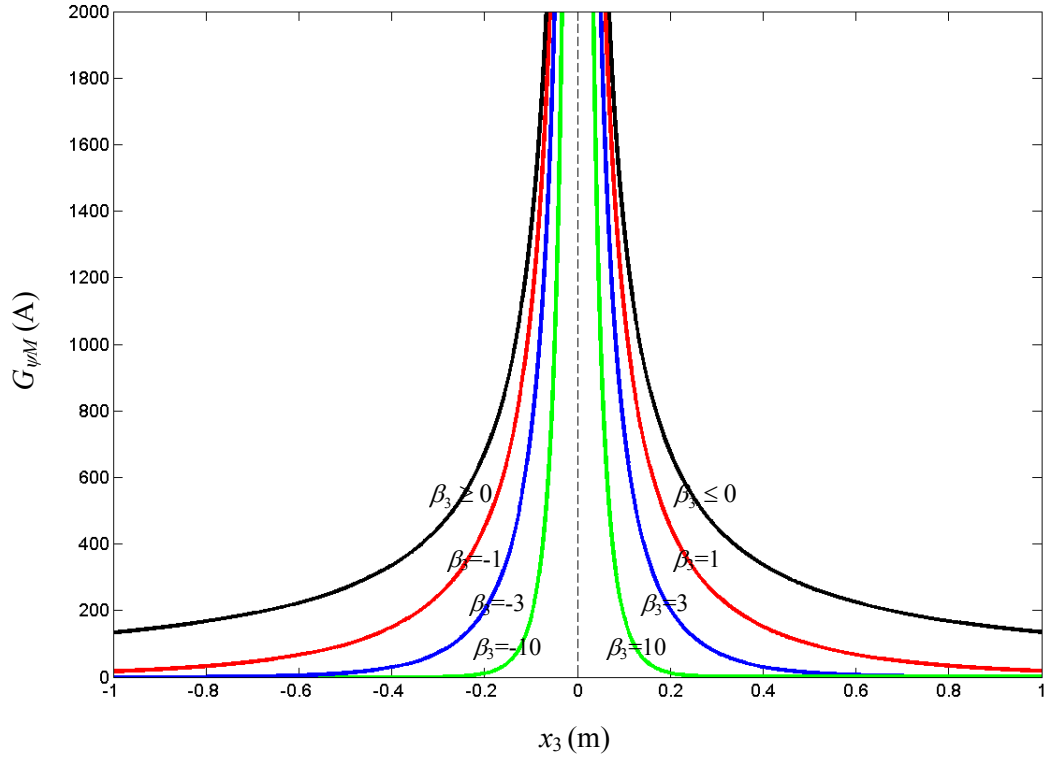


Figure 3.4: Distribution of the electromagnetic Green's function G_{ψ_M} along x_3 -axis for different gradient parameter β_3 ($= -10, -3, -1, 0, 1, 3, 10 \text{ m}^{-1}$) with $\beta_1 = \beta_2 = 0$.

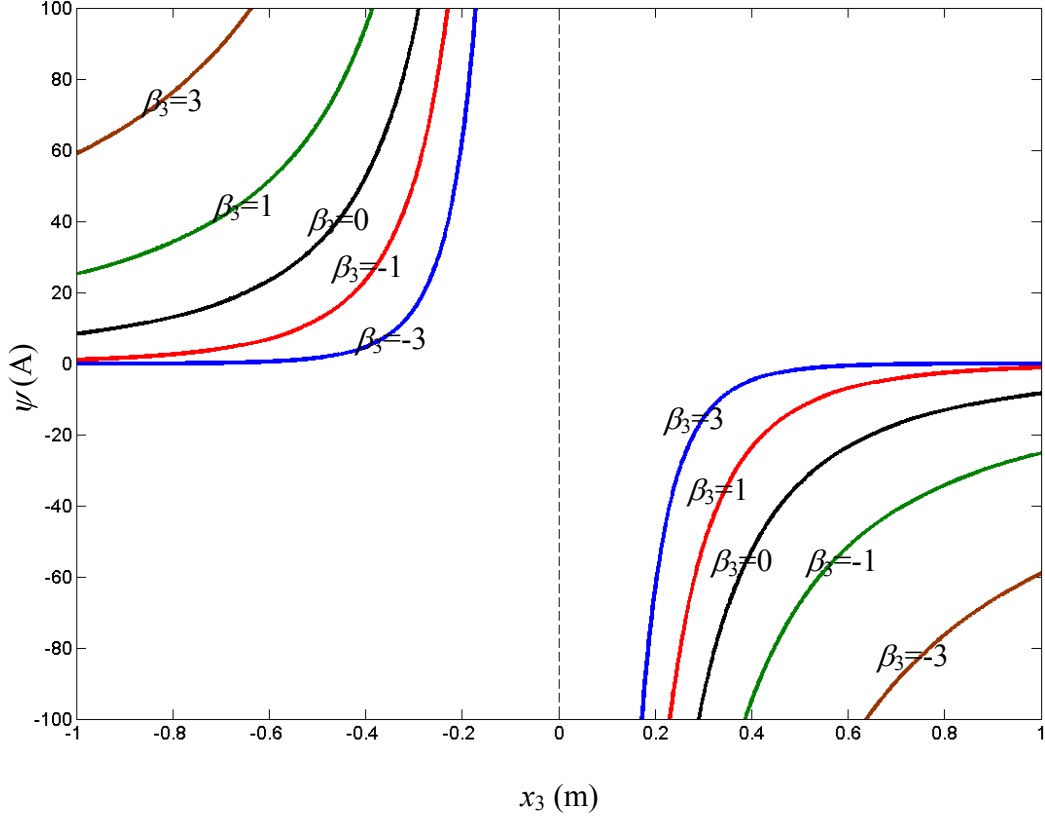


Figure 3.5: Distribution of the magnetic potential along x_3 -axis induced by a unit electric dipole ($p = 1$) at origin and along the uniaxial x_3 -direction for different gradient parameter $\beta_3 (= -3, -1, 0, 1, 3 \text{ m}^{-1})$ with $\beta_1 = \beta_2 = 0$.

It is observed from Eq. (3.25) that an electric dipole can also induce the magnetic field due to the magnetoelectric effect in multiferroic materials. To see this fact more clearly, we illustrate in Figure 3.5 the distribution of the magnetic potential along the x_3 -axis induced by a unit electric dipole ($p = 1$) at the origin and along the uniaxial x_3 -direction for different gradient parameter $\beta_3 (= -3, -1, 0, 1, 3 \text{ m}^{-1})$ with $\beta_1 = \beta_2 = 0$. Comparing Figure 3.5 to the Green's function $G_{\psi M}$ in Figure 3.4, it is interesting to observe that the distribution of the magnetic potential along the whole x_3 -axis induced by the unit electric dipole always depends on the value of the gradient parameter β_3 . It is further noticed from Figure 3.5 that

1. when $\beta_3 x_3 > 0$, the magnitude of the induced magnetic potential at any point is smaller than the corresponding one for the homogeneous material ($\beta_3 = 0$) at the same point, and
2. conversely when $\beta_3 x_3 < 0$, the magnitude of the induced magnetic potential at any point is larger than the corresponding one for homogeneous material ($\beta_3 = 0$) at the same point.

3.3 Conclusions

In this chapter, the 3D exact closed form electromagnetic Green's functions for a FGM uniaxial multiferroic space are derived by assuming the material to be exponentially graded in an arbitrary direction. The explicit expressions of the Green's functions are given in Eqs. (3.24), with their derivatives listed in Eqs. (3.26)–(3.28) of section 3.4.1. The corresponding boundary integral equations are also presented in section 3.4.2. Sharply different from the complicated Green's function expression in FGM transversely isotropic piezoelectric materials [60], the Green's functions in the FGM multiferroic space are expressed in terms of elementary functions only. Numerical examples of the Green's functions and electric-dipole solutions have been presented to demonstrate the possibility of tailoring the material behavior. In particular, it is shown that along the gradient orientation, amplitudes of the field response in a FGM multiferroic space can be modulated using different functional gradient factors, resulting in either reduced amplitude of the response, or the same values as those in the corresponding homogeneous materials (for the Green's functions). The derived Green's functions can be further employed to address inclusion problems in FGM multiferroic materials and can be implemented into the corresponding boundary element formulation to attack more complicated boundary value problems associated with FGM multiferroic materials. We point out that although the exact closed-form Green's functions are based on the special exponential variation, any smooth variation of the FGM can be treated within the boundary integral equation in a piecewise thin-layer manner [60].

3.4 Appendices

3.4.1 Derivatives of the Green's functions

Derivatives of the Green's functions are listed below. These field quantities are required to find the electric and magnetic fields, and electric displacements and magnetic fluxes. They are also required in the FGM boundary integral formulation as presented in section 3.4.2.

$$4\pi \frac{\partial G_{\phi P}}{\partial x_i} = - \sum_{k=1}^2 \frac{(\alpha_{11}^0 - \lambda_k \alpha_{33}^0)^2}{\delta_k \sqrt{\lambda_k}} \left(\frac{\beta_i}{r_k} + \frac{\eta_k x_i}{r_k^2} + \frac{x_i}{r_k^3} \right) e^{-\eta_k r_k - \sum_{m=1}^3 \beta_m x_m} \quad (3.26)$$

$$4\pi \frac{\partial G_{\phi M}}{\partial x_i} = 4\pi \frac{\partial G_{\psi P}}{\partial x_i} = \sum_{k=1}^2 \frac{(\alpha_{11}^0 - \lambda_k \alpha_{33}^0)(\kappa_{11}^0 - \lambda_k \kappa_{33}^0)}{\delta_k \sqrt{\lambda_k}} \left(\frac{\beta_i}{r_k} + \frac{\eta_k x_i}{r_k^2} + \frac{x_i}{r_k^3} \right) e^{-\eta_k r_k - \sum_{m=1}^3 \beta_m x_m} \quad (3.27)$$

$$4\pi \frac{\partial G_{\psi M}}{\partial x_i} = - \sum_{k=1}^2 \frac{(\kappa_{11}^0 - \lambda_k \kappa_{33}^0)^2}{\delta_k \sqrt{\lambda_k}} \left(\frac{\beta_i}{r_k} + \frac{\eta_k x_i}{r_k^2} + \frac{x_i}{r_k^3} \right) e^{-\eta_k r_k - \sum_{m=1}^3 \beta_m x_m} \quad (3.28)$$

where $i = 1, 2, 3$ and, of course, $\sum_{m=1}^3 \beta_m x_m = \beta_1 x_1 + \beta_2 x_2 + \beta_3 x_3$. We remark that in deriving the potential Green's functions and their derivatives, we have assumed that the point

charge is located at the origin. For applications of these Green's functions to a boundary integral equation formulation as described in section 3.4.2, the source point has to be arbitrary.

Let us assume that the point charge is located at an arbitrary source point $\mathbf{x}_s = (x_1^s, x_2^s, x_3^s)$, and the field (or observation) point is at $\mathbf{x}_f = (x_1^f, x_2^f, x_3^f)$. We then can make the following coordinate translation,

$$\tilde{x}_i = x_i^s - x_i^f \quad (3.29)$$

so that the point charge is located at the origin of the new coordinate system $(\tilde{x}_1, \tilde{x}_2, \tilde{x}_3)$. Therefore, all the Green's functions developed in this paper hold in the new coordinate system; however, the material coefficients vary exponentially in the new coordinates as follows.

$$[\kappa_{ii}(\tilde{\mathbf{x}}) \alpha_{ii}(\tilde{\mathbf{x}}) \mu_{ii}(\tilde{\mathbf{x}})] = [\tilde{\kappa}_{ii}^0 \tilde{\alpha}_{ii}^0 \tilde{\mu}_{ii}^0] \exp \left(2 \sum_{m=1}^3 \beta_m \tilde{x}_m \right) \quad (3.30)$$

where the three material constants $\tilde{\kappa}_{ii}^0$, $\tilde{\alpha}_{ii}^0$, and $\tilde{\mu}_{ii}^0$ are given by

$$\begin{aligned} \tilde{\kappa}_{ii}^0 &= \exp \left(2 \sum_{m=1}^3 \beta_m x_m^s \right) \kappa_{ii}^0 \\ \tilde{\alpha}_{ii}^0 &= \exp \left(2 \sum_{m=1}^3 \beta_m x_m^s \right) \alpha_{ii}^0 \\ \tilde{\mu}_{ii}^0 &= \exp \left(2 \sum_{m=1}^3 \beta_m x_m^s \right) \mu_{ii}^0 \end{aligned} \quad (3.31)$$

with κ_{ii}^0 , α_{ii}^0 , and μ_{ii}^0 being the material coefficients at the origin of the old coordinate system (x_1, x_2, x_3) .

3.4.2 Boundary integral equation formulation for an FGM multiferroic

For a uniaxial multiferroic material satisfying the constitutive relation (3.1), it can be easily shown that the following reciprocal property holds [64]

$$D_i^{(1)} E_i^{(2)} + B_i^{(1)} H_i^{(2)} = D_i^{(2)} E_i^{(1)} + B_i^{(2)} H_i^{(1)} \quad (3.32)$$

where the superscripts “(1)” and “(2)” denote two independent systems of the field quantities under different loadings, and the dummy index i takes the summation from 1 to 3. We emphasize that Eq. (3.32) holds for any spatial variation of the multiferroic material properties. Therefore, it also holds for the exponential variation as described by Eq. (3.2).

Integrating both sides of Eq. (3.32) with respect to the problem domain and making use of the divergence theorem, we obtain the following integral relation

$$\begin{aligned} \int_S [D_i^{(1)} \phi^{(2)} + B_i^{(1)} \psi^{(2)}] dS - \int_V [D_{i,i}^{(1)} \phi^{(2)} + B_{i,i}^{(1)} \psi^{(2)}] dV = \\ \int_S [D_i^{(2)} \phi^{(1)} + B_i^{(2)} \psi^{(1)}] dS - \int_V [D_{i,i}^{(2)} \phi^{(1)} + B_{i,i}^{(2)} \psi^{(1)}] dV \end{aligned} \quad (3.33)$$

where V is the problem domain and S is the boundary of domain V ; the subscript “ i ” denotes the derivative with respect to the coordinate x_i ; and the subscript n means the normal component of the field vector. In other words, for example, $D_n = D_i n_i$ with n_i being the outward normal at the boundary point.

We assume now that system (2) corresponds to the real boundary value problem in a FGM multiferroic domain and (1) to the corresponding Green’s function solution with $P = 1$ and $M = 0$ in Eq. (3.4). It can then be shown that the following integral equation expression holds for the electric potential ϕ at any point \mathbf{x}_s within the problem domain

$$\begin{aligned} \phi(\mathbf{x}_s) = & \int_S [D_n^P(\mathbf{x}_f; \mathbf{x}_s) \phi(\mathbf{x}_f) + B_n^P(\mathbf{x}_f; \mathbf{x}_s) \psi^{(2)}(\mathbf{x}_s)] dS \\ & - \int_S [G_{\phi P}(\mathbf{x}_f; \mathbf{x}_s) D_n(\mathbf{x}_f) + G_{\psi P}(\mathbf{x}_f; \mathbf{x}_s) B_n(\mathbf{x}_f)] dS \end{aligned} \quad (3.34)$$

where $G_{\phi P}$ and $G_{\psi P}$ are the (electric and magnetic) potential Green’s functions at x_f (due to a point electric charge of unit amplitude at x_s) given in Eqs. (3.24), and D_n^P and B_n^P are the normal components of the electric displacement and magnetic flux Green’s functions at x_f (due to a point electric charge of unit amplitude at x_s), defined as

$$\begin{aligned} D_n^P(\mathbf{x}_f; \mathbf{x}_s) &= D_i^P(\mathbf{x}_f; \mathbf{x}_s) n_i(\mathbf{x}_f) \\ B_n^P(\mathbf{x}_f; \mathbf{x}_s) &= B_i^P(\mathbf{x}_f; \mathbf{x}_s) n_i(\mathbf{x}_f) \end{aligned} \quad (3.35)$$

where $n_i(\mathbf{x}_f)$ is the outward normal at the boundary point \mathbf{x}_f , and are related to the potential Green’s functions through the following relations (for $i = 1, 2, 3$; no summation on repeated index i):

$$\begin{bmatrix} D_n^P(\mathbf{x}_f; \mathbf{x}_s) \\ B_n^P(\mathbf{x}_f; \mathbf{x}_s) \end{bmatrix} = - \begin{bmatrix} \kappa_{ii}(\mathbf{x}_f - \mathbf{x}_s) & \alpha_{ii}(\mathbf{x}_f - \mathbf{x}_s) \\ \alpha_{ii}(\mathbf{x}_f - \mathbf{x}_s) & \mu_{ii}(\mathbf{x}_f - \mathbf{x}_s) \end{bmatrix} \begin{bmatrix} \partial G_{\phi P}(\mathbf{x}_f; \mathbf{x}_s) / \partial x_i^f \\ \partial G_{\psi P}(\mathbf{x}_f; \mathbf{x}_s) / \partial x_i^f \end{bmatrix} \quad (3.36)$$

It is noted that the multiferroic material property matrix for $i = 2$ is the same as that for $i = 1$ since the material is uniaxial. In Eq. (3.36), we have also defined that $\mathbf{x}_f = (x_1^f, x_2^f, x_3^f)$.

We point out that in deriving Eq. (3.34), the electric and magnetic charges within the problem domain are assumed to be zero. Should one of them or both of them are nonzero, the particular solution method [65] or dual reciprocity method [34] can be easily applied to take care of the contribution from these body charges.

Similarly, if we let system (1) be the Green’s function solution with $P = 0$ and $M = 1$ in Eq. (3.4), then we arrive at the integral equation expression for the magnetic potential ψ at any point \mathbf{x}_s within the problem domain

$$\begin{aligned} \psi(\mathbf{x}_s) = & \int_S [D_n^M(\mathbf{x}_f; \mathbf{x}_s) \phi(\mathbf{x}_f) + B_n^M(\mathbf{x}_f; \mathbf{x}_s) \psi^{(2)}(\mathbf{x}_s)] dS \\ & - \int_S [G_{\phi M}(\mathbf{x}_f; \mathbf{x}_s) D_n(\mathbf{x}_f) + G_{\psi M}(\mathbf{x}_f; \mathbf{x}_s) B_n(\mathbf{x}_f)] dS \end{aligned} \quad (3.37)$$

where the definitions for the involved Green’s functions are similar to those in Eq. (3.34), except for the fact that the sources are different, due to a point electric charge in Eq. (3.34) and a point magnetic charge in Eq. (3.37).

Let the source point \mathbf{x}_s approach a point on the boundary of the problem domain, then Eqs. (3.34) and (3.37) form a pair of boundary integral equations from which the unknown boundary values for ϕ , ψ , D_n and B_n can be solved. Once these boundary values are solved, Eqs. (3.34) and (3.37) can be utilized to find the field quantities within the problem domain [64].

Chapter 4

Anisotropic elasticity of multilayered crystals deformed by a biperiodic network of misfit dislocations

4.1 Introduction

The exploration of dissimilar semiconductor heterostructures that are far beyond the limits of typical pseudomorphic (or coherent) epitaxy is being considered in order to provide greater functionality and configuration of highly integrated electronic and optoelectronic microsystems [66, 67]. One structural approach is the bonding [68] of mismatched semiconductors such as Si and GaAs that require structural defects to accommodate the strain at the interfaces.

Multilayered structures made of ultrathin lamellae exhibit excellent mechanical properties, such as higher yield strength, higher ductility and toughness, and creep resistance [69–72]. Periodic arrays of defects, such as dislocations, have been observed along the interfaces, which can enhance the macroscopic properties of the composite material [72]. Periodic boundary conditions are ubiquitous in describing crystalline states theoretically and computationally [73–76], and in this paper we develop a theoretical framework that accounts for the elastic properties of observed periodic dislocation arrays in multilayered structures.

The elastic fields for a multilayered composite containing one periodic (or biperiodic) array of interfacial misfit dislocations have been investigated by using Fourier or double Fourier series expansion methods [3, 77–81]. However, this method is limited and time consuming as it requires the inversion of a $6N \times 6N$ matrix for a laminated medium containing N interfaces. This is especially problematic when N is very large (say N equals 100, 1000, or 10,000), not to mention that the inversion of the $6N \times 6N$ matrix is only for one term in the Fourier or double Fourier series. Therefore, the cost of complete solutions by taking sufficiently large number of the Fourier or double Fourier series would be formidable. Due to the computational demands, previous calculations have been restricted to treating the elastic fields of isotropic or anisotropic two-layer systems deformed by a biperiodic network of misfit dislocations [78–80]. Even for the simpler two-dimensional

problem of periodic misfit dislocations, only the elastic field for layered structures containing a few layers has been calculated [3, 81]. Based on published reports, we concluded that the elasticity associated with a multilayered crystal system containing a biperiodic array of interfacial misfit dislocations is still far from complete.

In this research we propose an efficient method based on the Stroh formalism [35, 82, 83] and transfer matrix [83–85] techniques to investigate the displacement and stress fields associated with a biperiodic, hexagonal-based misfit dislocation network located along one planar interface in an anisotropic and multilayered crystal composite. It will be found that by utilizing the present approach, we can address a multilayered crystal composed of an arbitrary number of anisotropic (or isotropic) elastic layers.

4.2 Specification of the problem

We consider the deformation of a multilayered structure composed of a stack of $(N - 1)$ thin bonded anisotropic elastic layers, sandwiched between two semi-infinite anisotropic media denoted 1 and $N + 1$, as shown in Figure 4.1. A Cartesian coordinate system (x_1, x_2, x_3) is established in such a way that the bottom interface is at $x_3 = 0$ and the top interface is at $x_3 = H$, where H is the total thickness of the $(N - 1)$ thin anisotropic elastic layers. The homogeneous and anisotropic elastic thin layer k ($2 \leq k \leq N$) is bounded by its lower interface at $x_3 = z_{k-1}$ and upper interface at $x_3 = z_k$ with its thickness $h_k = z_k - z_{k-1}$, and the layers are numbered sequentially starting at 2 from the bottom thin layer. Apparently $z_N = H = \sum_{k=2}^N h_k$. A biperiodic, hexagonal misfit dislocation network that accommodates a lattice misfit between layer n and layer $n+1$ lies on the interface $x_3 = z_n$. The following boundary conditions are assumed: (i) except for the interface at $x_3 = z_n$ between layer n and layer $n + 1$, perfect bonding conditions exist between any two adjacent elastic media; (ii) continuity condition of tractions across the interface $x_3 = z_n$; (iii) linear variations of the relative interface displacement field across the interface $x_3 = z_n$ inside each biperiodic pattern of misfit dislocations [78, 80]. The multilayered structure discussed in this paper is general in the sense that if we let the elastic constants of the bottom (or top) semi-infinite medium be very small, the multilayered system is then built with a package of $(N - 1)$ thin bonded layers with a traction-free surface at $x_3 = 0$ (or $x_3 = H$), bounded by a semi-infinite medium. Furthermore if we let the elastic constants of both the two semi-infinite media be very small, the multilayered system is then made of a package of $(N - 1)$ thin bonded layers with two traction-free surfaces at $x_3 = 0$ and $x_3 = z_N$.

The displacement jumps across the interface $x_3 = z_n$ can be expanded into a biperiodic Fourier series as [78, 80]

$$[u_k^+ - u_k^-]_{x_3=z_n} = \Delta_k^{(\mathbf{G}=0)} + \sum_{\mathbf{G} \neq 0} \Delta_K^{(\mathbf{G})} e^{2\pi i(G_1 x_1 + G_2 x_2)} \quad (4.1)$$

which describes a function depending linearly on x_1 and x_2 inside the domain considered. In Eq. (4.1), \mathbf{G} is a reciprocal vector of the 2D lattice defined by the two periodic vectors \mathbf{a} and \mathbf{c} . If n and m are integers, then $\mathbf{G} = n\mathbf{a}^* + m\mathbf{c}^*$ in terms of the base vectors [79]. The components of \mathbf{G} with respect to the Cartesian coordinate system are $(G_1, G_2, 0)$. (It should be mentioned for clarity that we employ a different coordinate system than that adopted in

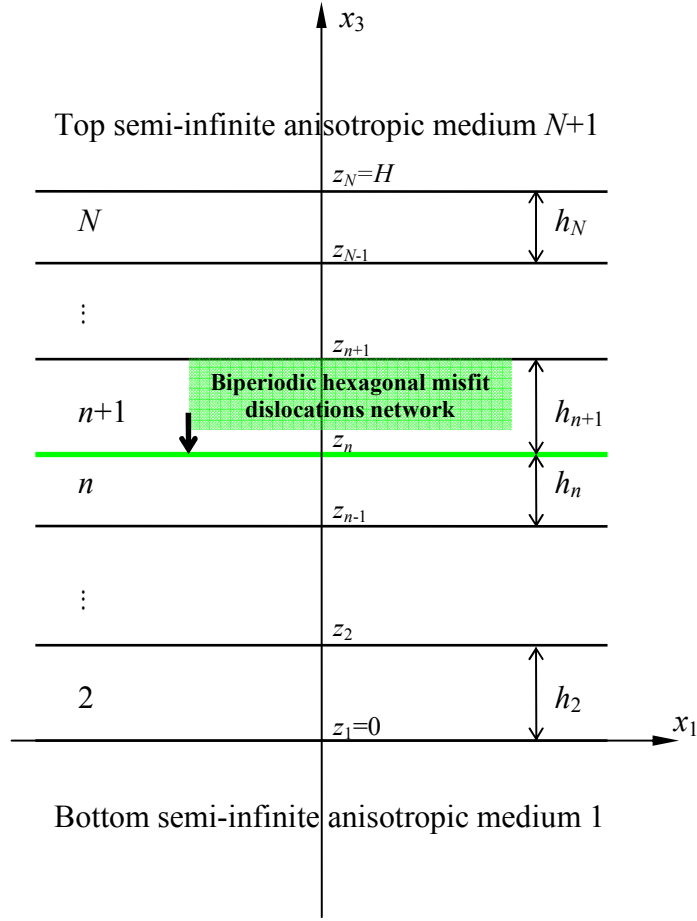


Figure 4.1: Cross section of a multilayered system with N interfaces and $N + 1$ anisotropic elastic media. A biperiodic, hexagonal, misfit dislocation network that accommodates a misfit dislocation between layer n and layer $n + 1$ lies on the interface $x_3 = z_n =$ of the multilayered structure.

Refs. 78–80.) The specific expressions of the coefficients $\Delta_K^{(G)}$ have been given in other work [78, 80]. In addition we can further take $\Delta_k^{(G=0)} = 0$ to enforce that the displacements are continuous at $x_1 = x_2 = 0$, $x_3 = z_n$.

4.3 Stroh formalism for biperiodic problems

In this section we first derive the expressions of displacement and stress fields in any homogeneous and anisotropic elastic layer by invoking the established Stroh formalism.

The linear constitutive equations, strain-displacement equations and equilibrium equations in the absence of body force can be expressed as [35]

$$\sigma_{ij} = c_{ijkl} \varepsilon_{ij} \quad (4.2a)$$

$$\varepsilon_{ij} = \frac{1}{2}(u_{i,j} + u_{j,i}) \quad (4.2b)$$

$$\sigma_{ij,j} = 0 \quad (4.2c)$$

where σ_{ij} , ε_{ij} and u_i are, respectively, the stress, strain and displacement; c_{ijkl} are the elastic moduli.

For a certain nonzero \mathbf{G} , we seek the solution of the displacement vector in the form

$$\mathbf{u} = \begin{bmatrix} u_1 \\ u_2 \\ u_3 \end{bmatrix} = e^{i(k_1 x_1 + k_2 x_2 + p x_3)} \begin{bmatrix} a_1 \\ a_2 \\ a_3 \end{bmatrix} \quad (4.3)$$

where p and a_i ($i = 1, 2, 3$) are unknowns, and

$$k_1 = 2\pi G_1 \quad k_2 = 2\pi G_2 \quad (G_1^2 + G_2^2 \neq 0) \quad (4.4)$$

Substitution of Eq. (4.3) into the strain-displacement relation Eq. (4.2b), and subsequently into the constitutive relation Eq. (4.2a) yields the traction vector (at $x_3 = \text{constant}$) as

$$\mathbf{t} = \begin{bmatrix} \sigma_{13} \\ \sigma_{23} \\ \sigma_{33} \end{bmatrix} = i e^{i(k_1 x_1 + k_2 x_2 + p x_3)} \begin{bmatrix} b_1 \\ b_2 \\ b_3 \end{bmatrix} \quad (4.5)$$

If we introduce two vectors

$$\mathbf{a} = [a_1 \quad a_2 \quad a_3]^T \quad \mathbf{b} = [b_1 \quad b_2 \quad b_3]^T \quad (4.6)$$

then it is found that the vector \mathbf{b} is related to vector \mathbf{a} through

$$\mathbf{b} = (\mathbf{R}^T + p\mathbf{T})\mathbf{a} = -\frac{1}{p}(\mathbf{Q} + p\mathbf{R})\mathbf{a} \quad (4.7)$$

where the superscript T denotes matrix transpose, and \mathbf{Q} , \mathbf{T} , \mathbf{R} are three 3×3 real matrices defined by

$$\begin{aligned}
\mathbf{Q} &= \mathbf{Q}^T \\
&= \begin{bmatrix} k_1^2 c_{11} + 2k_1 k_2 c_{16} + k_2^2 c_{66} & k_1^2 c_{16} + k_1 k_2 (c_{12} + c_{66}) + k_2^2 c_{26} & k_1^2 c_{15} + k_1 k_2 (c_{14} + c_{56}) + k_2^2 c_{46} \\ k_1^2 c_{16} + k_1 k_2 (c_{12} + c_{66}) + k_2^2 c_{26} & k_1^2 c_{66} + 2k_1 k_2 c_{26} + k_2^2 c_{22} & k_1^2 c_{56} + k_1 k_2 (c_{25} + c_{46}) + k_2^2 c_{24} \\ k_1^2 c_{15} + k_1 k_2 (c_{14} + c_{56}) + k_2^2 c_{46} & k_1^2 c_{56} + k_1 k_2 (c_{25} + c_{46}) + k_2^2 c_{24} & k_1^2 c_{55} + 2k_1 k_2 c_{45} + k_2^2 c_{44} \end{bmatrix} \\
\mathbf{T} &= \mathbf{T}^T \\
&= \begin{bmatrix} c_{55} & c_{45} & c_{35} \\ c_{45} & c_{44} & c_{34} \\ c_{35} & c_{34} & c_{33} \end{bmatrix} \\
\mathbf{R} &= \begin{bmatrix} k_1 c_{15} + k_2 c_{56} & k_1 c_{14} + k_2 c_{46} & k_1 c_{13} + k_2 c_{36} \\ k_1 c_{56} + k_2 c_{25} & k_1 c_{46} + k_2 c_{24} & k_1 c_{36} + k_2 c_{23} \\ k_1 c_{55} + k_2 c_{45} & k_1 c_{45} + k_2 c_{44} & k_1 c_{35} + k_2 c_{34} \end{bmatrix}
\end{aligned} \tag{4.8}$$

where the standard contracted notations $c_{\alpha\beta}$ for the elastic moduli c_{ijkl} have been adopted. In addition, the in-plane stresses can be expressed as

$$\begin{bmatrix} \sigma_{11} \\ \sigma_{22} \\ \sigma_{12} \end{bmatrix} = i e^{i(k_1 x_1 + k_2 x_2 + p x_3)} \times \begin{bmatrix} k_1 c_{11} + k_2 c_{16} + p c_{15} & k_1 c_{16} + k_2 c_{12} + p c_{14} & k_1 c_{15} + k_2 c_{14} + p c_{13} \\ k_1 c_{12} + k_2 c_{26} + p c_{25} & k_1 c_{26} + k_2 c_{22} + p c_{24} & k_1 c_{25} + k_2 c_{24} + p c_{23} \\ k_1 c_{16} + k_2 c_{66} + p c_{56} & k_1 c_{66} + k_2 c_{26} + p c_{46} & k_1 c_{56} + k_2 c_{46} + p c_{36} \end{bmatrix} \begin{bmatrix} a_1 \\ a_2 \\ a_3 \end{bmatrix} \tag{4.9}$$

The stress components should satisfy the equilibrium equations Eq. (4.2c), which in terms of the vector \mathbf{a} , yields the following eigenequation:

$$\{\mathbf{Q} + p(\mathbf{R} + \mathbf{R}^T) + p^2 \mathbf{T}\} \mathbf{a} = \mathbf{0} \tag{4.10}$$

It is observed that Eq. (4.10), derived for the biperiodic problem, is identical in structure to the Stroh formalism in terms of the 2D Fourier transform for three-dimensional (3D) problems [35, 82–85]. This agreement is somewhat expected given that the Fourier transform is a generalization of the Fourier series in the limit as the period of the Fourier series approaches infinity. With aid of Eq. (4.7), Eq. (4.10) can be recast into the following standard eigenvalue problem

$$\mathbf{N} \begin{bmatrix} \mathbf{a} \\ \mathbf{b} \end{bmatrix} = p \begin{bmatrix} \mathbf{a} \\ \mathbf{b} \end{bmatrix} \tag{4.11}$$

where

$$\mathbf{N} = \begin{bmatrix} -\mathbf{T}^{-1} \mathbf{R}^T & \mathbf{T}^{-1} \\ -\mathbf{Q} + \mathbf{R} \mathbf{T}^{-1} \mathbf{R}^T & -\mathbf{R} \mathbf{T}^{-1} \end{bmatrix} \tag{4.12}$$

We remark that, for any material anisotropy, expression of the material matrix \mathbf{N} is explicit.

For example, when the material is orthotropic, the explicit expression of \mathbf{N} is

$$\mathbf{N} = \begin{bmatrix} 0 & 0 & -k_1 & 1/c_{55} & 0 & 0 \\ 0 & 0 & -k_2 & 0 & 1/c_{44} & 0 \\ -k_1 c_{13}/c_{33} & -k_2 c_{23}/c_{33} & 0 & 0 & 0 & 1/c_{33} \\ -k_1^2(c_{11}-c_{13}^2/c_{33})-k_2^2 c_{66} & -k_1 k_2(c_{12}+c_{66}-c_{13}c_{23}/c_{33}) & 0 & 0 & 0 & -k_1 c_{13}/c_{33} \\ -k_1 k_2(c_{12}+c_{66}-c_{13}c_{23}/c_{33}) & -k_1^2 c_{66}-k_2^2(c_{22}-c_{23}^2/c_{33}) & 0 & 0 & 0 & -k_2 c_{23}/c_{33} \\ 0 & 0 & 0 & -k_1 & -k_2 & 0 \end{bmatrix} \quad (4.13)$$

Furthermore, if the material is isotropic, then \mathbf{N} is reduced to

$$\mathbf{N} = \begin{bmatrix} 0 & 0 & -k_1 & \frac{2}{c_{11}-c_{12}} & 0 & 0 \\ 0 & 0 & -k_2 & 0 & \frac{2}{c_{11}-c_{12}} & 0 \\ -\frac{k_1 c_{12}}{c_{11}} & -\frac{k_2 c_{12}}{c_{11}} & 0 & 0 & 0 & \frac{1}{c_{11}} \\ -k_1^2 \frac{c_{11}-c_{12}^2}{c_{11}} - k_2^2 \frac{c_{11}-c_{12}}{2} & -k_1 k_2 \frac{c_{11}^2+c_{11}c_{12}-2c_{12}^2}{2c_{11}} & 0 & 0 & 0 & -\frac{k_1 c_{12}}{c_{11}} \\ -k_1 k_2 \frac{c_{11}^2+c_{11}c_{12}-2c_{12}^2}{2c_{11}} & -k_1^2 \frac{c_{11}-c_{12}}{2} - k_2^2 \frac{c_{11}^2-c_{12}^2}{c_{11}} & 0 & 0 & 0 & -\frac{k_2 c_{12}}{c_{11}} \\ 0 & 0 & 0 & -k_1 & -k_2 & 0 \end{bmatrix} \quad (4.14)$$

where $c_{11} = [2\mu(1-\nu)]/(1-2\nu)$ and $c_{12} = (2\mu\nu)/(1-2\nu)$ with μ being the shear modulus and ν the Poisson's ratio.

Depending on the given material property (e.g., isotropic material), the six eigenvalues of Eq. (4.11) may not be distinct. Should repeated roots occur, a slight change in the material constants would result in distinct roots with negligible errors [64, 85]. In doing so, the following simple solution structure can still be applied. Let us assume that the first three eigenvalues of Eq. (4.11) have positive imaginary parts, and the remaining three eigenvalues are conjugate to the first three, i.e., $p_{i+3} = \bar{p}_i$, ($i = 1, 2, 3$). We distinguish the corresponding six eigenvectors by attaching a subscript to \mathbf{a} and \mathbf{b} . Then the general solutions for the displacement and traction vectors (of the x_3 -dependent factor) are

$$\begin{bmatrix} \mathbf{u} \\ -\mathbf{it} \end{bmatrix} = \begin{bmatrix} \mathbf{A} & \bar{\mathbf{A}} \\ \mathbf{B} & \bar{\mathbf{B}} \end{bmatrix} \begin{bmatrix} \langle e^{ip_\alpha x_3} \rangle & \mathbf{0} \\ \mathbf{0} & \langle e^{i\bar{p}_\alpha x_3} \rangle \end{bmatrix} \begin{bmatrix} \mathbf{K}_1 \\ \mathbf{K}_2 \end{bmatrix} \quad (4.15)$$

where \mathbf{K}_1 and \mathbf{K}_2 are two constant vectors to be determined, and

$$\mathbf{A} = [\mathbf{a}_1 \quad \mathbf{a}_2 \quad \mathbf{a}_3] \quad \mathbf{B} = [\mathbf{b}_1 \quad \mathbf{b}_2 \quad \mathbf{b}_3] \quad (4.16)$$

$$\langle e^{ip_\alpha x_3} \rangle = \text{diag} [e^{ip_1 x_3} \quad e^{ip_2 x_3} \quad e^{ip_3 x_3}] \quad \text{Im} \{p_j\} > 0, (j = 1-3)$$

It is easy to show that the two matrices \mathbf{A} and \mathbf{B} satisfy the following normalized orthogonal relationship [35]

$$\begin{bmatrix} \mathbf{B}^T & \mathbf{A}^T \\ \bar{\mathbf{B}}^T & \bar{\mathbf{A}}^T \end{bmatrix} \begin{bmatrix} \mathbf{A} & \bar{\mathbf{A}} \\ \mathbf{B} & \bar{\mathbf{B}} \end{bmatrix} = \begin{bmatrix} \mathbf{I} & \mathbf{0} \\ \mathbf{0} & \mathbf{I} \end{bmatrix} \quad (4.17)$$

The above orthogonal relationship provides us with a simple way of inverting the eigenvector matrix, which is required in forming the transfer matrix.

Furthermore, in view of the above orthogonal relationship, we can also introduce the generalized Barnett-Lothe tensors \mathbf{S} , \mathbf{H} , \mathbf{L} defined by [35]

$$\mathbf{S} = i(2\mathbf{A}\mathbf{B}^T - \mathbf{I}), \quad \mathbf{H} = 2i\mathbf{A}\mathbf{A}^T, \quad \mathbf{L} = -2i\mathbf{B}\mathbf{B}^T \quad (4.18)$$

with \mathbf{H} and \mathbf{L} being symmetric and positive definite, and \mathbf{SH} , \mathbf{LS} , $\mathbf{H}^{-1}\mathbf{S}$, \mathbf{SL}^{-1} being anti-symmetric. The generalized Barnett-Lothe tensors will be useful when addressing a semi-infinite medium. We further point out that, for isotropic materials, if we set

$$k_1 = \eta \cos \theta, \quad k_2 = \eta \sin \theta \quad (4.19)$$

where η is the norm of (k_1, k_2) , and define the following three vectors

$$\mathbf{x} = \begin{bmatrix} \sin \theta \\ -\cos \theta \\ 0 \end{bmatrix} \quad \mathbf{n} = \begin{bmatrix} 0 \\ 0 \\ -1 \end{bmatrix} \quad \mathbf{m} = \begin{bmatrix} \cos \theta \\ \sin \theta \\ 0 \end{bmatrix} \quad (4.20)$$

then the three generalized Barnett-Lothe tensors can be reduced to [35]

$$\begin{aligned} \mathbf{S} &= \frac{1-2\nu}{2(1-\nu)}(\mathbf{m}\mathbf{n}^T - \mathbf{n}\mathbf{m}^T), \\ \mathbf{H} &= \frac{1}{4\eta\mu(1-\nu)}[(3-4\nu)\mathbf{I} + \mathbf{x}\mathbf{x}^T], \\ \mathbf{L} &= \frac{\eta\mu}{1-\nu}(\mathbf{I} - \nu\mathbf{x}\mathbf{x}^T). \end{aligned} \quad (4.21)$$

With the displacement and traction vectors in Eq. (4.15), the in-plane stress components can be expressed in terms of them as

$$\begin{aligned} \begin{bmatrix} \sigma_{11} \\ \sigma_{22} \\ \sigma_{12} \end{bmatrix} &= \mathbf{i} \left\{ \begin{bmatrix} k_1 c_{11} + k_2 c_{16} & k_1 c_{16} + k_2 c_{12} & k_1 c_{15} + k_2 c_{14} \\ k_1 c_{12} + k_2 c_{26} & k_1 c_{26} + k_2 c_{22} & k_1 c_{25} + k_2 c_{24} \\ k_1 c_{16} + k_2 c_{66} & k_1 c_{66} + k_2 c_{26} & k_1 c_{56} + k_2 c_{46} \end{bmatrix} - \begin{bmatrix} c_{15} & c_{14} & c_{13} \\ c_{25} & c_{24} & c_{23} \\ c_{56} & c_{46} & c_{36} \end{bmatrix} \mathbf{T}^{-1} \mathbf{R}^T \right\} \mathbf{u} \\ &\quad + \begin{bmatrix} c_{15} & c_{14} & c_{13} \\ c_{25} & c_{24} & c_{23} \\ c_{56} & c_{46} & c_{36} \end{bmatrix} \mathbf{T}^{-1} \mathbf{t} \quad (4.22) \end{aligned}$$

4.4 Transfer matrix for the $(N-1)$ thin bonded layers

For a certain elastic layer k of finite thickness h_k with its lower surface at $x_3 = z_{k-1}$ ($k = 2, 3, \dots, N$), it follows from Eqs. (4.15) and (4.17) that \mathbf{K}_1 and \mathbf{K}_2 can be expressed in terms of the displacement and traction vectors at its lower interface $x_3 = z_{k-1}$ as

$$\begin{bmatrix} \mathbf{K}_1 \\ \mathbf{K}_2 \end{bmatrix} = \begin{bmatrix} \langle e^{-i p \alpha z_{k-1}} \rangle & \mathbf{0} \\ \mathbf{0} & \langle e^{-i \bar{p} \alpha z_{k-1}} \rangle \end{bmatrix} \begin{bmatrix} \mathbf{B}^T & \mathbf{A}^T \\ \bar{\mathbf{B}}^T & \bar{\mathbf{A}}^T \end{bmatrix} \begin{bmatrix} \mathbf{u} \\ -i\mathbf{t} \end{bmatrix}_{z_{k-1}} \quad (4.23)$$

Then the displacement and traction vectors at any position within this layer are related to the displacement and traction vectors at its lower interface $x_3 = z_{k-1}$ as follows

$$\begin{bmatrix} \mathbf{u} \\ -i\mathbf{t} \end{bmatrix} = \mathbf{E}_k(x_3 - z_{k-1}) \begin{bmatrix} \mathbf{u} \\ -i\mathbf{t} \end{bmatrix}_{z_{k-1}} \quad (4.24)$$

where

$$\mathbf{E}_k(x_3) = \begin{bmatrix} \mathbf{A} & \bar{\mathbf{A}} \\ \mathbf{B} & \bar{\mathbf{B}} \end{bmatrix} \begin{bmatrix} \langle e^{ip_\alpha x_3} \rangle & \mathbf{0} \\ \mathbf{0} & \langle e^{i\bar{p}_\alpha x_3} \rangle \end{bmatrix} \begin{bmatrix} \mathbf{B}^T & \mathbf{A}^T \\ \bar{\mathbf{B}}^T & \bar{\mathbf{A}}^T \end{bmatrix} \quad (4.25)$$

is called the transfer matrix (or the propagator matrix) [85]. In deriving the above expression of $\mathbf{E}_k(x_3)$, the orthogonal relationship in Eq. (4.17) has been utilized. Moreover, by utilizing the orthogonal relationships in Eqs. (4.17) and (4.11), the transfer matrix $\mathbf{E}_k(x_3)$ can also be expressed in terms of a matrix exponential as

$$\mathbf{E}_k(x_3) = \exp(i\mathbf{N}x_3) \quad (4.26)$$

which is strikingly simple and can be easily calculated even if the matrix \mathbf{N} is nonsemisimple when the material is (mathematically) degenerate such as isotropic material [35]. Eq. (4.26) demonstrates that by employing the matrix exponential for the transfer matrix, one can avoid directly solving the eigenvalue problem of Eq. (4.11).

It follows from Eq. (4.24) that the displacement and traction vectors at the upper interface $x_3 = z_k$ of layer k are related to those at the lower interface $x_3 = z_{k-1}$ through the following propagating relation

$$\begin{bmatrix} \mathbf{u} \\ -i\mathbf{t} \end{bmatrix}_{z_k} = \mathbf{E}_k(h_k) \begin{bmatrix} \mathbf{u} \\ -i\mathbf{t} \end{bmatrix}_{z_{k-1}} \quad (4.27)$$

Consequently, the solution at the interface $x_3 = z_n^-$ (here the superscript “−” indicates approaching the interface from below) of the multilayered system can be expressed by that at the bottom interface $x_3 = 0$ as

$$\begin{bmatrix} \mathbf{u} \\ -i\mathbf{t} \end{bmatrix}_{z_n^-} = \begin{bmatrix} \mathbf{Y}_{11} & \mathbf{Y}_{12} \\ \mathbf{Y}_{21} & \mathbf{Y}_{22} \end{bmatrix} \begin{bmatrix} \mathbf{u} \\ -i\mathbf{t} \end{bmatrix}_0 \quad (4.28)$$

where \mathbf{Y}_{11} , \mathbf{Y}_{12} , \mathbf{Y}_{21} , and \mathbf{Y}_{22} are four 3×3 matrices given by

$$\begin{bmatrix} \mathbf{Y}_{11} & \mathbf{Y}_{12} \\ \mathbf{Y}_{21} & \mathbf{Y}_{22} \end{bmatrix} = \mathbf{E}_n(h_n) \times \mathbf{E}_{n-1}(h_{n-1}) \times \cdots \times \mathbf{E}_3(h_3) \times \mathbf{E}_2(h_2) \quad (4.29)$$

Similarly, the solution at the top interface $x_3 = H$ of the multilayered system can be expressed by that at the interface $x_3 = z_n^+$ (here the superscript “+” indicates approaching the interface from above) as

$$\begin{bmatrix} \mathbf{u} \\ -i\mathbf{t} \end{bmatrix}_H = \begin{bmatrix} \tilde{\mathbf{Y}}_{11} & \tilde{\mathbf{Y}}_{12} \\ \tilde{\mathbf{Y}}_{21} & \tilde{\mathbf{Y}}_{22} \end{bmatrix} \begin{bmatrix} \mathbf{u} \\ -i\mathbf{t} \end{bmatrix}_{z_n^+} \quad (4.30)$$

where $\tilde{\mathbf{Y}}_{11}$, $\tilde{\mathbf{Y}}_{12}$, $\tilde{\mathbf{Y}}_{21}$, and $\tilde{\mathbf{Y}}_{22}$ are four 3×3 matrices given by

$$\begin{bmatrix} \tilde{\mathbf{Y}}_{11} & \tilde{\mathbf{Y}}_{12} \\ \tilde{\mathbf{Y}}_{21} & \tilde{\mathbf{Y}}_{22} \end{bmatrix} = \mathbf{E}_N(h_N) \times \mathbf{E}_{N-1}(h_{N-1}) \times \cdots \times \mathbf{E}_{n+2}(h_{n+2}) \times \mathbf{E}_{n+1}(h_{n+1}) \quad (4.31)$$

4.5 The general solution for the two semi-infinite media

Since $x_3 \rightarrow -\infty$ for the bottom semi-infinite medium, the solution for the bottom semi-infinite medium can be taken as

$$\begin{bmatrix} \mathbf{u} \\ -i\mathbf{t} \end{bmatrix} = 2i \begin{bmatrix} \bar{\mathbf{A}}_{(1)} \\ \bar{\mathbf{B}}_{(1)} \end{bmatrix} \langle e^{i\bar{p}_{\alpha(1)}x_3} \rangle \bar{\mathbf{B}}_{(1)}^T \mathbf{q}_b \quad (4.32)$$

where \mathbf{q}_b is a constant vector to be determined, and the subscript “(1)” is utilized to indicate the quantities associated with the bottom semi-infinite medium 1. The above general solution ensures that the elastic field approaches zero as $x_3 \rightarrow -\infty$.

Similarly, due to the fact that $x_3 \rightarrow +\infty$ for the top semi-infinite medium, then the general solution for the top semi-infinite medium can be taken as

$$\begin{bmatrix} \mathbf{u} \\ -i\mathbf{t} \end{bmatrix} = 2i \begin{bmatrix} \mathbf{A}_{(N+1)} \\ \mathbf{B}_{(N+1)} \end{bmatrix} \langle e^{ip_{\alpha(N+1)}(x_3-H)} \rangle \mathbf{B}_{(N+1)}^T \mathbf{q}_u \quad (4.33)$$

where \mathbf{q}_u is a constant vector to be determined, and the subscript $(N+1)$ is utilized to indicate the quantities associated with the top semi-infinite medium $N+1$. The above general solution ensures that the elastic field approaches zero as $x_3 \rightarrow +\infty$.

4.6 Solution of the total structure

Enforcing that the displacements and tractions are continuous across the bottom interface $x_3 = 0$, it follows from Eqs. (4.28) and (4.32) that we can arrive at the following relationship between the traction and displacement vectors at the interface $x_3 = z_n^-$

$$\mathbf{t}(z_n^-) = i \left[\mathbf{Y}_{21}(\mathbf{i}\mathbf{I} - \mathbf{S}_{(1)}) + \mathbf{Y}_{22}\mathbf{L}_{(1)} \right] \left[\mathbf{Y}_{11}(\mathbf{i}\mathbf{I} - \mathbf{S}_{(1)}) + \mathbf{Y}_{12}\mathbf{L}_{(1)} \right]^{-1} \mathbf{u}(z_n^-) \quad (4.34)$$

During the derivation of the above expression, Eq. (4.18) for the generalized Barnett-Lothe tensors has been used.

Similarly, due to the fact that the displacements and tractions are also continuous across the top of the interface $x_3 = H$, then it follows from Eqs. (4.30) and (4.33) that we can arrive at the following relationship between the traction and displacement vectors at the interface $x_3 = z_n^+$

$$\mathbf{t}(z_n^+) = -i \left[\tilde{\mathbf{Y}}_{12} + (\mathbf{S}_{(N+1)} + \mathbf{i}\mathbf{I})\mathbf{L}_{(N+1)}^{-1} \tilde{\mathbf{Y}}_{22} \right]^{-1} \left[\tilde{\mathbf{Y}}_{11} + (\mathbf{S}_{(N+1)} + \mathbf{i}\mathbf{I})\mathbf{L}_{(N+1)}^{-1} \tilde{\mathbf{Y}}_{21} \right] \mathbf{u}(z_n^+) \quad (4.35)$$

In view of Eq. (4.1) for the double Fourier series, the boundary conditions on the interface $x_3 = z_n$ can be recast into

$$\mathbf{t}(z_n^+) = \mathbf{t}(z_n^-), \mathbf{u}(z_n^+) - \mathbf{u}(z_n^-) = \underline{\Delta} \quad (4.36)$$

where

$$\underline{\Delta} = \left[\Delta_1^{(\mathbf{G})} \quad \Delta_2^{(\mathbf{G})} \quad \Delta_3^{(\mathbf{G})} \right]^T \quad (4.37)$$

Consequently it follows from Eqs. (4.34)–(4.36) that the displacement and traction vectors at $x_3 = z_n$ can be uniquely determined as

$$\begin{aligned}\mathbf{u}(z_n^-) &= -\underline{\underline{\Omega}}^{-1}\underline{\underline{\Delta}} \\ \mathbf{u}(z_n^+) &= (\mathbf{I} - \underline{\underline{\Omega}}^{-1})\underline{\underline{\Delta}} \\ \mathbf{t}(z_n^+) &= \mathbf{t}(z_n^-) \\ &= -i [\mathbf{Y}_{21}(\mathbf{iI} - \mathbf{S}_{(1)}) + \mathbf{Y}_{22}\mathbf{L}_{(1)}] [\mathbf{Y}_{11}(\mathbf{iI} - \mathbf{S}_{(1)}) + \mathbf{Y}_{12}\mathbf{L}_{(1)}]^{-1} \underline{\underline{\Omega}}^{-1}\underline{\underline{\Delta}}\end{aligned}\quad (4.38)$$

where

$$\begin{aligned}\underline{\underline{\Omega}} &= \mathbf{I} + [\tilde{\mathbf{Y}}_{11} + (\mathbf{S}_{(N+1)} + \mathbf{iI})\mathbf{L}_{(N+1)}^{-1}\tilde{\mathbf{Y}}_{21}]^{-1} [\tilde{\mathbf{Y}}_{12} + (\mathbf{S}_{(N+1)} + \mathbf{iI})\mathbf{L}_{(N+1)}^{-1}\tilde{\mathbf{Y}}_{22}] \\ &\quad \times [\mathbf{Y}_{21}(\mathbf{iI} - \mathbf{S}_{(1)}) + \mathbf{Y}_{22}\mathbf{L}_{(1)}] [\mathbf{Y}_{11}(\mathbf{iI} - \mathbf{S}_{(1)}) + \mathbf{Y}_{12}\mathbf{L}_{(1)}]^{-1}\end{aligned}\quad (4.39)$$

Once the displacement and traction vectors are known at the interface $x_3 = z_n$, the displacement and traction vectors at any position within layer k , ($2 \leq k \leq N$), of the layered system can be conveniently determined as

$$\begin{aligned}\begin{bmatrix} \mathbf{u} \\ -\mathbf{it} \end{bmatrix} &= \mathbf{E}_k(x_3 - z_{k-1}) \times \mathbf{E}_{k-1}(h_{k-1}) \times \cdots \times \mathbf{E}_3(h_3) \times \mathbf{E}_2(h_2) \times \begin{bmatrix} \mathbf{Y}_{11} & \mathbf{Y}_{12} \\ \mathbf{Y}_{21} & \mathbf{Y}_{22} \end{bmatrix}^{-1} \begin{bmatrix} \mathbf{u} \\ -\mathbf{it} \end{bmatrix}_{z_n^-} \\ &= \mathbf{E}_k(x_3 - z_{k-1}) \times \mathbf{E}_k(-h_k) \times \mathbf{E}_{k+1}(-h_{k+1}) \times \mathbf{E}_{n-1}(-h_{n-1}) \times \mathbf{E}_n(-h_n) \begin{bmatrix} \mathbf{u} \\ -\mathbf{it} \end{bmatrix}_{z_n^-}\end{aligned}\quad (4.40)$$

for $2 \leq k \leq n$ and $z_{k-1} < x_3 < z_k$, and

$$\begin{bmatrix} \mathbf{u} \\ -\mathbf{it} \end{bmatrix} = \mathbf{E}_k(x_3 - z_{k-1}) \times \mathbf{E}_{k-1}(h_{k-1}) \times \cdots \times \mathbf{E}_{n+2}(h_{n+2}) \times \mathbf{E}_{n+1}(h_{n+1}) \begin{bmatrix} \mathbf{u} \\ -\mathbf{it} \end{bmatrix}_{z_n^+} \quad (4.41)$$

for $n+1 \leq k \leq N$ and $z_{k-1} < x_3 < z_k$.

Similarly the displacement and traction vectors at any position within the bottom semi-infinite anisotropic medium ($x_3 < 0$) are given by

$$\begin{bmatrix} \mathbf{u} \\ -\mathbf{it} \end{bmatrix} = 2i \begin{bmatrix} \bar{\mathbf{A}}_{(1)} \\ \bar{\mathbf{B}}_{(1)} \end{bmatrix} \langle e^{i\bar{p}_{\alpha(1)}x_3} \rangle \bar{\mathbf{B}}_{(1)}^T [\mathbf{Y}_{11}(\mathbf{iI} - \mathbf{S}_{(1)}) + \mathbf{Y}_{12}\mathbf{L}_{(1)}]^{-1} \mathbf{u}(z_n^-) \quad (4.42)$$

and the displacement and traction vectors at any position within the top semi-infinite anisotropic medium ($x_3 > H$) are given by

$$\begin{bmatrix} \mathbf{u} \\ -\mathbf{it} \end{bmatrix} = 2i \begin{bmatrix} \mathbf{A}_{(N+1)} \\ \mathbf{B}_{(N+1)} \end{bmatrix} \langle e^{ip_{\alpha(N+1)}(x_3-H)} \rangle \mathbf{B}_{(N+1)}^T (\mathbf{S}_{(N+1)} + \mathbf{iI})^{-1} [\tilde{\mathbf{Y}}_{11} \quad \tilde{\mathbf{Y}}_{12}] \begin{bmatrix} \mathbf{u} \\ -\mathbf{it} \end{bmatrix}_{z_n^+} \quad (4.43)$$

Once the displacement and traction vectors are known, the distributions of the in-plane stresses σ_{11} , σ_{22} and σ_{12} can be determined through Eq. (4.22).

For $\mathbf{G} = \mathbf{0}$, the corresponding displacements are constant within each layer. In addition, the constant displacements are common for each layer due to the fact that $\Delta_k^{(\mathbf{G}=0)} = 0$, and therefore, can be chosen arbitrarily. For example they can be chosen to maintain $(0, 0, z_n)$ as a fixed point. Finally we can add together the results for different values of zero and nonzero values of \mathbf{G} .

4.7 Main features of the methodology

The main features of the methodology presented in this work are:

1. One needs only to invert several 3×3 matrices to arrive at the displacement and traction vectors at any position within the anisotropic multilayered crystal (see Eqs. (4.38)–(4.43)). Thus it is very suitable to address a crystal composed of an arbitrarily large number of layers. Due to the time saved, then it becomes feasible, by summing enough terms of the double Fourier series, to calculate the stress field close to the interface where the array of misfit dislocations is located. It is a great advance compared to the existing method, which is rather formidable and time consuming as it requires inverting a $6N \times 6N$ matrix for a multilayered structure with N interfaces. The earlier approach is particularly difficult when the value of N is very large (say a hundred layers).
2. When letting $k_2 = 0$ (or $k_1 = 0$), the derived solution can also be used to investigate the periodic problem in the x_1 (or x_2) direction. One example is a multilayered system containing an array of periodic misfit dislocations with Burgers vector $\hat{\mathbf{b}} = (\hat{b}_1, \hat{b}_2, \hat{b}_3)$ along the planar interface $x_3 = z_n$ [3]. In this case the 3D problem is reduced to a 2D one in which the solutions are independent of the x_2 (or the x_1) coordinate.
3. The solution of the eigenvalue problem Eq. (4.11) for the $(N - 1)$ thin layers can be circumvented due to the fact that the transfer matrix can be expressed in terms of matrix exponential (Eq. (4.25)). As a result, each thin layer can be made of either anisotropic material or the mathematically degenerated isotropic material. In general the eigenvalue problem Eq. (4.11) has to be solved for the two semi-infinite media since there is no such a concept of transfer matrix for a semi-infinite medium. On the other hand if the explicit expressions of the generalized Barnett-Lothe tensors \mathbf{S} , \mathbf{H} and \mathbf{L} are known for the involved material like the isotropic case (see Eq. (4.21)), then even the solution of the eigenvalue problem Eq. (4.11) for the two semi-infinite media is *unnecessary* if one is interested in the elastic fields in the welded $(N - 1)$ thin layers. In this special case, the elastic fields in the thin layers are completely determined by the transfer matrices \mathbf{Y}_{ij} , $\tilde{\mathbf{Y}}_{ij}$, ($i, j = 1, 2$) and the generalized Barnett-Lothe tensors $\mathbf{S}_{(1)}$, $\mathbf{L}_{(1)}$, $\mathbf{S}_{(N+1)}$, $\mathbf{L}_{(N+1)}$ (see Eqs. (4.38)–(4.41)).
4. Should there be any thick layer in the layered system, the corresponding transfer matrix can be normalized using the method proposed by Pan [83]. Furthermore, to accelerate the convergence of the Fourier series for observation points close to the dislocation segment, the explicit solution to the corresponding homogeneous space can be utilized so that the singular and slow convergent part can be analytically treated [86].

x_3 (nm)	0	2	6	8
(isotropic) σ_{11} (10^7 Pa)	$-19.9/-37.7$ ($-19.9/-37.7$)	$51.0/56.5$ ($50.8/56.5$)	$23.0/-2.71$ ($23.0/-2.6$)	$4.65/16.1$ ($4.7/16.1$)
(cubic) σ_{11} (10^7 Pa)	$-15.2/-40.8$	$49.1/70.4$	$12.2/-24.5$	$7.37/26.3$

Table 4.1: Values of σ_{11} on the two sides of each interface of the multilayer GaAs/Si/GaAs/Si/GaAs/Si with $N = 5$. The interface locations are denoted by x_3 . Two material cases are studied: elastically isotropic (assumed for demonstration purposes) and elastically cubic (true). The values in the parentheses in the second row are the results of Bonnet [3].

4.8 Application

To verify the correctness and to show the power of the method, we first consider a multilayered structure with $N = 5$, formed by four thin alternating GaAs and Si layers sandwiched between two semi-infinite media GaAs and Si. This problem was discussed by Bonnet [3] when the six alternating media were assumed to be isotropic. The thickness of each layer is 2 nm, and as a result, the five interfaces are located at $x_3 = 0, 2, 4, 6, 8$ nm. We consider the problem of a single array of periodic edge misfit dislocations with Burgers vector $\hat{\mathbf{b}} = (\hat{b}_1, \hat{b}_2, \hat{b}_3) = (0.3838 \text{ nm}, 0, 0)$ located along the central interface $x_3 = 4$ nm. The result is a sawtooth change of misfit displacement $\Delta u_k = u_k^{(n+1)} - u_k^{(n)}$, ($n = 3$) along the interface, which can be expanded into Fourier series [3]. The period Λ of the misfit dislocations is 9.7 nm. In addition the misfit dislocations are infinitely long in the x_2 -direction. As a result the problem is 2D in which the solutions are independent of the x_2 coordinate. Furthermore, we take $k_1 = 2\pi m/\Lambda$ with m being a nonzero integer and $k_2 = 0$ in our formulation. We calculate the in-plane stress component σ_{11} and the traction component σ_{33} along the x_3 -axis ($x_1 = 0$). First, as in Ref. 3, we assume that both GaAs and Si are isotropic with elastic constants $\mu_{\text{GaAs}} = 46.01 \text{ GPa}$, $\nu_{\text{GaAs}} = 0.24$, $\mu_{\text{Si}} = 66.11 \text{ GPa}$, $\nu_{\text{Si}} = 0.23$. The distributions of σ_{11} and σ_{33} along the x_3 -axis when each medium is isotropic are illustrated as dashed lines in Figures 4.2 and 4.3, and the values of σ_{11} on the two sides of the interfaces $x_3 = 0, 2, 6, 8$ nm are given in the second row of Table 4.1. It is observed that the present method based on the Stroh formalism and transfer matrix produces exactly the same the results as in Bonnet [3]. Consequently the correctness of the method is verified.

Both GaAs and Si are elastically anisotropic (cubic) with elastic constants $c_{11} = 118 \text{ GPa}$, $c_{12} = 53.5 \text{ GPa}$, $c_{44} = 59.4 \text{ GPa}$ for GaAs and $c_{11} = 165.7 \text{ GPa}$, $c_{12} = 63.9 \text{ GPa}$, $c_{44} = 79.6 \text{ GPa}$ for Si [3, 79, 80]. Therefore, it would be interesting to study the influence of material anisotropy on the misfit dislocation-induced field. The distributions of σ_{11} and σ_{33} along the x_3 -axis when each medium is anisotropic (cubic) are illustrated as solid lines in Figs 4.2 and 4.3 and the values of σ_{11} on the two sides of the interfaces $x_3 = 0, 2, 6$, and 8 nm are further listed in the third row of Table 4.1 for comparison with the corresponding isotropic case. Clearly both σ_{11} and σ_{33} based on the true anisotropic (cubic) material model are significantly different from the corresponding results when each medium is simplified to be isotropic. As such, the effect of semiconductor anisotropy on the misfit dislocation-induced stresses should be taken into consideration for more accurate

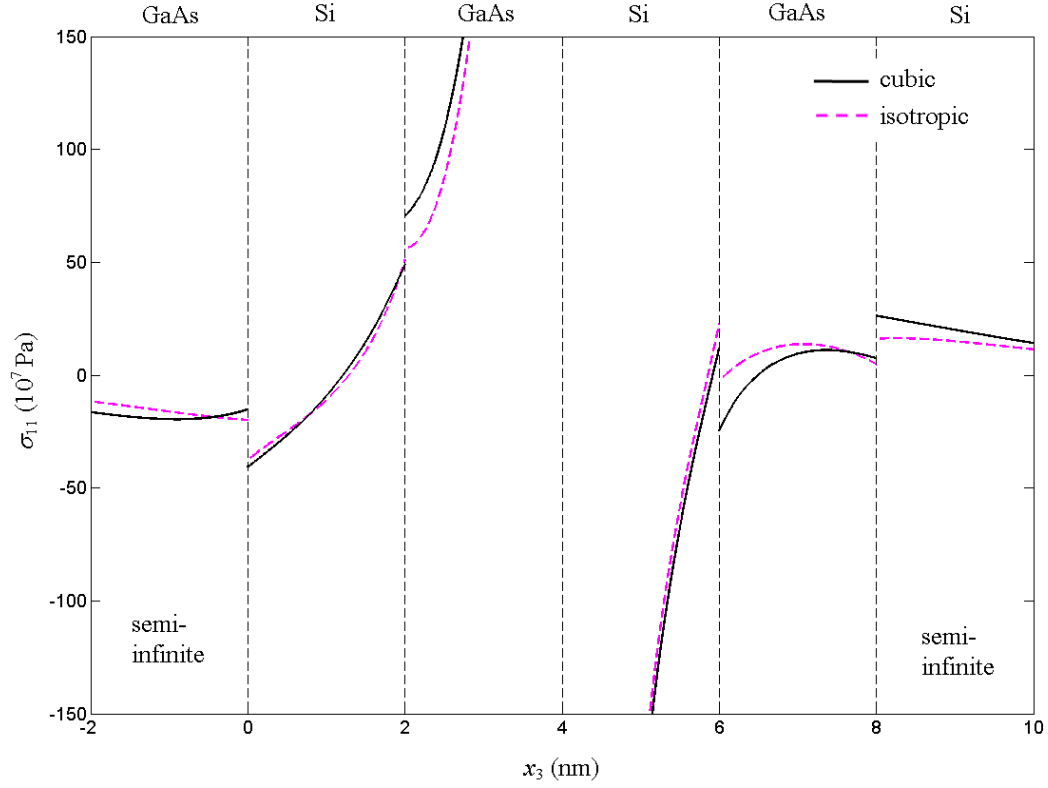


Figure 4.2: Distribution of the in-plane stress σ_{11} along the x_3 -axis ($x_1 = 0$) for a $N = 5$ multilayered structure formed by alternating GaAs and Si. The misfit dislocation array lies at the interface $x_3 = 4$ nm and is infinitely long in the x_2 -direction. The dark solid lines are the results when GaAs and Si are taken to be cubic and the pink dashed lines are the corresponding results when GaAs and Si are assumed to be isotropic.

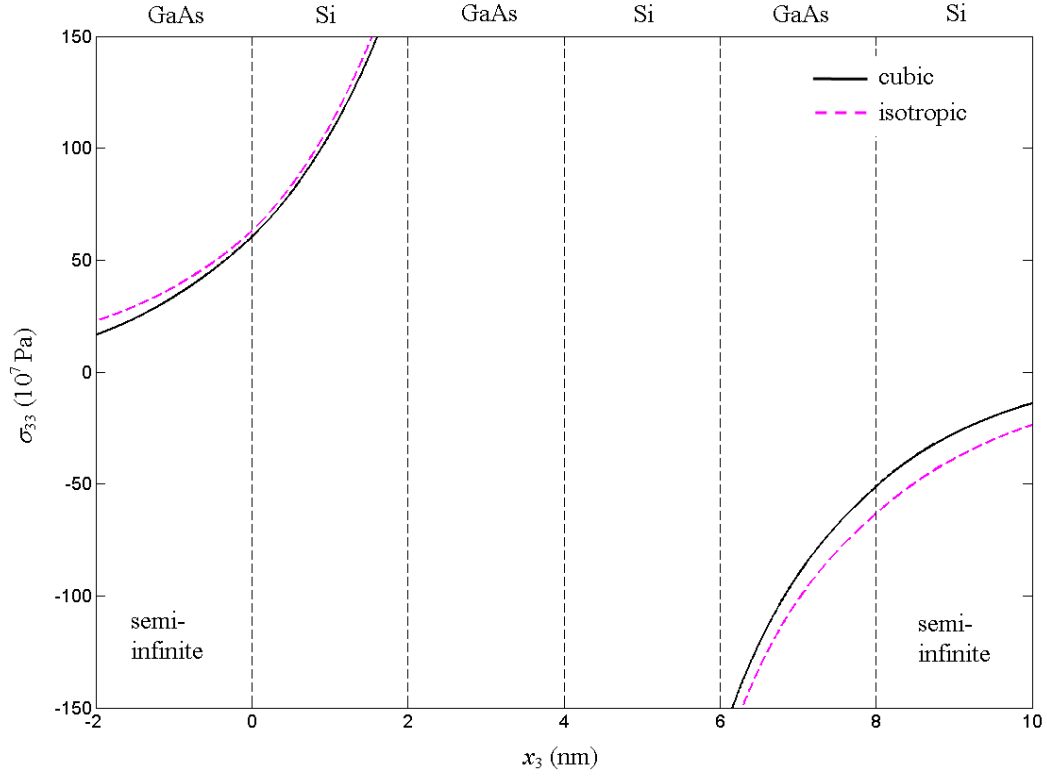


Figure 4.3: Distribution of the in-plane stress σ_{33} along the x_3 -axis ($x_1 = 0$) for a $N = 5$ multilayered structure formed by alternating GaAs and Si. The misfit dislocation array lies at the interface $x_3 = 4$ nm and is infinitely long in the x_2 -direction. The dark solid lines are the results when GaAs and Si are taken to be cubic and the pink dashed lines are the corresponding results when GaAs and Si are assumed to be isotropic.

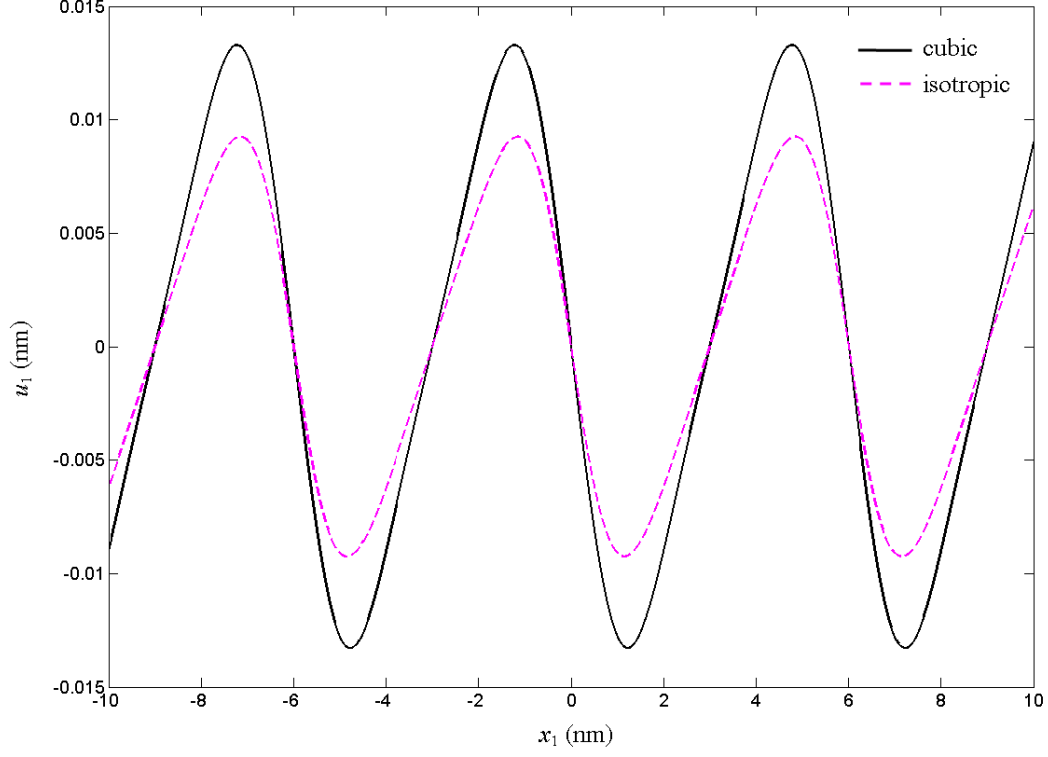


Figure 4.4: Periodic distribution of the horizontal displacement u_1 along the traction-free surface of the InAs thin film bonded to GaAs substrate. The misfit dislocation array lies at the InAs/GaAs interface. The dark solid line is the result when both the InAs thin film and GaAs substrate are taken to be cubic, whereas the pink dashed line is the corresponding result when both InAs and GaAs are assumed to be isotropic.

modelling of the multilayer GaAs/Si.

Next we consider an edge misfit dislocation array with Burgers vector $\hat{\mathbf{b}} = (\hat{b}_1, \hat{b}_2, \hat{b}_3) = (0.2 \text{ nm}, 0, 0)$ and the period $\Lambda = 6 \text{ nm}$ along the heterointerface between the InAs ($c_{11} = 83.29 \text{ GPa}$, $c_{12} = 45.26 \text{ GPa}$, $c_{44} = 39.59 \text{ GPa}$) thin film of thickness $h = 2 \text{ nm}$ and GaAs substrate with its cubic material properties given above. In this case $N = 2$. We illustrate in Figures 4.4 and 4.5 the induced horizontal displacement u_1 and vertical displacement u_3 along the traction-free surface of the InAs thin film. The solid lines in Figures 4.4 and 4.5 are the results when both the InAs thin film and GaAs substrate are taken to be anisotropic (cubic), whereas the dashed lines are the corresponding results when they are assumed to be isotropic (with $c_{11} = c_{12} + 2c_{44}$). Once again we observe that the isotropic assumption for the thin film and substrate could cause considerable error in displacement distribution. Therefore, our model, which includes the traction-free surface, semiconductor anisotropy, and misfit dislocation interaction among adjacent dislocations, can be combined with experimental measurements to accurately characterize the misfit dislocation induced elastic field in thin-film and superlattice structures [87–89].

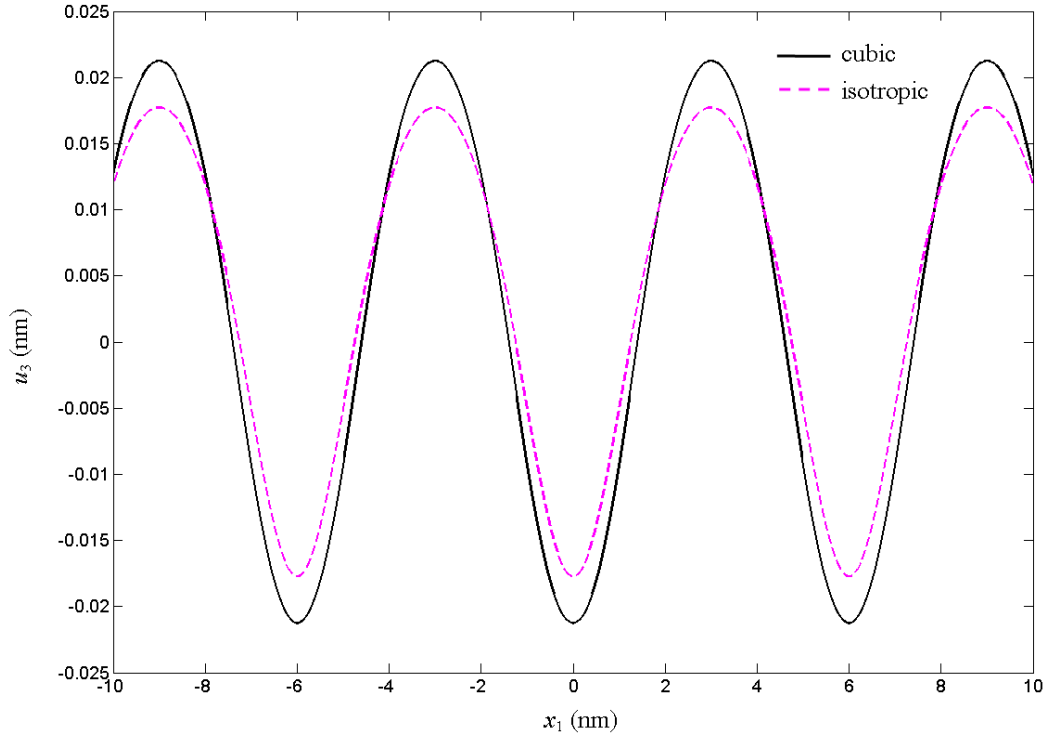


Figure 4.5: Periodic distribution of the horizontal displacement u_3 along the traction-free surface of the InAs thin film bonded to GaAs substrate. The misfit dislocation array lies at the InAs/GaAs interface. The dark solid line is the result when both the InAs thin film and GaAs substrate are taken to be cubic, whereas the pink dashed line is the corresponding result when both InAs and GaAs are assumed to be isotropic.

4.9 Conclusions

We have developed an efficient computational method based on double Fourier series expansion, the Stroh formalism, and transfer matrix method for calculating the elastic field associated with a semiconductor system composed of an arbitrarily number of thin bonded homogeneous and anisotropic elastic layers, sandwiched between two anisotropic semi-infinite media. One interface of the multilayered crystal contains a biperiodic array of misfit dislocations. The formulations presented are strikingly simple in that once the 6×6 matrix \mathbf{N} for each thin elastic layer and the Barnett-Lothe tensors \mathbf{L} and \mathbf{S} for the two semi-infinite media are determined, the displacement and traction vectors (and as a result the in-plane stresses) can be conveniently obtained. Numerical results show that the new method is correct and powerful, and that material anisotropy can significantly influence the misfit dislocation-induced physical quantities.

Chapter 5

Decay rates for a transversely isotropic piezoelectric hollow circular nanocolumn

5.1 Introduction

Decay rate of stresses and displacements along the longitudinal direction due to self-equilibrating loads acting at the end of the hollow or solid circular cylinder is an old but challenging mechanics problem. By employing the Love displacement solution, Klemm and Little [90] presented a complete analysis for a long solid circular cylinder with one end being traction-free and the other end under a self-equilibrated traction. Earlier investigators on the decay of the elastic field along solid circular cylinders include Purse (see Love [91]) who obtained the eigenfunctions governing axisymmetric torsion problem, and Little and Childs [92] who obtained a vector bi-orthogonality from Love's strain function. Later on Stephen and Wang [93] considered the self-equilibrated end load problem for a semi-infinite hollow circular cylinder by using the Papkovitch-Neuber solution to the elastostatic displacement equations of equilibrium, and derived solutions for both the axisymmetric and asymmetric cases. Stephen [94] further considered the decay rates for a compound circular cylinder of two materials having different stiffness. Ye [95, 96] studied the decay rates of angle-ply laminated hollow cylinders based on the recursive and approximation technique. Piezoelectric materials and structures have attracted great attention due to their capability of converting the mechanical energy into the electric one, and vice versa. As such, the corresponding Saint-Venant's principle in piezoelectricity has been investigated by many researchers e.g., [97]. These include decay rates under anti-plane [98] and plane [99, 100] deformations. However, to the best of the authors' knowledge, decay rate in three-dimensional (3D) piezoelectric hollow/solid cylinder has not been studied so far, which yet may have great technical applications to semiconductor industry as discussed below.

In recently years, various semiconductor nanostructures have been successfully grown to enhance optoelectronic and electronic properties. Among them, the novel nanopost and nanocolumn structures are particularly of promise, as reported by Chen et al. [101], Van Nostrand et al. [102], and Thillosen et al. [103]. However, the strain relaxation feature

along the nanopost or nanocolumn is critical from the device design point of view. Therefore, in this paper, we determine the exact decay rates of the elastic and electric fields along the growth direction of a piezoelectric hollow or solid nanocolumn by developing the general solution for the corresponding 3D problems [104, 105]. While the more general asymmetric case can be discussed by using the present formulation, we confine our attention to the torsional and torsionless axisymmetric cases. Numerical results presented clearly show the importance of the material anisotropy and electromechanical coupling on the decay rate of nanocolumns.

5.2 General Solutions of Transversely Isotropic Piezoelectric Solids

As shown in Figure 5.1, we attach a fixed Cartesian coordinate system (x, y, z) and a circular cylindrical coordinate system (r, θ, z) to the nanocolumn which is free-standing on a substrate [102]. For the transversely isotropic (or hexagonal crystal) piezoelectric hollow/solid circular nanocolumn with poling direction along the z -axis, the equilibrium equations in terms of the electric potential ϕ and the three displacements u, v, w along the x, y and z directions are (assuming also zero body force and zero electric charge density)

$$c_{11}u_{,xx} + \frac{1}{2}(c_{11} - c_{12})u_{,yy} + c_{44}u_{,zz} + \frac{1}{2}(c_{11} + c_{12})v_{,xy} + (c_{13} + c_{44})w_{,xz} + (e_{15} + e_{31})\phi_{,xz} = 0 \quad (5.1a)$$

$$\frac{1}{2}(c_{11} - c_{12})v_{,xx} + c_{11}v_{,yy} + c_{44}v_{,zz} + \frac{1}{2}(c_{11} + c_{12})u_{,xy} + (c_{13} + c_{44})w_{,yz} + (e_{31} + e_{15})\phi_{,yz} = 0 \quad (5.1b)$$

$$c_{44}(w_{,xx} + w_{,yy}) + c_{33}w_{,zz} + (c_{13} + c_{44})(u_{,xz} + v_{,yz}) + e_{15}(\phi_{,xx} + \phi_{,yy}) + e_{33}\phi_{,zz} = 0 \quad (5.1c)$$

$$e_{15}(w_{,xx} + w_{,yy}) + e_{33}w_{,zz} + (e_{15} + e_{31})(u_{,xz} + v_{,yz}) - \epsilon_{11}(\phi_{,xx} + \phi_{,yy}) - \epsilon_{33}\phi_{,zz} = 0 \quad (5.1d)$$

where $c_{ij}, e_{ij}, \epsilon_{ij}$ are, respectively, the elastic, piezoelectric and dielectric coefficients of the piezoelectric solid, and the symbol $u_{,xy}$ denotes differentiations of the elastic displacement component u with respect to x and y . In addition the linear constitutive equations in the Cartesian coordinate system are given by

$$\begin{bmatrix} \sigma_{xx} \\ \sigma_{yy} \\ \sigma_{zz} \\ \sigma_{zy} \\ \sigma_{zx} \\ \sigma_{xy} \\ D_x \\ D_y \\ D_z \end{bmatrix} = \begin{bmatrix} c_{11} & c_{12} & c_{13} & 0 & 0 & 0 & 0 & 0 & e_{31} \\ c_{12} & c_{11} & c_{13} & 0 & 0 & 0 & 0 & 0 & e_{31} \\ c_{13} & c_{13} & c_{33} & 0 & 0 & 0 & 0 & 0 & e_{33} \\ 0 & 0 & 0 & c_{44} & 0 & 0 & 0 & e_{15} & 0 \\ 0 & 0 & 0 & 0 & c_{44} & 0 & e_{15} & 0 & 0 \\ 0 & 0 & 0 & 0 & 0 & c_{66} & 0 & 0 & 0 \\ 0 & 0 & 0 & 0 & e_{15} & 0 & -\epsilon_{11} & 0 & 0 \\ 0 & 0 & 0 & e_{15} & 0 & 0 & 0 & -\epsilon_{11} & 0 \\ e_{31} & e_{31} & e_{33} & 0 & 0 & 0 & 0 & 0 & -\epsilon_{33} \end{bmatrix} \begin{bmatrix} \epsilon_{xx} \\ \epsilon_{yy} \\ \epsilon_{zz} \\ 2\epsilon_{zy} \\ 2\epsilon_{zx} \\ 2\epsilon_{xy} \\ -E_x \\ -E_y \\ -E_z \end{bmatrix} \quad (5.2)$$

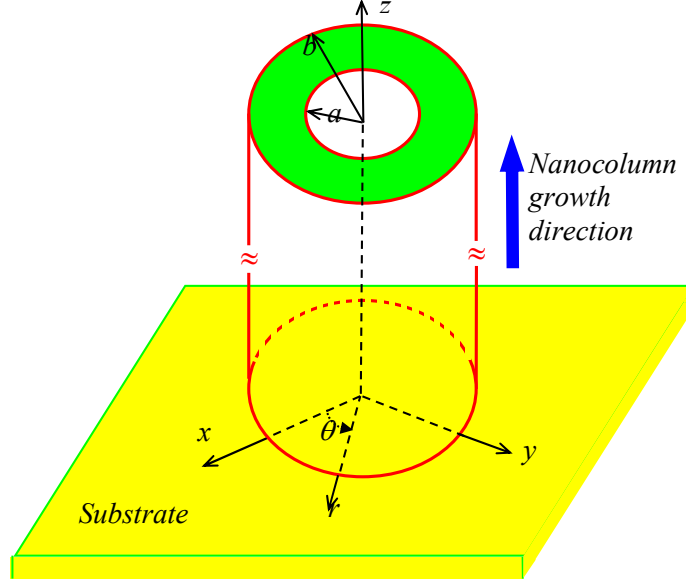


Figure 5.1: A simplified free-standing transversely isotropic piezoelectric nanocolumn over a substrate.

It is obvious that the xy -plane is the isotropic plane and the elastic and piezoelectric properties are uniform within this plane. In Eq. (5.2), $c_{66} = (c_{11} - c_{12})/2$ and

$$\begin{aligned} \epsilon_{xx} &= u_{,x} & \epsilon_{yy} &= v_{,y} & \epsilon_{zz} &= w_{,z} \\ \epsilon_{xy} &= \frac{1}{2}(u_{,y} + v_{,x}) & \epsilon_{zx} &= \frac{1}{2}(u_{,z} + w_{,x}) & \epsilon_{zy} &= \frac{1}{2}(v_{,z} + w_{,y}) \\ E_x &= -\phi_{,x} & E_y &= -\phi_{,y} & E_z &= -\phi_{,z} \end{aligned} \quad (5.3)$$

It can be shown that the displacements u , v , w , the electric potential ϕ , the stresses σ_{xx} , σ_{yy} , σ_{xy} , σ_{zz} , σ_{zx} , σ_{zy} , and the electric displacements D_x , D_y , D_z can all be concisely expressed in terms of a 3×1 harmonic function vector $\mathbf{P} = [\Phi_1 \ \Phi_2 \ \Phi_3]^T$ and a scalar harmonic function Φ_0 as [105]

$$\begin{aligned} u + iv &= \Lambda(\tilde{\mathbf{J}}\mathbf{P} + i\Phi_0) & \begin{bmatrix} w & \phi \end{bmatrix}^T &= \mathbf{K}\mathbf{P}_{,z}, \\ \sigma_{xx} + \sigma_{yy} &= 2(c_{66}\tilde{\mathbf{J}}\mathbf{H} - c_{44}\tilde{\mathbf{J}} - \tilde{\mathbf{I}}_0^T \mathbf{B}\mathbf{K})\mathbf{P}_{,zz} \\ \sigma_{xx} - \sigma_{yy} + 2i\sigma_{xy} &= 2c_{66}\Lambda^2(\tilde{\mathbf{J}}\mathbf{P} + i\Phi_0) \\ \begin{bmatrix} \sigma_{zz} \\ D_z \end{bmatrix} &= \mathbf{B}(\tilde{\mathbf{I}}_0\tilde{\mathbf{J}} + \mathbf{K})\mathbf{H}\mathbf{P}_{,zz} & \begin{bmatrix} \sigma_{zx} + i\sigma_{zy} \\ D_x + iD_y \end{bmatrix} &= \Lambda\mathbf{B}[(\tilde{\mathbf{I}}_0\tilde{\mathbf{J}} + \mathbf{K})\mathbf{P}_{,z} + i\tilde{\mathbf{I}}_0\Phi_{0,z}] \end{aligned} \quad (5.4)$$

where

$$\Lambda = \frac{\partial}{\partial x} + i\frac{\partial}{\partial y} \quad \tilde{\mathbf{J}} = \begin{bmatrix} 1 & 1 & 1 \end{bmatrix} \quad \tilde{\mathbf{I}}_0 = \begin{bmatrix} 1 & 0 \end{bmatrix}^T \quad (5.5a)$$

$$\mathbf{K} = \begin{bmatrix} \mathbf{k}_1 & \mathbf{k}_2 & \mathbf{k}_3 \end{bmatrix} \quad \mathbf{H} = \text{diag} \begin{bmatrix} \lambda_1 & \lambda_2 & \lambda_3 \end{bmatrix} \quad (5.5b)$$

$$\mathbf{u} = \begin{bmatrix} c_{13} + c_{44} \\ e_{15} + e_{31} \end{bmatrix} \quad \mathbf{A} = \begin{bmatrix} c_{33} & e_{33} \\ e_{33} & -\epsilon_{33} \end{bmatrix} \quad \mathbf{B} = \begin{bmatrix} c_{44} & e_{15} \\ e_{15} & -\epsilon_{11} \end{bmatrix} \quad (5.5c)$$

$$\mathbf{k}_i = \lambda_i(\mathbf{A} - \lambda_i\mathbf{B})^{-1}\mathbf{u} \quad (5.5d)$$

and Φ_i ($i = 0, 1, 2, 3$) satisfy

$$\Phi_{i,xx} + \Phi_{i,yy} + \lambda_i\Phi_{i,zz} = 0 \quad (i = 0, 1, 2, 3) \quad (5.6)$$

where $\lambda_0 = c_{44}/c_{66}$ and λ_i , ($i = 1, 2, 3$) are the three roots of the following cubic equation

$$a\lambda^3 + b\lambda^2 + c\lambda + d = 0 \quad (5.7)$$

with

$$\begin{aligned} a &= c_{11}(c_{44}\epsilon_{11} + e_{15}^2) \\ b &= -c_{11}(c_{33}\epsilon_{11} + c_{44}\epsilon_{33} + 2e_{15}e_{33}) - c_{44}(c_{44}\epsilon_{11} + e_{15}^2) \\ &\quad + \epsilon_{11}(c_{13} + c_{44})^2 - c_{44}(e_{15} + e_{31})^2 + 2e_{15}(c_{13} + c_{44})(e_{15} + e_{31}) \\ c &= c_{11}(c_{33}\epsilon_{33} + e_{33}^2) + c_{44}(c_{33}\epsilon_{11} + c_{44}\epsilon_{33} + 2e_{15}e_{33}) \\ &\quad - \epsilon_{33}(c_{13} + c_{44})^2 - 2e_{33}(c_{13} + c_{44})(e_{15} + e_{31}) + c_{33}(e_{15} + e_{31})^2 \\ d &= -c_{44}(c_{33}\epsilon_{33} + e_{33}^2) \end{aligned} \quad (5.8)$$

It shall be mentioned that the above general solution (5.4) is only valid when $\lambda_1 \neq \lambda_2 \neq \lambda_3$. Therefore, when addressing the corresponding purely elastic isotropic material case or any other possible material cases where repeated roots occur, a small perturbation is given to the material coefficients to make the three eigenvalues unequal so that the general solution presented in this paper can still be applied with negligible errors [64]. The above general solution (5.4) can also be easily expressed in the cylindrical coordinate system (r, θ, z) as follows

$$\begin{aligned} u_r + iu_\theta &= \Lambda_c(\tilde{\mathbf{J}}\mathbf{P} + i\Phi_0) \quad [w \quad \phi]^T = \mathbf{K}\mathbf{P}_{,z} \\ \sigma_{rr} + \sigma_{\theta\theta} &= 2(c_{66}\tilde{\mathbf{J}}\mathbf{H} - c_{44}\tilde{\mathbf{J}} - \tilde{\mathbf{I}}_0^T\mathbf{B}\mathbf{K})\mathbf{P}_{,zz} \\ \sigma_{rr} - \sigma_{\theta\theta} + 2i\sigma_{r\theta} &= 2c_{66}(\Lambda_c^2 - r^{-1}\Lambda_c)(\tilde{\mathbf{J}}\mathbf{P} + i\Phi_0) \\ \begin{bmatrix} \sigma_{zz} \\ D_z \end{bmatrix} &= \mathbf{B}(\tilde{\mathbf{I}}_0\tilde{\mathbf{J}} + \mathbf{K})\mathbf{H}\mathbf{P}_{,zz} \quad \begin{bmatrix} \sigma_{zr} + i\sigma_{z\theta} \\ D_r + iD_\theta \end{bmatrix} = \Lambda_c\mathbf{B}[(\tilde{\mathbf{I}}_0\tilde{\mathbf{J}} + \mathbf{K})\mathbf{P}_{,z} + i\tilde{\mathbf{I}}_0\Phi_{0,z}] \end{aligned} \quad (5.9)$$

where

$$\Lambda_c = \frac{\partial}{\partial r} + i\frac{1}{r}\frac{\partial}{\partial \theta} \quad \Lambda_c^2 - \frac{1}{r}\Lambda_c = \left(\frac{\partial}{\partial r} - \frac{1}{r} + i\frac{1}{r}\frac{\partial}{\partial \theta}\right)\left(\frac{\partial}{\partial r} + i\frac{1}{r}\frac{\partial}{\partial \theta}\right) \quad (5.10)$$

For the torsional axisymmetric deformation of the piezoelectric solid we have $u_r = w = \phi = \sigma_{rr} = \sigma_{\theta\theta} = \sigma_{zz} = \sigma_{zr} = D_r = D_z = 0$ and $\mathbf{P} = \mathbf{0}$. Then the general solution (5.9) is reduced to

$$u_\theta = \Phi_{0,r} \quad \sigma_{r\theta} = c_{66}(\Phi_{0,rr} - r^{-1}\Phi_{0,r}) \quad \begin{bmatrix} \sigma_{z\theta} \\ D_\theta \end{bmatrix} = \mathbf{B}\tilde{\mathbf{I}}_0\Phi_{0,rz} \quad (5.11)$$

On the other hand, for the torsionless axisymmetric deformation of the piezoelectric solid we have $u_\theta = \sigma_{r\theta} = \sigma_{z\theta} = D_\theta = 0$ and $\Phi_0 = 0$. For this case, the above general solution (5.9) is reduced to

$$\begin{aligned} u_r &= \tilde{\mathbf{J}}\mathbf{P}_{,r} \quad \begin{bmatrix} w & \phi \end{bmatrix}^T = \mathbf{K}\mathbf{P}_{,z} \\ \sigma_{rr} + \sigma_{\theta\theta} &= 2(c_{66}\tilde{\mathbf{J}}\mathbf{H} - c_{44}\tilde{\mathbf{J}} - \tilde{\mathbf{I}}_0^T\mathbf{B}\mathbf{K})\mathbf{P}_{,zz} \\ \sigma_{rr} - \sigma_{\theta\theta} &= 2c_{66}\tilde{\mathbf{J}}(\mathbf{P}_{,rr} - r^{-1}\mathbf{P}_{,r}) \\ \begin{bmatrix} \sigma_{zz} \\ D_z \end{bmatrix} &= \mathbf{B}(\tilde{\mathbf{I}}_0\tilde{\mathbf{J}} + \mathbf{K})\mathbf{H}\mathbf{P}_{,zz} \quad \begin{bmatrix} \sigma_{zr} \\ D_r \end{bmatrix} = \mathbf{B}(\tilde{\mathbf{I}}_0\tilde{\mathbf{J}} + \mathbf{K})\mathbf{P}_{,rz} \end{aligned} \quad (5.12)$$

5.3 Decay rates of the transversely isotropic piezoelectric nanocolumn

We assume that the circular hollow nanocolumn occupies the region $a \leq r \leq b$, $0 \leq z \leq +\infty$. In this investigation we only consider the torsional and torsionless axisymmetric deformations of the nanocolumn. The two lateral surfaces of the column $r = a$ and $r = b$ are traction-free, i.e.,

$$\sigma_{rr} = \sigma_{rz} = \sigma_{r\theta} = 0, \text{ on } r = a \text{ and } r = b \quad (5.13)$$

In addition either charge-free (insulating) condition $D_r = 0$ or electroded (conducting) condition $\phi = 0$ is imposed on the two surfaces $r = a$ and $r = b$.

5.3.1 Torsional Case

We first point out that the torsional case is purely elastic and that its solution is associated with the scalar harmonic function Φ_0 only. Assuming that the field quantity in the nanocolumn decays exponentially in its growth direction, we then write

$$\Phi_0 = B_1 J_0(\rho \sqrt{\lambda_0} r) e^{-\rho z} + B_2 Y_0(\rho \sqrt{\lambda_0} r) e^{-\rho z} \quad (5.14)$$

where B_1 and B_2 are two constants to be determined, J_n and Y_n are the n^{th} -order Bessel functions of the first and second kinds, respectively. Substituting Eq. (5.14) into the general solution (5.11) and imposing the traction-free boundary conditions $\sigma_{r\theta} = 0$ on $r = a$ and $r = b$, we arrive at the following homogeneous linear equations for B_1 and B_2 ,

$$\begin{bmatrix} J_2(\rho \sqrt{\lambda_0} a) & Y_2(\rho \sqrt{\lambda_0} a) \\ J_2(\rho \sqrt{\lambda_0} b) & Y_2(\rho \sqrt{\lambda_0} b) \end{bmatrix} \begin{bmatrix} B_1 \\ B_2 \end{bmatrix} = \begin{bmatrix} 0 \\ 0 \end{bmatrix} \quad (5.15)$$

A nontrivial solution to Eq. (5.15) yields the transcendental equation for ρ ,

$$J_2(\rho \sqrt{\lambda_0} a) Y_2(\rho \sqrt{\lambda_0} b) - Y_2(\rho \sqrt{\lambda_0} a) J_2(\rho \sqrt{\lambda_0} b) = 0 \quad (5.16)$$

which is identical to that derived by Stephen and Wang [93] if we set $k = \rho \sqrt{\lambda_0}$. Therefore, once the decay rate for the torsional deformation of an isotropic elastic hollow cylinder is

calculated, the torsional decay rate for the corresponding transversely isotropic piezoelectric nanocolumn can be simply found by dividing result by the factor $\sqrt{\lambda_0}$. In other words, the decay rate for the torsional case of the transversely isotropic piezoelectric nanocolumn is inversely proportional to the ratio $\sqrt{\lambda_0} = \sqrt{c_{44}/c_{66}}$.

5.3.2 Torsionless Case

Similarly, for this case, we assume that the physical quantity in the nanocolumn decays exponentially as

$$\mathbf{P} = e^{-\rho z} \left[\langle J_0(\rho \sqrt{\lambda_\alpha} r) \rangle \mathbf{C}_1 + \langle Y_0(\rho \sqrt{\lambda_\alpha} r) \rangle \mathbf{C}_2 \right] \quad (5.17)$$

where the pointed brackets $\langle * \rangle$ stand for a 3×3 diagonal matrix with its element varying with the index α , \mathbf{C}_1 and \mathbf{C}_2 are two 3×1 constant vectors to be determined. Substituting Eq. (5.17) into the general solution (5.12) and imposing the traction-free and charge-free (or electroded) boundary conditions on $r = a$ and $r = b$, we arrive at the following homogeneous linear equations for \mathbf{C}_1 and \mathbf{C}_2

$$\begin{aligned} \mathbf{A}_{11} \mathbf{C}_1 + \mathbf{A}_{12} \mathbf{C}_2 &= \mathbf{0} \\ \mathbf{A}_{21} \mathbf{C}_1 + \mathbf{A}_{22} \mathbf{C}_2 &= \mathbf{0} \end{aligned} \quad (5.18)$$

where the elements of the matrices A_{ij} are given below for different boundary conditions at $r = a$ and $r = b$.

If $r = a$ and $r = b$ are traction-free and charge-free ($D_r = 0$), then

$$\begin{aligned} \mathbf{A}_{11} &= \begin{bmatrix} (\tilde{\mathbf{I}}_0 \tilde{\mathbf{J}} + \mathbf{K}) \sqrt{\mathbf{H}} \langle J_1(\rho a \sqrt{\lambda_\alpha}) \rangle \\ 2c_{66} \tilde{\mathbf{J}} \sqrt{\mathbf{H}} \langle J_1(\rho a \sqrt{\lambda_\alpha}) \rangle - \rho a (c_{44} \tilde{\mathbf{J}} + \tilde{\mathbf{I}}_0^T \mathbf{B} \mathbf{K}) \langle J_0(\rho a \sqrt{\lambda_\alpha}) \rangle \end{bmatrix} \\ \mathbf{A}_{12} &= \begin{bmatrix} (\tilde{\mathbf{I}}_0 \tilde{\mathbf{J}} + \mathbf{K}) \sqrt{\mathbf{H}} \langle Y_1(\rho a \sqrt{\lambda_\alpha}) \rangle \\ 2c_{66} \tilde{\mathbf{J}} \sqrt{\mathbf{H}} \langle Y_1(\rho a \sqrt{\lambda_\alpha}) \rangle - \rho a (c_{44} \tilde{\mathbf{J}} + \tilde{\mathbf{I}}_0^T \mathbf{B} \mathbf{K}) \langle Y_0(\rho a \sqrt{\lambda_\alpha}) \rangle \end{bmatrix} \\ \mathbf{A}_{21} &= \begin{bmatrix} (\tilde{\mathbf{I}}_0 \tilde{\mathbf{J}} + \mathbf{K}) \sqrt{\mathbf{H}} \langle J_1(\rho b \sqrt{\lambda_\alpha}) \rangle \\ 2c_{66} \tilde{\mathbf{J}} \sqrt{\mathbf{H}} \langle J_1(\rho b \sqrt{\lambda_\alpha}) \rangle - \rho b (c_{44} \tilde{\mathbf{J}} + \tilde{\mathbf{I}}_0^T \mathbf{B} \mathbf{K}) \langle J_0(\rho b \sqrt{\lambda_\alpha}) \rangle \end{bmatrix} \\ \mathbf{A}_{22} &= \begin{bmatrix} (\tilde{\mathbf{I}}_0 \tilde{\mathbf{J}} + \mathbf{K}) \sqrt{\mathbf{H}} \langle Y_1(\rho b \sqrt{\lambda_\alpha}) \rangle \\ 2c_{66} \tilde{\mathbf{J}} \sqrt{\mathbf{H}} \langle Y_1(\rho b \sqrt{\lambda_\alpha}) \rangle - \rho b (c_{44} \tilde{\mathbf{J}} + \tilde{\mathbf{I}}_0^T \mathbf{B} \mathbf{K}) \langle Y_0(\rho b \sqrt{\lambda_\alpha}) \rangle \end{bmatrix} \end{aligned} \quad (5.19)$$

The condition that Eq. (5.18) admits a nontrivial solution yields the transcendental equation for ρ

$$\begin{vmatrix} \mathbf{A}_{11} & \mathbf{A}_{12} \\ \mathbf{A}_{21} & \mathbf{A}_{22} \end{vmatrix} = 0 \quad (5.23)$$

We remark that when the piezoelectric tensor vanishes (i.e., $e_{ij} = 0$), the problem decouples into purely elastic and purely dielectric ones. While the purely elastic case is still relative complicated, the purely dielectric case can be simply discussed below for different electric boundary conditions.

It is found that if both $r = a$ and $r = b$ of a dielectric hollow circular nanocolumn are charge-free, then the transcendental equation for ρ is

$$J_1(s\rho a)Y_1(s\rho b) - Y_1(s\rho a)J_1(s\rho b) = 0 \quad (5.24)$$

where

$$s = \sqrt{\frac{\epsilon_{33}}{\epsilon_{11}}} \quad (5.25)$$

If both $r = a$ and $r = b$ are electroded, then the transcendental equation for ρ is

$$J_0(s\rho a)Y_0(s\rho b) - Y_0(s\rho a)J_0(s\rho b) = 0 \quad (5.26)$$

If $r = a$ is charge-free whilst $r = b$ is electroded, then the transcendental equation for ρ is

$$J_1(s\rho a)Y_0(s\rho b) - Y_1(s\rho a)J_0(s\rho b) = 0 \quad (5.27)$$

If $r = a$ is electroded whilst $r = b$ is charge-free, then the transcendental equation for ρ is

$$J_0(s\rho a)Y_1(s\rho b) - Y_0(s\rho a)J_1(s\rho b) = 0 \quad (5.28)$$

The calculations show that the roots to the transcendental equations (5.24) and (5.26)–(5.28) are all real [93, 94].

5.4 Results and Discussions

First, our results are verified by comparison with existing isotropic solutions. It is noted that by using a small perturbation from isotropy to anisotropy, our decay rates based on the present formulation are in complete agreement with those in Little and Childs [92] for an isotropic elastic solid circular cylinder, and in Stephen and Wang [93] for an isotropic elastic hollow circular cylinder. For example we illustrate in Figure 5.2 the complex decay roots ρb for axisymmetric torsionless displacements for an isotropic elastic hollow cylinder with Poisson's ratio $\nu = 0.25$. It is observed that Figure 5.2 here is identical to Figure 3 in Stephen and Wang [93].

Next, we present specific results for the transversely isotropic piezoelectric GaN (gallium nitride) nanocolumn [102]. It is noted that GaN is a semiconductor compound with strong coupling between the electric and mechanical fields and with a wide energy bandgap [4, 5]. As such, the corresponding GaN nanopost and nanocolumn growth and overgrowth

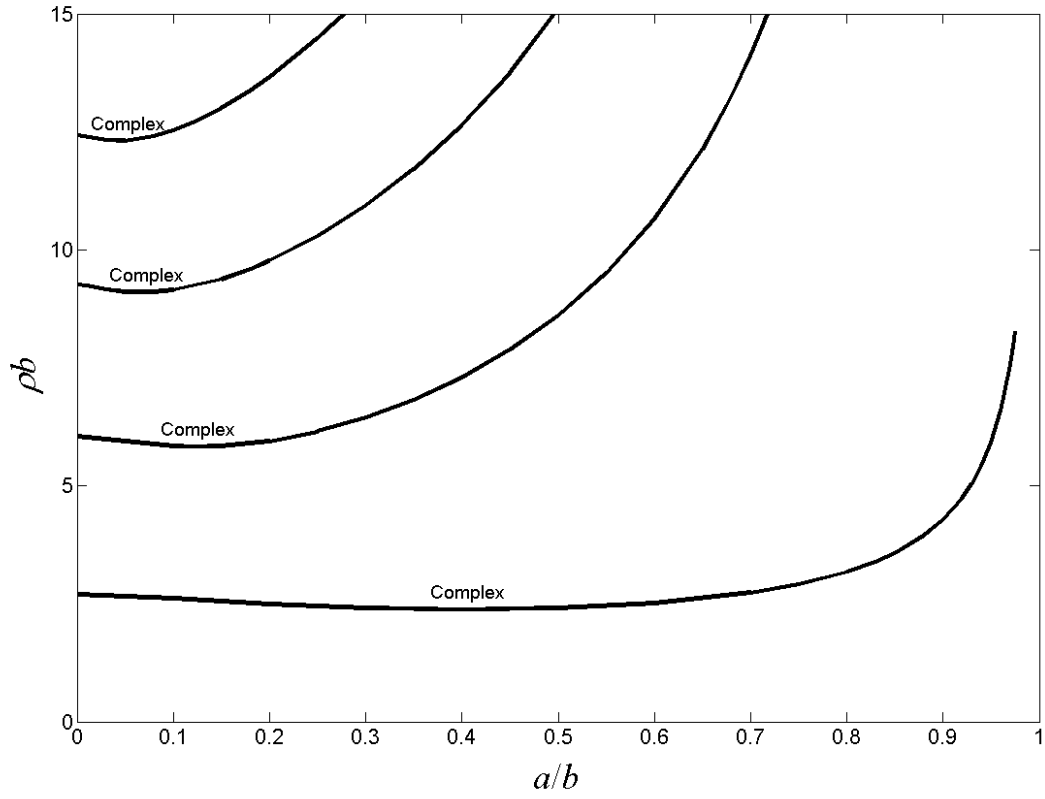


Figure 5.2: Dimensionless complex decay roots ρb under axisymmetric torsionless deformation for an isotropic elastic hollow nanocolumn with Poisson's ratio $\nu = 0.25$. Only real parts of the roots are shown.

$c_{11} = c_{22}$ (GPa)	390.0
c_{33}	398.0
c_{12}	145.0
$c_{13} = c_{23}$	106.0
$c_{44} = c_{55}$	105.0
$c_{66} [= (c_{11} - c_{12})/2]$	122.5
e_{15} (C/m ²)	-0.30
e_{31}	-0.33
e_{33}	0.65
$\epsilon_{11} = \epsilon_{22}$ (10 ⁻¹² C ² /(N · m ²))	78.8
ϵ_{33}	78.8

Table 5.1: Material properties of GaN [4, 5]

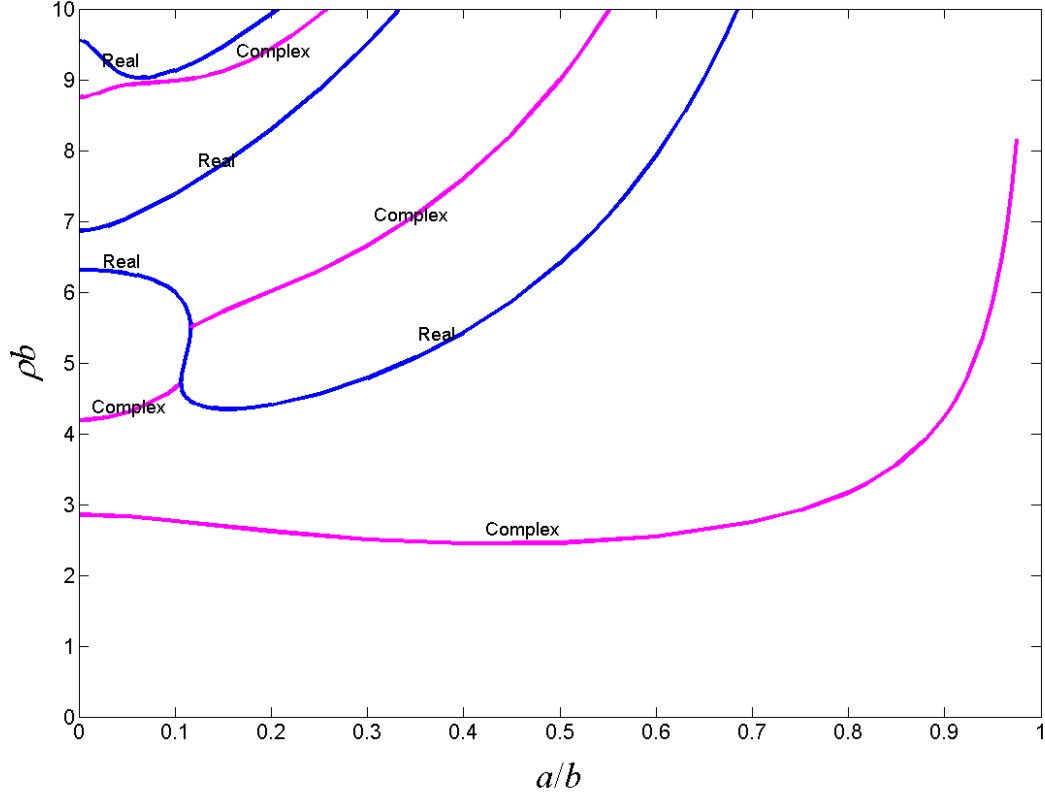


Figure 5.3: Dimensionless complex decay roots ρb under axisymmetric torsionless deformation for a transversely isotropic piezoelectric hollow GaN nanocolumn with boundary condition $D_r = 0$ on $r = a$ and $r = b$. Only real parts of the roots are shown.

have recently attracted wide attention in semiconductor community [101–103]. The material properties of the transversely isotropic (or hexagonal) GaN with its material symmetry axis along the z -direction are listed in Table 5.1.

Figure 5.3 demonstrates the dimensionless real and complex decay roots ρb under the axisymmetric torsionless deformation for the transversely isotropic piezoelectric hollow GaN nanocolumn. Both surfaces $r = a$ and $r = b$ are insulating, i.e., $D_r = 0$. Similarly, Figure 5.4 presents the corresponding results when both $r = a$ and $r = b$ are conducting (or electroded), i.e., $\phi = 0$. It is found that even for the axisymmetric torsionless case, there exists an intriguing interaction between the real and complex root loci due to the anisotropic effect and the electromechanical coupling (the piezoelectric effect). For the purely elastic and isotropic case, such interactions only occur for the non-axisymmetric deformation [94]. Different electrical boundary conditions (insulating or conducting) also influence the root loci. The decay rate, defined as the decay distance of end effects (or the strain relaxation rate), is the real part of the root with smallest positive real part. By comparing Figures 5.3 and 5.4, we find that when $a/b > 0.05$, the difference between the decay rates for the insulating and conducting cases is minimal. On the other hand, the discrepancy in decay rates for the two different electric conditions is most apparent for a solid cylinder: $\rho b = 2.855$ for insulating condition and $\rho b = 2.605$ for conducting condition.

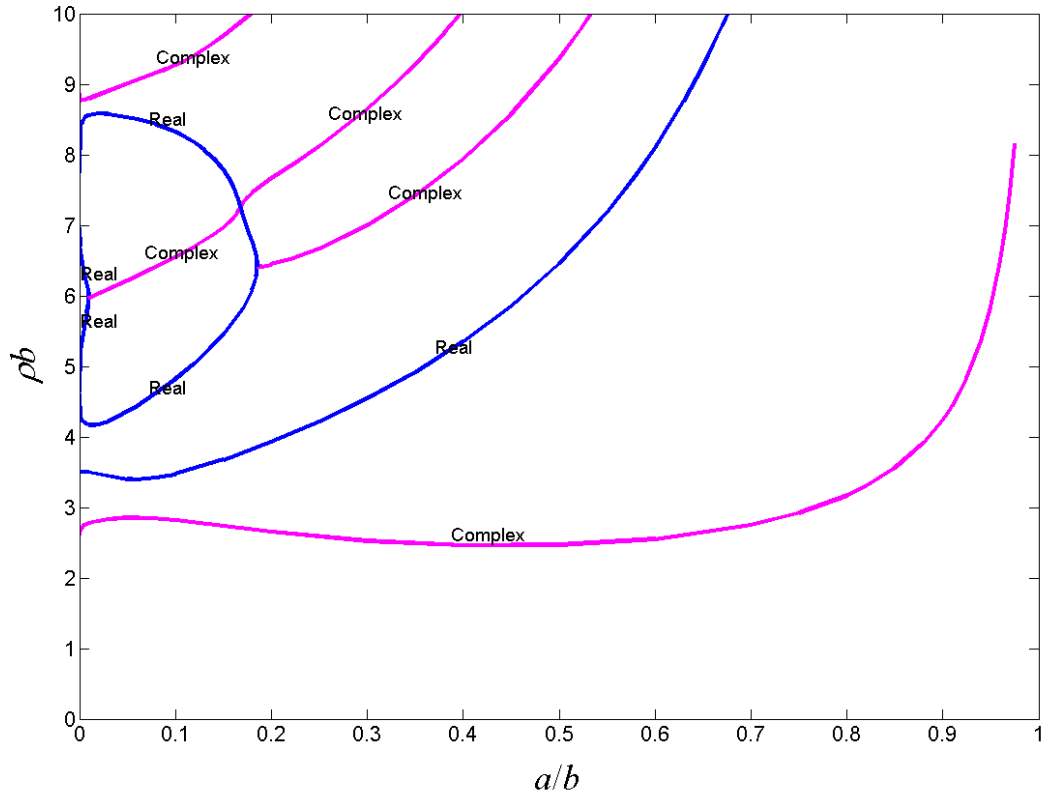


Figure 5.4: Dimensionless complex decay roots pb under axisymmetric torsionless deformation for a transversely isotropic piezoelectric hollow GaN nanocolumn with boundary condition $\phi = 0$ on $r = a$ and $r = b$. Only real parts of the roots are shown.

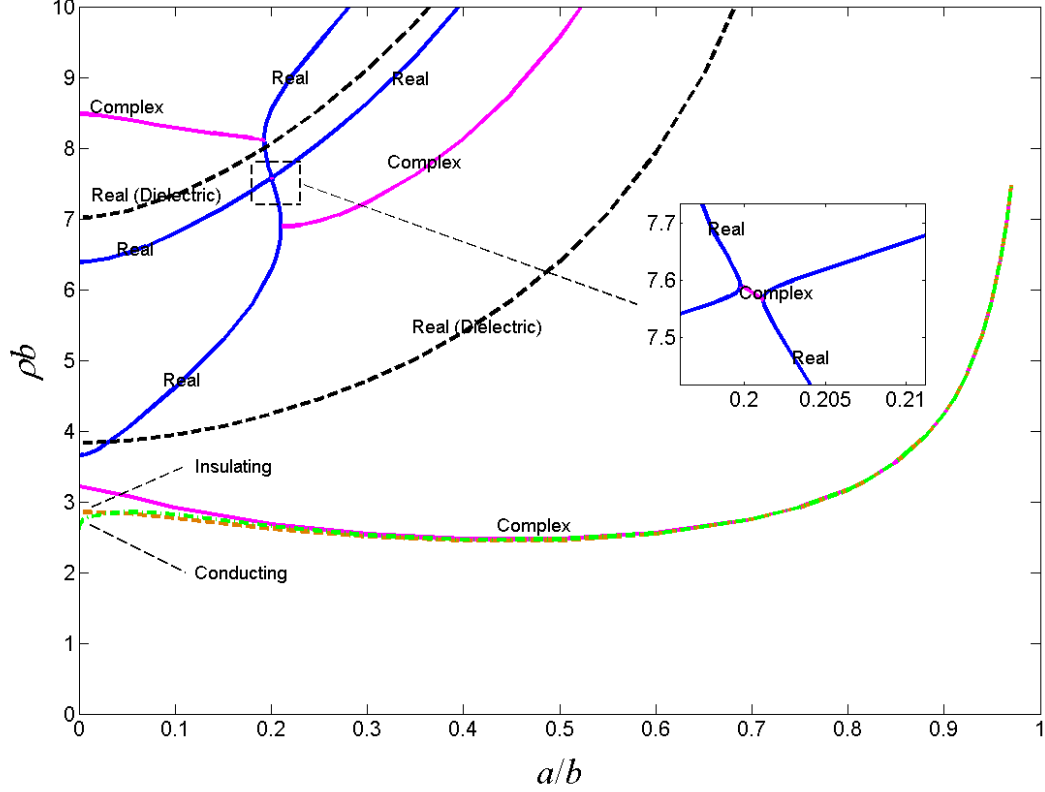


Figure 5.5: Dimensionless complex decay roots pb under axisymmetric torsionless deformation for a decoupled purely elastic and purely electric hollow GaN nanocolumn. The smallest decay model loci of the corresponding fully coupled piezoelectric case are also shown for comparison (the dashed line is for insulating and dash-dotted line for conducting boundary conditions on the two surface). Only real parts of the roots are shown.

We remark that Figure 5.3 should be extremely useful for the GaN nanopost and nanocolumn growth as the experimental environment is most likely insulating instead of conducting. For instance, for a solid GaN nanocolumn of radius $b = 100$ nm, using the normalized decay rate $pb = 2.855$, we find that the elastic and electric fields at the height $z = 161$ nm are reduced to 1% of the value at the bottom of the nanocolumn $z = 0$. We further observe from Figure 5.3 that for a hollow GaN nanocolumn, there is a special ratio a/b where the normalized decay rate reaches its minimum (i.e., $pb = 2.447$ at $a/b = 0.4$). When the wall of the hollow nanocolumn becomes thinner than $a/b = 0.4$, then the normalized decay rate increases. The thinner the hollow nanocolumn, the faster the elastic and electric fields decay.

In order to clearly demonstrate how the piezoelectricity influences the decay roots, we present in Figure 5.5 the decay roots for a GaN hollow nanocolumn by ignoring the piezoelectric effects (i.e., $e_{ij} = 0$). In Figure 5.5, besides the decoupled purely elastic roots under the traction-free boundary condition, the decoupled purely electric roots under the insulating boundary condition (by the marked dashed lines) are also presented for comparison. Furthermore, in Figure 5.5, we have redrawn (from Figures 5.3 and 5.4) the smallest decay mode loci for the corresponding fully coupled piezoelectric case (dashed line for the

insulating condition on the two surfaces, and dash-dotted line for the conducting condition on the two surfaces). By comparing Figure 5.5 with the previous two figures, 5.3 and 5.4, we observe that the piezoelectric effect can influence the root loci, especially those of the higher decay modes. As far as the decay rate is concerned, the piezoelectric effects must be taken into consideration for thick cylinders $a/b < 0.2$, and they can only be ignored for relatively thin cylinders $a/b > 0.2$. In other words, in the analysis of the strain and electric fields in GaN nanocolumn structures, it is recommended that the fully coupled piezoelectric model should be employed [1, 21, 22]. This is particularly true for the solid nanocolumn where a decay rate of $\rho b = 3.2213$ is predicted for the decoupled purely elastic case whilst $\rho b = 2.855$ and $\rho b = 2.605$ corresponding to the fully coupled piezoelectric case with insulating and conducting boundary conditions, respectively (Figure 5.5 for the smallest loci at $a/b = 0$). Figure 5.5 also indicates clearly that even for the decoupled piezoelectric case, an interaction between the real and complex root loci still exists. We remark that the decay roots for the axisymmetric torsionless displacements for an isotropic elastic hollow nanocolumn are all complex and there is no mode coupling phenomenon (see Figure 5.2 here or Figure 3 in Stephen and Wang [93]). Thus we conclude that the material anisotropy in nanocolumn can also significantly influence the decay roots.

5.5 Conclusions

Decay rate of the elastic and piezoelectric fields along a transversely isotropic piezoelectric hollow/solid circular nanocolumn is investigated in detail by developing the general solution for the corresponding 3D problem. It is shown clearly that the geometric parameter, material anisotropy, and piezoelectricity can all significantly affect the decay rate, thus influence the strain and electric field relaxation in the piezoelectric hollow/solid nanocolumn. Particularly, a solid GaN nanocolumn can have a decay rate of $\rho b = 3.2213$ for the decoupled purely elastic case, and $\rho b = 2.855$ and $\rho b = 2.605$ for the fully coupled piezoelectric case with insulating and conducting boundary conditions, respectively. This obviously indicates that the piezoelectric effect can not be ignored for a solid GaN nanocolumn as far as the decay rate is concerned. Results presented in this paper should be particularly useful to guide the nanopost and nanocolumn growth where the growth induced strain is critical to the corresponding semiconductor nanostructured devices. Even though only the simple axisymmetric case is discussed, the methodology can be easily extended to the more complicated asymmetric case. For the asymmetric case, due to the coupling between torsional and torsionless displacements, between mechanical and electric fields (the piezoelectric effects), and to the anisotropic effect, it is expected that the decay root loci for this situation are more complex than their isotropic counterparts.

Chapter 6

Electromagnetic Fields Induced by a Concentrated Heat Source in Multiferroic Materials

6.1 Introduction

Multiferroic materials simultaneously possess both ferroelectric and ferromagnetic (or antiferromagnetic) order in the same phase. They hold great potential for applications as the multiferroic coupling allows switching of the magnetic state by an electric field and likewise switching of the ferroelectric polarization by a magnetic field [38, 39, 42, 106, 107]. Significantly, multiferroics could lead to a new generation of memory and microwave devices that can be controlled both electrically and magnetically [42, 107].

The Green's functions in multiferroic materials can be utilized to tailor the magnetoelectric effect [41, 108] and to investigate inclusions of various shapes with spontaneous polarization and magnetization [48, 50]. Li and Li [50] obtained Green's functions for the uniaxial multiferroic material induced by a point electric or magnetic charge. The Green's functions for a uniaxial multiferroic half-space and bimaterial were addressed very recently [47]. The corresponding Green's functions for exponentially graded uniaxial multiferroic materials were also derived [109]. However, the aforementioned works on Green's functions in multiferroic materials [47, 50] were confined to the isothermal case in which the pyroelectric and pyromagnetic effects, which have been observed [110, 111] and which have found many applications both in science and technology [112, 113], were not taken into consideration. We also point out that thermal source is important in smart materials, as was discussed for piezoelectric [114] and magnetoelectroelastic [115] materials under the thermal source/loading in two dimension. A thermomagnetoelastic model was even proposed for earthquake source mechanism study [116].

Obtained in this research are the induced electromagnetic fields for a uniaxial multiferroic material and bimaterial subjected to a steady point heat source. In the course of elaborating our method we establish electromagnetic characteristic constants, λ_1 and λ_2 , to parameterize the multiferroic behavior. Both the nondegenerate case, in which the heat conduction characteristic constant λ_0 (the ratio of the transverse and axial thermal conductivity

tensor elements) is different from the two electromagnetic characteristic constants λ_1 and λ_2 , and the degenerate case, in which the heat conduction characteristic constant λ_0 is equal to one of the two electromagnetic characteristic constants λ_1 and λ_2 , are addressed. Once the Green's functions for a multiferroic full-space are known, the corresponding Green's functions for two bonded multiferroic half-spaces are obtained by the image method, with the twelve unknown constants being determined by inverting a simple 4×4 matrix [47].

6.2 A steady point heat source in a homogeneous uniaxial multiferroic material

The constitutive equations for a uniaxial multiferroic material with its unique axis along the x_3 -axis can be written as

$$\begin{aligned} \begin{bmatrix} D_1 \\ B_1 \end{bmatrix} &= \begin{bmatrix} \epsilon_{11} & \alpha_{11} \\ \alpha_{11} & \mu_{11} \end{bmatrix} \begin{bmatrix} E_1 \\ H_1 \end{bmatrix} & \begin{bmatrix} D_2 \\ B_2 \end{bmatrix} &= \begin{bmatrix} \epsilon_{11} & \alpha_{11} \\ \alpha_{11} & \mu_{11} \end{bmatrix} \begin{bmatrix} E_2 \\ H_2 \end{bmatrix} \\ \begin{bmatrix} D_3 \\ B_3 \end{bmatrix} &= \begin{bmatrix} \epsilon_{33} & \alpha_{33} \\ \alpha_{33} & \mu_{33} \end{bmatrix} \begin{bmatrix} E_3 \\ H_3 \end{bmatrix} + \begin{bmatrix} p \\ m \end{bmatrix} T \end{aligned} \quad (6.1)$$

where D_i and B_i ($i=1,2,3$) are the electric displacement and magnetic flux components (in the x_1 -, x_2 -, and x_3 -directions); E_i and H_i are electric field and magnetic field components; T is the temperature change; ϵ_{11} and ϵ_{33} are the two dielectric permittivity constants in the x_1 - and x_3 -directions, respectively; α_{11} and α_{33} are the two magnetoelectric constants (in the x_1 - and x_3 -directions); μ_{11} and μ_{33} are the two magnetic permeability constants (in the x_1 - and x_3 -directions); and p and m are, respectively, the pyroelectric and pyromagnetic constants (in the x_3 -direction).

The electric and magnetic fields are related to the electric potential ϕ and magnetic potential ψ through the following 2×1 column matrix relation

$$\begin{bmatrix} E_i \\ H_i \end{bmatrix} = - \begin{bmatrix} \phi_{,i} \\ \psi_{,i} \end{bmatrix} \quad (6.2)$$

where the subscript comma “,” followed by the index i ($i = 1, 2, 3$) denotes the derivative of the potential with respect to the coordinate x_i .

In the absence of free electric and magnetic charges, the electric displacement D_i and magnetic flux B_i satisfy the following Gauss' equations

$$\begin{aligned} \frac{\partial D_1}{\partial x_1} + \frac{\partial D_2}{\partial x_2} + \frac{\partial D_3}{\partial x_3} &= 0 \\ \frac{\partial B_1}{\partial x_1} + \frac{\partial B_2}{\partial x_2} + \frac{\partial B_3}{\partial x_3} &= 0 \end{aligned} \quad (6.3)$$

Substituting Eq. (6.2) into Eq. (6.1), and then the results into Eq. (6.3), we finally arrive at the following set of inhomogeneous partial differential equations for ϕ and ψ ,

$$\begin{bmatrix} \epsilon_{11} & \alpha_{11} \\ \alpha_{11} & \mu_{11} \end{bmatrix} \begin{bmatrix} \left(\frac{\partial^2}{\partial x_1^2} + \frac{\partial^2}{\partial x_2^2} \right) \phi \\ \left(\frac{\partial^2}{\partial x_1^2} + \frac{\partial^2}{\partial x_2^2} \right) \psi \end{bmatrix} + \begin{bmatrix} \epsilon_{33} & \alpha_{33} \\ \alpha_{33} & \mu_{33} \end{bmatrix} \begin{bmatrix} \frac{\partial^2 \phi}{\partial x_3^2} \\ \frac{\partial^2 \psi}{\partial x_3^2} \end{bmatrix} = \begin{bmatrix} p \\ m \end{bmatrix} \frac{\partial T}{\partial x_3} \quad (6.4)$$

In addition we assume that a steady point heat source of strength Q is located at the origin of a uniaxial multiferroic space. As a result the temperature T should satisfy the following 3D Poisson's equation

$$\frac{\partial^2 T}{\partial x_1^2} + \frac{\partial^2 T}{\partial x_2^2} + \frac{1}{\lambda_0} \frac{\partial^2 T}{\partial x_3^2} = -\frac{Q}{k_{11}} \delta(x_1) \delta(x_2) \delta(x_3), \quad (6.5)$$

where $\delta()$ is the Dirac delta function; $\lambda_0 = k_{11}/k_{33}$ is the dimensionless heat conduction characteristic constant; and k_{11} and k_{33} are two heat conductivity constants (in the x_1 - and x_3 -directions). It is obvious that for an isotropic thermal material, the heat conduction characteristic constant $\lambda_0=1$, whilst it can be larger or smaller than 1, depending whether the strong direction of the heat conduction is along x_1 - or x_3 -direction. Eq. (6.5) can be further expressed in the following standard form

$$\frac{\partial^2 T}{\partial x_1^2} + \frac{\partial^2 T}{\partial x_2^2} + \frac{\partial^2 T}{\partial (\sqrt{\lambda_0} x_3)^2} = -\frac{Q}{\tilde{k}} \delta(x_1) \delta(x_2) \delta(\sqrt{\lambda_0} x_3) \quad (6.6)$$

where $\tilde{k} = \sqrt{k_{11}k_{33}}$ can be considered as the effective heat conductivity. The solution to Eq. (6.6) can be expediently given by

$$T = \frac{Q}{4\pi\tilde{k}} \frac{1}{\sqrt{x_1^2 + x_2^2 + \lambda_0 x_3^2}}. \quad (6.7)$$

Inserting the above expression for the temperature T into Eq. (6.4), we arrive at

$$\begin{aligned} \begin{bmatrix} \epsilon_{11} & \alpha_{11} \\ \alpha_{11} & \mu_{11} \end{bmatrix} \begin{bmatrix} \left(\frac{\partial^2}{\partial x_1^2} + \frac{\partial^2}{\partial x_2^2} \right) \phi \\ \left(\frac{\partial^2}{\partial x_1^2} + \frac{\partial^2}{\partial x_2^2} \right) \psi \end{bmatrix} \\ + \begin{bmatrix} \epsilon_{33} & \alpha_{33} \\ \alpha_{33} & \mu_{33} \end{bmatrix} \begin{bmatrix} \frac{\partial^2 \phi}{\partial x_3^2} \\ \frac{\partial^2 \psi}{\partial x_3^2} \end{bmatrix} = -\frac{Q\sqrt{\lambda_0}x_3}{4\pi k_{33}(x_1^2 + x_2^2 + \lambda_0 x_3^2)^{3/2}} \begin{bmatrix} p \\ m \end{bmatrix} \end{aligned} \quad (6.8)$$

In the following we will decouple the coupled inhomogeneous partial differential equations (6.8) using the eigenvalue approach [47]. We first consider the following eigenvalue problem [47]

$$\left(\begin{bmatrix} \epsilon_{11} & \alpha_{11} \\ \alpha_{11} & \mu_{11} \end{bmatrix} - \lambda \begin{bmatrix} \epsilon_{33} & \alpha_{33} \\ \alpha_{33} & \mu_{33} \end{bmatrix} \right) \mathbf{v} = \begin{bmatrix} 0 \\ 0 \end{bmatrix} \quad (6.9)$$

The two eigenvalues λ_1 and λ_2 , which are termed the electromagnetic characteristic

constants, are given by [47]

$$\begin{aligned}
\lambda_1 &= \frac{\mu_{33}\varepsilon_{11} + \mu_{11}\varepsilon_{33} - 2\alpha_{11}\alpha_{33}}{2(\mu_{33}\varepsilon_{33} - \alpha_{33}^2)} \\
&\quad + \frac{\sqrt{(\mu_{11}\varepsilon_{33} - \mu_{33}\varepsilon_{11})^2 + 4(\alpha_{11}\mu_{33} - \alpha_{33}\mu_{11})(\alpha_{11}\varepsilon_{33} - \alpha_{33}\varepsilon_{11})}}{2(\mu_{33}\varepsilon_{33} - \alpha_{33}^2)} \\
\lambda_2 &= \frac{\mu_{33}\varepsilon_{11} + \mu_{11}\varepsilon_{33} - 2\alpha_{11}\alpha_{33}}{2(\mu_{33}\varepsilon_{33} - \alpha_{33}^2)} \\
&\quad - \frac{\sqrt{(\mu_{11}\varepsilon_{33} - \mu_{33}\varepsilon_{11})^2 + 4(\alpha_{11}\mu_{33} - \alpha_{33}\mu_{11})(\alpha_{11}\varepsilon_{33} - \alpha_{33}\varepsilon_{11})}}{2(\mu_{33}\varepsilon_{33} - \alpha_{33}^2)}
\end{aligned} \tag{6.10}$$

and the two eigenvectors associated with λ_1 and λ_2 are

$$\mathbf{v}_1 = \begin{bmatrix} -\alpha_{11} + \lambda_1\alpha_{33} \\ \varepsilon_{11} - \lambda_1\varepsilon_{33} \end{bmatrix} \quad \mathbf{v}_2 = \begin{bmatrix} -\alpha_{11} + \lambda_2\alpha_{33} \\ \varepsilon_{11} - \lambda_2\varepsilon_{33} \end{bmatrix} \tag{6.11}$$

Since the two matrices on the left-hand side of Eq. (6.9) are real and symmetric, it can be easily verified that the following orthogonal relationships with respect to the two symmetric matrices hold [47]

$$\begin{aligned}
\begin{bmatrix} \mathbf{v}_1^T \\ \mathbf{v}_2^T \end{bmatrix} \begin{bmatrix} \varepsilon_{33} & \alpha_{33} \\ \alpha_{33} & \mu_{33} \end{bmatrix} \begin{bmatrix} \mathbf{v}_1 & \mathbf{v}_2 \end{bmatrix} &= \begin{bmatrix} \delta_1 & 0 \\ 0 & \delta_2 \end{bmatrix} \\
\begin{bmatrix} \mathbf{v}_1^T \\ \mathbf{v}_2^T \end{bmatrix} \begin{bmatrix} \varepsilon_{11} & \alpha_{11} \\ \alpha_{11} & \mu_{11} \end{bmatrix} \begin{bmatrix} \mathbf{v}_1 & \mathbf{v}_2 \end{bmatrix} &= \begin{bmatrix} \lambda_1\delta_1 & 0 \\ 0 & \lambda_2\delta_2 \end{bmatrix}
\end{aligned} \tag{6.12}$$

where

$$\begin{aligned}
\delta_1 &= \alpha_{11}^2\varepsilon_{33} + \varepsilon_{11}^2\mu_{33} - 2\alpha_{11}\alpha_{33}\varepsilon_{11} + (\mu_{33}\varepsilon_{33} - \alpha_{33}^2)(\lambda_1^2\varepsilon_{33} - 2\lambda_1\varepsilon_{11}) \\
\delta_2 &= \alpha_{11}^2\varepsilon_{33} + \varepsilon_{11}^2\mu_{33} - 2\alpha_{11}\alpha_{33}\varepsilon_{11} + (\mu_{33}\varepsilon_{33} - \alpha_{33}^2)(\lambda_2^2\varepsilon_{33} - 2\lambda_2\varepsilon_{11})
\end{aligned} \tag{6.13}$$

We now introduce two new functions f and g , which are related to ϕ and ψ through

$$\begin{bmatrix} \phi \\ \psi \end{bmatrix} = \underline{\Phi} \begin{bmatrix} f \\ g \end{bmatrix} \tag{6.14}$$

where $\underline{\Phi} = [\mathbf{v}_1 \ \mathbf{v}_2]$.

In view of Eqs. (6.8), (6.12) and (6.14), the two new functions f and g satisfy the following two independent 3D Poisson's equations

$$\begin{aligned}
\left(\frac{\partial^2}{\partial x_1^2} + \frac{\partial^2}{\partial x_2^2} + \frac{1}{\lambda_1} \frac{\partial^2}{\partial x_3^2} \right) f &= \frac{c_1 \sqrt{\lambda_0} x_3}{(x_1^2 + x_2^2 + \lambda_0 x_3^2)^{3/2}} \\
\left(\frac{\partial^2}{\partial x_1^2} + \frac{\partial^2}{\partial x_2^2} + \frac{1}{\lambda_2} \frac{\partial^2}{\partial x_3^2} \right) g &= \frac{c_2 \sqrt{\lambda_0} x_3}{(x_1^2 + x_2^2 + \lambda_0 x_3^2)^{3/2}}
\end{aligned} \tag{6.15}$$

where the two constants c_1 and c_2 are given by

$$\begin{aligned} c_1 &= \frac{Q[p(\alpha_{11} - \lambda_1 \alpha_{33}) - m(\epsilon_{11} - \lambda_1 \epsilon_{33})]}{4\pi k_{33} \delta_1 \lambda_1} \\ c_2 &= \frac{Q[p(\alpha_{11} - \lambda_2 \alpha_{33}) - m(\epsilon_{11} - \lambda_2 \epsilon_{33})]}{4\pi k_{33} \delta_2 \lambda_2} \end{aligned} \quad (6.16)$$

In the following we will discuss the solutions to Eq. (6.15) according to whether the heat conduction characteristic constant λ_0 is equal to one of the two electromagnetic characteristic constants λ_1 and λ_2 . We assume that the two electromagnetic characteristic constants are distinct (which is true for a uniaxial material) in order to simplify our discussion. In the case of isotropy where $\lambda_1 = \lambda_2$, a small perturbation can be utilized to separate the two roots so that the solutions presented in this paper can still be utilized with neglected errors [117].

6.2.1 The nondegenerate case: $\lambda_1 \neq \lambda_2 \neq \lambda_0$

When $\lambda_1 \neq \lambda_2 \neq \lambda_0$, it can be easily checked that the solutions to Eq. (6.15) can be written as

$$\begin{aligned} f &= \text{sign}(x_3) \left[d_1 \ln R_1^* + \frac{\lambda_1 c_1}{\lambda_1 - \lambda_0} \ln R_0^* \right] \\ g &= \text{sign}(x_3) \left[d_2 \ln R_2^* + \frac{\lambda_2 c_2}{\lambda_2 - \lambda_0} \ln R_0^* \right] \end{aligned} \quad (6.17)$$

where $R_i^* = R_i + \sqrt{\lambda_i} |x_3|$ with $R_i = \sqrt{r^2 + \lambda_i x_3^2}$, and $r^2 = x_1^2 + x_2^2$ ($i = 0, 1, 2$); d_1 and d_2 are two unknown constants; and the sign function is defined as follows

$$\text{sign}(x_3) = \begin{cases} 1 & x_3 > 0 \\ -1 & x_3 < 0 \end{cases} \quad (6.18)$$

Due to the fact that the electric and magnetic potentials ϕ and ψ should be *continuous* across the plane $x_3 = 0$, then we have $\phi = \psi = 0$ (or, equivalently, $f = g = 0$) on $x_3 = 0$ in view of the fact that f and g are odd functions of x_3 . As a result it follows from Eq. (6.17) that the two unknown constants d_1 and d_2 can be uniquely determined to be

$$d_1 = -\frac{\lambda_1 c_1}{\lambda_1 - \lambda_0} \quad d_2 = -\frac{\lambda_2 c_2}{\lambda_2 - \lambda_0} \quad (6.19)$$

Consequently the expressions of f and g can be finally given by

$$\begin{aligned} f &= \frac{\lambda_1 c_1}{\lambda_1 - \lambda_0} \text{sign}(x_3) \ln \frac{R_0^*}{R_1^*} \\ g &= \frac{\lambda_2 c_2}{\lambda_2 - \lambda_0} \text{sign}(x_3) \ln \frac{R_0^*}{R_2^*} \end{aligned} \quad (6.20)$$

The expressions of the electric and magnetic potentials ϕ and ψ are thus given by

$$\begin{bmatrix} \phi \\ \psi \end{bmatrix} = \underline{\Phi} \begin{bmatrix} \frac{\lambda_1 c_1}{\lambda_1 - \lambda_0} \text{sign}(x_3) \ln \frac{R_0^*}{R_1^*} \\ \frac{\lambda_2 c_2}{\lambda_2 - \lambda_0} \text{sign}(x_3) \ln \frac{R_0^*}{R_2^*} \end{bmatrix} \quad (6.21)$$

which can be written more explicitly as

$$\begin{aligned} \phi &= \frac{\lambda_1 c_1 (\lambda_1 \alpha_{33} - \alpha_{11})}{\lambda_1 - \lambda_0} \text{sign}(x_3) \ln \frac{R_0^*}{R_1^*} + \frac{\lambda_2 c_2 (\lambda_2 \alpha_{33} - \alpha_{11})}{\lambda_2 - \lambda_0} \text{sign}(x_3) \ln \frac{R_0^*}{R_2^*} \\ \psi &= \frac{\lambda_1 c_1 (\epsilon_{11} - \lambda_1 \epsilon_{33})}{\lambda_1 - \lambda_0} \text{sign}(x_3) \ln \frac{R_0^*}{R_1^*} + \frac{\lambda_2 c_2 (\epsilon_{11} - \lambda_2 \epsilon_{33})}{\lambda_2 - \lambda_0} \text{sign}(x_3) \ln \frac{R_0^*}{R_2^*} \end{aligned} \quad (6.22)$$

The electric and magnetic fields induced by the point heat source can then be determined as

$$\begin{aligned} E_1 &= \frac{\lambda_1 c_1 (\alpha_{11} - \lambda_1 \alpha_{33})}{\lambda_1 - \lambda_0} \text{sign}(x_3) \left(\frac{x_1}{R_0 R_0^*} - \frac{x_1}{R_1 R_1^*} \right) \\ &\quad + \frac{\lambda_2 c_2 (\alpha_{11} - \lambda_2 \alpha_{33})}{\lambda_2 - \lambda_0} \text{sign}(x_3) \left(\frac{x_1}{R_0 R_0^*} - \frac{x_1}{R_2 R_2^*} \right) \\ E_2 &= \frac{\lambda_1 c_1 (\alpha_{11} - \lambda_1 \alpha_{33})}{\lambda_1 - \lambda_0} \text{sign}(x_3) \left(\frac{x_2}{R_0 R_0^*} - \frac{x_2}{R_1 R_1^*} \right) \\ &\quad + \frac{\lambda_2 c_2 (\alpha_{11} - \lambda_2 \alpha_{33})}{\lambda_2 - \lambda_0} \text{sign}(x_3) \left(\frac{x_2}{R_0 R_0^*} - \frac{x_2}{R_2 R_2^*} \right) \\ E_3 &= \frac{\lambda_1 c_1 (\alpha_{11} - \lambda_1 \alpha_{33})}{\lambda_1 - \lambda_0} \left(\frac{\sqrt{\lambda_0}}{R_0} - \frac{\sqrt{\lambda_1}}{R_1} \right) + \frac{\lambda_2 c_2 (\alpha_{11} - \lambda_2 \alpha_{33})}{\lambda_2 - \lambda_0} \left(\frac{\sqrt{\lambda_0}}{R_0} - \frac{\sqrt{\lambda_2}}{R_2} \right) \end{aligned} \quad (6.23)$$

$$\begin{aligned} H_1 &= \frac{\lambda_1 c_1 (\lambda_1 \epsilon_{33} - \epsilon_{11})}{\lambda_1 - \lambda_0} \text{sign}(x_3) \left(\frac{x_1}{R_0 R_0^*} - \frac{x_1}{R_1 R_1^*} \right) \\ &\quad + \frac{\lambda_2 c_2 (\lambda_2 \epsilon_{33} - \epsilon_{11})}{\lambda_2 - \lambda_0} \text{sign}(x_3) \left(\frac{x_1}{R_0 R_0^*} - \frac{x_1}{R_2 R_2^*} \right) \\ H_2 &= \frac{\lambda_1 c_1 (\lambda_1 \epsilon_{33} - \epsilon_{11})}{\lambda_1 - \lambda_0} \text{sign}(x_3) \left(\frac{x_2}{R_0 R_0^*} - \frac{x_2}{R_1 R_1^*} \right) \\ &\quad + \frac{\lambda_2 c_2 (\lambda_2 \epsilon_{33} - \epsilon_{11})}{\lambda_2 - \lambda_0} \text{sign}(x_3) \left(\frac{x_2}{R_0 R_0^*} - \frac{x_2}{R_2 R_2^*} \right) \\ H_3 &= \frac{\lambda_1 c_1 (\lambda_1 \epsilon_{33} - \epsilon_{11})}{\lambda_1 - \lambda_0} \left(\frac{\sqrt{\lambda_0}}{R_0} - \frac{\sqrt{\lambda_1}}{R_1} \right) + \frac{\lambda_2 c_2 (\lambda_2 \epsilon_{33} - \epsilon_{11})}{\lambda_2 - \lambda_0} \left(\frac{\sqrt{\lambda_0}}{R_0} - \frac{\sqrt{\lambda_2}}{R_2} \right) \end{aligned} \quad (6.24)$$

It is observed from the above two expressions that the horizontal electric and magnetic fields E_1 , E_2 , H_1 , H_2 are odd functions of x_3 , and are zero on the horizontal plane $x_3 = 0$. On the other hand, the vertical electric and magnetic fields E_3 and H_3 are even functions of x_3 , inversely proportional to $r = \sqrt{x_1^2 + x_2^2}$ on the horizontal plane $x_3 = 0$, and are zero on the x_3 -axis excluding the origin. The electric displacements and magnetic fluxes can be determined by using Eq. (6.1) and the above two expressions.

6.2.2 The degenerate case: $\lambda_1 = \lambda_0$ ($\lambda_1 \neq \lambda_2$)

Next we address the degenerate case $\lambda_1 = \lambda_0$ ($\lambda_1 \neq \lambda_2$). Applying the L'Hospital's rule to Eq. (6.21) when $\lambda_1 \rightarrow \lambda_0$ yields the expressions of the electric potential ϕ and magnetic potential ψ as follows

$$\begin{bmatrix} \phi \\ \psi \end{bmatrix} = \underline{\Phi} \begin{bmatrix} -\frac{c_1 \sqrt{\lambda_0} x_3}{2R_0} \\ \frac{\lambda_2 c_2}{\lambda_2 - \lambda_0} \text{sign}(x_3) \ln \frac{R_0^*}{R_2^*} \end{bmatrix} \quad (6.25)$$

which can be written more explicitly as

$$\begin{aligned} \phi &= \frac{\sqrt{\lambda_0} c_1 (\alpha_{11} - \lambda_0 \alpha_{33}) x_3}{2R_0} + \frac{\lambda_2 c_2 (\lambda_2 \alpha_{33} - \alpha_{11})}{\lambda_2 - \lambda_0} \text{sign}(x_3) \ln \frac{R_0^*}{R_2^*} \\ \psi &= \frac{\sqrt{\lambda_0} c_1 (\lambda_0 \epsilon_{33} - \epsilon_{11}) x_3}{2R_0} + \frac{\lambda_2 c_2 (\epsilon_{11} - \lambda_2 \epsilon_{33})}{\lambda_2 - \lambda_0} \text{sign}(x_3) \ln \frac{R_0^*}{R_2^*} \end{aligned} \quad (6.26)$$

The electric and magnetic fields induced by the point heat source can then be determined as

$$\begin{aligned} E_1 &= \frac{\sqrt{\lambda_0} c_1 (\alpha_{11} - \lambda_0 \alpha_{33}) x_1 x_3}{2R_0^3} + \frac{\lambda_2 c_2 (\alpha_{11} - \lambda_2 \alpha_{33})}{\lambda_2 - \lambda_0} \text{sign}(x_3) \left(\frac{x_1}{R_0 R_0^*} - \frac{x_1}{R_2 R_2^*} \right) \\ E_2 &= \frac{\sqrt{\lambda_0} c_1 (\alpha_{11} - \lambda_0 \alpha_{33}) x_2 x_3}{2R_0^3} + \frac{\lambda_2 c_2 (\alpha_{11} - \lambda_2 \alpha_{33})}{\lambda_2 - \lambda_0} \text{sign}(x_3) \left(\frac{x_2}{R_0 R_0^*} - \frac{x_2}{R_2 R_2^*} \right) \\ E_3 &= \frac{\sqrt{\lambda_0} c_1 (\lambda_0 \alpha_{33} - \alpha_{11}) r^2}{2R_0^3} + \frac{\lambda_2 c_2 (\alpha_{11} - \lambda_2 \alpha_{33})}{\lambda_2 - \lambda_0} \left(\frac{\sqrt{\lambda_0}}{R_0} - \frac{\sqrt{\lambda_2}}{R_2} \right) \end{aligned} \quad (6.27)$$

$$\begin{aligned} H_1 &= \frac{\sqrt{\lambda_0} c_1 (\lambda_0 \epsilon_{33} - \epsilon_{11}) x_1 x_3}{2R_0^3} + \frac{\lambda_2 c_2 (\lambda_2 \epsilon_{33} - \epsilon_{11})}{\lambda_2 - \lambda_0} \text{sign}(x_3) \left(\frac{x_1}{R_0 R_0^*} - \frac{x_1}{R_2 R_2^*} \right) \\ H_2 &= \frac{\sqrt{\lambda_0} c_1 (\lambda_0 \epsilon_{33} - \epsilon_{11}) x_2 x_3}{2R_0^3} + \frac{\lambda_2 c_2 (\lambda_2 \epsilon_{33} - \epsilon_{11})}{\lambda_2 - \lambda_0} \text{sign}(x_3) \left(\frac{x_2}{R_0 R_0^*} - \frac{x_2}{R_2 R_2^*} \right) \\ H_3 &= \frac{\sqrt{\lambda_0} c_1 (\epsilon_{11} - \lambda_0 \epsilon_{33}) r^2}{2R_0^3} + \frac{\lambda_2 c_2 (\lambda_2 \epsilon_{33} - \epsilon_{11})}{\lambda_2 - \lambda_0} \left(\frac{\sqrt{\lambda_0}}{R_0} - \frac{\sqrt{\lambda_2}}{R_2} \right) \end{aligned} \quad (6.28)$$

Similar to the nondegenerate case, we also observe that, for the degenerate case, the horizontal electric and magnetic fields are odd functions of x_3 , and are zero on the horizontal plane $x_3 = 0$. On the other hand, the vertical electric and magnetic fields are even functions of x_3 , are inversely proportional to r when $x_3 = 0$, and are zero on the x_3 axis excluding the origin. The electric displacements and magnetic fluxes can be similarly determined by using Eq. (6.1) and the above two expressions.

Before ending this section, we add that the other degenerate case $\lambda_1 = \lambda_0$ ($\lambda_1 \neq \lambda_2$) can be discussed similarly. The results obtained in this section can be further applied to derive the electromagnetic Green's functions for a uniaxial multiferroic bimerial induced by a steady point heat source, which will be discussed in detail in the ensuing section.

6.3 A steady point heat source in a homogeneous uniaxial multiferroic bimaterial

In this section we investigate the electromagnetic fields in two bonded multiferroic half-spaces induced by a steady point heat source. We assume that both half-spaces are uniaxial multiferroic materials having the unique axis along the x_3 -axis, and that the interface $x_3 = 0$ of the two multiferroic half-spaces are perfect. Namely, the temperature, electric potential, magnetic potential, normal heat flux, normal electric displacement and normal magnetic flux are all *continuous* across the interface $x_3 = 0$. Without loss of generality, a steady point heat source of strength Q is assumed to be located at $x_1 = x_2 = 0$, $x_3 = h$ ($h > 0$) in the upper half-space of the multiferroic bimaterial. In the following the subscripts “1” and “2” to vectors or matrices and the superscripts “(1)” and “(2)” to scalars are used to identify the quantities in the upper and lower half spaces, respectively. In addition, we only consider the nondegenerate case for the two multiferroic half-spaces in which the heat conduction characteristic constant is different from the electromagnetic characteristic constants, i.e., $\lambda_1^{(i)} \neq \lambda_2^{(i)} \neq \lambda_0^{(i)}$, ($i = 1, 2$).

First, making use of the image method [47] and enforcing the continuity conditions of temperature and normal heat flux across the interface $x_3 = 0$, we arrive at the temperature field in the uniaxial bimaterial as follows,

$$T^{(1)} = \frac{Q}{4\pi\tilde{k}^{(1)}\sqrt{x_1^2 + x_2^2 + \lambda_0^{(1)}(x_3 - h)^2}} + \frac{Q(\tilde{k}^{(1)} - \tilde{k}^{(2)})}{4\pi\tilde{k}^{(1)}(\tilde{k}^{(1)} + \tilde{k}^{(2)})\sqrt{x_1^2 + x_2^2 + \lambda_0^{(1)}(x_3 + h)^2}} \quad (6.29a)$$

for $x_3 > 0$, and

$$T^{(2)} = \frac{Q}{2\pi(\tilde{k}^{(1)} + \tilde{k}^{(2)})\sqrt{x_1^2 + x_2^2 + (\sqrt{\lambda_0^{(2)}}x_3 - \sqrt{\lambda_0^{(1)}}h)^2}} \quad (6.29b)$$

for $x_3 < 0$.

It can be found that the electric and magnetic potentials in the bimaterial, induced by the temperature field (6.29), take the following forms,

$$\begin{bmatrix} \phi^{(1)} \\ \psi^{(1)} \end{bmatrix} = \underline{\Phi}_1 \begin{bmatrix} L_{10} \ln R_{10}^+ + L_{11} \ln R_{11}^+ + L_{12} \ln R_{12}^+ + \frac{\lambda_1^{(1)} c_1}{\lambda_1^{(1)} - \lambda_0^{(1)}} \text{sign}(x_3 - h) \ln \frac{R_0^+}{R_1^+} + \frac{\lambda_1^{(1)} e_1}{\lambda_1^{(1)} - \lambda_0^{(1)}} \ln R_{00}^+ \\ L_{20} \ln R_{20}^+ + L_{21} \ln R_{21}^+ + L_{22} \ln R_{22}^+ + \frac{\lambda_2^{(1)} c_2}{\lambda_2^{(1)} - \lambda_0^{(1)}} \text{sign}(x_3 - h) \ln \frac{R_0^+}{R_2^+} + \frac{\lambda_2^{(1)} e_2}{\lambda_2^{(1)} - \lambda_0^{(1)}} \ln R_{00}^+ \end{bmatrix} \quad (6.30)$$

for $x_3 > 0$, and

$$\begin{bmatrix} \phi^{(2)} \\ \psi^{(2)} \end{bmatrix} = \underline{\Phi}_2 \begin{bmatrix} L_{30} \ln R_{10}^- + L_{31} \ln R_{11}^- + L_{32} \ln R_{12}^- + \frac{\lambda_1^{(2)} e_3}{\lambda_1^{(2)} - \lambda_0^{(2)}} \ln R_{00}^- \\ L_{40} \ln R_{20}^- + L_{41} \ln R_{21}^- + L_{42} \ln R_{22}^- + \frac{\lambda_2^{(2)} e_4}{\lambda_2^{(2)} - \lambda_0^{(2)}} \ln R_{00}^- \end{bmatrix} \quad (6.31)$$

for $x_3 < 0$, where L_{ij} ($i = 1, 2, 3, 4$, $j = 0, 1, 2$) are the unknown coefficients to be determined, and

$$\begin{aligned} R_i^* &= \sqrt{x_1^2 + x_2^2 + \lambda_i^{(1)}(x_3 - h)^2} + \sqrt{\lambda_i^{(1)}} |x_3 - h| \\ R_{ij}^+ &= \sqrt{x_1^2 + x_2^2 + (\sqrt{\lambda_i^{(1)}} x_3 + \sqrt{\lambda_j^{(1)}} h)^2} + \sqrt{\lambda_i^{(1)}} x_3 + \sqrt{\lambda_j^{(1)}} h \\ R_{ij}^- &= \sqrt{x_1^2 + x_2^2 + (\sqrt{\lambda_i^{(2)}} x_3 - \sqrt{\lambda_j^{(1)}} h)^2} + \sqrt{\lambda_j^{(1)}} h - \sqrt{\lambda_i^{(2)}} x_3 \end{aligned} \quad (6.32)$$

where here $i, j = 0, 1, 2$. Furthermore, $c_1, c_2, e_1, e_2, e_3, e_4$ in Eq. (6.30) are given by

$$c_1 = -\frac{Q(p^{(1)}\Phi_{11}^{(1)} + m^{(1)}\Phi_{21}^{(1)})}{4\pi k_{33}^{(1)}\delta_1^{(1)}\lambda_1^{(1)}} \quad c_2 = -\frac{Q(p^{(1)}\Phi_{12}^{(1)} + m^{(1)}\Phi_{22}^{(1)})}{4\pi k_{33}^{(1)}\delta_2^{(1)}\lambda_2^{(1)}} \quad (6.33a)$$

$$e_1 = \frac{Q(\tilde{k}^{(2)} - \tilde{k}^{(1)})(p^{(1)}\Phi_{11}^{(1)} + m^{(1)}\Phi_{21}^{(1)})}{4\pi k_{33}^{(1)}\delta_1^{(1)}\lambda_1^{(1)}(\tilde{k}^{(1)} + \tilde{k}^{(2)})} \quad e_2 = \frac{Q(\tilde{k}^{(2)} - \tilde{k}^{(1)})(p^{(1)}\Phi_{12}^{(1)} + m^{(1)}\Phi_{22}^{(1)})}{4\pi k_{33}^{(1)}\delta_2^{(1)}\lambda_2^{(1)}(\tilde{k}^{(1)} + \tilde{k}^{(2)})} \quad (6.33b)$$

$$e_3 = \frac{Q\sqrt{\lambda_0^{(2)}}(p^{(2)}\Phi_{11}^{(2)} + m^{(2)}\Phi_{21}^{(2)})}{2\pi\delta_1^{(2)}\lambda_1^{(2)}(\tilde{k}^{(1)} + \tilde{k}^{(2)})} \quad e_4 = \frac{Q\sqrt{\lambda_0^{(2)}}(p^{(2)}\Phi_{12}^{(2)} + m^{(2)}\Phi_{22}^{(2)})}{2\pi\delta_2^{(2)}\lambda_2^{(2)}(\tilde{k}^{(1)} + \tilde{k}^{(2)})} \quad (6.33c)$$

with $\Phi_{11}^{(i)} = \lambda_1^{(i)}\alpha_{33}^{(i)} - \alpha_{11}^{(i)}$, $\Phi_{12}^{(i)} = \lambda_2^{(i)}\alpha_{33}^{(i)} - \alpha_{11}^{(i)}$, $\Phi_{21}^{(i)} = \varepsilon_{11}^{(i)} - \lambda_1\varepsilon_{33}^{(i)}$, and $\Phi_{22}^{(i)} = \varepsilon_{11}^{(i)} - \lambda_2\varepsilon_{33}^{(i)}$ being the four components of $\underline{\Phi}_i$.

Then, by enforcing the continuity conditions of the electric and magnetic potentials as well as the normal electric displacement and normal magnetic flux across the interface $x_3 = 0$, the twelve unknowns L_{ij} ($i = 1, 2, 3, 4$, $j = 0, 1, 2$) can be uniquely determined to be

$$\begin{bmatrix} L_{10} & L_{11} & L_{12} \\ L_{20} & L_{21} & L_{22} \\ L_{30} & L_{31} & L_{32} \\ L_{40} & L_{41} & L_{42} \end{bmatrix} = \begin{bmatrix} \Phi_{11}^{(1)} & \Phi_{12}^{(1)} & -\Phi_{11}^{(2)} & -\Phi_{12}^{(2)} \\ \Phi_{21}^{(1)} & \Phi_{22}^{(1)} & -\Phi_{21}^{(2)} & -\Phi_{22}^{(2)} \\ J_{11}^{(1)} & J_{12}^{(1)} & J_{11}^{(2)} & J_{12}^{(2)} \\ J_{21}^{(1)} & J_{22}^{(1)} & J_{21}^{(2)} & J_{22}^{(2)} \end{bmatrix}^{-1} \begin{bmatrix} \xi_{10} & \xi_{11} & \xi_{12} \\ \xi_{20} & \xi_{21} & \xi_{22} \\ \xi_{30} & \xi_{31} & \xi_{32} \\ \xi_{40} & \xi_{41} & \xi_{42} \end{bmatrix} \quad (6.34)$$

where

$$\begin{aligned} J_{11}^{(i)} &= \sqrt{\lambda_1^{(i)}}(\varepsilon_{33}^{(i)}\Phi_{11}^{(i)} + \alpha_{33}^{(i)}\Phi_{21}^{(i)}), \quad J_{12}^{(i)} = \sqrt{\lambda_2^{(i)}}(\varepsilon_{33}^{(i)}\Phi_{12}^{(i)} + \alpha_{33}^{(i)}\Phi_{22}^{(i)}) \\ J_{21}^{(i)} &= \sqrt{\lambda_1^{(i)}}(\alpha_{33}^{(i)}\Phi_{11}^{(i)} + \mu_{33}^{(i)}\Phi_{21}^{(i)}), \quad J_{22}^{(i)} = \sqrt{\lambda_2^{(i)}}(\alpha_{33}^{(i)}\Phi_{12}^{(i)} + \mu_{33}^{(i)}\Phi_{22}^{(i)}) \end{aligned} \quad (6.35)$$

where here $i = 1, 2$ and

$$\begin{bmatrix} \xi_{10} \\ \xi_{20} \\ \xi_{30} \\ \xi_{40} \end{bmatrix} = \begin{bmatrix} \frac{\Phi_{11}^{(1)} \lambda_1^{(1)} (c_1 - e_1)}{\lambda_1^{(1)} - \lambda_0^{(1)}} + \frac{\Phi_{12}^{(1)} \lambda_2^{(1)} (c_2 - e_2)}{\lambda_2^{(1)} - \lambda_0^{(1)}} + \frac{\Phi_{11}^{(2)} \lambda_1^{(2)} e_3}{\lambda_1^{(2)} - \lambda_0^{(2)}} + \frac{\Phi_{12}^{(2)} \lambda_2^{(2)} e_4}{\lambda_2^{(2)} - \lambda_0^{(2)}} \\ \frac{\Phi_{21}^{(1)} \lambda_1^{(1)} (c_1 - e_1)}{\lambda_1^{(1)} - \lambda_0^{(1)}} + \frac{\Phi_{22}^{(1)} \lambda_2^{(1)} (c_2 - e_2)}{\lambda_2^{(1)} - \lambda_0^{(1)}} + \frac{\Phi_{21}^{(2)} \lambda_1^{(2)} e_3}{\lambda_1^{(2)} - \lambda_0^{(2)}} + \frac{\Phi_{22}^{(2)} \lambda_2^{(2)} e_4}{\lambda_2^{(2)} - \lambda_0^{(2)}} \\ \frac{J_{11}^{(1)} \sqrt{\lambda_0^{(1)} \lambda_1^{(1)}} (c_1 + e_1)}{\lambda_0^{(1)} - \lambda_1^{(1)}} + \frac{J_{12}^{(1)} \sqrt{\lambda_0^{(1)} \lambda_2^{(1)}} (c_2 + e_2)}{\lambda_0^{(1)} - \lambda_2^{(1)}} + \frac{J_{11}^{(2)} \sqrt{\lambda_0^{(2)} \lambda_1^{(2)}} e_3}{\lambda_0^{(2)} - \lambda_1^{(2)}} + \frac{J_{12}^{(2)} \sqrt{\lambda_0^{(2)} \lambda_2^{(2)}} e_4}{\lambda_0^{(2)} - \lambda_2^{(2)}} + \frac{Q(p^{(2)} - p^{(1)})}{2\pi(\tilde{k}^{(1)} + \tilde{k}^{(2)})} \\ \frac{J_{21}^{(1)} \sqrt{\lambda_0^{(1)} \lambda_1^{(1)}} (c_1 + e_1)}{\lambda_0^{(1)} - \lambda_1^{(1)}} + \frac{J_{22}^{(1)} \sqrt{\lambda_0^{(1)} \lambda_2^{(1)}} (c_2 + e_2)}{\lambda_0^{(1)} - \lambda_2^{(1)}} + \frac{J_{21}^{(2)} \sqrt{\lambda_0^{(2)} \lambda_1^{(2)}} e_3}{\lambda_0^{(2)} - \lambda_1^{(2)}} + \frac{J_{22}^{(2)} \sqrt{\lambda_0^{(2)} \lambda_2^{(2)}} e_4}{\lambda_0^{(2)} - \lambda_2^{(2)}} + \frac{Q(m^{(2)} - m^{(1)})}{2\pi(\tilde{k}^{(1)} + \tilde{k}^{(2)})} \end{bmatrix} \quad (6.36)$$

and

$$\begin{bmatrix} \xi_{11} & \xi_{12} \\ \xi_{21} & \xi_{22} \\ \xi_{31} & \xi_{32} \\ \xi_{41} & \xi_{42} \end{bmatrix} = \begin{bmatrix} -\Phi_{11}^{(1)} & -\Phi_{21}^{(1)} \\ -\Phi_{12}^{(1)} & -\Phi_{22}^{(1)} \\ J_{11}^{(1)} & J_{21}^{(1)} \\ J_{12}^{(1)} & J_{22}^{(1)} \end{bmatrix} \begin{bmatrix} \frac{\lambda_1^{(1)} c_1}{\lambda_1^{(1)} - \lambda_0^{(1)}} & 0 \\ 0 & \frac{\lambda_2^{(1)} c_2}{\lambda_2^{(1)} - \lambda_0^{(1)}} \end{bmatrix} \quad (6.37)$$

It is observed from Eq. (6.34) that the twelve unknowns L_{ij} can be simply determined by inverting a *single* 4×4 matrix. This concise procedure is similar to that for the corresponding isothermal case [47]. Once the electric and magnetic potentials in the multiferroic bimaterial are obtained, the electric and magnetic fields as well as electric displacements and magnetic fluxes can be found by taking the derivatives of the electric and magnetic potentials.

6.4 Conclusions

The three-dimensional electromagnetic Green's function solutions for a steady-state point heat source in a uniaxial multiferroic material and bimaterial are derived. The Green's function expressions for a multiferroic full-space are given in Eqs. (6.22)–(6.24) for the nondegenerate case $\lambda_1 \neq \lambda_2 \neq \lambda_0$ and in Eqs. (6.26)–(6.28) for the degenerate case $\lambda_1 = \lambda_0$ ($\lambda_1 \neq \lambda_2$). The electromagnetic fields induced by a steady point heat source at the origin of a uniaxial multiferroic full-space with the x_3 -axis being its uniaxial axis exhibit the following properties:

1. The electric and magnetic potentials as well as the horizontal electric and magnetic fields (and as a result the horizontal electric displacements and magnetic fluxes) are odd functions of x_3 , and are zero on the horizontal plane $x_3 = 0$.
2. The vertical electric and magnetic fields (and as a result the vertical electric displacements and magnetic fluxes) are even functions of x_3 , and are inversely proportional to r when $x_3 = 0$, and are zero on the x_3 -axis excluding the origin.

The Green's function solutions for two bonded multiferroic half-spaces are presented in Eqs. (6.30) and (6.31) with the twelve constants L_{ij} being determined by Eq. (6.34). We further remark that by making use of the image method discussed in Section 6.3, the point heat source induced electromagnetic Green's functions in a multiferroic half-space with

various surface electromagnetic boundary conditions [47] can also be derived, and that the influence of the temperature on the electric and magnetic fields will be pursued using the developed Green's functions.

Chapter 7

Effective Properties of Multilayered Functionally Graded Multiferroic Composites

7.1 Introduction

Functionally graded materials (FGMs) and composites possess various attractive properties and have been the fields of intensive investigation. Recently, a first-order shear deformation model was proposed for isotropic elastic FGM plate [118]. The structural stability of FGM panels under aero-thermal loads [119] and dynamic stability of FGM cylindrical shells under a period axial loading [120] were also studied numerically. While Chen et al. [121] calculated the dispersion curves for an elastic FGM plate, Yang and Chen [122] analyzed the free vibration and buckling of elastic FGM beams weakened by edge cracks. Besides the elastic FGM structures, piezoelectric FGM structures were also investigated, as in [123] where the transient piezothermoelastic behavior of an FGM thermopiezoelectric hollow sphere was studied to demonstrate the influence of the FGMs on the field quantities.

Recently, the coupling between the magnetic and electric fields has attracted wide attention in composites as this is an intrinsic fascinating property in multiferroics [39, 106, 124]. This coupling, also called magnetoelectric (ME) effect, can be described as an induced electric polarization under an external magnetic field or an induced magnetization under an external electric field. It has been found that the ME effect in artificial multiferroic composites consisting of ferromagnetic and ferroelectric phases, which is achieved through the product property, can be several orders larger than that observed in natural single-phase materials, such as the antiferromagnetic Cr_2O_3 crystal [39, 124–127]. Up to now several approaches have been developed to predict the ME effect in multiferroic particulate or laminate composites: (i) the micromechanics approach such as the Mori-Tanaka mean field method, the dilute concentration method and the self-consistent method [128, 129]; (ii) the Green's function method [130]; (iii) the method by Milgrom and Shtrikman for two-phase fibrous composites, which establishes a correspondence between the uncoupled and coupled problems [131, 132]; (iv) the method by Harshé for layered composites with 2–2 connectivity [44, 133–135]; (v) the equivalent circuit method (particularly for the analysis

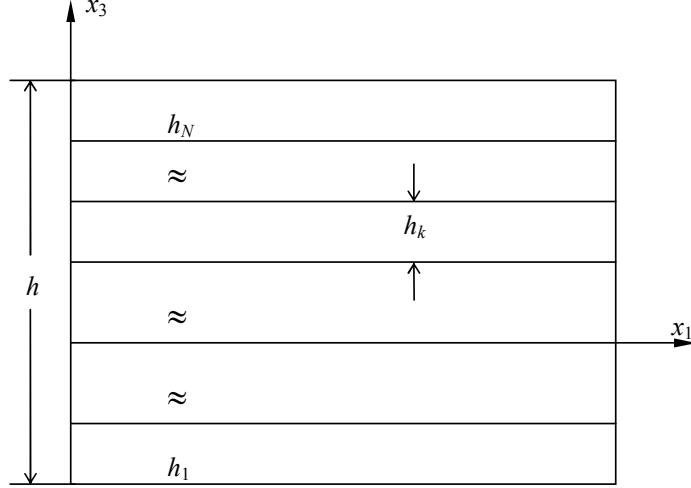


Figure 7.1: Multilayered multiferroic (2-2) composites. h_k is the thickness of the k^{th} layer, and h is the total thickness of the composite.

of the resonance ME effect) [136, 137].

In this research we extend the micromechanics approach proposed by Qu and Cherkaoui [138] to the study of the effective properties including the ME effect and the thermal properties of a magnetoelectric multiferroic multilayer composite with 2–2 connectivity of the phases, as shown in Figure 7.1. We find that this micromechanics approach is rather efficient in the sense that: (i) explicit expressions of the effective properties of the layered multiferroic composites can be obtained; (ii) the ME effect of the 2–2 type piezoelectric-magnetostrictive films on an elastic substrate can be expediently investigated and the influence of the substrate on the ME response is found to be in qualitative agreement with recent observations and calculations [106, 130, 139]; (iii) the ME effect of the multilayered FGM multiferroic composites, which have recently been successfully fabricated [53], can also be easily obtained.

7.2 Effective Properties of Multilayered Multiferroic Composites

The linear constitutive equations of a homogeneous multiferroic material can be written as

$$\begin{aligned}\sigma_{ij} &= C_{ijkl}S_{kl} - e_{kij}E_k - q_{kij}H_k - \beta_{ij}\theta \\ D_k &= e_{kij}S_{ij} + \epsilon_{kl}E_l + \alpha_{kl}H_l + p_k\theta \\ B_k &= q_{kij}S_{ij} + \alpha_{lk}E_l + \mu_{kl}H_l + m_k\theta\end{aligned}\tag{7.1}$$

where σ_{ij} and S_{ij} are the stress and strain components; D_i and E_i are the electric displacement and electric fields; B_i and H_i are the magnetic flux and magnetic fields; θ is the temperature change; C_{ijkl} , ϵ_{kl} and μ_{kl} are the elastic, the dielectric permittivity, and magnetic permeability coefficients, respectively; e_{kij} , q_{kij} and α_{kl} are the piezoelectric, piezomag-

netic and magnetoelectric coefficients, respectively; β_{ij} , p_k and m_k are the thermal stress, pyroelectric and pyromagnetic coefficients, respectively.

If we define the following vector notations:

$$\underline{\sigma}_n = \begin{bmatrix} \sigma_{33} \\ \sigma_{23} \\ \sigma_{13} \\ D_3 \\ B_3 \end{bmatrix} \quad \underline{\sigma}_t = \begin{bmatrix} \sigma_{11} \\ \sigma_{22} \\ \sigma_{12} \\ D_1 \\ D_2 \\ B_1 \\ B_2 \end{bmatrix} \quad \mathbf{S}_n = \begin{bmatrix} S_{33} \\ 2S_{23} \\ 2S_{13} \\ -E_3 \\ -H_3 \end{bmatrix} \quad \mathbf{S}_t = \begin{bmatrix} S_{11} \\ S_{22} \\ 2S_{12} \\ -E_1 \\ -E_2 \\ -H_1 \\ -H_2 \end{bmatrix} \quad (7.2)$$

then the constitutive equations (7.1) can be equivalently written the following concise matrix form

$$\underline{\sigma}_n = \mathbf{C}_{nn}\mathbf{S}_n + \mathbf{C}_{nt}\mathbf{S}_t - \underline{\beta}_n \theta \quad \underline{\sigma}_t = \mathbf{C}_{tn}\mathbf{S}_n + \mathbf{C}_{tt}\mathbf{S}_t - \underline{\beta}_t \theta \quad (7.3)$$

where \mathbf{C}_{nn} , \mathbf{C}_{nt} , \mathbf{C}_{tn} , and \mathbf{C}_{tt} are the generalized Voigt matrices given by

$$\mathbf{C}_{nn} = \mathbf{C}_{nn}^T = \begin{bmatrix} C_{33} & C_{34} & C_{35} & e_{33} & q_{33} \\ C_{34} & C_{44} & C_{45} & e_{34} & q_{34} \\ C_{35} & C_{45} & C_{55} & e_{35} & q_{35} \\ e_{33} & e_{34} & e_{35} & -\epsilon_{33} & -\alpha_{33} \\ q_{33} & q_{34} & q_{35} & -\alpha_{33} & -\mu_{33} \end{bmatrix} \quad (7.4)$$

$$\mathbf{C}_{nt} = \begin{bmatrix} C_{13} & C_{23} & C_{36} & e_{13} & e_{23} & q_{13} & q_{23} \\ C_{14} & C_{24} & C_{46} & e_{14} & e_{24} & q_{14} & q_{24} \\ C_{15} & C_{25} & C_{56} & e_{15} & e_{25} & q_{15} & q_{25} \\ e_{31} & e_{32} & e_{36} & -\epsilon_{13} & -\epsilon_{23} & -\alpha_{31} & -\alpha_{32} \\ q_{31} & q_{32} & q_{36} & -\alpha_{13} & -\alpha_{23} & -\mu_{13} & -\mu_{23} \end{bmatrix}, \quad \mathbf{C}_{tn} = \mathbf{C}_{nt}^T \quad (7.5)$$

$$\mathbf{C}_{tt} = \mathbf{C}_{tt}^T = \begin{bmatrix} C_{11} & C_{12} & C_{16} & e_{11} & e_{21} & q_{11} & q_{21} \\ C_{12} & C_{22} & C_{26} & e_{12} & e_{22} & q_{12} & q_{22} \\ C_{16} & C_{26} & C_{66} & e_{16} & e_{26} & q_{16} & q_{26} \\ e_{11} & e_{12} & e_{16} & -\epsilon_{11} & -\epsilon_{12} & -\alpha_{11} & -\alpha_{12} \\ e_{21} & e_{22} & e_{26} & -\epsilon_{12} & -\epsilon_{22} & -\alpha_{21} & -\alpha_{22} \\ q_{11} & q_{12} & q_{16} & -\alpha_{11} & -\alpha_{21} & -\mu_{11} & -\mu_{12} \\ q_{21} & q_{22} & q_{26} & -\alpha_{12} & -\alpha_{22} & -\mu_{12} & -\mu_{22} \end{bmatrix} \quad (7.6)$$

$$\underline{\beta}_n = [\beta_{33} \quad \beta_{23} \quad \beta_{13} \quad -p_3 \quad -m_3]^T \quad (7.7)$$

$$\underline{\beta}_t = [\beta_{11} \quad \beta_{22} \quad \beta_{12} \quad -p_1 \quad -p_2 \quad -m_1 \quad -m_2]^T \quad (7.8)$$

with T denoting matrix transpose. It is observed that \mathbf{C}_{nn} and \mathbf{C}_{tt} are symmetric but not positive definite. Now we consider a multiferroic multilayered composite consisting of N layers of homogeneous multiferroic materials as shown in Fig. 1. In the following we will attach a superscript “ (k) ” to the quantities associated with layer k ($k = 1, 2, \dots, N$). Therefore for the k^{th} multiferroic layer, it follows from Eq. (7.1) that

$$\underline{\sigma}_n^{(k)} = \mathbf{C}_{nn}^{(k)}\mathbf{S}_n^{(k)} + \mathbf{C}_{nt}^{(k)}\mathbf{S}_t^{(k)} - \underline{\beta}_n^{(k)}\theta^{(k)} \quad (7.9a)$$

$$\underline{\sigma}_t^{(k)} = \mathbf{C}_{tn}^{(k)}\mathbf{S}_n^{(k)} + \mathbf{C}_{tt}^{(k)}\mathbf{S}_t^{(k)} - \underline{\beta}_t^{(k)}\theta^{(k)} \quad (7.9b)$$

It is further assumed that: (i) each homogeneous layer is under a uniform state of deformation; (ii) the temperature is uniform over the whole representative volume element (RVE); (iii) the layers are perfectly bonded together, i.e., tractions, normal electric displacement, normal magnetic flux, displacements, electric potential and magnetic potential are all continuous across the layer interface. Based on these assumptions, we then have

$$\underline{\sigma}_n^{(k)} = \underline{\sigma}_n, \mathbf{S}_t^{(k)} = \mathbf{S}_t, \theta^{(k)} = \theta, \text{ for } k = 1, 2, \dots, N \quad (7.10)$$

In view of Eq. (7.10), Eq. (7.9a) can then be further cast into

$$\mathbf{S}_n^{(k)} = (\mathbf{C}_{nn}^{(k)})^{-1} \underline{\sigma}_n - (\mathbf{C}_{nn}^{(k)})^{-1} \mathbf{C}_{nt}^{(k)} \mathbf{S}_t + (\mathbf{C}_{nn}^{(k)})^{-1} \underline{\beta}_n^{(k)} \theta \quad (7.11)$$

Taking the average of $\mathbf{S}_n^{(k)}$ over the RVE, we obtain the following

$$\mathbf{S}_n = \sum_{k=1}^N v_k \mathbf{S}_n^{(k)} = \sum_{k=1}^N v_k (\mathbf{C}_{nn}^{(k)})^{-1} \underline{\sigma}_n - \sum_{k=1}^N v_k (\mathbf{C}_{nn}^{(k)})^{-1} \mathbf{C}_{nt}^{(k)} \mathbf{S}_t + \sum_{k=1}^N v_k (\mathbf{C}_{nn}^{(k)})^{-1} \underline{\beta}_n^{(k)} \theta \quad (7.12)$$

where $v_k = h_k/h$ is the volume fraction of the k th layer. By rearranging the terms in Eq. (7.12), we arrive at

$$\underline{\sigma}_n = \bar{\mathbf{C}}_{nn} \mathbf{S}_n + \bar{\mathbf{C}}_{nt} \mathbf{S}_t - \bar{\underline{\beta}}_n \theta \quad (7.13)$$

where

$$\bar{\mathbf{C}}_{nn} = \left[\sum_{k=1}^N v_k (\mathbf{C}_{nn}^{(k)})^{-1} \right]^{-1} \quad (7.14)$$

$$\bar{\mathbf{C}}_{nt} = \bar{\mathbf{C}}_{nn} \left[\sum_{k=1}^N v_k (\mathbf{C}_{nn}^{(k)})^{-1} \mathbf{C}_{nt}^{(k)} \right] \quad (7.15)$$

$$\bar{\underline{\beta}}_n = \bar{\mathbf{C}}_{nn} \sum_{k=1}^N v_k (\mathbf{C}_{nn}^{(k)})^{-1} \underline{\beta}_n^{(k)} \quad (7.16)$$

Substitution of Eq. (7.11) into Eq. (7.9b) yields

$$\begin{aligned} \underline{\sigma}_t^{(k)} &= \mathbf{C}_{tn}^{(k)} (\mathbf{C}_{nn}^{(k)})^{-1} \underline{\sigma}_n \\ &+ \left[\mathbf{C}_{tt}^{(k)} - \mathbf{C}_{tn}^{(k)} (\mathbf{C}_{nn}^{(k)})^{-1} \mathbf{C}_{nt}^{(k)} \right] \mathbf{S}_t + \left[\mathbf{C}_{tn}^{(k)} (\mathbf{C}_{nn}^{(k)})^{-1} \underline{\beta}_n^{(k)} - \underline{\beta}_t^{(k)} \right] \theta \end{aligned} \quad (7.17)$$

Taking the average of $\underline{\sigma}_t^{(k)}$ over the RVE, we then obtain

$$\begin{aligned} \underline{\sigma}_t &= \sum_{k=1}^N v_k \underline{\sigma}_t^{(k)} = \sum_{k=1}^N v_k \mathbf{C}_{tn}^{(k)} (\mathbf{C}_{nn}^{(k)})^{-1} \underline{\sigma}_n \\ &+ \sum_{k=1}^N v_k \left[\mathbf{C}_{tt}^{(k)} - \mathbf{C}_{tn}^{(k)} (\mathbf{C}_{nn}^{(k)})^{-1} \mathbf{C}_{nt}^{(k)} \right] \mathbf{S}_t + \sum_{k=1}^N v_k \left[\mathbf{C}_{tn}^{(k)} (\mathbf{C}_{nn}^{(k)})^{-1} \underline{\beta}_n^{(k)} - \underline{\beta}_t^{(k)} \right] \theta \end{aligned} \quad (7.18)$$

Substitution of Eq. (7.13) into Eq. (7.18) results in

$$\underline{\sigma}_t = \bar{\mathbf{C}}_{tn} \mathbf{S}_n + \bar{\mathbf{C}}_{tt} \mathbf{S}_t - \bar{\underline{\beta}}_t \theta \quad (7.19)$$

where

$$\bar{\mathbf{C}}_{tn} = \left[\sum_{k=1}^N v_k \mathbf{C}_{tn}^{(k)} (\mathbf{C}_{nn}^{(k)})^{-1} \right] \bar{\mathbf{C}}_{nn} \quad (7.20)$$

$$\bar{\mathbf{C}}_{tt} = \sum_{k=1}^N v_k \mathbf{C}_{tt}^{(k)} + \sum_{k=1}^N v_k \mathbf{C}_{tn}^{(k)} (\mathbf{C}_{nn}^{(k)})^{-1} (\bar{\mathbf{C}}_{nt} - \mathbf{C}_{nt}^{(k)}) \quad (7.21)$$

$$\bar{\underline{\beta}}_t = \sum_{k=1}^N v_k \underline{\beta}_t^{(k)} + \sum_{k=1}^N v_k \mathbf{C}_{tn}^{(k)} (\mathbf{C}_{nn}^{(k)})^{-1} (\bar{\underline{\beta}}_n - \underline{\beta}_n^{(k)}) \quad (7.22)$$

It can be easily proved that the following symmetry properties exist

$$\bar{\mathbf{C}}_{nn} = \bar{\mathbf{C}}_{nn}^T \quad \bar{\mathbf{C}}_{tt} = \bar{\mathbf{C}}_{tt}^T \quad \bar{\mathbf{C}}_{tn} = \bar{\mathbf{C}}_{nt}^T \quad (7.23)$$

Now the effective properties of the multilayered multiferroic composite have been completely determined. It is observed that the above derivations are basically an extension of the approach proposed by Qu and Cherkaoui [138] to multiferroic composites including also the thermal effect. Next we present three practical cases as applications of the above formulas, which further demonstrate the efficiency and versatility of the proposed approach.

7.3 Applications

7.3.1 Effective properties of a multiferroic composite composed of an orthotropic piezoelectric phase and an orthotropic magnetostrictive phase

By using Eqs. (7.14)–(7.16) and (7.20)–(7.22), the effective properties of the orthotropic piezoelectric-magnetostrictive bilayer composite as shown in Figure 7.2 can be explicitly determined as follows.

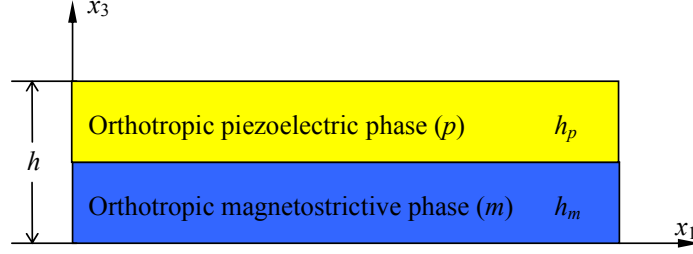


Figure 7.2: A multiferroic composite composed of an orthotropic piezoelectric phase and an orthotropic magnetostrictive phase.

The nonzero components of $\bar{\mathbf{C}}_{nn}$:

$$\begin{aligned}
 \bar{C}_{33} &= \frac{1}{\Delta} \left(\frac{v_p C_{33}^{(p)}}{\epsilon_{33}^{(p)} \tilde{C}_{33}^{(p)}} + \frac{v_m}{\epsilon_{33}^{(m)}} \right) \left(\frac{v_m C_{33}^{(m)}}{\mu_{33}^{(m)} \tilde{C}_{33}^{(m)}} + \frac{v_p}{\mu_{33}^{(p)}} \right) \\
 \bar{C}_{44} &= \frac{C_{44}^{(p)} C_{44}^{(m)}}{v_p C_{44}^{(m)} + v_m C_{44}^{(p)}} \\
 \bar{C}_{55} &= \frac{C_{55}^{(p)} C_{55}^{(m)}}{v_p C_{55}^{(m)} + v_m C_{55}^{(p)}} \\
 \bar{e}_{33} &= \frac{v_p e_{33}}{\Delta \epsilon_{33}^{(p)} \tilde{C}_{33}^{(p)}} \left(\frac{v_m C_{33}^{(m)}}{\mu_{33}^{(m)} \tilde{C}_{33}^{(m)}} + \frac{v_p}{\mu_{33}^{(p)}} \right) \\
 \bar{q}_{33} &= \frac{v_m q_{33}}{\Delta \mu_{33}^{(m)} \tilde{C}_{33}^{(m)}} \left(\frac{v_p C_{33}^{(p)}}{\epsilon_{33}^{(p)} \tilde{C}_{33}^{(p)}} + \frac{v_m}{\epsilon_{33}^{(m)}} \right) \\
 \bar{\epsilon}_{33} &= \frac{1}{\Delta} \left[\left(\frac{v_p}{\tilde{C}_{33}^{(p)}} + \frac{v_m}{\tilde{C}_{33}^{(m)}} \right) \left(\frac{v_m C_{33}^{(m)}}{\mu_{33}^{(m)} \tilde{C}_{33}^{(m)}} + \frac{v_p}{\mu_{33}^{(p)}} \right) + \frac{v_m^2 q_{33}^2}{(\mu_{33}^{(m)})^2 (\tilde{C}_{33}^{(m)})^2} \right] \\
 \bar{\mu}_{33} &= \frac{1}{\Delta} \left[\left(\frac{v_p}{\tilde{C}_{33}^{(p)}} + \frac{v_m}{\tilde{C}_{33}^{(m)}} \right) \left(\frac{v_p C_{33}^{(p)}}{\epsilon_{33}^{(p)} \tilde{C}_{33}^{(p)}} + \frac{v_m}{\epsilon_{33}^{(m)}} \right) + \frac{v_p^2 e_{33}^2}{(\epsilon_{33}^{(p)})^2 (\tilde{C}_{33}^{(p)})^2} \right] \\
 \bar{\alpha}_{33} &= -\frac{v_p v_m e_{33} q_{33}}{\epsilon_{33}^{(p)} \mu_{33}^{(m)} \tilde{C}_{33}^{(p)} \tilde{C}_{33}^{(m)} \Delta}
 \end{aligned} \tag{7.24}$$

where $\tilde{C}_{33}^{(p)} = C_{33}^{(p)} + e_{33}^2 / \epsilon_{33}^{(p)}$ and $\tilde{C}_{33}^{(m)} = C_{33}^{(m)} + q_{33}^2 / \mu_{33}^{(m)}$ are respectively the piezoelectrically and piezomagnetically stiffened elastic constants, and

$$\begin{aligned}
 \Delta &= \left(\frac{v_p}{\tilde{C}_{33}^{(p)}} + \frac{v_m}{\tilde{C}_{33}^{(m)}} \right) \left(\frac{v_p C_{33}^{(p)}}{\epsilon_{33}^{(p)} \tilde{C}_{33}^{(p)}} + \frac{v_m}{\epsilon_{33}^{(m)}} \right) \left(\frac{v_m C_{33}^{(m)}}{\mu_{33}^{(m)} \tilde{C}_{33}^{(m)}} + \frac{v_p}{\mu_{33}^{(p)}} \right) \\
 &+ \frac{v_m^2 q_{33}^2}{(\mu_{33}^{(m)})^2 (\tilde{C}_{33}^{(m)})^2} \left(\frac{v_p C_{33}^{(p)}}{\epsilon_{33}^{(p)} \tilde{C}_{33}^{(p)}} + \frac{v_m}{\epsilon_{33}^{(m)}} \right) + \frac{v_p^2 e_{33}^2}{(\epsilon_{33}^{(p)})^2 (\tilde{C}_{33}^{(p)})^2} \left(\frac{v_m C_{33}^{(m)}}{\mu_{33}^{(m)} \tilde{C}_{33}^{(m)}} + \frac{v_p}{\mu_{33}^{(p)}} \right)
 \end{aligned} \tag{7.25}$$

The nonzero components of $\bar{\mathbf{C}}_m (= \bar{\mathbf{C}}_m^T)$:

$$\begin{aligned}
\bar{C}_{13} &= \frac{v_p \left[\bar{C}_{33}(\epsilon_{33}^{(p)} C_{13}^{(p)} + e_{33} e_{31}) + \bar{e}_{33}(e_{33} C_{13}^{(p)} - e_{31} C_{33}^{(p)}) \right]}{\epsilon_{33}^{(p)} \tilde{C}_{33}^{(p)}} \\
&\quad + \frac{v_m \left[\bar{C}_{33}(\mu_{33}^{(m)} C_{13}^{(m)} + q_{33} q_{31}) + \bar{q}_{33}(q_{33} C_{13}^{(m)} - q_{31} C_{33}^{(m)}) \right]}{\mu_{33}^{(m)} \tilde{C}_{33}^{(m)}} \\
\bar{C}_{23} &= \frac{v_p \left[\bar{C}_{33}(\epsilon_{33}^{(p)} C_{23}^{(p)} + e_{33} e_{32}) + \bar{e}_{33}(e_{33} C_{23}^{(p)} - e_{32} C_{33}^{(p)}) \right]}{\epsilon_{33}^{(p)} \tilde{C}_{33}^{(p)}} \\
&\quad + \frac{v_m \left[\bar{C}_{33}(\mu_{33}^{(m)} C_{23}^{(m)} + q_{33} q_{32}) + \bar{q}_{33}(q_{32} C_{33}^{(m)} - q_{33} C_{23}^{(m)}) \right]}{\mu_{33}^{(m)} \tilde{C}_{33}^{(m)}},
\end{aligned} \tag{7.26a}$$

$$\bar{e}_{24} = \frac{v_p e_{24} \bar{C}_{44}}{C_{44}^{(p)}} \quad \bar{e}_{15} = \frac{v_p e_{15} \bar{C}_{55}}{C_{55}^{(p)}}, \quad \bar{q}_{24} = \frac{v_m q_{24} \bar{C}_{44}}{C_{44}^{(m)}} \quad \bar{q}_{15} = \frac{v_m q_{15} \bar{C}_{55}}{C_{55}^{(m)}} \tag{7.26b}$$

$$\begin{aligned}
\bar{e}_{31} &= \frac{v_p \left[\bar{e}_{33}(\epsilon_{33}^{(p)} C_{13}^{(p)} + e_{33} e_{31}) + \bar{\epsilon}_{33}(e_{31} C_{33}^{(p)} - e_{33} C_{13}^{(p)}) \right]}{\epsilon_{33}^{(p)} \tilde{C}_{33}^{(p)}} \\
&\quad + \frac{v_m \left[\bar{e}_{33}(\mu_{33}^{(m)} C_{13}^{(m)} + q_{33} q_{31}) + \bar{\alpha}_{33}(q_{33} C_{13}^{(m)} - q_{31} C_{33}^{(m)}) \right]}{\mu_{33}^{(m)} \tilde{C}_{33}^{(m)}} \\
\bar{e}_{32} &= \frac{v_p \left[\bar{e}_{33}(\epsilon_{33}^{(p)} C_{23}^{(p)} + e_{33} e_{32}) + \bar{\epsilon}_{33}(e_{32} C_{33}^{(p)} - e_{33} C_{23}^{(p)}) \right]}{\epsilon_{33}^{(p)} \tilde{C}_{33}^{(p)}} \\
&\quad + \frac{v_m \left[\bar{e}_{33}(\mu_{33}^{(m)} C_{23}^{(m)} + q_{33} q_{32}) + \bar{\alpha}_{33}(q_{32} C_{33}^{(m)} - q_{33} C_{23}^{(m)}) \right]}{\mu_{33}^{(m)} \tilde{C}_{33}^{(m)}} \\
\bar{q}_{31} &= \frac{v_p \left[\bar{q}_{33}(\epsilon_{33}^{(p)} C_{13}^{(p)} + e_{33} e_{31}) + \bar{\alpha}_{33}(e_{31} C_{33}^{(p)} - e_{33} C_{13}^{(p)}) \right]}{\epsilon_{33}^{(p)} \tilde{C}_{33}^{(p)}} \\
&\quad + \frac{v_m \left[\bar{q}_{33}(\mu_{33}^{(m)} C_{13}^{(m)} + q_{33} q_{31}) + \bar{\mu}_{33}(q_{31} C_{33}^{(m)} - q_{33} C_{13}^{(m)}) \right]}{\mu_{33}^{(m)} \tilde{C}_{33}^{(m)}} \\
\bar{q}_{32} &= \frac{v_p \left[\bar{q}_{33}(\epsilon_{33}^{(p)} C_{23}^{(p)} + e_{33} e_{32}) + \bar{\alpha}_{33}(e_{32} C_{33}^{(p)} - e_{33} C_{23}^{(p)}) \right]}{\epsilon_{33}^{(p)} \tilde{C}_{33}^{(p)}} \\
&\quad + \frac{v_m \left[\bar{q}_{33}(\mu_{33}^{(m)} C_{23}^{(m)} + q_{33} q_{32}) + \bar{\mu}_{33}(q_{32} C_{33}^{(m)} - q_{33} C_{23}^{(m)}) \right]}{\mu_{33}^{(m)} \tilde{C}_{33}^{(m)}}
\end{aligned} \tag{7.26c}$$

The nonzero components of $\bar{\mathbf{C}}_{tt}$:

$$\begin{aligned}
\bar{C}_{11} &= v_p C_{11}^{(p)} + v_m C_{11}^{(m)} + \frac{v_p}{\epsilon_{33}^{(p)} \bar{C}_{33}^{(p)}} \left[\epsilon_{33}^{(p)} C_{13}^{(p)} (\bar{C}_{13} - C_{13}^{(p)}) + e_{33} C_{13}^{(p)} (\bar{e}_{31} - e_{31}) \right. \\
&\quad \left. + e_{33} e_{31} (\bar{C}_{13} - C_{13}^{(p)}) - e_{31} (\bar{e}_{31} - e_{31}) C_{33}^{(p)} \right] \\
&\quad + \frac{v_m}{\mu_{33}^{(m)} \bar{C}_{33}^{(m)}} \left[\mu_{33}^{(m)} C_{13}^{(m)} (\bar{C}_{13} - C_{13}^{(m)}) + q_{33} C_{13}^{(m)} (\bar{q}_{31} - q_{31}) \right. \\
&\quad \left. + q_{33} q_{31} (\bar{C}_{13} - C_{13}^{(m)}) - q_{31} C_{33}^{(m)} (\bar{q}_{31} - q_{31}) \right] \\
\bar{C}_{12} &= v_p C_{12}^{(p)} + v_m C_{12}^{(m)} + \frac{v_p}{\epsilon_{33}^{(p)} \bar{C}_{33}^{(p)}} \left[\epsilon_{33}^{(p)} C_{13}^{(p)} (\bar{C}_{23} - C_{23}^{(p)}) + e_{33} C_{13}^{(p)} (\bar{e}_{32} - e_{32}) \right. \\
&\quad \left. + e_{33} e_{31} (\bar{C}_{23} - C_{23}^{(p)}) - e_{31} (\bar{e}_{32} - e_{32}) C_{33}^{(p)} \right] \\
&\quad + \frac{v_m}{\mu_{33}^{(m)} \bar{C}_{33}^{(m)}} \left[\mu_{33}^{(m)} C_{13}^{(m)} (\bar{C}_{23} - C_{23}^{(m)}) + q_{33} C_{13}^{(m)} (\bar{q}_{32} - q_{32}) \right. \\
&\quad \left. + q_{33} q_{31} (\bar{C}_{23} - C_{23}^{(m)}) - q_{31} C_{33}^{(m)} (\bar{q}_{32} - q_{32}) \right] \\
\bar{C}_{22} &= v_p C_{22}^{(p)} + v_m C_{22}^{(m)} + \frac{v_p}{\epsilon_{33}^{(p)} \bar{C}_{33}^{(p)}} \left[\epsilon_{33}^{(p)} C_{23}^{(p)} (\bar{C}_{23} - C_{23}^{(p)}) + e_{33} C_{23}^{(p)} (\bar{e}_{32} - e_{32}) \right. \\
&\quad \left. + e_{33} e_{32} (\bar{C}_{23} - C_{23}^{(p)}) - e_{32} (\bar{e}_{32} - e_{32}) C_{33}^{(p)} \right] \\
&\quad + \frac{v_m}{\mu_{33}^{(m)} \bar{C}_{33}^{(m)}} \left[\mu_{33}^{(m)} C_{23}^{(m)} (\bar{C}_{23} - C_{23}^{(m)}) + q_{33} C_{23}^{(m)} (\bar{q}_{32} - q_{32}) \right. \\
&\quad \left. + q_{33} q_{32} (\bar{C}_{23} - C_{23}^{(m)}) - q_{32} C_{33}^{(m)} (\bar{q}_{32} - q_{32}) \right] \\
\bar{C}_{66} &= v_p C_{66}^{(p)} + v_m C_{66}^{(m)}
\end{aligned} \tag{7.27a}$$

$$\begin{aligned}
\bar{\epsilon}_{11} &= v_p \epsilon_{11}^{(p)} + v_m \epsilon_{11}^{(m)} + \frac{v_p v_m e_{15}^2}{v_p C_{55}^{(m)} + v_m C_{55}^{(p)}} \\
\bar{\epsilon}_{22} &= v_p \epsilon_{22}^{(p)} + v_m \epsilon_{22}^{(m)} + \frac{v_p v_m e_{24}^2}{v_p C_{44}^{(m)} + v_m C_{44}^{(p)}} \\
\bar{\mu}_{11} &= v_p \mu_{11}^{(p)} + v_m \mu_{11}^{(m)} + \frac{v_p v_m q_{15}^2}{v_p C_{55}^{(m)} + v_m C_{55}^{(p)}} \\
\bar{\mu}_{22} &= v_p \mu_{22}^{(p)} + v_m \mu_{22}^{(m)} + \frac{v_p v_m q_{24}^2}{v_p C_{44}^{(m)} + v_m C_{44}^{(p)}} \\
\bar{\alpha}_{11} &= -\frac{v_p v_m e_{15} q_{15}}{v_p C_{55}^{(m)} + v_m C_{55}^{(p)}} \quad \bar{\alpha}_{22} = -\frac{v_p v_m e_{24} q_{24}}{v_p C_{44}^{(m)} + v_m C_{44}^{(p)}}
\end{aligned} \tag{7.27b}$$

The nonzero components of $\underline{\tilde{\beta}}_n$:

$$\begin{aligned}
\bar{\beta}_{33} &= \frac{v_p \left[(\epsilon_{33}^{(p)} \bar{C}_{33} + e_{33} \bar{e}_{33}) \beta_{33}^{(p)} + (\bar{e}_{33} C_{33}^{(p)} - e_{33} \bar{C}_{33}) p_3^{(p)} \right]}{\epsilon_{33}^{(p)} \tilde{C}_{33}^{(p)}} \\
&\quad + \frac{v_m \left[(\mu_{33}^{(m)} \bar{C}_{33} + q_{33} \bar{q}_{33}) \beta_{33}^{(m)} + (\bar{q}_{33} C_{33}^{(m)} - q_{33} \bar{C}_{33}) m_3^{(m)} \right]}{\mu_{33}^{(m)} \tilde{C}_{33}^{(m)}} \\
&\quad + \frac{v_p \bar{q}_{33} m_3^{(p)}}{\mu_{33}^{(p)}} + \frac{v_m \bar{e}_{33} p_3^{(m)}}{\epsilon_{33}^{(m)}} \\
\bar{p}_3 &= \frac{v_p \left[(\bar{e}_{33} C_{33}^{(p)} + e_{33} \bar{e}_{33}) p_3^{(p)} + (\bar{e}_{33} e_{33} - \epsilon_{33}^{(p)} \bar{e}_{33}) \beta_{33}^{(p)} \right]}{\epsilon_{33}^{(p)} \tilde{C}_{33}^{(p)}} \\
&\quad + \frac{v_m \left[(\bar{\alpha}_{33} C_{33}^{(m)} + q_{33} \bar{e}_{33}) m_3^{(m)} + (\bar{\alpha}_{33} q_{33} - \mu_{33}^{(m)} \bar{e}_{33}) \beta_{33}^{(m)} \right]}{\mu_{33}^{(m)} \tilde{C}_{33}^{(m)}} \\
&\quad + \frac{v_p \bar{\alpha}_{33} m_3^{(p)}}{\mu_{33}^{(p)}} + \frac{v_m \bar{e}_{33} p_3^{(m)}}{\epsilon_{33}^{(m)}} \\
\bar{m}_3 &= \frac{v_p \left[(\bar{\alpha}_{33} C_{33}^{(p)} + e_{33} \bar{q}_{33}) p_3^{(p)} + (\bar{\alpha}_{33} e_{33} - \epsilon_{33}^{(p)} \bar{q}_{33}) \beta_{33}^{(p)} \right]}{\epsilon_{33}^{(p)} \tilde{C}_{33}^{(p)}} \\
&\quad + \frac{v_m \left[(\bar{\mu}_{33} C_{33}^{(m)} + q_{33} \bar{q}_{33}) m_3^{(m)} + (\bar{\mu}_{33} q_{33} - \mu_{33}^{(m)} \bar{q}_{33}) \beta_{33}^{(m)} \right]}{\mu_{33}^{(m)} \tilde{C}_{33}^{(m)}} \\
&\quad + \frac{v_p \bar{\mu}_{33} m_3^{(p)}}{\mu_{33}^{(p)}} + \frac{v_m \bar{\alpha}_{33} p_3^{(m)}}{\epsilon_{33}^{(m)}}
\end{aligned} \tag{7.28}$$

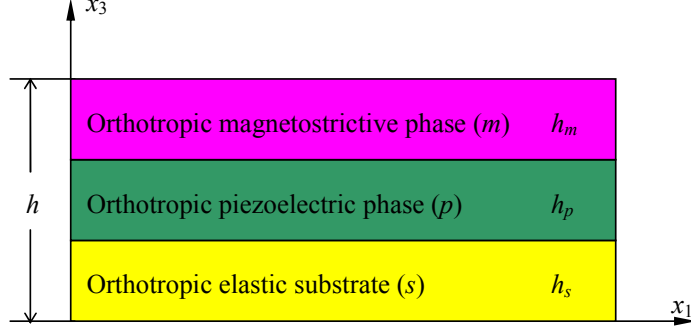


Figure 7.3: A multiferroic composite composed of an orthotropic piezoelectric phase, an orthotropic magnetostrictive phase and an orthotropic elastic substrate.

The nonzero components of $\underline{\bar{\beta}}_t$:

$$\begin{aligned}
\bar{\beta}_{11} &= v_p \beta_{11}^{(p)} + v_m \beta_{11}^{(m)} \\
&+ \frac{v_p \left[(\epsilon_{33}^{(p)} C_{13}^{(p)} + e_{33} e_{31}) (\bar{\beta}_{33} - \beta_{33}^{(p)}) + (e_{31} C_{33}^{(p)} - e_{33} C_{13}^{(p)}) (\bar{p}_3 - p_3^{(p)}) \right]}{\epsilon_{33}^{(p)} \tilde{C}_{33}^{(p)}} \\
&+ \frac{v_m \left[(\mu_{33}^{(m)} C_{13}^{(m)} + q_{33} q_{31}) (\bar{\beta}_{33} - \beta_{33}^{(m)}) + (q_{31} C_{33}^{(m)} - q_{33} C_{13}^{(m)}) (\bar{m}_3 - m_3^{(m)}) \right]}{\mu_{33}^{(m)} \tilde{C}_{33}^{(m)}} \\
\bar{\beta}_{22} &= v_p \beta_{22}^{(p)} + v_m \beta_{22}^{(m)} \\
&+ \frac{v_p \left[(\epsilon_{33}^{(p)} C_{23}^{(p)} + e_{33} e_{32}) (\bar{\beta}_{33} - \beta_{33}^{(p)}) + (e_{32} C_{33}^{(p)} - e_{33} C_{23}^{(p)}) (\bar{p}_3 - p_3^{(p)}) \right]}{\epsilon_{33}^{(p)} \tilde{C}_{33}^{(p)}} \\
&+ \frac{v_m \left[(\mu_{33}^{(m)} C_{23}^{(m)} + q_{33} q_{32}) (\bar{\beta}_{33} - \beta_{33}^{(m)}) + (q_{32} C_{33}^{(m)} - q_{33} C_{23}^{(m)}) (\bar{m}_3 - m_3^{(m)}) \right]}{\mu_{33}^{(m)} \tilde{C}_{33}^{(m)}}
\end{aligned} \tag{7.29}$$

It is of interest to point out that our numerical results for the multiferroic BaTiO₃-CoFe₂O₄ layered composite (the material properties of BaTiO₃ and CoFe₂O₄ are taken from Ref. 140) based on the above formulas are in agreement with Figures 3–5 in Ref. [129], while the values of ME coefficient $\bar{\alpha}_{11}$ are twice of those in Figure 2 of Ref. 129.

7.3.2 Effective properties of a multiferroic composite composed of an orthotropic piezoelectric phase, an orthotropic magnetostrictive phase, and an orthotropic elastic substrate

We next consider the orthotropic piezoelectric-magnetostrictive bilayer film on an orthotropic elastic substrate, as shown in Figure 7.3. Here we are particularly interested in the influence of the elastic substrate on the ME effect. Using Eqs. (7.14)–(7.16) and (7.20)–(7.22), we can arrive at the following concise expressions for the three effective ME coefficients $\bar{\alpha}_{11}$,

$\bar{\alpha}_{22}$, and $\bar{\alpha}_{33}$

$$\bar{\alpha}_{11} = -\frac{v_p v_m e_{15} q_{15}}{v_p C_{55}^{(m)} + v_m C_{55}^{(p)} + v_s \frac{C_{55}^{(p)} C_{55}^{(m)}}{C_{55}^{(s)}}} \quad (7.30)$$

$$\bar{\alpha}_{22} = -\frac{v_p v_m e_{24} q_{24}}{v_p C_{44}^{(m)} + v_m C_{44}^{(p)} + v_s \frac{C_{44}^{(p)} C_{44}^{(m)}}{C_{44}^{(s)}}} \quad (7.31)$$

$$\bar{\alpha}_{33} = -\frac{v_p v_m e_{33} q_{33}}{\epsilon_{33}^{(p)} \mu_{33}^{(m)} \tilde{C}_{33}^{(p)} \tilde{C}_{33}^{(m)} \Delta_1}, \quad (7.32)$$

where

$$\begin{aligned} \Delta_1 = & \left(\frac{v_p}{\tilde{C}_{33}^{(p)}} + \frac{v_m}{\tilde{C}_{33}^{(m)}} + \frac{v_s}{C_{33}^{(s)}} \right) \left(\frac{v_p C_{33}^{(p)}}{\epsilon_{33}^{(p)} \tilde{C}_{33}^{(p)}} + \frac{v_m}{\epsilon_{33}^{(m)}} + \frac{v_s}{\epsilon_{33}^{(s)}} \right) \left(\frac{v_m C_{33}^{(m)}}{\mu_{33}^{(m)} \tilde{C}_{33}^{(m)}} + \frac{v_p}{\mu_{33}^{(p)}} + \frac{v_s}{\mu_{33}^{(s)}} \right) \\ & + \frac{v_p^2 e_{33}^2}{(\epsilon_{33}^{(p)})^2 (\tilde{C}_{33}^{(p)})^2} \left(\frac{v_m C_{33}^{(m)}}{\mu_{33}^{(m)} \tilde{C}_{33}^{(m)}} + \frac{v_p}{\mu_{33}^{(p)}} + \frac{v_s}{\mu_{33}^{(s)}} \right) \\ & + \frac{v_m^2 q_{33}^2}{(\mu_{33}^{(m)})^2 (\tilde{C}_{33}^{(m)})^2} \left(\frac{v_p C_{33}^{(p)}}{\epsilon_{33}^{(p)} \tilde{C}_{33}^{(p)}} + \frac{v_m}{\epsilon_{33}^{(m)}} + \frac{v_s}{\epsilon_{33}^{(s)}} \right) \end{aligned} \quad (7.33)$$

It is observed from Eqs. (7.30)–(7.33) that the existence of the elastic substrate will always cause a drop in the ME effect, which is in qualitative agreement with recent observations and calculations [106, 130, 139]. In order to demonstrate clearly the influence of the substrate on the ME effect, we show in Figs. 4 and 5 the dependence of the ME coefficients $\bar{\alpha}_{11}$ and $\bar{\alpha}_{33}$ on the BaTiO₃ volume fraction $v = v_p/(v_p + v_m)$ for a series of the substrate volume fraction $\bar{v}_s = v_s/(v_p + v_m)$. During the calculation the magnetostrictive phase is CoFe₂O₄, and the pertinent material properties of the elastic substrate are: $C_{33}^{(s)} = 195 \times 10^9 \text{ N/m}^2$, $C_{44}^{(s)} = C_{55}^{(s)} = 65 \times 10^9 \text{ N/m}^2$, $\epsilon_{33}^{(s)} = 9.6\epsilon_0$, $\mu_{33}^{(s)} = 10\mu_0$. A dramatic, factor-of-2 decrease in $\bar{\alpha}_{11}$ (see Figure 7.4) and a more dramatic, factor-of-3 decrease in $\bar{\alpha}_{33}$ (see Figure 7.5) are observed when the BaTiO₃-CoFe₂O₄ film is deposited on the elastic substrate with a volume fraction of only 50% of the film. Further increase in the substrate volume v_s leads to continuous decreases in $\bar{\alpha}_{11}$ and $\bar{\alpha}_{33}$, and the ME coupling eventually vanishes when the volume of the elastic substrate of volume is roughly 10 times of the film volume.

7.3.3 Effective properties of a multiferroic composite composed of an orthotropic FGM piezoelectric phase and an orthotropic FGM magnetostrictive phase

Finally, we consider an orthotropic FGM piezoelectric phase located in the domain of $0 \leq x_3 \leq h_p$ which is perfectly bonded to an orthotropic FGM magnetostrictive phase located in the domain of $-h_m \leq x_3 \leq 0$, as shown in Figure 7.6. Furthermore we assume that the

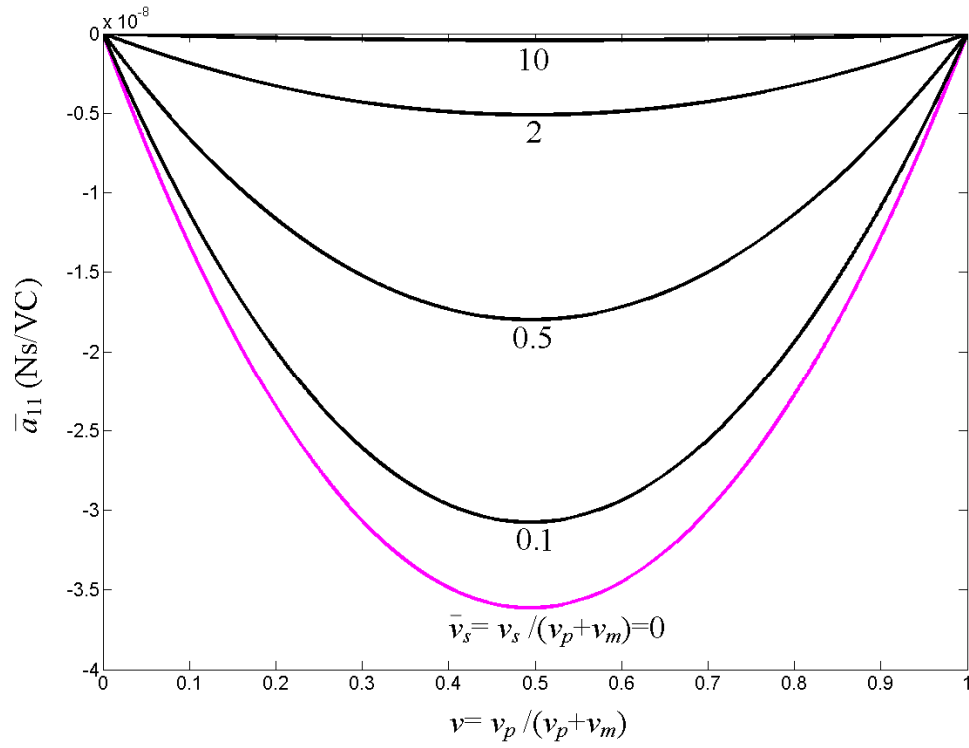


Figure 7.4: Variation of the ME coefficient \bar{a}_{11} vs. the BaTiO_3 volume fraction for a series of the substrate volume fraction \bar{v}_s . The multiferroic composite is composed of a CoFe_2O_4 – BaTiO_3 bilayer on an elastic substrate.

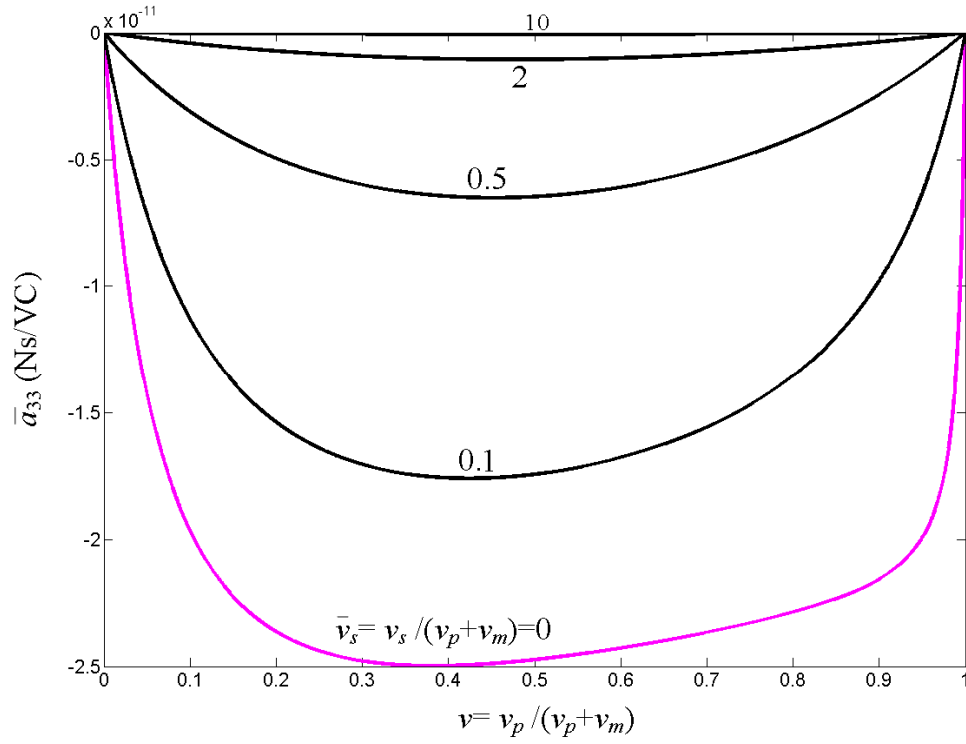


Figure 7.5: Variation of the ME coefficient \bar{a}_{33} vs. the BaTiO_3 volume fraction for a series of the substrate volume fraction \bar{v}_s . The multiferroic composite is composed of a CoFe_2O_4 – BaTiO_3 bilayer on an elastic substrate.

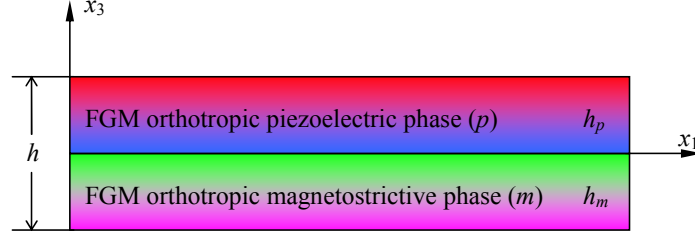


Figure 7.6: A multiferroic composite composed of a functionally graded orthotropic piezoelectric phase and a functionally graded orthotropic magnetostrictive phase.

material properties of the FGM piezoelectric and magnetostrictive phases vary along the thickness direction as

$$\begin{bmatrix} C_{ij}^{(p)}(x_3) & \epsilon_{ij}^{(p)}(x_3) & e_{ij}(x_3) \end{bmatrix} = f(x_3) \begin{bmatrix} C_{ij}^{0(p)} & \epsilon_{ij}^{0(p)} & e_{ij}^0 \end{bmatrix} \quad (7.34)$$

for $0 \leq x_3 \leq h_p$, and

$$\begin{bmatrix} C_{ij}^{(m)}(x_3) & \mu_{ij}^{(m)}(x_3) & q_{ij}(x_3) \end{bmatrix} = g(x_3) \begin{bmatrix} C_{ij}^{0(m)} & \mu_{ij}^{0(m)} & q_{ij}^0 \end{bmatrix} \quad (7.35)$$

for $-h_m \leq x_3 \leq 0$, where $C_{ij}^{0(p)}$, $\epsilon_{ij}^{0(p)}$, e_{ij}^0 , and $C_{ij}^{0(m)}$, $\mu_{ij}^{0(m)}$, q_{ij}^0 are the corresponding material constants at $x_3 = 0$. Apparently $f(0) = g(0) = 1$.

When calculating the effective properties, we can divide the two FGM phases into many thin homogeneous layers. By using Eqs. (7.14)–(7.16) and (7.20)–(7.22) and taking the limit (i.e., letting the thickness of the thin layer approach zero), the two in-plane effective ME coefficients $\bar{\alpha}_{11}$ and $\bar{\alpha}_{22}$ can be finally derived as

$$\begin{aligned} \bar{\alpha}_{11} &= -\frac{v_p v_m e_{15}^0 q_{15}^0}{C_{55}^{0(m)} h^{-1} \int_0^{h_p} \frac{dx}{f(x)} + C_{55}^{0(p)} h^{-1} \int_0^{h_m} \frac{dx}{g(-x)}} \\ \bar{\alpha}_{22} &= -\frac{v_p v_m e_{24}^0 q_{24}^0}{C_{44}^{(m)} h^{-1} \int_0^{h_p} \frac{dx}{f(x)} + C_{44}^{0(p)} h^{-1} \int_0^{h_m} \frac{dx}{g(-x)}} \end{aligned} \quad (7.36)$$

It is clear that one need only to carry out two line integrals in order to arrive at the two ME coefficients.

In the following we consider two specific examples: (i) When both $f(x_3)$ and $g(x_3)$ are linear functions of x_3 described by

$$f(x_3) = 1 + \lambda_p \tilde{x}_3 \quad g(x_3) = 1 - \lambda_m \tilde{x}_3 \quad (7.37)$$

where $\lambda_p > -1/v_p$, $\lambda_m > -1/v_m$, $\tilde{x}_3 = x_3/h$, and λ_p and λ_m are two dimensionless material constants. Then we have

$$\begin{aligned} \bar{\alpha}_{11} &= -\frac{v_p v_m e_{15}^0 q_{15}^0}{\lambda_p^{-1} \ln(1 + \lambda_p v_p) C_{55}^{0(m)} + \lambda_m^{-1} \ln(1 + \lambda_m v_m) C_{55}^{0(p)}} \\ \bar{\alpha}_{22} &= -\frac{v_p v_m e_{24}^0 q_{24}^0}{\lambda_p^{-1} \ln(1 + \lambda_p v_p) C_{44}^{0(m)} + \lambda_m^{-1} \ln(1 + \lambda_m v_m) C_{44}^{0(p)}} \end{aligned} \quad (7.38)$$

(ii) When both $f(x_3)$ and $g(x_3)$ are exponential functions of x_3 described by

$$f(x_3) = \exp(\lambda_p \tilde{x}_3) \quad g(x_3) = \exp(-\lambda_m \tilde{x}_3) \quad (7.39)$$

then we have

$$\begin{aligned} \bar{\alpha}_{11} &= - \frac{v_p v_m e_{15}^0 q_{15}^0}{\lambda_p^{-1} [1 - \exp(-\lambda_p v_p)] C_{55}^{0(m)} + \lambda_m^{-1} [1 - \exp(-\lambda_m v_m)] C_{55}^{0(p)}} \\ \bar{\alpha}_{22} &= - \frac{v_p v_m e_{24}^0 q_{24}^0}{\lambda_p^{-1} [1 - \exp(-\lambda_p v_p)] C_{44}^{0(m)} + \lambda_m^{-1} [1 - \exp(-\lambda_m v_m)] C_{44}^{0(p)}} \end{aligned} \quad (7.40)$$

We demonstrate in Figures 7.7 and 7.8 the ME coefficient $\bar{\alpha}_{11}$ as a function of the BaTiO₃ volume fraction v_p and the gradient parameter λ_p for a linearly and exponentially varied FGM BaTiO₃ bonded to a homogeneous CoFe₂O₄ layer. During the calculation the material properties of the FGM BaTiO₃ at $x_3 = 0$ are again taken from Ref. 140. It is observed that for both linearly and exponentially varied FGM BaTiO₃ the ME effect can be significantly enhanced when $\lambda_p > 0$ whilst it is reduced when $\lambda_p < 0$. It is also interesting to observe from Figure 7.8 that the ME effect will reach a minimum when $\lambda_p \leq -20$ for an exponentially varied FGM BaTiO₃.

7.4 Conclusion

Theoretical modeling of the effective properties including the ME effect of multiferroic 2–2 connectivity composites has been rigorously developed based on the micromechanics scheme originally proposed by Qu and Cherkaoui [138] for multilayered elastic composites. As applications we first presented the explicit expressions for all the effective moduli of the multiferroic composite composed of an orthotropic piezoelectric phase and an orthotropic magnetostrictive phase. We then derived the three effective ME coefficients $\bar{\alpha}_{11}$, $\bar{\alpha}_{22}$, and $\bar{\alpha}_{33}$ for the multiferroic composite composed of an orthotropic piezoelectric phase, an orthotropic magnetostrictive phase and an orthotropic elastic substrate. Finally, we presented the two in-plane effective ME coefficients $\bar{\alpha}_{11}$ and $\bar{\alpha}_{22}$ for the multiferroic composite composed of an orthotropic FGM piezoelectric phase and an orthotropic FGM magnetostrictive phase. In addition, for the reduced simple cases, our results are in agreement with recent experimental observations and theoretical studies [106, 129, 130, 139].

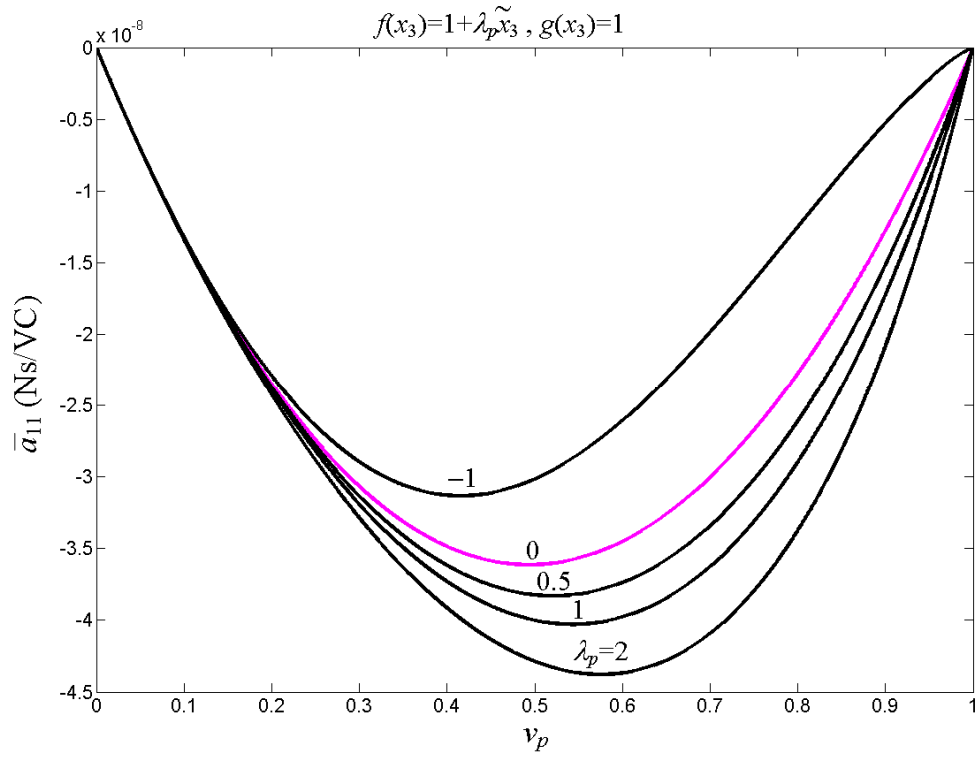


Figure 7.7: Variation of the ME coefficient \bar{a}_{11} vs. the FGM BaTiO₃ volume fraction v_p for a series gradient parameter λ_p with a linearly varied FGM BaTiO₃ bonded to a homogeneous CoFe₂O₄ layer.

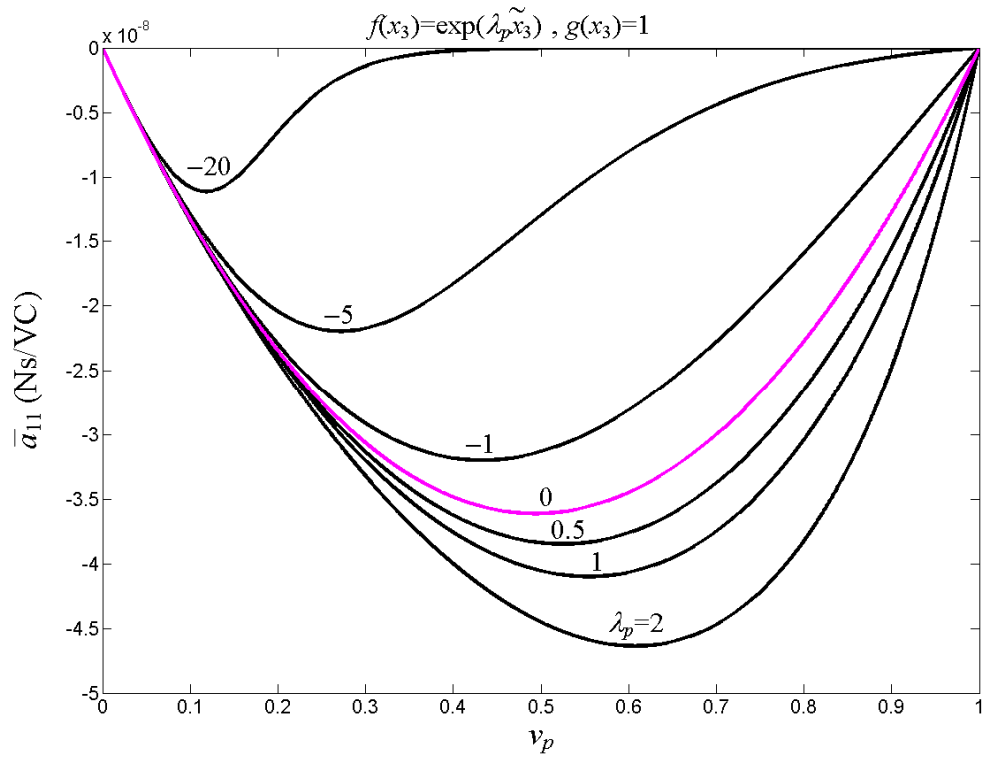


Figure 7.8: Variation of the ME coefficient \bar{a}_{11} vs. the FGM BaTiO₃ volume fraction v_p for a series gradient parameter λ_p with an exponentially varied FGM BaTiO₃ bonded to a homogeneous CoFe₂O₄ layer.

Chapter 8

Two-Dimensional Green's Functions in Anisotropic Multiferroic Bimaterials with a Viscous Interface

8.1 Introduction

Artificial multiferroic composites made of ferromagnetic and ferroelectric phases can exhibit a magnetoelectric (ME) effect, which is absent in the constituents and which can be several orders larger than that observed in natural single-phase multiferroic materials [108, 124, 127, 132]. The ME effect in the multiferroic composite is achieved through the product property: a magnetic field applied to the multiferroic composite will induce a strain in the ferromagnetic phase which is passed through the interface to the ferroelectric phase, where it induces an electric polarization. Thus the interface in multiferroic composites is critical in achieving the ME effect. In fact it has been found that any imperfection or non-ideal coupling at the interface will always cause a reduction in the ME effect in multiferroic laminated or fibrous composites [108, 141, 142].

At elevated working temperatures exceeding about one-third of the homologous temperature, mass transport becomes important along high diffusivity path such as interface or grain boundary [143–146] suggested that the microscopically mass diffusion-controlled mechanism can be macroscopically described by the linear law for a viscous interface: $\dot{\delta} = \tau/\eta$, where $\dot{\delta}$ is the sliding velocity (i.e., the differentiation of the relative sliding with respect to time t), τ is the interfacial shear stress and η is the interfacial viscosity which can be determined experimentally and theoretically [145–149]. Furthermore the viscous interface has been utilized to model incoherent interfaces between metal films and amorphous substrates to quantitatively study dislocation core spreading in thin films [150]. There are also plenty of cases in which the interface in multiferroic composites should be considered as viscous. The direct bonding of PZT and Terfenol-D disks with conductive epoxy is one of the most effective methods to achieve a giant ME response [108, 127]. The melting temperatures of PZT and Terfenol-D are higher than 1100°K, while the melting temperature of epoxy is only around 340–380°K [151]. If the multiferroic composite works at a room temperature (say 300°K), then the interfacial bonding should be considered as viscous.

Therefore, there is an urgent need to understand the potential effect of viscous interface on the multiphase field quantities in multiferroic composites. This motivates us to introduce the viscous interface into the anisotropic multiferroic composites and subsequently to study the multi-field response in terms of the powerful and elegant Green's function method.

This paper is structured as follows. In Section 8.2, the Stroh formalism suitable for two-dimensional problems in generally anisotropic multiferroic materials in the presence of viscous interface is presented. In Section 8.3, based on a novel approach, we present, in terms of a unified formalism, the elegant time-dependent (quasi-static) Green's function solutions for an anisotropic magneto-electroelastic multiferroic bimaterial with a viscous interface subjected to an extended line force and an extended line dislocation located in the upper half-plane. It is emphasized that the method proposed in this section is very simple and concise, and it is technically more attractive than previous approaches. In Section 8.4, the derived exact closed-form Green's functions are physically interpreted in terms of the static and moving image singularities in the form of an extended line force and an extended line dislocation. We derive in Section 8.5 the time-dependent image force for the extended line dislocation due to its interaction with the nearby viscous interface. In this section some special cases of the image force expressions are discussed in detail to demonstrate the influence of the viscous interface on the mobility of the dislocation, and certain important features are observed. We draw our conclusions in Section 8.6.

8.2 Basic Formulations

The basic equations for an anisotropic and linearly multiferroic material are [140]

$$\begin{aligned}\sigma_{ij} &= C_{ijkl}u_{k,l} + e_{kij}\phi_{,k} + q_{kij}\varphi_{,k} \\ D_k &= e_{kij}u_{i,j} - \epsilon_{kl}\phi_{,l} - \alpha_{lk}\varphi_{,l} \\ B_k &= q_{kij}u_{i,j} - \alpha_{kl}\phi_{,l} - \mu_{kl}\varphi_{,l} \\ \sigma_{ij,j} &= 0 \quad D_{i,i} = 0 \quad B_{i,i} = 0 \quad \text{where } i, j, k, l = 1, 2, 3\end{aligned}\tag{8.1}$$

where repeated indices mean summation, a comma follows by i stands for the derivative with respect to the i^{th} spatial coordinate; u_i , ϕ and φ are the elastic displacement, electric potential and magnetic potential; σ_{ij} , D_i and B_i are the stress, electric displacement and magnetic induction; C_{ijkl} , ϵ_{ij} and μ_{ij} are the elastic, dielectric and magnetic permeability coefficients, respectively; e_{ijk} , q_{ijk} and α_{ij} are the piezoelectric, piezomagnetic and magnetoelectric coefficients, respectively.

For two-dimensional problems in which all quantities depend only on x_1 and x_2 , one can seek the solution in the form of

$$\mathbf{u} = [u_1 \quad u_2 \quad u_3 \quad \phi \quad \varphi]^T = \mathbf{a}f(x_1 + px_2, t),\tag{8.2}$$

where (u_1, u_2) are the elastic displacements in the x_1x_2 -plane and u_3 is the anti-plane elastic displacement perpendicular to the x_1x_2 -plane; \mathbf{a} is a constant vector; p is a complex number or the Stroh eigenvalue; $f(z, t)$ is an analytic function of the complex variable z and the real time variable t . The appearance of the time t comes from the influence of the viscous

interface under quasi-static deformation. It can be verified that all equations in (8.1) are satisfied for an arbitrary analytic function $f(z, t)$ if

$$[\mathbf{Q} + p(\mathbf{R} + \mathbf{R}^T) + p^2\mathbf{T}] \mathbf{a} = \mathbf{0} \quad (8.3)$$

where the 5×5 real matrix \mathbf{R} and the two 5×5 symmetric real matrices \mathbf{Q} and \mathbf{T} are defined by

$$\begin{aligned} \mathbf{Q} &= \begin{bmatrix} \mathbf{Q}^E & \mathbf{e}_{11} & \mathbf{q}_{11} \\ \mathbf{e}_{11}^T & -\varepsilon_{11} & -\alpha_{11} \\ \mathbf{q}_{11}^T & -\alpha_{11} & -\mu_{11} \end{bmatrix} & \mathbf{R} &= \begin{bmatrix} \mathbf{R}^E & \mathbf{e}_{21} & \mathbf{q}_{21} \\ \mathbf{e}_{21}^T & -\varepsilon_{12} & -\alpha_{21} \\ \mathbf{q}_{21}^T & -\alpha_{12} & -\mu_{12} \end{bmatrix} \\ \mathbf{T} &= \begin{bmatrix} \mathbf{T}^E & \mathbf{e}_{22} & \mathbf{q}_{22} \\ \mathbf{e}_{22}^T & -\varepsilon_{22} & -\alpha_{22} \\ \mathbf{q}_{22}^T & -\alpha_{22} & -\mu_{22} \end{bmatrix} \end{aligned} \quad (8.4)$$

where

$$(\mathbf{Q}^E)_{ik} = C_{i1k1}, (\mathbf{R}^E)_{ik} = C_{i1k2}, (\mathbf{T}^E)_{ik} = C_{i2k2}, (\mathbf{e}_{ij})_m = e_{ijm}, (\mathbf{q}_{ij})_m = q_{ijm} \quad (8.5)$$

For a stable material with positive-definite energy density (elastic strain energy and electromagnetic energy), the ten roots of Eq. (8.3) form five distinct conjugate pairs with non-zero imaginary parts (see section 8.7). Let p_i (where $i = 1, 2, 3, 4, 5$) be the five distinct roots with positive imaginary parts and \mathbf{a}_i the associated eigenvectors, then the general solution is given by

$$\begin{aligned} \mathbf{u} &= [u_1 \ u_2 \ u_3 \ \phi \ \varphi]^T = \mathbf{A}\mathbf{f}(z, t) + \bar{\mathbf{A}}\bar{\mathbf{f}}(z, t) \\ \underline{\Phi} &= [\Phi_1 \ \Phi_2 \ \Phi_3 \ \Phi_4 \ \Phi_5]^T = \mathbf{B}\mathbf{f}(z, t) + \bar{\mathbf{B}}\bar{\mathbf{f}}(z, t) \\ \mathbf{b}_i &= (\mathbf{R}^T + p_i\mathbf{T})\mathbf{a}_i = \frac{-1}{p_i}(\mathbf{Q} + p_i\mathbf{R})\mathbf{a}_i, (i = 1 - 5) \\ \mathbf{A} &= [\mathbf{a}_1 \ \mathbf{a}_2 \ \mathbf{a}_3 \ \mathbf{a}_4 \ \mathbf{a}_5], \mathbf{B} = [\mathbf{b}_1 \ \mathbf{b}_2 \ \mathbf{b}_3 \ \mathbf{b}_4 \ \mathbf{b}_5] \\ \mathbf{f}(z, t) &= [f_1(z_1, t) \ f_2(z_2, t) \ f_3(z_3, t) \ f_4(z_4, t) \ f_5(z_5, t)]^T \\ z_i &= x_1 + p_i x_2, \text{Im}\{p_i\} > 0, (i = 1, 2, 3, 4, 5) \end{aligned} \quad (8.6)$$

where the overbar denotes complex conjugate, and the extended stress function vector $\underline{\Phi}$ is defined, in terms of the stresses, electric displacements and magnetic inductions, as follows

$$\begin{aligned} \sigma_{i1} &= -\Phi_{i,2} & \sigma_{i2} &= \Phi_{i,1} & (i = 1, 2, 3) \\ D_1 &= -\Phi_{4,2} & D_2 &= \Phi_{4,1} \\ B_1 &= -\Phi_{5,2} & B_2 &= \Phi_{5,1} \end{aligned} \quad (8.7)$$

In addition, the two matrices \mathbf{A} and \mathbf{B} satisfy the following normalized orthogonal relationship [35]

$$\begin{bmatrix} \mathbf{B}^T & \mathbf{A}^T \\ \bar{\mathbf{B}}^T & \bar{\mathbf{A}}^T \end{bmatrix} \begin{bmatrix} \mathbf{A} & \bar{\mathbf{A}} \\ \mathbf{B} & \bar{\mathbf{B}} \end{bmatrix} = \mathbf{I} \quad (8.8)$$

Furthermore, the following three real matrices \mathbf{S} , \mathbf{H} and \mathbf{L} , which are called the Barnett-Lothe tensors, can be introduced [35]

$$\mathbf{S} = i(2\mathbf{A}\mathbf{B}^T - \mathbf{I}) \quad \mathbf{H} = 2i\mathbf{A}\mathbf{A}^T \quad \mathbf{L} = -2i\mathbf{B}\mathbf{B}^T \quad (8.9)$$

with \mathbf{H} and \mathbf{L} being symmetric, and $\mathbf{S}\mathbf{H}$, $\mathbf{L}\mathbf{S}$, $\mathbf{H}^{-1}\mathbf{S}$, $\mathbf{S}\mathbf{L}^{-1}$ being anti-symmetric.

8.3 General Solution for the Green's Functions

Let us assume that the anisotropic multiferroic materials 1 and 2 occupy, respectively, the half-planes $x_2 > 0$ and $x_2 < 0$. At the initial moment we introduce at the location $[\hat{x}_1, \hat{x}_2]$, ($\hat{x}_2 > 0$) in the upper half-plane an extended line force $\hat{\mathbf{f}} = [f_1 \ f_2 \ f_3 \ -f_e \ -f_m]^T$ and an extended line dislocation $\hat{\mathbf{b}} = [b_1 \ b_2 \ b_3 \ \Delta\phi \ \Delta\varphi]^T$ where b_i ($i = 1, 2, 3$) are three displacement jumps across the slip plane while $\Delta\phi$ and $\Delta\varphi$ are jumps in electric potential and magnetic potential. In the following, the superscripts “(1)” and “(2)” (or the subscripts 1 and 2 to the vectors and matrices) will be used to identify the quantities in the upper and lower half-planes, respectively. The two anisotropic multiferroic half-planes are bonded together through a viscous interface at $x_2 = 0$. The boundary conditions on the viscous interface (where $x_2 = 0$) can be expressed as [143, 152, 153]

$$\begin{aligned} \sigma_{12}^{(1)} &= \sigma_{12}^{(2)} & \sigma_{22}^{(1)} &= \sigma_{22}^{(2)} & \sigma_{32}^{(1)} &= \sigma_{32}^{(2)} & D_2^{(1)} &= D_2^{(2)} & B_2^{(1)} &= B_2^{(2)} \\ u_1^{(1)} &= u_1^{(2)} & u_2^{(1)} &= u_2^{(2)} & u_3^{(1)} &= u_3^{(2)} & \phi^{(1)} &= \phi^{(2)} & \varphi^{(1)} &= \varphi^{(2)} \end{aligned} \quad (8.10)$$

for $t = 0$, and

$$\begin{aligned} \sigma_{22}^{(1)} &= \sigma_{22}^{(2)} & D_2^{(1)} &= D_2^{(2)} & B_2^{(1)} &= B_2^{(2)} \\ u_2^{(1)} &= u_2^{(2)} & \phi^{(1)} &= \phi^{(2)} & \varphi^{(1)} &= \varphi^{(2)} \\ \sigma_{12}^{(1)} &= \sigma_{12}^{(2)} = \eta_1(\dot{u}_1^{(1)} - \dot{u}_1^{(2)}) & \sigma_{32}^{(1)} &= \sigma_{32}^{(2)} = \eta_3(\dot{u}_3^{(1)} - \dot{u}_3^{(2)}) \end{aligned} \quad (8.11)$$

for $t > 0$. An overdot denotes the derivative with respect to the time t ; η_1 and η_3 are the viscous coefficients in the x_1 and x_3 directions, respectively. Due to the fact that on the interface $x_2 = 0$ we have $z_1 = z_2 = z_3 = z_4 = z_5 = z$, ($z = x_1 + ix_2$), then during the analysis we can first replace z_k , ($k = 1, 2, 3, 4, 5$) by the common complex variable z [153–155]. After the analysis is finished, we can then change z back to the corresponding complex variables.

The above boundary conditions at the interface (where $x_2 = 0$) can also be concisely and equivalently expressed in terms of the extended displacement and extended stress function vectors as

$$\underline{\Phi}_1 = \underline{\Phi}_2 \quad \mathbf{u}_1 = \mathbf{u}_2 \quad (8.12)$$

for $t = 0$, and

$$\underline{\Phi}_1 = \underline{\Phi}_2 \quad \dot{\mathbf{u}}_1 - \dot{\mathbf{u}}_2 = \underline{\Lambda} \underline{\Phi}_{2,1} \quad (8.13)$$

for $t > 0$, where $\underline{\Lambda}$ is a 5×5 real and diagonal matrix defined by

$$\underline{\Lambda} = \text{diag}[\eta_1^{-1} \ 0 \ \eta_3^{-1} \ 0 \ 0] \quad (8.14)$$

The boundary conditions at the interface $x_2 = 0$ in Eq. (8.13) can further be expressed in terms of the analytic function vectors $\mathbf{f}_1(z, t)$ and $\mathbf{f}_2(z, t)$ as

$$\mathbf{B}_1 \mathbf{f}_1^+(x_1, t) + \bar{\mathbf{B}}_1 \bar{\mathbf{f}}_1^-(x_1, t) = \mathbf{B}_2 \mathbf{f}_2^-(x_1, t) + \bar{\mathbf{B}}_2 \bar{\mathbf{f}}_2^+(x_1, t) \quad (8.15)$$

$$\begin{aligned} \mathbf{A}_1 \dot{\mathbf{f}}_1^+(x_1, t) + \bar{\mathbf{A}}_1 \dot{\bar{\mathbf{f}}}_1^-(x_1, t) \\ - \mathbf{A}_2 \dot{\mathbf{f}}_2^-(x_1, t) - \bar{\mathbf{A}}_2 \dot{\bar{\mathbf{f}}}_2^+(x_1, t) = \underline{\Lambda} \left[\mathbf{B}_2 \mathbf{f}_2^-(x_1, t) + \bar{\mathbf{B}}_2 \bar{\mathbf{f}}_2^+(x_1, t) \right] \end{aligned} \quad (8.16)$$

Both of the above equations are for $t > 0$.

It follows from Eq. (8.15) that

$$\begin{aligned}\mathbf{f}_1(z, t) &= \mathbf{B}_1^{-1} \bar{\mathbf{B}}_2 \bar{\mathbf{f}}_2(z, t) + \mathbf{f}_0(z) - \mathbf{B}_1^{-1} \bar{\mathbf{B}}_1 \bar{\mathbf{f}}_0(z) \\ \bar{\mathbf{f}}_1(z, t) &= \bar{\mathbf{B}}_1^{-1} \mathbf{B}_2 \mathbf{f}_2(z, t) + \bar{\mathbf{f}}_0(z) - \bar{\mathbf{B}}_1^{-1} \mathbf{B}_1 \mathbf{f}_0(z)\end{aligned}\quad (8.17)$$

where $\mathbf{f}_0(z)$ is the analytic function vector in a homogeneous plane occupied by material 1 given by

$$\mathbf{f}_0(z) = \frac{1}{2\pi i} \langle \ln(z - \hat{z}_\alpha) \rangle (\mathbf{A}_1^T \hat{\mathbf{f}} + \mathbf{B}_1^T \hat{\mathbf{b}}) \quad (8.18)$$

with $\hat{z}_\alpha = \hat{x}_1 + p_\alpha \hat{x}_2$, and $\langle * \rangle$ a 5×5 diagonal matrix in which each component is varied according to the Greek index α (from 1 to 5).

Substituting the above expressions into Eq. (8.16) and eliminating $\mathbf{f}_1^+(x_1, t), \bar{\mathbf{f}}_1^-(x_1, t)$, we finally obtain

$$\bar{\mathbf{N}} \bar{\mathbf{B}}_2 \bar{\mathbf{f}}_2^+(x_1, t) - i \underline{\Lambda} \bar{\mathbf{B}}_2 \bar{\mathbf{f}}_2^+(x_1, t) = \mathbf{N} \mathbf{B}_2 \mathbf{f}_2^-(x_1, t) + i \underline{\Lambda} \mathbf{B}_2 \mathbf{f}_2^-(x_1, t) \quad (8.19)$$

for $t > 0$ at the interface $x_2 = 0$, where \mathbf{N} is a 5×5 Hermitian matrix given by

$$\begin{aligned}\mathbf{N} &= \bar{\mathbf{M}}_1^{-1} + \mathbf{M}_2^{-1} = \mathbf{L}_1^{-1} + \mathbf{L}_2^{-1} + i(\mathbf{S}_1 \mathbf{L}_1^{-1} - \mathbf{S}_2 \mathbf{L}_2^{-1}) \\ \mathbf{M}_k^{-1} &= i \mathbf{A}_k \mathbf{B}_k^{-1} = (\mathbf{I} - i \mathbf{S}_k) \mathbf{L}_k^{-1} \quad (k = 1, 2)\end{aligned}\quad (8.20)$$

Due to the fact that \mathbf{N} is a 5×5 Hermitian matrix, we can further write \mathbf{N} as

$$\mathbf{N} = \bar{\mathbf{N}}^T = \begin{bmatrix} N_{11} & N_{12} & N_{13} & N_{14} & N_{15} \\ \bar{N}_{12} & N_{22} & N_{23} & N_{24} & N_{25} \\ \bar{N}_{13} & \bar{N}_{23} & N_{33} & N_{34} & N_{35} \\ \bar{N}_{14} & \bar{N}_{24} & \bar{N}_{34} & N_{44} & N_{45} \\ \bar{N}_{15} & \bar{N}_{25} & \bar{N}_{35} & \bar{N}_{45} & N_{55} \end{bmatrix} \quad (8.21)$$

It is apparent that the left-hand side of Eq. (8.19) is analytic in the upper half-plane, while the right-hand side of Eq. (8.19) is analytic in the lower half-plane. Consequently the continuity condition in Eq. (8.19) implies that the left- and right-hand sides of Eq. (8.19) are identically zero in the upper and lower half-planes, respectively. It then follows that

$$\mathbf{N} \mathbf{B}_2 \mathbf{f}_2(z, t) + i \underline{\Lambda} \mathbf{B}_2 \mathbf{f}_2(z, t) = \mathbf{0}, \quad \text{Im}\{z\} < 0 \quad (8.22)$$

We next consider the following eigenvalue problem

$$(\underline{\Lambda} - \lambda \mathbf{N}) \mathbf{v} = \mathbf{0} \quad (8.23)$$

It is observed that in total there exist five eigenvalues to the above eigenvalue problem. Furthermore, these five eigenvalues λ_i ($i = 1, 2, 3, 4, 5$) can be explicitly determined as

$$\begin{aligned}\lambda_1 &= \frac{a_1 + \sqrt{a_1^2 - 4a_0a_2}}{2a_2} > 0 \\ \lambda_2 &= \frac{a_1 - \sqrt{a_1^2 - 4a_0a_2}}{2a_2} > 0 \\ \lambda_3 &= \lambda_4 = \lambda_5 = 0\end{aligned}\quad (8.24)$$

where

$$a_2 = |\mathbf{N}|, \quad a_1 = \frac{\hat{N}_{11}}{\eta_1} + \frac{\hat{N}_{33}}{\eta_3}, \quad a_0 = \frac{1}{\eta_1 \eta_3} \begin{vmatrix} N_{22} & N_{24} & N_{25} \\ \bar{N}_{24} & N_{44} & N_{45} \\ \bar{N}_{25} & \bar{N}_{45} & N_{55} \end{vmatrix}, \quad (8.25)$$

with \hat{N}_{ij} denoting the cofactors of the matrix \mathbf{N} .

We specially choose the eigenvectors associated with the three zero eigenvalues $\lambda_3 = \lambda_4 = \lambda_5 = 0$ as

$$\mathbf{v}_3 = \begin{bmatrix} 0 \\ 1 \\ 0 \\ 0 \\ 0 \end{bmatrix}, \quad \mathbf{v}_4 = \begin{bmatrix} 0 \\ -N_{24} \\ 0 \\ N_{22} \\ 0 \end{bmatrix}, \quad \mathbf{v}_5 = \begin{bmatrix} 0 \\ N_{24}N_{45} - N_{25}N_{44} \\ 0 \\ N_{25}\bar{N}_{24} - N_{45}N_{22} \\ N_{22}N_{44} - N_{24}\bar{N}_{24} \end{bmatrix} \quad (8.26)$$

so that the following orthogonal relationships with respect to the Hermitian matrix \mathbf{N} and to the real and diagonal matrix $\underline{\Lambda}$ hold:

$$\begin{aligned} \bar{\Psi}^T \mathbf{N} \Psi &= \underline{\Lambda}_0 = \text{diag} [\delta_1 \quad \delta_2 \quad \delta_3 \quad \delta_4 \quad \delta_5] \\ \bar{\Psi}^T \underline{\Lambda} \Psi &= \text{diag} [\lambda_1 \delta_1 \quad \lambda_2 \delta_2 \quad \lambda_3 \delta_3 \quad \lambda_4 \delta_4 \quad \lambda_5 \delta_5] \end{aligned} \quad (8.27)$$

where $\delta_k = \bar{\mathbf{v}}_k^T \mathbf{N} \mathbf{v}_k$ ($k = 1-5$) are nonzero real values and

$$\underline{\Psi} = [\mathbf{v}_1 \quad \mathbf{v}_2 \quad \mathbf{v}_3 \quad \mathbf{v}_4 \quad \mathbf{v}_5] \quad (8.28)$$

In addition, due to the fact that $\bar{\mathbf{v}}_i^T \underline{\Lambda} \mathbf{v}_i = \lambda_i \delta_i > 0$ ($i = 1, 2$), then δ_1 and δ_2 are positive.

Next we introduce the following new analytic function vector $\underline{\Omega}(z, t)$

$$\mathbf{B}_2 \mathbf{f}_2(z, t) = \underline{\Psi} \underline{\Omega}(z, t) \quad (8.29)$$

Employing the orthogonal relationship in Eq. (8.27), then Eq. (8.22) can be decoupled into

$$\dot{\Omega}_k(z, t) + i\lambda_k \Omega'_k(z, t) = 0; \quad k = 1, 2, 3, 4, 5; \quad \text{Im}\{z\} < 0 \quad (8.30)$$

whose solutions can be conveniently given by

$$\Omega_k(z, t) = \Omega_k(z - i\lambda_k t, 0); \quad k = 1, 2, 3, 4, 5; \quad \text{Im}\{z\} < 0 \quad (8.31)$$

The above expression indicates that once the initial state $\Omega_k(z, 0)$ is known, then one only needs to replace the complex variable z by $z - i\lambda_k t$ to arrive at the expression of $\Omega_k(z, t)$. In view of the fact that at the initial moment $t = 0$, the interface is a perfect one, then we arrive at the following

$$\mathbf{f}_2(z, 0) = 2\mathbf{B}_2^{-1} \mathbf{N}^{-1} \mathbf{L}_1^{-1} \mathbf{B}_1 \mathbf{f}_0(z), \quad \text{Im}\{z\} < 0 \quad (8.32)$$

Consequently, it follows from Eq. (8.29) and the above expression that

$$\begin{aligned} \underline{\Omega}(z, 0) &= 2\underline{\Psi}^{-1} \mathbf{N}^{-1} \mathbf{L}_1^{-1} \mathbf{B}_1 \mathbf{f}_0(z) = \\ &= \frac{1}{\pi i} \underline{\Psi}^{-1} \mathbf{N}^{-1} \mathbf{L}_1^{-1} \mathbf{B}_1 \langle \ln(z - \hat{z}_\alpha) \rangle (\mathbf{A}_1^T \hat{\mathbf{f}} + \mathbf{B}_1^T \hat{\mathbf{b}}), \quad \text{Im}\{z\} < 0 \end{aligned} \quad (8.33)$$

Therefore, we can conveniently write down the expression of $\underline{\Omega}(z, t)$ as

$$\underline{\Omega}(z, t) = \frac{1}{\pi i} \sum_{k=1}^5 \langle \ln(z - i\lambda_{\alpha}t - \hat{z}_k) \rangle \underline{\Psi}^{-1} \mathbf{N}^{-1} \mathbf{L}_1^{-1} \mathbf{B}_1 \mathbf{I}_k (\mathbf{A}_1^T \hat{\mathbf{f}} + \mathbf{B}_1^T \hat{\mathbf{b}}), \text{Im}\{z\} < 0 \quad (8.34)$$

where

$$\begin{aligned} \mathbf{I}_1 &= \text{diag}[1 \ 0 \ 0 \ 0 \ 0], \mathbf{I}_2 = \text{diag}[0 \ 1 \ 0 \ 0 \ 0], \mathbf{I}_3 = \text{diag}[0 \ 0 \ 1 \ 0 \ 0] \\ \mathbf{I}_4 &= \text{diag}[0 \ 0 \ 0 \ 1 \ 0], \mathbf{I}_5 = \text{diag}[0 \ 0 \ 0 \ 0 \ 1] \end{aligned} \quad (8.35)$$

Substituting the above into Eq. (8.29), and then the results into Eq. (8.17), we can obtain the two analytic function vectors $\mathbf{f}_1(z, t)$ and $\mathbf{f}_2(z, t)$ as

$$\mathbf{f}_2(z, t) = \frac{1}{\pi i} \sum_{k=1}^5 \mathbf{B}_2^{-1} \underline{\Psi} \langle \ln(z - i\lambda_{\alpha}t - \hat{z}_k) \rangle \underline{\Psi}^{-1} \mathbf{N}^{-1} \mathbf{L}_1^{-1} \mathbf{B}_1 \mathbf{I}_k (\mathbf{A}_1^T \hat{\mathbf{f}} + \mathbf{B}_1^T \hat{\mathbf{b}}) \quad (8.36)$$

for $\text{Im}\{z\} < 0$, and

$$\begin{aligned} \mathbf{f}_1(z, t) &= -\frac{1}{\pi i} \sum_{k=1}^5 \mathbf{B}_1^{-1} \underline{\Psi} \langle \ln(z + i\lambda_{\alpha}t + \bar{z}_k) \rangle \underline{\Psi}^{-1} \bar{\mathbf{N}}^{-1} \mathbf{L}_1^{-1} \bar{\mathbf{B}}_1 \mathbf{I}_k (\bar{\mathbf{A}}_1^T \hat{\mathbf{f}} + \bar{\mathbf{B}}_1^T \hat{\mathbf{b}}) \\ &\quad + \frac{1}{2\pi i} \mathbf{B}_1^{-1} \bar{\mathbf{B}}_1 \langle \ln(z - \bar{z}_{\alpha}) \rangle (\bar{\mathbf{A}}_1^T \hat{\mathbf{f}} + \bar{\mathbf{B}}_1^T \hat{\mathbf{b}}) + \frac{1}{2\pi i} \langle \ln(z - \hat{z}_{\alpha}) \rangle (\mathbf{A}_1^T \hat{\mathbf{f}} + \mathbf{B}_1^T \hat{\mathbf{b}}) \end{aligned} \quad (8.37)$$

for $\text{Im}\{z\} > 0$.

The above expressions are in fact only valid along the x_1 -axis. We can further write down the full-field expressions of $\mathbf{f}_1(z, t)$ and $\mathbf{f}_2(z, t)$ as

$$\begin{aligned} \mathbf{f}_1(z, t) &= -\frac{1}{\pi i} \sum_{m=1}^5 \sum_{k=1}^5 \langle \ln(z_{\alpha} + i\lambda_{m}t - \bar{z}_k) \rangle \mathbf{B}_1^{-1} \underline{\Psi} \mathbf{I}_m \underline{\Lambda}_0^{-1} \underline{\Psi}^T \mathbf{L}_1^{-1} \bar{\mathbf{B}}_1 \mathbf{I}_k (\bar{\mathbf{A}}_1^T \hat{\mathbf{f}} + \bar{\mathbf{B}}_1^T \hat{\mathbf{b}}) \\ &\quad + \frac{1}{2\pi i} \sum_{k=1}^5 \langle \ln(z_{\alpha} - \bar{z}_k) \rangle \mathbf{B}_1^{-1} \bar{\mathbf{B}}_1 \mathbf{I}_k (\bar{\mathbf{A}}_1^T \hat{\mathbf{f}} + \bar{\mathbf{B}}_1^T \hat{\mathbf{b}}) + \frac{1}{2\pi i} \langle \ln(z_{\alpha} - \hat{z}_{\alpha}) \rangle (\mathbf{A}_1^T \hat{\mathbf{f}} + \mathbf{B}_1^T \hat{\mathbf{b}}) \end{aligned} \quad (8.38)$$

for $x_2 > 0$, and

$$\mathbf{f}_2(z, t) = \frac{1}{\pi i} \sum_{m=1}^5 \sum_{k=1}^5 \langle \ln(z_{\alpha}^* - i\lambda_{m}t - \hat{z}_k) \rangle \mathbf{B}_2^{-1} \underline{\Psi} \mathbf{I}_m \underline{\Lambda}_0^{-1} \underline{\Psi}^T \mathbf{L}_1^{-1} \mathbf{B}_1 \mathbf{I}_k (\mathbf{A}_1^T \hat{\mathbf{f}} + \mathbf{B}_1^T \hat{\mathbf{b}}) \quad (8.39)$$

for $x_2 < 0$, where the superscript ‘*’ is utilized to distinguish the Stroh eigenvalues associated with the lower half-plane (z_{α}^*) from those associated with the upper half-plane (z_{α}). One can observe that the derived time-dependent multiferroic Green’s function solutions (8.38) and (8.39) are even more concise and elegant than previously obtained ones for the purely elastic bimaterial [153]. Substitution of Eqs. (8.38) and (8.39) into Eq.(8.6) will yield

the expressions of \mathbf{u} and Φ . For example, the tractions, normal electric displacement and normal magnetic induction are distributed along the interface $x_2 = 0$ as

$$\begin{bmatrix} \sigma_{12} & \sigma_{22} & \sigma_{32} & D_2 & B_2 \end{bmatrix}^T = \frac{2}{\pi} \text{Im} \left\{ \sum_{m=1}^5 \underline{\Psi} \mathbf{I}_m \underline{\Delta}_0^{-1} \underline{\Psi}^T \mathbf{L}_1^{-1} \mathbf{B}_1 < \frac{1}{x_1 - i\lambda_m t - \hat{z}_\alpha} > (\mathbf{A}_1^T \hat{\mathbf{f}} + \mathbf{B}_1^T \hat{\mathbf{b}}) \right\}, \quad (8.40)$$

for $-\infty < x_1 < +\infty$, $t \geq 0$.

It also follows from Eqs. (8.38) and (8.39) that at the initial moment $t = 0$,

$$\begin{aligned} \mathbf{f}_1(z, 0) = & \frac{1}{2\pi i} \sum_{k=1}^5 \langle \ln(z_\alpha - \bar{z}_k) \rangle \mathbf{B}_1^{-1} (\mathbf{I} - 2\bar{\mathbf{N}}^{-1} \mathbf{L}_1^{-1}) \bar{\mathbf{B}}_1 \mathbf{I}_k (\bar{\mathbf{A}}_1^T \hat{\mathbf{f}} + \bar{\mathbf{B}}_1^T \hat{\mathbf{b}}) \\ & + \frac{1}{2\pi i} \langle \ln(z_\alpha - \hat{z}_\alpha) \rangle (\mathbf{A}_1^T \hat{\mathbf{f}} + \mathbf{B}_1^T \hat{\mathbf{b}}) \end{aligned} \quad (8.41)$$

for $x_2 > 0$, and

$$\mathbf{f}_2(z, 0) = \frac{1}{\pi i} \sum_{k=1}^5 \langle \ln(z_\alpha^* - \hat{z}_k) \rangle \mathbf{B}_2^{-1} \mathbf{N}^{-1} \mathbf{L}_1^{-1} \mathbf{B}_1 \mathbf{I}_k (\mathbf{A}_1^T \hat{\mathbf{f}} + \mathbf{B}_1^T \hat{\mathbf{b}}), \quad (8.42)$$

for $x_2 < 0$, which are just the bimaterial Green's functions with a perfect interface derived by [156]. On the other extreme case when $t \rightarrow \infty$, we have

$$\begin{aligned} \mathbf{f}_1(z, \infty) = & \frac{1}{2\pi i} \sum_{k=1}^5 \langle \ln(z_\alpha - \bar{z}_k) \rangle \mathbf{B}_1^{-1} [\mathbf{I} - 2\underline{\Psi} (\mathbf{I}_3 + \mathbf{I}_4 + \mathbf{I}_5) \underline{\Delta}_0^{-1} \underline{\Psi}^T \mathbf{L}_1^{-1}] \bar{\mathbf{B}}_1 \mathbf{I}_k (\bar{\mathbf{A}}_1^T \hat{\mathbf{f}} + \bar{\mathbf{B}}_1^T \hat{\mathbf{b}}) \\ & + \frac{1}{2\pi i} \langle \ln(z_\alpha - \hat{z}_\alpha) \rangle (\mathbf{A}_1^T \hat{\mathbf{f}} + \mathbf{B}_1^T \hat{\mathbf{b}}) \end{aligned} \quad (8.43)$$

for $x_2 > 0$, and

$$\mathbf{f}_2(z, \infty) = \frac{1}{\pi i} \sum_{k=1}^5 \langle \ln(z_\alpha^* - \hat{z}_k) \rangle \mathbf{B}_2^{-1} \underline{\Psi} (\mathbf{I}_3 + \mathbf{I}_4 + \mathbf{I}_5) \underline{\Delta}_0^{-1} \underline{\Psi}^T \mathbf{L}_1^{-1} \mathbf{B}_1 \mathbf{I}_k (\mathbf{A}_1^T \hat{\mathbf{f}} + \mathbf{B}_1^T \hat{\mathbf{b}}) \quad (8.44)$$

for $x_2 < 0$, which are the results for a free-sliding interface on which the two shear stresses are zero.

We add that the method presented in this paper is not limited to the Green's functions for an extended line force and an extended line dislocation. It can also be easily adopted to derive Green's functions for other types of singularities, such as concentrated couples and line heat sources once the Green's functions due to these singularities for a perfect bimaterial interface are known.

8.4 Image Singularities

Here it is of particular interest to look into the physical meanings of the obtained Green's function solutions (8.38) and (8.39). The last term on the right-hand side of Eq. (8.38)

represents the Green's function for an infinite multiferroic space with singularities in the form of an extended line force $\hat{\mathbf{f}}$ and an extended line dislocation $\hat{\mathbf{b}}$ located at $[x_1, x_2] = [\hat{x}_1, \hat{x}_2]$. In the following we will demonstrate that (i) the first and second terms on the right-hand side of Eq. (8.38) represent fifty time-dependent and twenty five time-independent Green's functions for the infinite space occupied by material 1 whose singularities are also in the form of an extended line force and an extended line dislocation located in $x_2 < 0$, and (ii) Eq. (8.39) represents fifty time-dependent and twenty five time-independent Green's functions for the infinite space occupied by material 2 whose singularities are also in the form of an extended line force and an extended line dislocation located in $x_2 > 0$.

The moving singularities of the first term in Eq. (8.38) are located at

$$z_n + i\lambda_k t - \bar{z}_m = x_1 + p_n x_2 + i\lambda_k t - \hat{x}_1 - \bar{p}_m \hat{x}_2 = 0 \quad (8.45)$$

where $n, m = 1, 2, 3, 4, 5; k = 1, 2$, while the static singularities of the first and second terms in Eq. (8.38) are located at

$$z_n - \bar{z}_m = x_1 + p_n x_2 - \hat{x}_1 - \bar{p}_m \hat{x}_2 = 0 \quad (8.46)$$

where $n, m = 1, 2, 3, 4, 5$. We let p', p'' be, respectively, the real and imaginary parts of p . If we equal the real and imaginary parts of Eqs. (8.45) and (8.46), then the locations $[x_1^{nmk}(t), x_2^{nmk}(t)]$ of the moving singularities and the locations $[x_1^{nm}, x_2^{nm}]$ of the static singularities for the upper half-plane are found to be

$$x_1^{nmk}(t) = \hat{x}_1 + \frac{\lambda_k p'_n t + (p'_n p''_m + p'_m p''_n) \hat{x}_2}{p''_n} \quad x_2^{nmk}(t) = -\frac{\lambda_k t + p''_m \hat{x}_2}{p''_n} \quad (8.47)$$

where $n, m = 1, 2, 3, 4, 5; k = 1, 2$, and

$$x_1^{nm} = \hat{x}_1 + \frac{(p'_n p''_m + p'_m p''_n) \hat{x}_2}{p''_n} \quad x_2^{nm} = -\frac{p''_m \hat{x}_2}{p''_n}, \quad (8.48)$$

where $n, m = 1, 2, 3, 4, 5$.

Due to the fact that $p''_n, p''_m, \lambda_k > 0$, then $[x_1^{nmk}(t), x_2^{nmk}(t)]$ and $[x_1^{nm}, x_2^{nm}]$ exist, and also $x_2^{nmk}(t) < 0$ and $x_2^{nm} < 0$, which means that the moving and static image singularities for the upper half-plane are always located in the lower half-plane. In addition it is observed from Eq. (8.47) that the moving image singularities for the upper half-plane move further away from the interface as the time evolves.

The moving image singularities in Eq. (8.39) are located at

$$z_n^* - i\lambda_k t - \hat{z}_m = x_1 + p_n^* x_2 - i\lambda_k t - \hat{x}_1 - p_m \hat{x}_2 = 0 \quad (8.49)$$

where $n, m = 1, 2, 3, 4, 5; k = 1, 2$, while the static singularities in Eq. (8.39) are located at

$$z_n^* - \hat{z}_m = x_1 + p_n^* x_2 - \hat{x}_1 - p_m \hat{x}_2 = 0 \quad (8.50)$$

where $n, m = 1, 2, 3, 4, 5$. Equating the real and imaginary parts of Eqs. (8.49) and (8.50), the locations $[x_1^{*nmk}(t), x_2^{*nmk}(t)]$ of the moving singularities and the locations $[x_1^{*nm}, x_2^{*nm}]$ of the static singularities for the lower half-plane are

$$x_1^{*nmk}(t) = \hat{x}_1 - \frac{\lambda_k (p'_n)^* t + (p'_n)^* p''_m - p'_m (p'_n)^* \hat{x}_2}{(p''_n)^*} \quad x_2^{*nmk}(t) = \frac{\lambda_k t + p''_m \hat{x}_2}{(p''_n)^*} \quad (8.51)$$

where $n, m = 1, 2, 3, 4, 5; k = 1, 2$, and

$$x_1^{*nm} = \hat{x}_1 - \frac{((p'_n)^* p''_m - p'_m (p''_n)^*) \hat{x}_2}{(p''_n)^*}, \quad x_2^{*nm} = \frac{p''_m \hat{x}_2}{(p''_n)^*}, \quad (8.52)$$

where $n, m = 1, 2, 3, 4, 5$.

Due to the fact that $(p''_n)^*, p''_m, \lambda_k > 0$, then $[x_1^{*nmk}(t), x_2^{*nmk}(t)]$ and $[x_1^{*nm}, x_2^{*nm}]$ exist, and also $x_2^{*nmk}(t) > 0$ and $x_2^{*nm} > 0$, which means that the moving and static image singularities for the lower half-plane are always located in the upper half-plane. In addition it is observed from Eq. (8.51) that the moving image singularities for the lower half-plane also move further away from the interface as the time evolves.

Based on the previous results, we can further write Eqs. (8.38) and (8.39) into the following equivalent forms:

$$\begin{aligned} \mathbf{f}_1(z, t) = & \frac{1}{2\pi i} \sum_{n=1}^5 \sum_{m=1}^5 \sum_{k=1}^2 \langle \ln[z_\alpha - z_\alpha^{nmk}(t)] \rangle (\mathbf{A}_1^T \hat{\mathbf{f}}_{nmk} + \mathbf{B}_1^T \hat{\mathbf{b}}_{nmk}) \\ & + \frac{1}{2\pi i} \sum_{n=1}^5 \sum_{m=1}^5 \langle \ln(z_\alpha - z_\alpha^{nm}) \rangle (\mathbf{A}_1^T \hat{\mathbf{f}}_{nm} + \mathbf{B}_1^T \hat{\mathbf{b}}_{nm}) \\ & + \frac{1}{2\pi i} \langle \ln(z_\alpha - \hat{z}_\alpha) \rangle (\mathbf{A}_1^T \hat{\mathbf{f}} + \mathbf{B}_1^T \hat{\mathbf{b}}) \end{aligned} \quad (8.53)$$

for $x_2 > 0$, and

$$\begin{aligned} \mathbf{f}_2(z, t) = & \frac{1}{2\pi i} \sum_{n=1}^5 \sum_{m=1}^5 \sum_{k=1}^2 \langle \ln[z_\alpha^* - z_\alpha^{*nmk}(t)] \rangle (\mathbf{A}_2^T \hat{\mathbf{f}}_{nmk}^* + \mathbf{B}_2^T \hat{\mathbf{b}}_{nmk}^*) \\ & + \frac{1}{2\pi i} \sum_{n=1}^5 \sum_{m=1}^5 \langle \ln(z_\alpha^* - z_\alpha^{*nm}) \rangle (\mathbf{A}_2^T \hat{\mathbf{f}}_{nm}^* + \mathbf{B}_2^T \hat{\mathbf{b}}_{nm}^*) \end{aligned} \quad (8.54)$$

for $x_2 < 0$, where

$$\begin{aligned} z_\alpha^{nmk}(t) &= x_1^{nmk}(t) + p_\alpha x_2^{nmk}(t) \\ z_\alpha^{nm} &= x_1^{nm} + p_\alpha x_2^{nm} \end{aligned} \quad (8.55)$$

$$\begin{aligned} z_\alpha^{*nmk}(t) &= x_1^{*nmk}(t) + p_\alpha^* x_2^{*nmk}(t) \\ z_\alpha^{*nm} &= x_1^{*nm} + p_\alpha^* x_2^{*nm} \end{aligned} \quad (8.56)$$

where $n, m = 1, 2, 3, 4, 5; k = 1, 2$, and

$$\begin{aligned} \hat{\mathbf{f}}_{nmk} &= -4 \operatorname{Re} \left\{ \mathbf{B}_1 \mathbf{I}_n \mathbf{B}_1^{-1} \underline{\Psi} \mathbf{I}_k \underline{\Lambda}_0^{-1} \underline{\Psi}^T \mathbf{L}_1^{-1} \bar{\mathbf{B}}_1 \mathbf{I}_m (\bar{\mathbf{A}}_1^T \hat{\mathbf{f}} + \bar{\mathbf{B}}_1^T \hat{\mathbf{b}}) \right\} \\ \hat{\mathbf{b}}_{nmk} &= -4 \operatorname{Re} \left\{ \mathbf{A}_1 \mathbf{I}_n \mathbf{B}_1^{-1} \underline{\Psi} \mathbf{I}_k \underline{\Lambda}_0^{-1} \underline{\Psi}^T \mathbf{L}_1^{-1} \bar{\mathbf{B}}_1 \mathbf{I}_m (\bar{\mathbf{A}}_1^T \hat{\mathbf{f}} + \bar{\mathbf{B}}_1^T \hat{\mathbf{b}}) \right\} \\ \hat{\mathbf{f}}_{nm} &= 2 \operatorname{Re} \left\{ \mathbf{B}_1 \mathbf{I}_n \mathbf{B}_1^{-1} [\mathbf{I} - 2 \underline{\Psi} (\mathbf{I}_3 + \mathbf{I}_4 + \mathbf{I}_5) \underline{\Lambda}_0^{-1} \underline{\Psi}^T \mathbf{L}_1^{-1}] \bar{\mathbf{B}}_1 \mathbf{I}_m (\bar{\mathbf{A}}_1^T \hat{\mathbf{f}} + \bar{\mathbf{B}}_1^T \hat{\mathbf{b}}) \right\} \\ \hat{\mathbf{b}}_{nm} &= 2 \operatorname{Re} \left\{ \mathbf{A}_1 \mathbf{I}_n \mathbf{B}_1^{-1} [\mathbf{I} - 2 \underline{\Psi} (\mathbf{I}_3 + \mathbf{I}_4 + \mathbf{I}_5) \underline{\Lambda}_0^{-1} \underline{\Psi}^T \mathbf{L}_1^{-1}] \bar{\mathbf{B}}_1 \mathbf{I}_m (\bar{\mathbf{A}}_1^T \hat{\mathbf{f}} + \bar{\mathbf{B}}_1^T \hat{\mathbf{b}}) \right\} \end{aligned} \quad (8.57)$$

$$\begin{aligned}
\hat{\mathbf{f}}_{nmk}^* &= 4 \operatorname{Re} \left\{ \mathbf{B}_2 \mathbf{I}_n \mathbf{B}_2^{-1} \underline{\Psi} \mathbf{I}_k \underline{\Lambda}_0^{-1} \bar{\Psi}^T \mathbf{L}_1^{-1} \mathbf{B}_1 \mathbf{I}_m (\mathbf{A}_1^T \hat{\mathbf{f}} + \mathbf{B}_1^T \hat{\mathbf{b}}) \right\} \\
\hat{\mathbf{b}}_{nmk}^* &= 4 \operatorname{Re} \left\{ \mathbf{A}_2 \mathbf{I}_n \mathbf{B}_2^{-1} \underline{\Psi} \mathbf{I}_k \underline{\Lambda}_0^{-1} \bar{\Psi}^T \mathbf{L}_1^{-1} \mathbf{B}_1 \mathbf{I}_m (\mathbf{A}_1^T \hat{\mathbf{f}} + \mathbf{B}_1^T \hat{\mathbf{b}}) \right\} \\
\hat{\mathbf{f}}_{nm}^* &= 4 \operatorname{Re} \left\{ \mathbf{B}_2 \mathbf{I}_n \mathbf{B}_2^{-1} \underline{\Psi} (\mathbf{I}_3 + \mathbf{I}_4 + \mathbf{I}_5) \underline{\Lambda}_0^{-1} \bar{\Psi}^T \mathbf{L}_1^{-1} \mathbf{B}_1 \mathbf{I}_m (\mathbf{A}_1^T \hat{\mathbf{f}} + \mathbf{B}_1^T \hat{\mathbf{b}}) \right\} \\
\hat{\mathbf{b}}_{nm}^* &= 4 \operatorname{Re} \left\{ \mathbf{A}_2 \mathbf{I}_n \mathbf{B}_2^{-1} \underline{\Psi} (\mathbf{I}_3 + \mathbf{I}_4 + \mathbf{I}_5) \underline{\Lambda}_0^{-1} \bar{\Psi}^T \mathbf{L}_1^{-1} \mathbf{B}_1 \mathbf{I}_m (\mathbf{A}_1^T \hat{\mathbf{f}} + \mathbf{B}_1^T \hat{\mathbf{b}}) \right\}
\end{aligned} \tag{8.58}$$

The first term in Eq. (8.53) represents fifty time-dependent Green's functions with singularities located at $[x_1^{nmk}(t), x_2^{nmk}(t)]$. These moving image singularities consist of an extended line force $\hat{\mathbf{f}}_{nmk}$ and an extended line dislocation $\hat{\mathbf{b}}_{nmk}$. The second term in Eq. (8.53) represents twenty five time-independent Green's functions with singularities located at $[x_1^{nm}, x_2^{nm}]$. These static image singularities consist of an extended line force $\hat{\mathbf{f}}_{nm}$ and an extended line dislocation $\hat{\mathbf{b}}_{nm}$. The first term in Eq. (8.54) represents fifty time-dependent Green's functions with singularities located at $[x_1^{*nmk}(t), x_2^{*nmk}(t)]$. These moving image singularities consist of an extended line force $\hat{\mathbf{f}}_{nmk}^*$ and an extended line dislocation $\hat{\mathbf{b}}_{nmk}^*$. The second term in Eq. (8.54) represents twenty five time-independent Green's functions with singularities located at $[x_1^{*nm}, x_2^{*nm}]$. These static image singularities consist of an extended line force $\hat{\mathbf{f}}_{nm}^*$ and an extended line dislocation $\hat{\mathbf{b}}_{nm}^*$. In addition all the moving singularities originate from the locations of the static singularities due to the fact that $x_1^{nmk}(0) = x_1^{nm}$, $x_2^{nmk}(0) = x_2^{nm}$, $x_1^{*nmk}(0) = x_1^{*nm}$, and $x_2^{*nmk}(0) = x_2^{*nm}$ by noticing Eqs. (8.47), (8.48), (8.51) and (8.52). It can be easily checked from Eq. (8.57) that the total extended force due to the moving and static image singularities $\sum_{n=1}^5 \sum_{m=1}^5 \sum_{k=1}^2 \hat{\mathbf{f}}_{nmk} + \sum_{n=1}^5 \sum_{m=1}^5 \hat{\mathbf{f}}_{nm}$ and the total extended dislocation due to the moving and static image singularities $\sum_{n=1}^5 \sum_{m=1}^5 \sum_{k=1}^2 \hat{\mathbf{b}}_{nmk} + \sum_{n=1}^5 \sum_{m=1}^5 \hat{\mathbf{b}}_{nm}$ for the upper half-plane are exactly the same as those for a perfect interface. Similarly it can be easily checked from Eq. (8.58) that the total extended force due to the moving and static image singularities $\sum_{n=1}^5 \sum_{m=1}^5 \sum_{k=1}^2 \hat{\mathbf{f}}_{nmk}^* + \sum_{n=1}^5 \sum_{m=1}^5 \hat{\mathbf{f}}_{nm}^*$ and the total extended dislocation due to the moving and static image singularities $\sum_{n=1}^5 \sum_{m=1}^5 \sum_{k=1}^2 \hat{\mathbf{b}}_{nmk}^* + \sum_{n=1}^5 \sum_{m=1}^5 \hat{\mathbf{b}}_{nm}^*$ for the lower half-plane are also exactly the same as those for a perfect interface.

In summary, twenty five *static* image singularities and fifty *moving* image singularities, which originate from the locations of the static image singularities, in the form of an extended line force and an extended line dislocation for the upper or the lower half-plane are needed to exactly satisfy the boundary conditions on a viscous interface. For a perfect interface only the twenty five static image singularities are needed (and in the context of pure elasticity, the number is reduced to nine [157]). In addition it is observed from Eqs. (8.47) and (8.48) that the locations of the twenty five image singularities for the upper half-plane are independent of the property of the lower half-plane, while the locations of the fifty *moving* image singularities are reliant on the properties of both half-planes as well as the viscous coefficients. It is found from Eqs. (8.51) and (8.52) that the locations of all the static and moving image singularities for the lower half-plane are dependent on the properties of both half-planes as well as the viscous coefficients.

The discussions presented in this section are restricted to mathematically non-degenerate materials. It is expected that for degenerate materials such as the isotropic material the static and moving image singularities are not simply concentrated forces and dislocations.

For the mathematically degenerate materials, some of the twenty five static image singularities may coalesce into one static singularity and some of the fifty moving singularities may also converge into one moving singularity, resulting in static and moving double-forces, concentrated couples and other higher-order singularities. It should be pointed out that even though the image singularity discussions for an isotropic elastic half-plane and for an isotropic elastic bimaterial with a perfect interface have been carried out [158, 159], the corresponding discussions for an isotropic elastic bimaterial with a viscous interface is still unavailable.

8.5 Time-Dependent Image Force on an Extended Line Dislocation

Here we are also much interested in the image force on the extended line dislocation $\hat{\mathbf{b}}$ (with $\hat{\mathbf{f}} = 0$) due to its interaction with the nearby viscous interface. By using the Peach-Koehler formulation [35, 151, 160], the time-dependent image force acting on the extended line dislocation can be finally derived as

$$\begin{aligned} F_2(t) &= \frac{\hat{\mathbf{b}}^T}{4\pi\hat{x}_2} \left[2\text{Re}\{\mathbf{N}^{-1}\} - \mathbf{L}_1 - 2 \sum_{n=1}^5 \sum_{m=1}^5 \sum_{k=1}^2 \text{Re} \left\{ \mathbf{Y}_{nmk} \frac{\lambda_k t}{\lambda_k t + i(\bar{p}_n - p_m)\hat{x}_2} \right\} \right] \hat{\mathbf{b}} \\ F_1(t) &= 0 \end{aligned} \quad (8.59)$$

where F_1 and F_2 are respectively the components of the image force along the x_1 and x_2 directions, and

$$\begin{aligned} \mathbf{Y}_{nmk} &= \bar{\mathbf{Y}}_{mnk}^T = (\bar{\mathbf{B}}_1 \mathbf{I}_n \bar{\mathbf{B}}_1^{-1}) (\underline{\Psi} \mathbf{I}_k \underline{\Lambda}_0^{-1} \bar{\Psi}^T) (\mathbf{B}_1 \mathbf{I}_m \mathbf{B}_1^{-1})^T \\ &= (\bar{\mathbf{B}}_1 \mathbf{I}_n \bar{\mathbf{B}}_1^{-1}) \left(\frac{\mathbf{v}_k \bar{\mathbf{v}}_k^T}{\delta_k} \right) (\mathbf{B}_1 \mathbf{I}_m \mathbf{B}_1^{-1})^T \end{aligned} \quad (8.60)$$

It is observed that the term in the square brackets on the right-hand side of Eq. (8.59) is a 5×5 time-dependent real and symmetric matrix. In the following we look into the above image force expression in more detail.

8.5.1 Isotropic elastic bimaterials

First it should be stressed that Eq. (8.45) is still valid for any kind of mathematically degenerate materials such as the isotropic elastic material. For example if we assume that both half-planes are isotropic elastic, then $p_1 = p_2 = p_3 = p_4 = p_5 = i$. Consequently we have

$$F_2(t) = \frac{\hat{\mathbf{b}}^T}{4\pi\hat{x}_2} \left[2\text{Re}\{\mathbf{N}^{-1}\} - \mathbf{L}_1 - 2 \sum_{k=1}^2 \frac{\lambda_k t}{\lambda_k t + 2\hat{x}_2} \text{Re} \left(\frac{\mathbf{v}_k \bar{\mathbf{v}}_k^T}{\delta_k} \right) \right] \hat{\mathbf{b}}. \quad (8.61)$$

Due to the fact that the Barnett-Lothe tensors \mathbf{S} , \mathbf{H} and \mathbf{L} for isotropic elastic materials are well known [35], then it is not difficult to determine the explicit value of the above

expression for an elastic dislocation $\hat{\mathbf{b}} = [b_1 \ b_2 \ b_3 \ 0 \ 0]^T$ as

$$F_2(t) = \frac{\mu_1}{4\pi\hat{x}_2(1-\nu_1)(1-\beta^2)} \left[(\alpha + \beta^2)(b_1^2 + b_2^2) - \frac{t(\alpha + 1)}{t + 2t_1}(b_1^2 + \beta^2 b_2^2) \right] + \frac{\mu_1 b_3^2}{4\pi\hat{x}_2} \left(\frac{\mu_2 - \mu_1}{\mu_1 + \mu_2} - \frac{t}{t + 2t_2} \frac{2\mu_2}{\mu_1 + \mu_2} \right) \quad (8.62)$$

where α and β are Dundurs constants given by

$$\alpha = \frac{\mu_2(1-\nu_1) - \mu_1(1-\nu_2)}{\mu_2(1-\nu_1) + \mu_1(1-\nu_2)} \quad \beta = \frac{\mu_2(1-2\nu_1) - \mu_1(1-2\nu_2)}{2[\mu_2(1-\nu_1) + \mu_1(1-\nu_2)]}, \quad (8.63)$$

with μ_i and ν_i ($i = 1, 2$) being the shear moduli and Poisson's ratios, and t_1 and t_2 being two relaxation times given by

$$t_1 = \frac{\hat{x}_2}{\lambda_1} = \frac{2\hat{x}_2\eta_1(1-\nu_1)(1-\beta^2)}{\mu_1(\alpha+1)} \quad t_2 = \frac{\hat{x}_2}{\lambda_2} = \frac{\hat{x}_2\eta_3(\mu_1+\mu_2)}{\mu_1\mu_2} \quad (8.64)$$

If $\eta_1 = \eta_3$ and $0 < \nu_i \leq 1/2$, then it can be easily found that $t_1 < t_2$. In addition $F_2(t)$ is a monotonically decreasing function of t . It is observed that the second term in Eq. (8.62) gives the time-dependent image force due to a screw dislocation b_3 , which is in agreement with the recent result by Wang and Pan [161]. However, the first term in Eq. (8.62) gives the time-dependent image force due to an edge dislocation with Burgers vector (b_1, b_2) , which is new in the literature. At $t = 0$, the first term in Eq. (8.62) is the same as that obtained by Dundurs & Sendeckyj [162] for a perfect interface (also see Ref. 35). It is observed that the first term in Eq. (8.62) depends not only on $b_1^2 + b_2^2$ but also on $b_1^2 + \beta^2 b_2^2$, thus it varies with the direction of the vector (b_1, b_2) . This observation is different from the invariant phenomenon for a perfect interface [35]. When $t \rightarrow \infty$, Eq. (8.62) becomes

$$F_2(\infty) = -\frac{\mu_1 [b_1^2 - \alpha b_2^2 + (1-\nu_1)b_3^2]}{4\pi\hat{x}_2(1-\nu_1)} \quad (8.65)$$

which can be reduced to that derived by Chen et al. [163, eq. (27)] for an edge dislocation ($b_3 = 0$) interacting with a free-sliding interface on which the two shear stresses σ_{12} and σ_{32} are zero. In addition if the two isotropic elastic half-planes possess the same material properties, i.e., $\mu_1 = \mu_2 = \mu$, $\nu_1 = \nu_2 = \nu$, then Eq. (8.62) is further reduced to

$$F_2(t) = -\frac{\mu t}{4\pi\hat{x}_2} \left[\frac{b_1^2}{(1-\nu)(t+2t_1)} + \frac{b_3^2}{t+2t_2} \right] \leq 0, \quad (8.66)$$

where

$$t_1 = \frac{2\hat{x}_2\eta_1(1-\nu)}{\mu} \quad t_2 = \frac{2\hat{x}_2\eta_3}{\mu} \quad (8.67)$$

Equation (8.66) implies that the elastic dislocation is always attracted to the viscous interface at any nonzero time, and that the image force will always be null if the dislocation only contains the b_2 component.

8.5.2 Transversely isotropic multiferroic bimetals

Here we consider a practical situation in which the two multiferroic half-planes are both transversely isotropic, with x_1x_2 -plane being the isotropic plane. If the extended line dislocation contains only the b_1 and b_2 components, then the result is identical to that presented in the previous subsection due the fact that the x_1x_2 -plane is an isotropic plane. We thus consider the two multiferroic half-planes with a screw dislocation $\hat{\mathbf{b}} = [0 \ 0 \ b_3 \ \Delta\phi \ \Delta\varphi]^T$. In this case, it follows from Eq. (8.59) that

$$F_2(t) = \frac{1}{4\pi\hat{x}_2} \left[\mathbf{b}_0^T \left(\frac{4t_0}{t+2t_0} \mathbf{E}^{-1} - \mathbf{C}_1 \right) \mathbf{b}_0 + \frac{2t}{t+2t_0} \tilde{\mathbf{b}}_0^T \mathbf{M} \tilde{\mathbf{b}}_0 \right], \quad (8.68)$$

where

$$\mathbf{C} = \begin{bmatrix} C_{44} & e_{15} & q_{15} \\ e_{15} & -\varepsilon_{11} & -\alpha_{11} \\ q_{15} & -\alpha_{11} & -\mu_{11} \end{bmatrix} \quad \mathbf{E} = \begin{bmatrix} E_{11} & E_{12} & E_{13} \\ E_{12} & E_{22} & E_{23} \\ E_{13} & E_{23} & E_{33} \end{bmatrix} \equiv \mathbf{C}_1^{-1} + \mathbf{C}_2^{-1} \quad (8.69)$$

$$\mathbf{M} = \begin{bmatrix} E_{22} & E_{23} \\ E_{23} & E_{33} \end{bmatrix}^{-1}$$

$$\mathbf{b}_0 = [b_3 \ \Delta\phi \ \Delta\varphi]^T \quad \tilde{\mathbf{b}}_0 = [\Delta\phi \ \Delta\varphi]^T \quad (8.70)$$

and t_0 is a relaxation time defined by

$$t_0 = \frac{\hat{x}_3 \eta_3 |\mathbf{E}|}{E_{22}E_{33} - E_{23}^2} > 0 \quad (8.71)$$

8.5.3 Relaxation time

It is observed from the previous two subsections that *two positive real relaxation times* are inherent in the time-dependent image force expression for an extended line dislocation interacting with a viscous interface between two isotropic elastic half-planes or between two transversely isotropic multiferroic half-planes. For a generally anisotropic multiferroic bimaterial with a viscous interface, if we introduce the following relaxation times

$$t_{nmk} = \bar{t}_{mnk} = i(\bar{p}_n - p_m)/(2\lambda_k), \quad (n, m = 1, 2, 3, 4, 5, \ k = 1, 2) \quad (8.72)$$

then Eq. (8.59) can be further expressed in terms of these relaxation times as

$$F_2(t) = \frac{\hat{\mathbf{b}}^T}{4\pi\hat{x}_2} \left[2\text{Re}\{\mathbf{N}^{-1}\} - \mathbf{L}_1 - 2 \sum_{n=1}^5 \sum_{m=1}^5 \sum_{k=1}^2 \text{Re} \left\{ \mathbf{Y}_{nmk} \frac{t}{t+2t_{nmk}} \right\} \right] \hat{\mathbf{b}}. \quad (8.73)$$

It is observed from Eq. (8.72) that *there exist in total as many as 50 relaxation times*, among which ten are positive real while the other forty are complex with positive real parts and form twenty distinct conjugate pairs. For example, if the two half-planes are occupied by orthotropic elastic materials, then the Stroh eigenvalues and the Hermitian

matrix \mathbf{N} can be obtained explicitly [155, 164]. In this case *there exist four relaxation times* t_k ($k = 1, 2, 3, 4$), given by

$$\begin{aligned} t_1 &= \frac{\sqrt{\xi} \left[\frac{1}{2}(s+1) \right]^{\frac{1}{2}}}{\lambda_1} & t_{2,3} &= \frac{\sqrt{\xi} \left(\left[\frac{1}{2}(s+1) \right]^{\frac{1}{2}} \pm \left[\frac{1}{2}(s-1) \right]^{\frac{1}{2}} \right)}{\lambda_1} \\ t_4 &= \frac{\sqrt{C_{55}^{(1)}/C_{44}^{(1)}}}{\lambda_2}, \end{aligned} \quad (8.74)$$

where $\xi = \sqrt{\rho_{11}/\rho_{22}}$ and $s = (1 + \rho_{11}\rho_{22} - (1 + \rho_{12})^2)/(2\sqrt{\rho_{11}\rho_{22}}) > -1$ with $\rho_{\gamma\beta} = C_{\gamma\beta}^{(1)}/C_{66}^{(1)}$; and the two eigenvalues λ_1, λ_2 are determined by

$$\lambda_1 = \frac{N_{22}}{\eta_1(N_{11}N_{22} - N_{12}\bar{N}_{12})} \quad \lambda_2 = \frac{1}{\eta_3 N_{33}}. \quad (8.75)$$

It is observed from Eq. (8.74) that t_1 and t_4 are always real; while t_2 and t_3 are real when $s \geq 1$, and complex conjugate when $-1 < s < 1$.

8.5.4 Image force for a perfect interface at the initial moment

At the initial moment $t = 0$, the image force can be expressed as

$$F_2(0) = \frac{\hat{\mathbf{b}}^T}{4\pi\hat{x}_2} [2\text{Re}\{\mathbf{N}^{-1}\} - \mathbf{L}_1] \hat{\mathbf{b}} \quad (8.76)$$

which is consistent with the result obtained by Ting & Barnett [165] for a perfect interface between two anisotropic elastic half-planes.

8.5.5 Image force for a free-sliding interface when time approaches infinity

When time $t \rightarrow \infty$, the viscous interface will evolve into a free-sliding one on which the shear stresses σ_{12} and σ_{32} are zero. It follows from Eq. (8.59) that

$$F_2(\infty) = \frac{\hat{\mathbf{b}}^T}{4\pi\hat{x}_2} \left[2\text{Re} \left\{ \mathbf{N}^{-1} - \sum_{n=1}^5 \sum_{m=1}^5 \sum_{k=1}^2 \mathbf{Y}_{nmk} \right\} - \mathbf{L}_1 \right] \hat{\mathbf{b}}. \quad (8.77)$$

If we employ the following identity

$$\begin{aligned} \mathbf{N}^{-1} - \sum_{n=1}^5 \sum_{m=1}^5 \sum_{k=1}^2 \mathbf{Y}_{nmk} &= \mathbf{N}^{-1} - \underline{\Psi}(\mathbf{I}_1 + \mathbf{I}_2)\underline{\Lambda}_0^{-1}\underline{\Psi}^T \\ &= \sum_{k=3}^5 \frac{\mathbf{v}_k \bar{\mathbf{v}}_k^T}{\delta_k} = \begin{bmatrix} 0 & 0 & 0 & 0 & 0 \\ 0 & k_{22} & 0 & k_{24} & k_{25} \\ 0 & 0 & 0 & 0 & 0 \\ 0 & \bar{k}_{24} & 0 & k_{44} & k_{45} \\ 0 & \bar{k}_{25} & 0 & \bar{k}_{45} & k_{55} \end{bmatrix} \end{aligned} \quad (8.78)$$

where k_{ij} can be concisely given by

$$\begin{bmatrix} k_{22} & k_{24} & k_{25} \\ \bar{k}_{24} & k_{44} & k_{45} \\ \bar{k}_{25} & \bar{k}_{45} & k_{55} \end{bmatrix} = \begin{bmatrix} N_{22} & N_{24} & N_{25} \\ \bar{N}_{24} & N_{44} & N_{45} \\ \bar{N}_{25} & \bar{N}_{45} & N_{55} \end{bmatrix}^{-1} \quad (8.79)$$

then Eq. (8.77) can be further simplified as

$$F_2(\infty) = \frac{1}{4\pi\hat{x}_2} [2\tilde{\mathbf{b}}^T \text{Re}\{\tilde{\mathbf{N}}^{-1}\} \tilde{\mathbf{b}} - \hat{\mathbf{b}}^T \mathbf{L}_1 \hat{\mathbf{b}}] \quad (8.80)$$

where

$$\tilde{\mathbf{b}} = [b_2 \quad \Delta\phi \quad \Delta\varphi]^T \quad (8.81)$$

$$\tilde{\mathbf{N}} = \begin{bmatrix} N_{22} & N_{24} & N_{25} \\ \bar{N}_{24} & N_{44} & N_{45} \\ \bar{N}_{25} & \bar{N}_{45} & N_{55} \end{bmatrix} \quad (8.82)$$

Expression (8.80) indicates that (i) all the rest components in \mathbf{N} except for those appearing in $\tilde{\mathbf{N}}$ have no influence on $F_2(\infty)$; (ii) the material properties in the lower multiferroic half-plane have no influence on $F_2(\infty)$ for an elastic dislocation $\hat{\mathbf{b}} = [b_1 \ 0 \ b_3 \ 0 \ 0]^T$ (i.e., $\tilde{\mathbf{b}} = \mathbf{0}$), and (iii) $F_2(\infty)$ varies with rotations about the x_3 -axis due to the fact that the term $\tilde{\mathbf{b}}^T \text{Re}\{\tilde{\mathbf{N}}^{-1}\} \tilde{\mathbf{b}}$ changes with rotations about the x_3 -axis, which is quite different to the invariance property of the image force with the orientation of the perfect interface [35, 165]. Furthermore Eq. (8.80) for the image force on an extended dislocation interacting with a free-sliding interface is strikingly simple! It is of interest to notice that Wang et al. [166] have derived an expression for the image force on a line dislocation interacting with a free-sliding interface between two piezoelectric half-planes. In the context of multiferroic bimaterial, that expression can be slightly modified as

$$F_2(\infty) = \frac{\hat{\mathbf{b}}^T}{4\pi\hat{x}_2} \left[2\text{Re} \left\{ \begin{bmatrix} \mathbf{J}_1 \mathbf{N} \\ \mathbf{J}_2 \end{bmatrix}^{-1} \begin{bmatrix} \mathbf{J}_1 \\ \mathbf{0}_{2 \times 5} \end{bmatrix} \right\} - \mathbf{L}_1 \right] \hat{\mathbf{b}}, \quad (8.83)$$

where

$$\mathbf{J}_1 = \begin{bmatrix} 0 & 1 & 0 & 0 & 0 \\ 0 & 0 & 0 & 1 & 0 \\ 0 & 0 & 0 & 0 & 1 \end{bmatrix} \quad \mathbf{J}_2 = \begin{bmatrix} 1 & 0 & 0 & 0 & 0 \\ 0 & 0 & 1 & 0 & 0 \end{bmatrix} \quad (8.84)$$

Even though it can be proved that Eqs. (8.80) and (8.83) are equivalent, Eq. (8.83) is still not as explicit and concise as Eq. (8.80).

8.5.6 A comparison of image force $F_2(0)$ with $F_2(\infty)$

Here it is of interest to compare the value of the image force $F_2(0)$ for a perfect interface with that of $F_2(\infty)$ for a free-sliding interface. It follows from Eqs. (8.76) and (8.77) that

$$F_2(0) - F_2(\infty) = \frac{1}{2\pi\hat{x}_2} \left[\frac{(\hat{\mathbf{b}}^T \mathbf{v}_1)(\bar{\mathbf{v}}_1^T \hat{\mathbf{b}})}{\delta_1} + \frac{(\hat{\mathbf{b}}^T \mathbf{v}_2)(\bar{\mathbf{v}}_2^T \hat{\mathbf{b}})}{\delta_2} \right] \geq 0 \quad (8.85)$$

due to the fact that both δ_1 and δ_2 are positive. Equation (8.85) states that the image force on an extended line dislocation interacting with a perfect interface is always equal to or larger than that on the same dislocation interacting with a free-sliding interface. In other words a free-sliding interface is *more attractive* to the extended line dislocation than a perfect interface. If the two multiferroic half-planes are exactly the same, then $F_2(\infty) \leq F_2(0) = 0$, which means that the dislocation is always attracted to a free-sliding interface between two identical multiferroic half-planes. If we can find a real extended Burgers vector $\hat{\mathbf{b}}$ which is orthogonal to both \mathbf{v}_1 and \mathbf{v}_2 , i.e., $\mathbf{v}_1^T \hat{\mathbf{b}} = \mathbf{v}_2^T \hat{\mathbf{b}} = 0$, then $F_2(0) \equiv F_2(\infty)$. Let $\mathbf{v}'_i, \mathbf{v}''_i$ be, respectively, the real and imaginary parts of \mathbf{v}_i . Then the condition $\hat{\mathbf{b}}^T \mathbf{v}_1 = \hat{\mathbf{b}}^T \mathbf{v}_2 = 0$ is equivalent to the following set of four independent linear algebraic equations for the unknown $\hat{\mathbf{b}}$,

$$\begin{bmatrix} \mathbf{v}'_1 & \mathbf{v}''_1 & \mathbf{v}'_2 & \mathbf{v}''_2 \end{bmatrix}^T \hat{\mathbf{b}} = \mathbf{0}_{4 \times 1} \quad (8.86)$$

through which we can find at least a nonzero solution for the five-dimension real vector $\hat{\mathbf{b}}$. In other words we can always find an extended line dislocation $\hat{\mathbf{b}}$ such that the image force on the dislocation interacting with a perfect interface is just equal to that on the same dislocation interacting with a free-sliding interface.

8.6 Conclusions

We have derived the elegant and exact closed-form Green's functions Eqs. (8.38) and (8.39) for a generally anisotropic multiferroic bimaterial with a viscous interface subjected to an extended line force and an extended line dislocation in the upper half-plane. The obtained Green's function solutions are then interpreted physically in terms of the image singularities in the form of an extended line force and an extended line dislocation. It is found that *twenty five static* image singularities and *fifty moving* image singularities in the form of an extended line force and an extended line dislocation for the upper or lower half-plane are needed to satisfy exactly the interfacial conditions on a viscous interface. For a perfect interface, on the other hand, *only twenty five static image* singularities are needed. (In the context of pure elasticity, the number is further reduced to *nine* [157].) The image force on an extended line dislocation due to its interaction with the viscous interface is further derived, given explicitly by Eqs. (8.59) and (8.60). In order to better understand the influence of the viscous interface on the mobility of the extended line dislocation, we then look into the image force expression for six different cases: (i) isotropic elastic bimaterials, (ii) transversely isotropic multiferroic bimaterials with the symmetry axes along the x_3 -axis, (iii) relaxation time, (iv) image force at the initial moment for a perfect interface, (v) image force at infinite time for a free-sliding interface, and (vi) a comparison of the image force at the initial moment to that at infinite time. The results show that

1. the derived image force expression is valid for any kind of mathematical degenerate materials;
2. as many as *fifty relaxation times* are needed to describe the time-dependent image force (see Eq. (8.73)) for a viscous interface between two generally anisotropic multiferroic half-planes, and

3. a free-sliding interface is *more attractive* to the line dislocation than a perfect interface.

It is expected that the Green's functions presented in this paper could be directly applied to the study of dislocation induced mobility in novel multiferroic bimetals. For more complicated boundary value problems, the derived exact closed-form Green's functions can be utilized as the kernel functions in any boundary integral formulation. Since only the boundary of the problem needs to be discretized, field concentration and singularity can be more efficiently handled than the domain-based discretization method.

8.7 An appendix: Proof that p cannot be real in Eq. (8.3)

If we choose $u_k = a_k f(z_p)$ ($k = 1, 2, 3$), $\phi = a_4 f(z_p)$ and $\varphi = a_5 f(z_p)$ with $z_p = x_1 + px_2$, then differentiation of u_k , ϕ and φ leads to

$$\begin{aligned} u_{k,l} &= (\delta_{l1} + p\delta_{l2})a_k f'(z_p) \\ \phi_{,l} &= (\delta_{l1} + p\delta_{l2})a_4 f'(z_p) \quad \varphi_{,l} = (\delta_{l1} + p\delta_{l2})a_5 f'(z_p) \end{aligned} \quad (8.87)$$

where δ_{li} is the Kronecker delta.

Consequently, satisfaction of $\sigma_{ij,j} = 0$, $D_{i,i} = 0$, and $B_{i,i} = 0$ yields (assuming constant material properties in the solid)

$$(C_{ijks}a_k + e_{sij}a_4 + q_{sij}a_5)(\delta_{j1} + p\delta_{j2})(\delta_{s1} + p\delta_{s2}) = 0 \quad (8.88a)$$

$$(e_{iks}a_k - \epsilon_{is}a_4 - \alpha_{is}a_5)(\delta_{i1} + p\delta_{i2})(\delta_{s1} + p\delta_{s2}) = 0 \quad (8.88b)$$

$$(q_{iks}a_k - \alpha_{is}a_4 - \mu_{is}a_5)(\delta_{i1} + p\delta_{i2})(\delta_{s1} + p\delta_{s2}) = 0 \quad (8.88c)$$

If p were real, multiplication of Eqs. (8.88a), (8.88b), and (8.88c) by a_i , a_4 and a_5 , respectively, and subtraction of the results would lead to

$$\begin{aligned} C_{ijks} [a_i(\delta_{j1} + p\delta_{j2})] [a_k(\delta_{s1} + p\delta_{s2})] + \epsilon_{is} [a_4(\delta_{i1} + p\delta_{i2})] [a_4(\delta_{s1} + p\delta_{s2})] \\ + 2\alpha_{is} [a_4(\delta_{i1} + p\delta_{i2})] [a_5(\delta_{s1} + p\delta_{s2})] + \mu_{is} [a_5(\delta_{i1} + p\delta_{i2})] [a_5(\delta_{s1} + p\delta_{s2})] = 0 \end{aligned} \quad (8.89)$$

which violates the positive definite (elastic and electromagnetic) energy conditions

$$C_{ijks}u_{i,j}u_{k,s} > 0 \quad \epsilon_{is}E_iE_s + 2\alpha_{is}E_iH_s + \mu_{is}H_iH_s > 0 \quad (8.90)$$

where $E_i = -\phi_{,i}$ and $H_i = -\varphi_{,i}$ are the electric field and magnetic field, respectively.

It then follows that the ten eigenvalues of Eq. (8.3) should form five conjugate pairs since all the three matrices \mathbf{Q} , \mathbf{R} , and \mathbf{T} in Eq. (8.3) are real.

Chapter 9

Role of Material Property Gradient and Anisotropy in Thermoelectric Materials

9.1 Introduction

Thermoelectric materials, which possess the inherent property of coupled transport of heat and electricity, are becoming increasingly important in the field of energy production, conversion, conservation, and nondestructive testing (NDT) [167–172]. Recently nanostructural thermoelectric materials have shown great promise for thermoelectric applications because these nanostructural materials can reduce the thermal conductivity more than the electrical conductivity by interface scattering. In other words, with these novel materials, one can achieve an increase in the power factor, with the consequence of increasing the thermoelectric figure of merit ZT [173–176].

It has been discovered that the noncontacting thermoelectric technique can be used to detect various imperfections in conducting metals exhibiting thermoelectric effect when the specimen to be tested is subjected to directional heating and cooling [167, 177, 178]. The physics of the process is relatively simple: An external heating or cooling is applied to the specimen to produce a modest temperature gradient in the test material domain. Since the host material and the inclusions (more accurately called inhomogeneities) within it have different material properties, different temperature field and thus different thermoelectric potentials will be induced along the interfaces between the host material and inclusion. These potential differences will drive opposite thermoelectric currents (and thus two local current loops) inside and outside the inclusion, which can be finally detected by scanning the specimen with a sensitive magnetometer. It should be pointed out that, the capability of detecting these imperfections depends on the thermoelectric background signal produced by the intrinsic anisotropy and inhomogeneity (or grading composition) of the material. In other words, a clear understanding of the effect of both anisotropy and inhomogeneity on the material response is required. Nayfeh et al. [168] presented an analytic model to calculate the magnetic field produced by thermoelectric currents in homogeneous but anisotropic materials under two-dimensional (2D) heating and cooling. Carreon et al. [169], on the other hand, presented another analytic model to calculate the normal and tangential magnetic fields produced by thermoelectric currents in an isotropic but linearly gradient slender

rectangular bar under axial heating and cooling. However, since most materials are both inhomogeneous and anisotropic (even though weakly), a study is needed on the coupling influence of the material anisotropy and inhomogeneity on the material response, which motivates this investigation. For simplicity, here we consider an exponentially graded anisotropic material under 2D heating and cooling, and we derive the explicit solutions by converting the original problem into two inhomogeneous Helmholtz equations via eigenvalue/eigenvector separation. The corresponding 2D problem in homogeneous anisotropic materials is also discussed by means of the elegant complex variable method. These include the explicit solutions for a line heat source in an infinite homogeneous anisotropic material and in one of two bonded anisotropic half-planes. The correctness of the methods is verified by reducing our results to the existing simple solutions obtained by Nayfeh et al. [168], and by comparing the results from our eigenvalue/eigenvector separation approach and complex-variable method. The effect of the material gradient and anisotropy on the induced fields is clearly demonstrated and its impact on the nondestructive evaluation of materials is also discussed.

9.2 A Line Heat Source in an Infinite Exponentially Gradient Anisotropic Thermoelectric Material

In this section, we present an analytic model to predict the magnetic background signal caused in inhomogeneous anisotropic media.

For anisotropic materials, the electrical current density \mathbf{j} and thermal heat flux \mathbf{h} vectors are related to both electric potential Φ and temperature T through [168, 170]

$$\begin{aligned} j_i &= -\sigma_{ij}\Phi_{,j} - \epsilon_{ij}T_{,j} \\ h_i &= -\bar{\epsilon}_{ij}\Phi_{,j} - \kappa_{ij}T_{,j} \end{aligned} \quad (9.1)$$

where the subscript “, j ” to Φ and T denotes the derivative with respect to the j^{th} coordinate x_j ($x_1 = x$, $x_2 = y$, $x_3 = z$), σ_{ij} denotes the electrical conductivity measured at a uniform temperature, κ_{ij} is the thermal conductivity at zero electrical field, ϵ_{ij} and $\bar{\epsilon}_{ij}$ are thermoelectric coupling coefficients. These coupling coefficients can be expressed in terms of the absolute thermoelectric power S and the electrical conductivity σ_{ij} of the material as $\epsilon_{ij} = S\sigma_{ij}$ and $\bar{\epsilon}_{ij} = ST\sigma_{ij}$. Furthermore, for gradient materials as studied in this section, σ_{ij} , κ_{ij} , ϵ_{ij} and $\bar{\epsilon}_{ij}$ are all functions of the coordinates $x_1 = x$, $x_2 = y$, $x_3 = z$.

The electrical current density and thermal heat flux vectors should satisfy the following equations

$$\begin{aligned} \nabla \cdot \mathbf{j} &= 0 \\ \nabla \cdot \mathbf{h} &= q_{\text{gen}} \end{aligned} \quad (9.2)$$

where q_{gen} is the power generated per unit volume. It is obvious that the induced electrical current density (thus the magnetic field) is proportional to the strength of the heat power emanated from the source. Thus the magnitude of the induced magnetic field can be controlled by the applied temperature source so that the associated magneto-thermal transport effect can be neglected.

Let us consider an infinite line heat source in an infinite inhomogeneous anisotropic material. We first assume that σ_{ij} , κ_{ij} , ϵ_{ij} and $\bar{\epsilon}_{ij}$ are exponentially varied in the xy -plane in the same manner along the x and y directions as follows,

$$\begin{bmatrix} \sigma_{ij} & \epsilon_{ij} & \bar{\epsilon}_{ij} & \kappa_{ij} \end{bmatrix} = \exp(2\beta_1 x + 2\beta_2 y) \begin{bmatrix} \sigma_{ij}^0 & \epsilon_{ij}^0 & \bar{\epsilon}_{ij}^0 & \kappa_{ij}^0 \end{bmatrix} \quad (9.3)$$

where σ_{ij}^0 , ϵ_{ij}^0 , $\bar{\epsilon}_{ij}^0$, κ_{ij}^0 , β_1 and β_2 are all material constants.

We point out that functionally graded materials (FGMs) can be fabricated for special applications [51, 52]. They can be varied in many different ways and in different orientations in the space. The exponential variation is a special case which has been investigated in the FGM community for over twenty years [59, 60]. For such a special variation, it is often possible to derive either an analytical solution or even an exact-closed form solution (as the one presented in this paper), serving as benchmarks for future numerical simulation. However, other complicated spatial variation can be piecewise approximated when solving the real problem via a boundary integral equation formulation. In particular, when the material gradients are not too large, the exponential variation in material properties studied here will approximate a linear variation in material properties. We also point out that closed-form solutions can still be obtained for some non-exponential variations of the material properties [179, 180].

Under the above assumption, the principal directions of the electrical conductivity, thermal conductivity and thermoelectric coupling tensors do not change at different locations. Furthermore, for the convenience of analysis, we assume that the electrical conductivity, thermal conductivity and thermoelectric coupling tensors all exhibit the same principal directions, though their degree of anisotropy might be very different [168]. Without loss of generality, in the following we assume that the three Cartesian coordinates x , y and z are established along the principal directions. The infinite line heat source is parallel to the z -axis and passes through $x = x_0$ and $y = y_0$. Therefore, we can write $q_{\text{gen}} = Q\delta(x - x_0)\delta(y - y_0)$, where Q denotes the total heat power emanated from a unit length of the line source and $\delta(\cdot)$ is the Dirac delta function. Consequently the problem becomes two dimensional, with the electric potential and temperature being only functions of the coordinates x and y . By keeping the above assumptions in mind and by substituting Eq. (9.1) into Eq. (9.2), we finally obtain the following set of coupled inhomogeneous partial differential equations

$$\begin{aligned} & \begin{bmatrix} \sigma_1^0 & \epsilon_1^0 \\ \epsilon_1^0 & \frac{\kappa(\epsilon_2^0)^2}{\eta\sigma_2^0} \end{bmatrix} \begin{bmatrix} \frac{\partial^2 \Phi}{\partial x^2} \\ \frac{\partial^2 T}{\partial x^2} \end{bmatrix} + \begin{bmatrix} \sigma_2^0 & \epsilon_2^0 \\ \epsilon_2^0 & \frac{(\epsilon_2^0)^2}{\eta\sigma_2^0} \end{bmatrix} \begin{bmatrix} \frac{\partial^2 \Phi}{\partial y^2} \\ \frac{\partial^2 T}{\partial y^2} \end{bmatrix} \\ & + 2\beta_1 \begin{bmatrix} \sigma_1^0 & \epsilon_1^0 \\ \epsilon_1^0 & \frac{\kappa(\epsilon_2^0)^2}{\eta\sigma_2^0} \end{bmatrix} \begin{bmatrix} \frac{\partial \Phi}{\partial x} \\ \frac{\partial T}{\partial x} \end{bmatrix} + 2\beta_2 \begin{bmatrix} \sigma_2^0 & \epsilon_2^0 \\ \epsilon_2^0 & \frac{(\epsilon_2^0)^2}{\eta\sigma_2^0} \end{bmatrix} \begin{bmatrix} \frac{\partial \Phi}{\partial y} \\ \frac{\partial T}{\partial y} \end{bmatrix} \\ & = - \frac{\exp(-2\beta_1 x_0 - 2\beta_2 y_0)(\epsilon_2^0)^2 Q}{\eta\sigma_2^0 \kappa_2^0} \delta(x - x_0)\delta(y - y_0) \begin{bmatrix} 0 \\ 1 \end{bmatrix} \quad (9.4) \end{aligned}$$

where $\eta = \epsilon_2^0 \bar{\epsilon}_2^0 / (\sigma_2^0 \kappa_2^0)$ is the dimensionless thermoelectric coupling parameter. We mention that during the derivation, we have utilized the identity $\epsilon_1^0 / \epsilon_2^0 = \bar{\epsilon}_1^0 / \bar{\epsilon}_2^0$. It is also

worthy to point out that, for typical metals the coupling parameter η is relatively small, somewhere between 10^{-3} and 10^{-2} [167–169].

In order to solve Eq. (9.4), we next consider the following eigenvalue problem:

$$\begin{bmatrix} \sigma_1^0 & \epsilon_1^0 \\ \epsilon_1^0 & \frac{\kappa(\epsilon_2^0)^2}{\eta\sigma_2^0} \end{bmatrix} \mathbf{v} = \lambda \begin{bmatrix} \sigma_2^0 & \epsilon_2^0 \\ \epsilon_2^0 & \frac{(\epsilon_2^0)^2}{\eta\sigma_2^0} \end{bmatrix} \mathbf{v} \quad (9.5)$$

The two eigenvalues of the above equation can be easily determined as

$$\begin{aligned} \lambda_1 &= \frac{\sigma + \kappa - 2\epsilon + \eta + \sqrt{(\sigma - \kappa)^2 - 4\eta(\sigma - \epsilon)(\epsilon - \kappa)}}{2(1 - \eta)} > 0 \\ \lambda_2 &= \frac{\sigma + \kappa - 2\epsilon - \eta - \sqrt{(\sigma - \kappa)^2 - 4\eta(\sigma - \epsilon)(\epsilon - \kappa)}}{2(1 - \eta)} > 0 \end{aligned} \quad (9.6)$$

where $\sigma = \sigma_1^0/\sigma_2^0$, $\epsilon = \epsilon_1^0/\epsilon_2^0$, and $\kappa = \kappa_1^0/\kappa_2^0$ are ratios of the material properties. The two eigenvectors associated with the eigenvalues are

$$\mathbf{v}_1 = \begin{bmatrix} \epsilon_2^0(\lambda_1 - \epsilon) \\ \sigma_2^0(\sigma - \lambda_1) \end{bmatrix} \quad \mathbf{v}_2 = \begin{bmatrix} \epsilon_2^0(\lambda_2 - \epsilon) \\ \sigma_2^0(\sigma - \lambda_2) \end{bmatrix} \quad (9.7)$$

Apparently due to the fact that both matrices in Eq. (9.5) are real and symmetric, then we have the following orthogonal relationships

$$\begin{aligned} \begin{bmatrix} \mathbf{v}_1^T \\ \mathbf{v}_2^T \end{bmatrix} \begin{bmatrix} \sigma_2^0 & \epsilon_2^0 \\ \epsilon_2^0 & \frac{(\epsilon_2^0)^2}{\eta\sigma_2^0} \end{bmatrix} \begin{bmatrix} \mathbf{v}_1 & \mathbf{v}_2 \end{bmatrix} &= \begin{bmatrix} \delta_1 & 0 \\ 0 & \delta_2 \end{bmatrix} \\ \begin{bmatrix} \mathbf{v}_1^T \\ \mathbf{v}_2^T \end{bmatrix} \begin{bmatrix} \sigma_1^0 & \epsilon_1^0 \\ \epsilon_1^0 & \frac{\kappa(\epsilon_2^0)^2}{\eta\sigma_2^0} \end{bmatrix} \begin{bmatrix} \mathbf{v}_1 & \mathbf{v}_2 \end{bmatrix} &= \begin{bmatrix} \lambda_1\delta_1 & 0 \\ 0 & \lambda_2\delta_2 \end{bmatrix} \end{aligned} \quad (9.8)$$

where

$$\begin{aligned} \delta_1 &= \sigma_2^0(\epsilon_2^0)^2 \left[(\lambda_1 - \epsilon)(2\sigma - \epsilon - \lambda_1) + \frac{(\sigma - \lambda_1)^2}{\eta} \right] > 0 \\ \delta_2 &= \sigma_2^0(\epsilon_2^0)^2 \left[(\lambda_2 - \epsilon)(2\sigma - \epsilon - \lambda_2) + \frac{(\sigma - \lambda_2)^2}{\eta} \right] > 0 \end{aligned} \quad (9.9)$$

Now we introduce two new functions F and G which are related to electric potential and temperature through

$$\begin{bmatrix} \Phi \\ T \end{bmatrix} = \begin{bmatrix} \mathbf{v}_1 & \mathbf{v}_2 \end{bmatrix} \begin{bmatrix} F \\ G \end{bmatrix} \quad (9.10)$$

In view of the orthogonal relationships in Eq. (9.8), Eq. (9.4) can now be decoupled into

$$\begin{aligned} \frac{\partial^2 F}{\partial x^2} + \frac{1}{\lambda_1} \frac{\partial^2 F}{\partial y^2} + 2\beta_1 \frac{\partial F}{\partial x} + \frac{2\beta_2}{\lambda_1} \frac{\partial F}{\partial y} &= -\frac{2\pi e^{-\beta_1 x_0 - \beta_2 y_0} P_1}{\sqrt{\lambda_1}} \delta(x - x_0) \delta(y - y_0) \\ \frac{\partial^2 G}{\partial x^2} + \frac{1}{\lambda_2} \frac{\partial^2 G}{\partial y^2} + 2\beta_1 \frac{\partial G}{\partial x} + \frac{2\beta_2}{\lambda_2} \frac{\partial G}{\partial y} &= -\frac{2\pi e^{-\beta_1 x_0 - \beta_2 y_0} P_2}{\sqrt{\lambda_2}} \delta(x - x_0) \delta(y - y_0) \end{aligned} \quad (9.11)$$

where

$$\begin{aligned} P_1 &= \frac{\exp(-\beta_1 x_0 - \beta_2 y_0)(\sigma - \lambda_1)(\epsilon_2^0)^2 Q}{2\pi\eta\kappa_2^0\sqrt{\lambda_1}\delta_1} \\ P_2 &= \frac{\exp(-\beta_1 x_0 - \beta_2 y_0)(\sigma - \lambda_2)(\epsilon_2^0)^2 Q}{2\pi\eta\kappa_2^0\sqrt{\lambda_2}\delta_2} \end{aligned} \quad (9.12)$$

Equation (9.11) can be equivalently expressed by

$$\begin{aligned} \frac{\partial^2 F}{\partial x^2} + \frac{\partial^2 F}{\partial(\sqrt{\lambda_1}y)^2} + 2\beta_1 \frac{\partial F}{\partial x} + \frac{2\beta_2}{\sqrt{\lambda_1}} \frac{\partial F}{\partial(\sqrt{\lambda_1}y)} = \\ -2\pi\exp(-\beta_1 x_0 - \beta_2 y_0)P_1\delta(x-x_0)\delta(\sqrt{\lambda_1}y - \sqrt{\lambda_1}y_0) \\ \frac{\partial^2 G}{\partial x^2} + \frac{\partial^2 G}{\partial(\sqrt{\lambda_2}y)^2} + 2\beta_1 \frac{\partial G}{\partial x} + \frac{2\beta_2}{\sqrt{\lambda_2}} \frac{\partial G}{\partial(\sqrt{\lambda_2}y)} = \\ -2\pi\exp(-\beta_1 x_0 - \beta_2 y_0)P_2\delta(x-x_0)\delta(\sqrt{\lambda_2}y - \sqrt{\lambda_2}y_0) \end{aligned} \quad (9.13)$$

In order to solve Eq. (9.13), we further introduce two new functions such that

$$F = \exp(-\beta_1 x - \beta_2 y)f \quad G = \exp(-\beta_1 x - \beta_2 y)g \quad (9.14)$$

As a result, Eq. (9.13) can be expressed into two inhomogeneous Helmholtz equations for f and g as

$$\begin{aligned} \frac{\partial^2 f}{\partial x^2} + \frac{\partial^2 f}{\partial(\sqrt{\lambda_1}y)^2} - \rho_1^2 f &= -2\pi P_1\delta(x-x_0)\delta(\sqrt{\lambda_1}y - \sqrt{\lambda_1}y_0) \\ \frac{\partial^2 g}{\partial x^2} + \frac{\partial^2 g}{\partial(\sqrt{\lambda_2}y)^2} - \rho_2^2 g &= -2\pi P_2\delta(x-x_0)\delta(\sqrt{\lambda_2}y - \sqrt{\lambda_2}y_0) \end{aligned} \quad (9.15)$$

where

$$\rho_1 = \sqrt{\beta_1^2 + \frac{\beta_2^2}{\lambda_1}} \quad \rho_2 = \sqrt{\beta_1^2 + \frac{\beta_2^2}{\lambda_2}} \quad (9.16)$$

The solutions to Eq. (9.15) can now be conveniently given by

$$\begin{aligned} f &= P_1 K_0 \left[\rho_1 \sqrt{(x-x_0)^2 + \lambda_1(y-y_0)^2} \right] \\ g &= P_2 K_0 \left[\rho_2 \sqrt{(x-x_0)^2 + \lambda_2(y-y_0)^2} \right] \end{aligned} \quad (9.17)$$

where K_n is the n^{th} order modified Bessel function of the second kind.

In view of Eqs. (9.10), (9.14) and (9.17), the electric potential and the temperature induced by the line heat source can be determined as

$$\begin{aligned}
\frac{\Phi}{Q} &= \frac{\epsilon_2^{03} (\sigma - \lambda_1)(\lambda_1 - \epsilon)}{2\pi\eta\kappa_2^0\sqrt{\lambda_1}\delta_1} \frac{K_0 \left[\rho_1 \sqrt{(x-x_0)^2 + \lambda_1(y-y_0)^2} \right]}{\exp[\beta_1(x+x_0) + \beta_2(y+y_0)]} \\
&\quad + \frac{\epsilon_2^{03} (\sigma - \lambda_2)(\lambda_2 - \epsilon)}{2\pi\eta\kappa_2^0\sqrt{\lambda_2}\delta_2} \frac{K_0 \left[\rho_2 \sqrt{(x-x_0)^2 + \lambda_2(y-y_0)^2} \right]}{\exp[\beta_1(x+x_0) + \beta_2(y+y_0)]} \\
\frac{T}{Q} &= \frac{\sigma_2^0(\epsilon_2^0)^2(\sigma - \lambda_1)^2}{2\pi\eta\kappa_2^0\sqrt{\lambda_1}\delta_1} \frac{K_0 \left[\rho_1 \sqrt{(x-x_0)^2 + \lambda_1(y-y_0)^2} \right]}{\exp[\beta_1(x+x_0) + \beta_2(y+y_0)]} \\
&\quad + \frac{\sigma_2^0(\epsilon_2^0)^2(\sigma - \lambda_2)^2}{2\pi\eta\kappa_2^0\sqrt{\lambda_2}\delta_2} \frac{K_0 \left[\rho_2 \sqrt{(x-x_0)^2 + \lambda_2(y-y_0)^2} \right]}{\exp[\beta_1(x+x_0) + \beta_2(y+y_0)]}
\end{aligned} \tag{9.18}$$

When $\beta_1 = \beta_2 = 0$ for the homogeneous material, the present solutions are reduced to those in Nayfeh et al. [168] by noticing the following asymptotic behavior for $K_0(x)$

$$K_0(x) \rightarrow -\ln(x/2) - \gamma \text{ when } x \rightarrow 0^+ \tag{9.19}$$

with $\gamma = 0.57721$ being the Euler constant.

Once we obtain the expressions for the electric potential and temperature, it is not difficult to derive the electrical current density and heat flux vectors as follows.

$$\begin{aligned}
j_1 &= \frac{Q\sigma_2^0\epsilon_2^{03}(\sigma - \lambda_1)(\sigma - \epsilon)}{2\pi\eta\kappa_2^0\sqrt{\lambda_1}\delta_1} Y_1(x, y, \lambda_1, \rho_1) \\
&\quad + \frac{Q\sigma_2^0\epsilon_2^{03}(\sigma - \lambda_2)(\sigma - \epsilon)}{2\pi\eta\kappa_2^0\sqrt{\lambda_2}\delta_2} Y_1(x, y, \lambda_2, \rho_2) \\
j_2 &= \frac{Q\sigma_2^0\epsilon_2^{03}(\sigma - \lambda_1)(\sigma - \epsilon)}{2\pi\eta\kappa_2^0\sqrt{\lambda_1}\delta_1} Y_2(x, y, \lambda_1, \rho_1) \\
&\quad + \frac{Q\sigma_2^0\epsilon_2^{03}(\sigma - \lambda_2)(\sigma - \epsilon)}{2\pi\eta\kappa_2^0\sqrt{\lambda_2}\delta_2} Y_2(x, y, \lambda_2, \rho_2)
\end{aligned} \tag{9.20}$$

$$\begin{aligned}
h_1 &= \frac{Q\sigma_2^0(\epsilon_2^0)^2(\sigma - \lambda_1)[\sigma - \lambda_1 + \eta(\lambda_1 - \epsilon)]}{2\pi\eta\sqrt{\lambda_1}\delta_1} Y_1(x, y, \lambda_1, \rho_1) \\
&\quad + \frac{Q\sigma_2^0(\epsilon_2^0)^2(\sigma - \lambda_2)[\sigma - \lambda_2 + \eta(\lambda_2 - \epsilon)]}{2\pi\eta\sqrt{\lambda_2}\delta_1} Y_1(x, y, \lambda_2, \rho_2) \\
h_2 &= \frac{Q\sigma_2^0(\epsilon_2^0)^2(\sigma - \lambda_1)[\sigma - \lambda_1 + \eta(\lambda_1 - \epsilon)]}{2\pi\eta\sqrt{\lambda_1}\delta_1} Y_2(x, y, \lambda_1, \rho_1) \\
&\quad + \frac{Q\sigma_2^0(\epsilon_2^0)^2(\sigma - \lambda_1)[\sigma - \lambda_1 + \eta(\lambda_1 - \epsilon)]}{2\pi\eta\sqrt{\lambda_1}\delta_1} Y_2(x, y, \lambda_2, \rho_2)
\end{aligned} \tag{9.21}$$

where the functions Y_1 and Y_2 are defined as

$$\begin{aligned}
Y_1(x, y, \lambda, \rho) &= \frac{\beta_1 \lambda K_0 \left[\rho \sqrt{(x-x_0)^2 + \lambda(y-y_0)^2} \right]}{\exp[-\beta_1(x-x_0) - \beta_2(y-y_0)]} \\
&\quad + \frac{\rho \lambda (x-x_0) K_1 \left[\rho \sqrt{(x-x_0)^2 + \lambda(y-y_0)^2} \right]}{\exp[-\beta_1(x-x_0) - \beta_2(y-y_0)] \sqrt{(x-x_0)^2 + \lambda(y-y_0)^2}} \\
Y_2(x, y, \lambda, \rho) &= \frac{\beta_2 K_0 \left[\rho \sqrt{(x-x_0)^2 + \lambda(y-y_0)^2} \right]}{\exp[-\beta_1(x-x_0) - \beta_2(y-y_0)]} \\
&\quad + \frac{\rho \lambda (y-y_0) K_1 \left[\rho \sqrt{(x-x_0)^2 + \lambda(y-y_0)^2} \right]}{\exp[-\beta_1(x-x_0) - \beta_2(y-y_0)] \sqrt{(x-x_0)^2 + \lambda(y-y_0)^2}}
\end{aligned} \tag{9.22}$$

The magnetic field can be obtained from the Maxwell's equation $\nabla \times \mathbf{H} = \mathbf{j}$ by integration. For the current 2D problem, we have

$$H_z = \int j_1 dy \quad \text{or} \quad H_z = - \int j_2 dx \tag{9.23}$$

which can be solved by simple numerical quadrature. It is interesting to point out that if the anisotropic effect is ignored by letting $\sigma, \epsilon, \kappa \rightarrow 1$, the inhomogeneity of the material as described by Eq. (9.3) will not produce any nonvanishing thermoelectric current distribution and the associated nonvanishing thermoelectric magnetic field. This fact can be easily observed from the previous theoretic development.

This analytical solution can be utilized to study the effect of the grading composition on the material behavior/response under different loadings, with the results being applied as guideline in non-contacting and nondestructive evaluation of materials. However, in order to verify the correctness of the derived solution, we now present the complex variable method for the corresponding anisotropic but homogeneous ($\beta_1 = \beta_2 = 0$) material case. It is shown that the solution based on the complex variable method is elegant. Furthermore, the corresponding bimaterial case can be also obtained in a very concise form. Our solution contains many previous results as special cases, and in Section 9.4, numerical results will be presented for both grading and homogeneous material cases based on the two different solution approaches. The effect of the material grading composition and anisotropy is further discussed, showing clearly the importance of them on the material response.

9.3 Complex Variable Formulation for Homogeneous Anisotropic Thermoelectric Materials and its Applications

In the following discussions we will first present the basic complex variable formulation for 2D problems in homogeneous anisotropic thermoelectric materials. Then we derive

the explicit solutions for a line heat source in a homogeneous anisotropic thermoelectric material and in one of two bonded anisotropic thermoelectric half-planes, demonstrating the proposed complex variable method.

9.3.1 Complex Variable Formulation

For homogeneous materials ($\beta_1 = \beta_2 = 0$) in the absence of line source, it is found from Eq. (9.4) that

$$\begin{bmatrix} \sigma_1 & \epsilon_1 \\ \epsilon_1 & \frac{\kappa \epsilon_2^2}{\eta \sigma_2} \end{bmatrix} \begin{bmatrix} \frac{\partial^2 \Phi}{\partial x^2} \\ \frac{\partial^2 T}{\partial x^2} \end{bmatrix} + \begin{bmatrix} \sigma_2 & \epsilon_2 \\ \epsilon_2 & \frac{\epsilon_2^2}{\eta \sigma_2} \end{bmatrix} \begin{bmatrix} \frac{\partial^2 \Phi}{\partial y^2} \\ \frac{\partial^2 T}{\partial y^2} \end{bmatrix} = 0 \quad (9.24)$$

If we further introduce two functions F and G defined in Eq. (9.10), it is found that

$$\frac{\partial^2 F}{\partial x^2} + \frac{1}{\lambda_1} \frac{\partial^2 F}{\partial y^2} = 0 \quad \frac{\partial^2 G}{\partial x^2} + \frac{1}{\lambda_2} \frac{\partial^2 G}{\partial y^2} = 0, \quad (9.25)$$

whose general solutions can be conveniently given by

$$F = \text{Im} \{f_1(z_1)\} \quad G = \text{Im} \{f_2(z_2)\} \quad (9.26)$$

where $z_1 = x + i\sqrt{\lambda_1}y$, $z_2 = x + i\sqrt{\lambda_2}y$. Consequently the electric potential and temperature can be expressed as

$$\mathbf{u} = \begin{bmatrix} \Phi \\ T \end{bmatrix} = \mathbf{A} \text{Im} \{\mathbf{f}(z)\}, \quad (9.27)$$

where

$$\mathbf{A} = [\mathbf{v}_1 \quad \mathbf{v}_2] \quad \mathbf{f}(z) = [f_1(z_1) \quad f_2(z_2)]^T \quad (9.28)$$

On the other hand, in the absence of source, we can introduce two functions ϕ_1 and ϕ_2 such that

$$\begin{aligned} j_1 &= -\frac{\partial \phi_1}{\partial y} & j_2 &= \frac{\partial \phi_1}{\partial x} \\ h_1 &= -\frac{\eta \sigma_2 \kappa_2}{\epsilon_2^2} \frac{\partial \phi_2}{\partial y} & h_2 &= \frac{\eta \sigma_2 \kappa_2}{\epsilon_2^2} \frac{\partial \phi_2}{\partial x} \end{aligned} \quad (9.29)$$

As a result, it follows that the two functions ϕ_1 and ϕ_2 can also be concisely expressed in terms of the analytic function vector $\mathbf{f}(z)$ as

$$\underline{\phi} = \begin{bmatrix} \phi_1 \\ \phi_2 \end{bmatrix} = \mathbf{B} \text{Re} \{\mathbf{f}(z)\}, \quad (9.30)$$

where

$$\mathbf{B} = \begin{bmatrix} \sigma_2 & \epsilon_2 \\ \epsilon_2 & \frac{\epsilon_2^2}{\eta \sigma_2} \end{bmatrix} \mathbf{A} \begin{bmatrix} \sqrt{\lambda_1} & 0 \\ 0 & \sqrt{\lambda_2} \end{bmatrix} = \begin{bmatrix} \sqrt{\lambda_1} \sigma_2 \epsilon_2 (\sigma - \epsilon) & \sqrt{\lambda_2} \sigma_2 \epsilon_2 (\sigma - \epsilon) \\ \sqrt{\lambda_1} \epsilon_2^2 \left(\lambda_1 - \epsilon + \frac{\sigma - \lambda_1}{\eta} \right) & \sqrt{\lambda_2} \epsilon_2^2 \left(\lambda_2 - \epsilon + \frac{\sigma - \lambda_2}{\eta} \right) \end{bmatrix} \quad (9.31)$$

The electrical current density and heat flux vectors can be obtained from Eqs. (9.29) and (9.30) as

$$\begin{aligned} \begin{bmatrix} j_1 \\ h_1 \end{bmatrix} &= \begin{bmatrix} 1 & 0 \\ 0 & \frac{\eta \sigma_2 \kappa_2}{\epsilon_2^2} \end{bmatrix} \mathbf{B} \begin{bmatrix} \sqrt{\lambda_1} & 0 \\ 0 & \sqrt{\lambda_2} \end{bmatrix} \text{Im} \{ \mathbf{f}'(z) \} \\ \begin{bmatrix} j_2 \\ h_2 \end{bmatrix} &= \begin{bmatrix} 1 & 0 \\ 0 & \frac{\eta \sigma_2 \kappa_2}{\epsilon_2^2} \end{bmatrix} \mathbf{B} \text{Re} \{ \mathbf{f}'(z) \} \end{aligned} \quad (9.32)$$

Due to the fact that $\nabla \times \mathbf{H} = \mathbf{j}$, or equivalently

$$\frac{\partial H_z}{\partial y} = j_1 \quad \frac{\partial H_z}{\partial x} = -j_2 \quad (9.33)$$

then the nonzero magnetic field component H_z can also be concisely expressed in terms of $\mathbf{f}(z)$ as

$$H_z = -\phi_1 = -[1 \ 0] \mathbf{B} \text{Re} \{ \mathbf{f}(z) \} = \sigma_2 \epsilon_2 (\epsilon - \sigma) [\sqrt{\lambda_1} \ \sqrt{\lambda_2}] \text{Re} \{ \mathbf{f}(z) \} \quad (9.34)$$

In addition it is found that the matrix \mathbf{AB}^{-1} is symmetric, real, and positive definite given by

$$\mathbf{AB}^{-1} = (\mathbf{AB}^{-1})^T = \sum_{k=1}^2 \left(\begin{bmatrix} \frac{\epsilon_2^2 (\lambda_k - \epsilon)^2}{\delta_k \sqrt{\lambda_k}} & \frac{\sigma_2 \epsilon_2 (\lambda_k - \epsilon) (\sigma - \lambda_k)}{\delta_k \sqrt{\lambda_k}} \\ \frac{\sigma_2 \epsilon_2 (\lambda_k - \epsilon) (\sigma - \lambda_k)}{\delta_k \sqrt{\lambda_k}} & \frac{\sigma_2^2 (\sigma - \lambda_k)^2}{\delta_k \sqrt{\lambda_k}} \end{bmatrix} \right) \quad (9.35)$$

9.3.2 Applications

In the following we apply the derived complex variable formulation to two interesting problems in order to demonstrate its versatility.

A Steady Line Heat Source in a Homogeneous Thermoelectric Material

We first consider a steady line heat source of strength Q located at origin in a homogeneous material. It follows from Eq. (9.30) that

$$\mathbf{f}(z) = \frac{i \epsilon_2^2 Q}{2\pi \eta \sigma_2 \kappa_2} \langle \ln(z_\alpha) \rangle \mathbf{B}^{-1} \begin{bmatrix} 0 \\ 1 \end{bmatrix} \quad (9.36)$$

where $\langle \ln(z_\alpha) \rangle = \text{diag}[\ln(z_1) \ \ln(z_2)]$.

Consequently the electric potential and temperature can be obtained from Eq. (9.27), while the electrical current density and heat flux vectors can be obtained from Eq. (9.32). Particularly it follows from Eq. (9.34) that

$$H_z = \frac{Q \epsilon_2 (\epsilon - \sigma)}{2\pi \kappa_2 (\lambda_1 - \lambda_2) (1 - \eta)} \left[\tan^{-1} \left(\frac{\sqrt{\lambda_1} y}{x} \right) - \tan^{-1} \left(\frac{\sqrt{\lambda_2} y}{x} \right) \right] \quad (9.37)$$

which is just the result obtained by Nayfeh et al. [168]. Thus the correctness of the complex variable method is verified. In addition it is observed that the solution procedure presented here is very simple as compared to previous methods in this field.

A Steady Line Heat Source in Anisotropic Thermoelectric Bimaterials

Next we consider a steady line heat source of strength Q located at $(0, d)$, $d > 0$, in the upper one of two bonded different anisotropic half-planes $y > 0$ (#1) and $y < 0$ (#2). It is assumed that the principal directions for both half-planes are parallel to the x - and y -axes. In addition, the superscripts “(1)” and “(2)” are attached to scalars in the upper and lower half-planes, respectively, while the subscripts 1 and 2 are attached to matrices/vectors in the upper and lower half-planes, respectively. In the following derivations, we will first replace the complex variables z_1 and z_2 by the common complex variable $z = x + iy$ due to the fact that $z_1 = z_2 = z$ on the real axis [153]. When the analysis is finished, the complex variable $z = x + iy$ shall be changed back to the corresponding complex variables z_1 and z_2 .

We assume that the interface between the two half-planes, at $y = 0$, is perfect, i.e. [167],

$$\Phi^{(1)} = \Phi^{(2)} \quad T^{(1)} = T^{(2)} \quad j_2^{(1)} = j_2^{(2)} \quad h_2^{(1)} = h_2^{(2)} \quad (9.38)$$

The above continuity conditions on the interface $y = 0$ can also be equivalently expressed as

$$\mathbf{u}_1 = \mathbf{u}_2 \quad \underline{\varphi}_1 = \underline{\Lambda} \underline{\varphi}_2 \quad (9.39)$$

where $\underline{\Lambda}$ is a 2×2 diagonal matrix defined by

$$\underline{\Lambda} = \text{diag} \left[1 \quad \frac{\eta^{(2)} \sigma_2^{(2)} \kappa_2^{(2)} \epsilon_2^{(1)2}}{\eta^{(1)} \sigma_2^{(1)} \kappa_2^{(1)} \epsilon_2^{(2)2}} \right] \quad (9.40)$$

In view of Eqs. (9.27) and (9.30), the interfacial continuity conditions at $y = 0$ in Eq. (9.39) can also be expressed in terms of the two analytic function vectors $\mathbf{f}_1(z)$ and $\mathbf{f}_2(z)$ as

$$\mathbf{A}_1 \mathbf{f}_1^+(x) - \mathbf{A}_1 \bar{\mathbf{f}}_1^-(x) = \mathbf{A}_2 \mathbf{f}_2^-(x) - \mathbf{A}_2 \bar{\mathbf{f}}_2^+(x) \quad (9.41a)$$

$$\mathbf{B}_1 \mathbf{f}_1^+(x) + \mathbf{B}_1 \bar{\mathbf{f}}_1^-(x) = \underline{\Lambda} \mathbf{B}_2 \mathbf{f}_2^-(x) + \underline{\Lambda} \mathbf{B}_2 \bar{\mathbf{f}}_2^+(x) \quad (9.41b)$$

It follows from Eq. (9.41a) that

$$\begin{aligned} \mathbf{f}_1(z) &= -\mathbf{A}_1^{-1} \mathbf{A}_2 \bar{\mathbf{f}}_2(z) + \mathbf{f}_0(z) + \bar{\mathbf{f}}_0(z) \\ \bar{\mathbf{f}}_1(z) &= -\mathbf{A}_1^{-1} \mathbf{A}_2 \mathbf{f}_2(z) + \mathbf{f}_0(z) + \bar{\mathbf{f}}_0(z) \end{aligned} \quad (9.42)$$

where $\mathbf{f}_0(z)$ is the analytic function vector for a line heat source located at $(0, d)$, $d > 0$, in a homogeneous infinite plane given by

$$\mathbf{f}_0(z) = \frac{i(\epsilon_2^{(1)})^2 Q}{2\pi \eta^{(1)} \sigma_2^{(1)} \kappa_2^{(1)}} \langle \ln(z - i\sqrt{\lambda_\alpha d}) \rangle \mathbf{B}_1^{-1} \begin{bmatrix} 0 \\ 1 \end{bmatrix} \quad (9.43)$$

Substituting Eq. (9.42) into Eq. (9.41b), we finally obtain

$$\mathbf{f}_2(z) = 2\mathbf{B}_2^{-1} (\mathbf{A}_1 \mathbf{B}_1^{-1} \underline{\Lambda} + \mathbf{A}_2 \mathbf{B}_2^{-1})^{-1} \mathbf{A}_1 \mathbf{f}_0(z) \quad (9.44)$$

Consequently we can derive the expression of $\mathbf{f}_1(z)$ as

$$\mathbf{f}_1(z) = \mathbf{f}_0(z) + \mathbf{A}_1^{-1} (\mathbf{A}_1 \mathbf{B}_1^{-1} \underline{\Lambda} - \mathbf{A}_2 \mathbf{B}_2^{-1}) (\mathbf{A}_1 \mathbf{B}_1^{-1} \underline{\Lambda} + \mathbf{A}_2 \mathbf{B}_2^{-1})^{-1} \mathbf{A}_1 \bar{\mathbf{f}}_0(z) \quad (9.45)$$

Therefore, the full-field expressions of $\mathbf{f}_1(z)$ and $\mathbf{f}_2(z)$ are obtained as follows,

$$\mathbf{f}_1(z) = \frac{i(\epsilon_2^{(1)})^2 Q}{2\pi\eta^{(1)}\sigma_2^{(1)}\kappa_2^{(1)}} \left[\langle \ln(z_\alpha - i\sqrt{\lambda_\alpha}d) \rangle + \sum_{k=1}^2 \langle \ln(z_\alpha + i\sqrt{\lambda_k}d) \rangle \mathbf{M}\mathbf{I}_k \right] \mathbf{B}_1^{-1} \begin{bmatrix} 0 \\ 1 \end{bmatrix} \quad (9.46)$$

$$\mathbf{f}_2(z) = \frac{i(\epsilon_2^{(1)})^2 Q}{2\pi\eta^{(1)}\sigma_2^{(1)}\kappa_2^{(1)}} \sum_{k=1}^2 \langle \ln(z_\alpha^* - i\sqrt{\lambda_k}d) \rangle \mathbf{N}\mathbf{I}_k \mathbf{B}_1^{-1} \begin{bmatrix} 0 \\ 1 \end{bmatrix} \quad (9.47)$$

where the superscript “*” is utilized to distinguish the eigenvalues associated with the lower half-plane from those associated with the upper half-plane, and

$$\mathbf{I}_1 = \text{diag} [1 \quad 0] \quad \mathbf{I}_2 = \text{diag} [0 \quad 1] \quad (9.48)$$

$$\begin{aligned} \mathbf{M} &= \mathbf{A}_1^{-1} (\mathbf{A}_2 \mathbf{B}_2^{-1} - \mathbf{A}_1 \mathbf{B}_1^{-1} \underline{\Delta}) (\mathbf{A}_2 \mathbf{B}_2^{-1} + \mathbf{A}_1 \mathbf{B}_1^{-1} \underline{\Delta})^{-1} \mathbf{A}_1 \\ \mathbf{N} &= 2\mathbf{B}_2^{-1} (\mathbf{A}_2 \mathbf{B}_2^{-1} + \mathbf{A}_1 \mathbf{B}_1^{-1} \underline{\Delta})^{-1} \mathbf{A}_1 \end{aligned} \quad (9.49)$$

It follows from Eq. (9.34) that the induced magnetic field in the upper half-plane $y > 0$ is given by

$$\begin{aligned} H_z^{(1)} &= \frac{\epsilon_2^{(1)2} Q}{2\pi\eta^{(1)}\sigma_2^{(1)}\kappa_2^{(1)}} [1 \quad 0] \times \\ &\mathbf{B}_1 \left[\left\langle \tan^{-1} \left(\frac{\sqrt{\lambda_\alpha}(y-d)}{x} \right) \right\rangle + \sum_{k=1}^2 \left\langle \tan^{-1} \left(\frac{\sqrt{\lambda_\alpha}y + \sqrt{\lambda_k}d}{x} \right) \right\rangle \mathbf{M}\mathbf{I}_k \right] \mathbf{B}_1^{-1} \begin{bmatrix} 0 \\ 1 \end{bmatrix} \end{aligned} \quad (9.50)$$

while that in the lower half-plane $y < 0$ is given by

$$H_z^{(2)} = \frac{\epsilon_2^{(1)2} Q}{2\pi\eta^{(1)}\sigma_2^{(1)}\kappa_2^{(1)}} [1 \quad 0] \mathbf{B}_2 \sum_{k=1}^2 \left\langle \tan^{-1} \left(\frac{\sqrt{\lambda_\alpha^*}y - \sqrt{\lambda_k}d}{x} \right) \right\rangle \mathbf{N}\mathbf{I}_k \mathbf{B}_1^{-1} \begin{bmatrix} 0 \\ 1 \end{bmatrix} \quad (9.51)$$

9.4 Numerical Examples

In this section, we first consider the following material properties

$$\begin{aligned} \sigma_2^0 &= 5.7 \times 10^5 \text{ A}/(\text{m} \cdot \text{V}) & \kappa_2^0 &= 7.3 \text{ W}/(\text{m} \cdot ^\circ\text{C}) & \epsilon_2^0 &= -2.793 \text{ A}/(\text{m} \cdot ^\circ\text{C}) \\ \sigma &= 1.023 & \kappa &= 1.01 & \epsilon &= 1.055 \end{aligned}$$

which are typical values of a homogeneous Ti-6Al-4V, the popular aerospace titanium alloy. In addition we take the thermoelectric coupling parameter $\eta = 10^{-2}$. Figure 9.1 demonstrates the distributions of the electric current density component j_1 along the x -axis ($y = 0$) induced by a line heat source of unit strength ($Q = 1$) located at origin for different values of the gradient parameter $\beta_1 = -5, -1, 0, 1, 5 \text{ m}^{-1}$ with $\beta_2 = 0$ (in this way the material is gradient along the x -direction). It is observed from this figure that the induced j_1 for nonzero β_1 is no longer anti-symmetric with respect to the origin. The

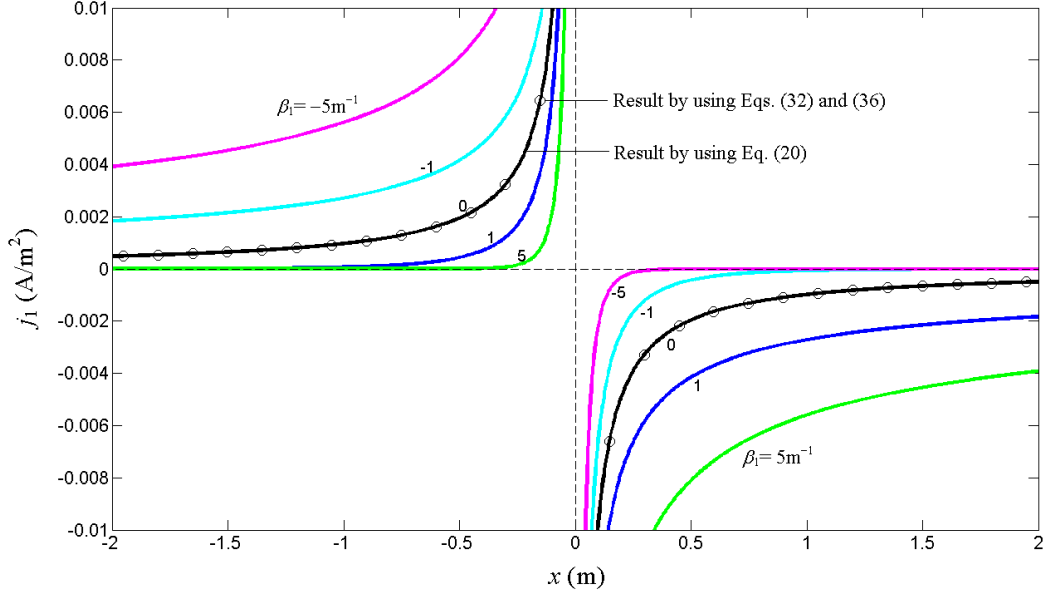


Figure 9.1: Distributions of the thermoelectric current density component j_1 along the x -axis ($y = 0$) induced by a line heat source of unit strength ($Q = 1$) located at origin for different values of the gradient parameter $\beta_1 = -5, -1, 0, 1, 5 \text{ m}^{-1}$ with $\beta_2 = 0$. The result for the homogeneous material case ($\beta_1 = \beta_2 = 0$) is the same as that based on the complex variable method (Eqs. (9.32) and (9.36)) as shown in open circles.

magnitude of j_1 at $x > 0$ (or $x < 0$) is greater (or lower) than that at $-x$ for $\beta_1 > 0$ (or $\beta_1 < 0$). In addition the magnitude difference becomes larger when the absolute value of β_1 increases. Therefore, the material property gradient in an anisotropic material can exert a significant influence on the induced thermoelectric currents, and consequently on the magnetic field. Shown in Figure 9.1 is also the electric current density component j_1 for the homogeneous but anisotropic material using Eqs. (4.32) and (4.36) based on the complex-variable method (in open circles). It is clear that for this case, both solutions (eigenvalue/eigenvector separation based and complex-variable based) predict exactly the same results, which partially and mutually verify the correctness of the derived solutions.

Next we present in Figure 9.2 the distribution of the electric current density component j_1 along the x -axis ($y = 0$) induced by a line heat source of unit strength ($Q = 1$) located at origin for different combinations of the material property ratios σ , κ and ϵ with $\beta_1 = 1 \text{ m}^{-1}$ and $\beta_2 = 0$. The values of σ_2^0 , κ_2^0 , ϵ_2^0 and η are also the same as before. It is clearly observed that the magnitude of j_1 decreases as the material anisotropic effect becomes weak (i.e., the ratios σ , κ and ϵ are close to 1) and that there is no induced electric current density when the material is isotropic ($\sigma = \kappa = \epsilon = 1$) even it is inhomogeneous.

9.5 Conclusion

In this research we presented analytical expressions of the electric potential, temperature, electric current densities and thermal fluxes due to a steady line heat source in the

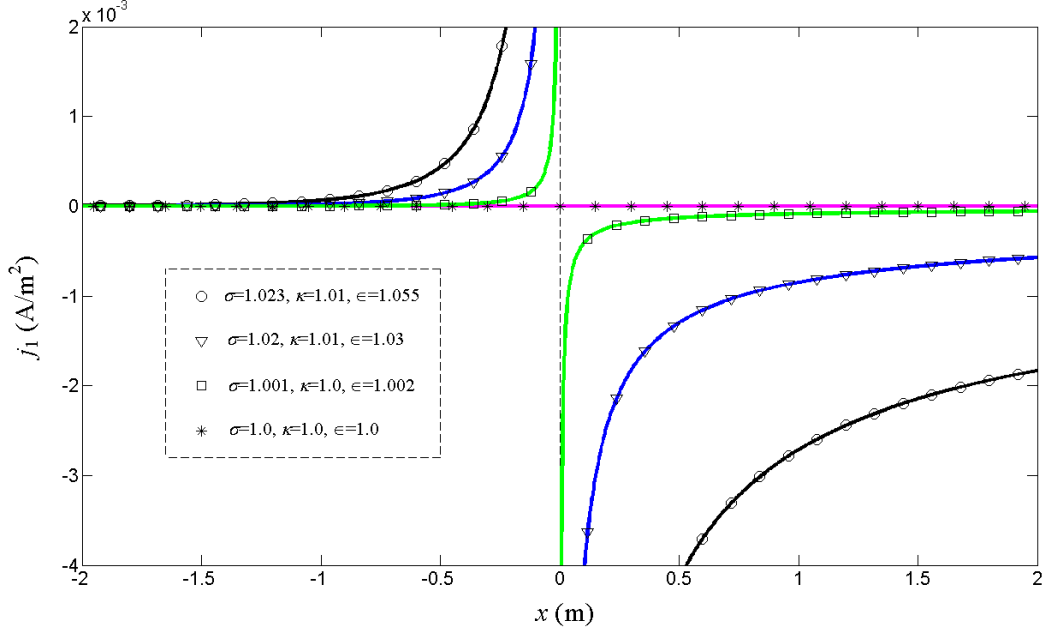


Figure 9.2: Distribution of the thermoelectric current density component j_1 along the x -axis ($y = 0$) induced by a line heat source of unit strength ($Q = 1$) located at origin for different combinations of the material property ratios σ , κ and ϵ with $\beta_1 = 1 \text{ m}^{-1}$ and $\beta_2 = 0$.

exponentially gradient and anisotropic thermoelectric material by introducing the eigenvalue/eigenvector separation approach. We also developed an elegant complex variable formulation to study 2D problems in the corresponding anisotropic but homogeneous thermoelectric material, which was also utilized to verify the eigenvalue based solutions for the special case (i.e., when the material is homogeneous). The correctness of the developed solutions was further verified by reducing to the existing solutions for some special cases. Our numerical results clearly indicate the effect of both material anisotropy and gradient on the induced thermoelectric current density and thus the magnetic fields to be detected by the magnetometer. Recent theoretical and experimental studies have shown that the material anisotropy is required in this special noncontacting nondestructive evaluation approach. However, since most materials are both anisotropic and inhomogeneous, the spurious signal from material grading as well as anisotropy has to be clearly separated from the true signal due to the material flaw. The solutions presented can be directly used to calculate the background signal for given material anisotropy and grading (in the term of exponential variation), and therefore, comparing this signal with the detected signal by the magnetometer will help to identify the potential material flaw in the specimen.

Besides their direct applications to the nondestructive evaluation, it is expected that the solutions developed in this research can be also applied to other practical 2D problems (for example, a crack on the interface between two anisotropic half-planes, or an elliptical anisotropic cylinder embedded in another anisotropic matrix). Results of these problems, which are pertinent to noncontacting thermoelectric NDT, will be reported later.

Chapter 10

Elastic And Electric Fields Induced By QWR In Bimaterial Plane

In this chapter, we develop the anisotropic bimaterial Green's functions in terms of the efficient and powerful Stroh formalism and the corresponding BEM program for the analysis of the strain energy density and the relative strain energy for a QWR free-standing on or embedded in an anisotropic semiconductor substrate. To treat the misfit lattice eigenstrain within the QWR, we first convert the associated area integral to a line integral along the interface of the QWR and its substrate. Then we discretize the boundary with constant elements so that the involved kernel integration can be carried out in an exact closed form, which is solved for the boundary (interface) values. The induced elastic field inside and outside the QWR can be obtained using the solved interface values. We remark that in order to apply our bimaterial program to the free-standing QWR case, we only need to assume that the material stiffness in the upper half-plane is much smaller than that in the lower half-plane substrate.

Our bimaterial BEM program is first tested against various existing results. It is then applied to calculate the strain energy density and the relative strain energy in the InAs (111) QWR which is free-standing on or embedded in the GaAs substrate. Our numerical results show that, for the case of an isosceles triangle QWR on the substrate, the strain energy density within the QWR strongly depends on the base angle of the triangle. We also observe that the magnitude of the relative strain energy for this case increases with increasing side angle. For a square QWR either free standing on or embedded in the substrate, we found that the magnitude of the relative strain energy increases with increasing depth of the QWR to the substrate surface. Our numerical examples demonstrate the significant influence of the QWR shape and the QWR location on both the strain energy density and the relative strain energy in the QWR, which should be particularly useful to the successful growth of QWRs via epitaxial approach.

This chapter is organized as follows: In Section 10.1, the boundary integral equation and the required four sets of Green's functions for the bimaterial matrix are presented. Numerical examples are presented in Section 10.2, and conclusions are drawn in Section 10.3.

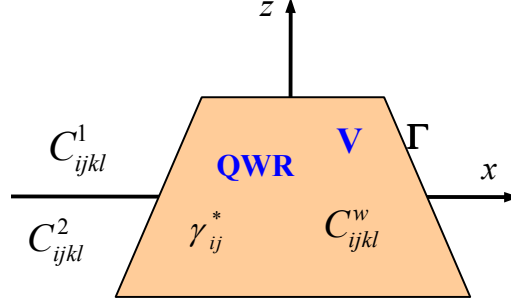


Figure 10.1: A general QWR within a bimaterial substrate: An eigenstrain γ_{ij}^* is applied to the QWR which is an arbitrarily shaped polygon.

10.1 Bimaterial Green's Functions

We assume that there is a QWR of arbitrary shape within a bimaterial substrate. A uniform eigenstrain γ_{ij}^* field is applied inside the QWR as shown in Figure 10.1. The elastic moduli in the QWR, material 1 and material 2 are denoted, respectively, as c_{ijkl}^w , c_{ijkl}^1 and c_{ijkl}^2 . In each domain, the basic equations remain the same as in section 2.2.

It is noted that in order to solve the discretized boundary integral equations, the involved Green's functions U_{ij} and T_{ij} and their integrations on each element are required. These are presented below.

In the boundary integral equation (2.14) for the QWR domain, only the full-plane Green's functions are required, which can be expressed as [25],

$$U_{jk}(\mathbf{X}, \mathbf{x}) = \frac{1}{\pi} \text{Im} \{ A_{jr} \ln(z_r - s_r) A_{kr} \} \quad (10.1)$$

for the displacement, and

$$T_{jk}(\mathbf{X}, \mathbf{x}) = -\frac{1}{\pi} \text{Im} \left\{ B_{jr} \frac{p_r n_1 - n_3}{z_r - s_r} A_{kr} \right\} \quad (10.2)$$

for the traction. In Eqs. (10.1) and (10.2), n_1 and n_3 are the outward normal components at point \mathbf{x} , and the complex variables z_r and s_r ($r = 1, 2, 3$) are defined by

$$z_r = x + p_r z \quad (10.3)$$

$$s_r = X + p_r Z \quad (10.4)$$

In Eqs. (10.3) and (10.4), p_r ($r = 1, 2, 3$) are the Stroh eigenvalues of the QWR material, which are related to the elastic moduli only, and \mathbf{A} and \mathbf{B} are the corresponding matrices of Stroh eigenvectors [1, 35].

For the matrix domain (i.e., the bimaterial substrate), due to the relative locations of the source and field points, there are four sets of Green's functions. Again, these Green's functions were derived in terms of the Lekhnitskii formalism [64]. However, the Stroh formalism is more convenient and efficient [35]. Therefore, we first present these bimaterial Green's functions in the Stroh formalism. We refer to Figure 10.1 where materials 1 and 2 occupy the half-plane $z > 0$ and $z < 0$, respectively.

First, let the source point $\mathbf{X} = (X, Z)$ be in material 1 ($z > 0$). Then, if the field point $\mathbf{x} = (x, z)$ is in the $z > 0$ half-plane, the displacement and traction Green's functions can be expressed as

$$U_{kj}^1 = \frac{1}{\pi} \text{Im} \{ A_{jr}^1 \ln(z_r - s_r) A_{kr}^1 + \sum_{v=1}^4 [A_{jr}^1 \ln(z_r - \bar{s}_v) Q_{rk}^{11,v}] \} \quad (10.5)$$

$$T_{kj}^1 = -\frac{1}{\pi} \text{Im} \{ B_{jr}^1 \frac{p_r^1 n_1 - n_3}{z_r - s_r} A_{kr}^1 + \sum_{v=1}^4 [B_{jr}^1 \frac{p_r^1 n_1 - n_3}{z_r - \bar{s}_v} Q_{rk}^{11,v}] \} \quad (10.6)$$

On the other hand, if the field point is in the $z < 0$ half-plane, then

$$U_{kj}^2 = \frac{1}{\pi} \text{Im} \sum_{v=1}^4 [A_{jr}^2 \ln(z_r - s_v) Q_{rk}^{12,v}] \quad (10.7)$$

$$T_{kj}^2 = -\frac{1}{\pi} \text{Im} \sum_{v=1}^4 [B_{jr}^2 \frac{p_r^2 n_1 - n_3}{z_r - s_v} Q_{rk}^{12,v}] \quad (10.8)$$

Now, let the source point (X, Z) be in material 2 ($z < 0$). Then, if the field point (x, z) is in the $z > 0$ half-plane, we have

$$U_{kj}^1 = \frac{1}{\pi} \text{Im} \sum_{v=1}^4 [A_{jr}^1 \ln(z_r - s_v) Q_{rk}^{21,v}] \quad (10.9)$$

$$T_{kj}^1 = -\frac{1}{\pi} \text{Im} \sum_{v=1}^4 [B_{jr}^1 \frac{p_r^1 n_1 - n_3}{z_r - s_v} Q_{rk}^{21,v}] \quad (10.10)$$

On the other hand, if the field point is in the $z < 0$ half-plane,

$$U_{kj}^2 = \frac{1}{\pi} \text{Im} \{ A_{jr}^2 \ln(z_r - s_r) A_{kr}^2 + \sum_{v=1}^4 [A_{jr}^2 \ln(z_r - \bar{s}_v) Q_{rk}^{22,v}] \} \quad (10.11)$$

$$T_{kj}^2 = -\frac{1}{\pi} \text{Im} \{ B_{jr}^2 \frac{p_r^2 n_1 - n_3}{z_r - s_r} A_{kr}^2 + \sum_{v=1}^4 [B_{jr}^2 \frac{p_r^2 n_1 - n_3}{z_r - \bar{s}_v} Q_{rk}^{22,v}] \} \quad (10.12)$$

In Eqs. (10.5)–(10.12), the superscript 1 or 2 to p , \mathbf{A} , and \mathbf{B} denotes that these eigenvalues and their corresponding matrices of eigenvectors belong to material 1 or 2. The matrix \mathbf{Q} depends on the relative locations of the source and field points. Assuming that the source point is in the half-plane of material λ (where $\lambda = 1$ or 2), then \mathbf{Q} can be expressed as

$$Q_{rk}^{\lambda\lambda,v} = K_{rj}^{\lambda\lambda} (I_v)_j \bar{A}_{kj}^{\lambda} \quad (10.13)$$

if the field point is in the half-plane of material λ , and

$$Q_{rk}^{\lambda\mu,v} = K_{rj}^{\lambda\mu} (I_v)_j A_{kj}^{\lambda} \quad (10.14)$$

if the field point is in the other half-plane of material μ (where $\mu \neq \lambda$). In Eqs. (10.13) and (10.14), the matrix \mathbf{K} is given by

$$\mathbf{K}^{\lambda\lambda} = (\mathbf{A}^{\lambda})^{-1} (\mathbf{M}^{\lambda} + \bar{\mathbf{M}}^{\mu})^{-1} (\mathbf{M}^{\mu} - \bar{\mathbf{M}}^{\lambda}) \bar{\mathbf{A}}^{\lambda} \quad (10.15)$$

$$\mathbf{K}^{\lambda\mu} = (\mathbf{A}^{\mu})^{-1} (\mathbf{M}^{\mu} + \bar{\mathbf{M}}^{\lambda})^{-1} (\mathbf{M}^{\lambda} + \bar{\mathbf{M}}^{\lambda}) \mathbf{A}^{\lambda} \quad (10.16)$$

with $\mathbf{M}^\lambda = -i\mathbf{B}^\lambda(\mathbf{A}^\lambda)^{-1}$ (where $\lambda = 1$ or 2) and the diagonal matrix \mathbf{I}_v has the following expression for different indexes v ,

$$\mathbf{I}_1 = \text{diag}[1, 0, 0] \quad \mathbf{I}_2 = \text{diag}[0, 1, 0] \quad \mathbf{I}_3 = \text{diag}[0, 0, 1] \quad (10.17)$$

10.1.1 Integration of Bimaterial Green's Functions

In order to carry out the line integral of the involved Green's functions over each constant element (e.g., along the n^{th} element Γ_n), we let the generic element start from point 1, (x_1, z_1) and end at point 2, (x_2, z_2) , with length $l = [(x_2 - x_1)^2 + (z_2 - z_1)^2]^{1/2}$. Then, the integration of the involved Green's displacements and tractions (only the integral variable-dependent function) for the QWR (which requires only the infinite-plane Green's functions) can be carried out, which has been expressed in section 2.3.

We point out that similar expressions can be found for the integration of the bimaterial Green's functions in the substrate. Let the source point \mathbf{X} be in material 1, if the field point \mathbf{x} is in material 1, the corresponding integrals are

$$\begin{aligned} h_r^1(x, z) &= \int_{\Gamma_n} \ln(z_r^1 - s_r^1) d\Gamma_n \\ &= l \left\{ \frac{(x_1 + p_r^1 z_1) - s_r^1}{(x_2 - x_1) + p_r^1 (z_2 - z_1)} \ln \left[\frac{(x_2 + p_r^1 z_2) - s_r^1}{(x_1 + p_r^1 z_1) - s_r^1} \right] \right. \\ &\quad \left. + \ln(x_2 + p_r^1 z_2 - s_r^1) - 1 \right\} \end{aligned} \quad (10.18)$$

$$\begin{aligned} w_{rv}^1(x, z) &= \int_{\Gamma_n} \ln(z_r^1 - \bar{s}_v^1) d\Gamma_n \\ &= l \left\{ \frac{(x_1 + p_r^1 z_1) - \bar{s}_v^1}{(x_2 - x_1) + p_r^1 (z_2 - z_1)} \ln \left[\frac{(x_2 + p_r^1 z_2) - \bar{s}_v^1}{(x_1 + p_r^1 z_1) - \bar{s}_v^1} \right] \right. \\ &\quad \left. + \ln(x_2 + p_r^1 z_2 - \bar{s}_v^1) - 1 \right\} \end{aligned} \quad (10.19)$$

and

$$g_r^1(x, z) = \int_{\Gamma_n} \frac{1}{z_r^1 - s_r^1} d\Gamma_n = l \left[\frac{1}{(x_2 - x_1) + p_r^1 (z_2 - z_1)} \ln \left(\frac{x_2 + p_r^1 z_2 - s_r^1}{x_1 + p_r^1 z_1 - s_r^1} \right) \right] \quad (10.20)$$

$$d_{rv}^1(x, z) = \int_{\Gamma_n} \frac{1}{z_r^1 - \bar{s}_v^1} d\Gamma_n = l \left[\frac{1}{(x_2 - x_1) + p_r^1 (z_2 - z_1)} \ln \left(\frac{x_2 + p_r^1 z_2 - \bar{s}_v^1}{x_1 + p_r^1 z_1 - \bar{s}_v^1} \right) \right] \quad (10.21)$$

When source point \mathbf{X} is in material 1, and the field point \mathbf{x} is in material 2, the corre-

sponding integrals are

$$\begin{aligned}
h_{rv}^{21}(x, z) &= \int_{\Gamma_n} \ln(z_r^2 - s_v^1) d\Gamma_n \\
&= l \left\{ \frac{(x_1 + p_r^2 z_1) - s_v^1}{(x_2 - x_1) + p_r^2(z_2 - z_1)} \ln \left[\frac{(x_2 + p_r^2 z_2) - s_v^1}{(x_1 + p_r^2 z_1) - s_v^1} \right] \right. \\
&\quad \left. + \ln(x_2 + p_r^2 z_2 - s_v^1) - 1 \right\}
\end{aligned} \tag{10.22}$$

and

$$g_{rv}^{21}(x, z) = \int_{\Gamma_n} \frac{1}{z_r^2 - s_v^1} d\Gamma_n = l \left[\frac{1}{(x_2 - x_1) + p_r^2(z_2 - z_1)} \ln \left(\frac{x_2 + p_r^2 z_2 - s_v^1}{x_1 + p_r^2 z_1 - s_v^1} \right) \right] \tag{10.23}$$

When source point \mathbf{X} is in material 2, and the field point \mathbf{x} is in material 1, the corresponding integrals are

$$\begin{aligned}
h_{rv}^{12}(x, z) &= \int_{\Gamma_n} \ln(z_r^1 - s_v^2) d\Gamma_n \\
&= l \left\{ \frac{(x_1 + p_r^1 z_1) - s_v^2}{(x_2 - x_1) + p_r^1(z_2 - z_1)} \ln \left[\frac{(x_2 + p_r^1 z_2) - s_v^2}{(x_1 + p_r^1 z_1) - s_v^2} \right] \right. \\
&\quad \left. + \ln(x_2 + p_r^1 z_2 - s_v^2) - 1 \right\}
\end{aligned} \tag{10.24}$$

and

$$g_{rv}^{12}(x, z) = \int_{\Gamma_n} \frac{1}{z_r^1 - s_v^2} d\Gamma_n = l \left[\frac{1}{(x_2 - x_1) + p_r^1(z_2 - z_1)} \ln \left(\frac{x_2 + p_r^1 z_2 - s_v^2}{x_1 + p_r^1 z_1 - s_v^2} \right) \right] \tag{10.25}$$

When source point \mathbf{X} is in material 2, and the field point \mathbf{x} is in material 2, the corresponding integrals are

$$\begin{aligned}
h_r^2(x, z) &= \int_{\Gamma_n} \ln(z_r^2 - s_r^2) d\Gamma_n \\
&= l \left\{ \frac{(x_1 + p_r^2 z_1) - s_r^2}{(x_2 - x_1) + p_r^2(z_2 - z_1)} \ln \left[\frac{(x_2 + p_r^2 z_2) - s_r^2}{(x_1 + p_r^2 z_1) - s_r^2} \right] \right. \\
&\quad \left. + \ln(x_2 + p_r^2 z_2 - s_r^2) - 1 \right\}
\end{aligned} \tag{10.26}$$

$$\begin{aligned}
w_{rv}^2(x, z) &= \int_{\Gamma_n} \ln(z_r^2 - \bar{s}_v^2) d\Gamma_n \\
&= l \left\{ \frac{(x_1 + p_r^2 z_1) - \bar{s}_v^2}{(x_2 - x_1) + p_r^2(z_2 - z_1)} \ln \left[\frac{(x_2 + p_r^2 z_2) - \bar{s}_v^2}{(x_1 + p_r^2 z_1) - \bar{s}_v^2} \right] \right. \\
&\quad \left. + \ln(x_2 + p_r^2 z_2 - \bar{s}_v^2) - 1 \right\}
\end{aligned} \tag{10.27}$$

and

$$g_r^2(x, z) = \int_{\Gamma_n} \frac{1}{z_r^2 - s_r^2} d\Gamma_n = l \left[\frac{1}{(x_2 - x_1) + p_r^2(z_2 - z_1)} \ln \left(\frac{x_2 + p_r^2 z_2 - s_r^2}{x_1 + p_r^2 z_1 - s_r^2} \right) \right] \quad (10.28)$$

$$d_{rv}^2(x, z) = \int_{\Gamma_n} \frac{1}{z_r^2 - \bar{s}_v^2} d\Gamma_n = l \left[\frac{1}{(x_2 - x_1) + p_r^2(z_2 - z_1)} \ln \left(\frac{x_2 + p_r^2 z_2 - \bar{s}_v^2}{x_1 + p_r^2 z_1 - \bar{s}_v^2} \right) \right] \quad (10.29)$$

10.1.2 Derivatives of Bimaterial Green's Functions

In order to obtain the strain and stress fields, we also need to take the derivative of the Green's displacement and traction with respect to the source point, and then find the corresponding integration. The integration of the involved Green's function derivatives for the QWR domain can be written as

$$h_{r,x} = \int_{\Gamma_n} \frac{\partial \ln(z_r - s_r)}{\partial x} d\Gamma_n = - \frac{l}{(x_2 - x_1) + p_r(z_2 - z_1)} \ln \left(\frac{x_2 + p_r z_2 - s_r}{x_1 + p_r z_1 - s_r} \right) \quad (10.30)$$

$$h_{r,z} = p_r h_{r,x} \quad (10.31)$$

$$\begin{aligned} g_{r,x} &= \int_{\Gamma_n} \frac{\partial}{\partial x} \frac{1}{z_r - s_r} d\Gamma_n \\ &= \frac{l}{(x_2 - x_1) + p_r(z_2 - z_1)} \left[-\frac{1}{x_2 + p_r z_2 - s_r} + \frac{1}{x_1 + p_r z_1 - s_r} \right] \end{aligned} \quad (10.32)$$

$$g_{r,z} = p_r g_{r,x} \quad (10.33)$$

Again, similar expressions can be found for the corresponding bimaterial substrate.

10.2 Numerical Examples

Before applying our solution to examine the strain energy in QWR system, we have first checked our program for the reduced cases with existing solutions [181]. We found that our solution can be reduced exactly to the existing exact closed-form results [181]. Other numerical tests have also carried out, all showing that our solution and program are correct. Therefore, after validation, we now apply our solution to calculate the relative strain energy, defined in section 10.2.1, and the distribution of the strain energy density. We remark that while our BEM formulation can be applied to more complicated situations, here we only study the reduced case where the QWR is free-standing on or embedded in the half-plane substrate. The half-plane model is reduced from our bimaterial result by setting the upper half-plane ($z > 0$) with very low material stiffness as compared to the lower half-plane substrate (The material stiffness in the upper half-space is equal to 10^{-10} times the material stiffness in the lower half-space).

10.2.1 Definition of the Relative Strain Energy

During growth of QWR nanostructures, strain energy in the QWR plays an important role. Therefore, its calculation and prediction are of great interest. Following [29], the strain

energy in the QWR can be expressed as

$$W = \frac{1}{2} \int_V \sigma_{ij}(\gamma_{ij} - \gamma_{ij}^*) dV \quad (10.34)$$

We remark that the integrand $\sigma_{ij}(\gamma_{ij} - \gamma_{ij}^*)/2$ is the strain energy density within the QWR, which will be also calculated and studied.

Applying the Gauss divergence theorem and assuming that the eigenstrain is uniform inside the QWR, the total elastic strain energy of QWR in Eq. (10.34) can be expressed alternatively as

$$W = \frac{1}{2} \int_{\Gamma} t_i u_i d\Gamma - \frac{1}{2} \int_{\Gamma} t_k^{(fw)} u_k d\Gamma + \frac{1}{2} \int_V C_{ijkl} \gamma_{ij}^* \gamma_{kl}^* dV \quad (10.35)$$

where Γ is the boundary of the QWR. While the first boundary integration on the right-hand side of Eq. (10.35) represents the work done by the traction acting on the boundary, the second boundary integration represents the work done by the traction associated with the eigenstrain as we recall that $t_k^{(fw)} = C_{ijkl} \gamma_{ij}^* n_l$. The last volumetric integration corresponds to the initial constant strain energy of the eigenstrain field, i.e., the constant strain energy in the wetting layer (i.e., the thin layer covers the substrate) due to the misfit strain [182].

In QWR growth, one of the important parameters is the relative strain energy Λ [182, 183]. Namely, the ratio of the strain energy change relative to the constant strain energy in the wetting layer due to the misfit strain over the constant strain energy, as defined below

$$\Lambda \equiv \frac{W - \frac{1}{2} \int_V C_{ijkl} \gamma_{ij}^* \gamma_{kl}^* dV}{\frac{1}{2} \int_V C_{ijkl} \gamma_{ij}^* \gamma_{kl}^* dV} = \frac{\frac{1}{2} \int_{\Gamma} t_i u_i d\Gamma - \frac{1}{2} \int_{\Gamma} t_k^{(fw)} u_k d\Gamma}{\frac{1}{2} \int_V C_{ijkl} \gamma_{ij}^* \gamma_{kl}^* dV} \quad (10.36)$$

where Λ is also called the relative strain energy, which will be numerically examined in the next section. We remark that while various energetic parameters were introduced for characterizing defect dynamics [184], this relative strain energy has been successfully applied in the prediction of new QWR formation and QWR array patterns under the Stranski-Krastanow growth mode [182, 183, 185].

10.2.2 Variation of Relative Strain Energy with QWR Depth

We first apply our bimaterial BEM program to study the problem where a square InAs(111) QWR growing on a GaAs(111) substrate (Figure 10.2). The material properties of InAs and GaAs in the (111)-direction are obtained by coordinate transform from those in the (001)-directions [186]. The QWR has a dimension of 20 nm \times 20 nm and a uniform misfit strain field $\gamma_{xx}^* = \gamma_{yy}^* = \gamma_{zz}^* = 0.07$. The boundary condition on the surface of the substrate is assumed to be traction-free. While a total free-standing QWR on the substrate is illustrated in Figure 10.2a, a fully embedded QWR is shown in Figure 10.2c. We let d be the depth of the QWR, measured from the bottom side of the QWR to the surface of substrate (Figure 10.2b). We then calculate the relative strain energy (i.e., Eq. (10.36)) of the QWR as a function of depth d , varying from -10 nm (Figure 10.2a) to 70 nm, at the interval of 5 nm. Figure 10.3 shows clearly that with increasing depth d , the magnitude of the relative

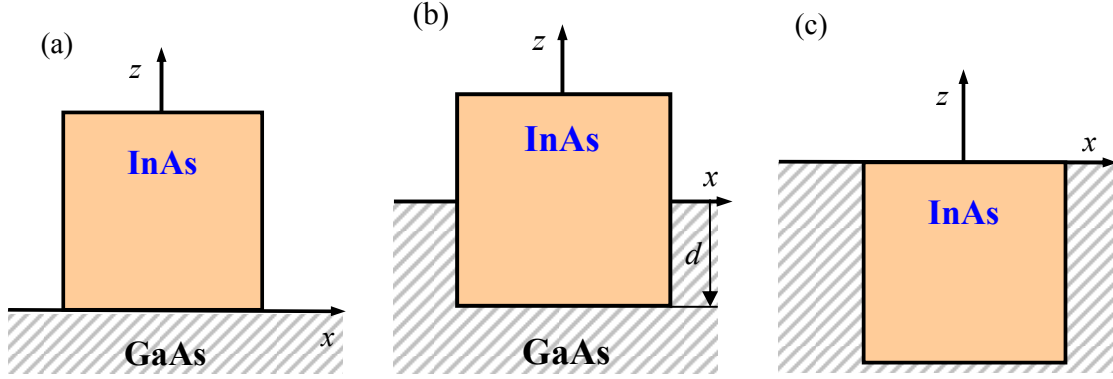


Figure 10.2: Geometry of a square InAs QWR on or inside the GaAs substrate. Shown in (a) to (c) are the three special cases: Namely, totally free-standing (a), half free-standing (half-in and half-out in (b)), and fully embedded (c).

strain energy increases, reaching the value when the QWR is within an infinite substrate ($= -0.19$). In other words, bringing an embedded QWR to the surface will decrease the relative strain energy. This is true since with increasing surface area of the QWR to the air, more surface energy will be released, resulting in small relative strain energy. This important feature could represent the competition between the surface and bulk energies i.e. [187, 188], and should be particularly interesting to epitaxial growth.

10.2.3 Effect of QWR Shape on Relative Strain Energy and Distribution of Strain Energy Density

We assume now that there is an isosceles triangle of InAs (111) QWR, free-standing on the GaAs (111) substrate. The base angle of the triangle varies from 30° to 75° while the area of triangle maintains the same. The misfit strain is again uniform, i.e. $\gamma_{xx}^* = \gamma_{yy}^* = \gamma_{zz}^* = 0.07$. The boundary condition on the surface of the substrate is traction-free. Both the relative strain energy and strain energy density in the QWR are investigated.

The relative strain energy for the triangular QWR with different base angles are listed in Table 10.1 and its variation with the base angle are also shown in Figure 10.4. It is observed that the magnitude of the relative strain energy increases with increasing base angle of the QWR triangle. In other words, the steeper the QWR is, the larger the magnitude of the relative strain energy becomes.

The contours of the strain energy density for these free-standing triangular QWRs are plotted in Figures 10.5 and 10.6. It is clear that the strain energy density distribution is strongly influenced by the QWR shape. Particularly at the locations near the vertex and base corners, the strain energy densities are quite different among these triangles. We further observed that the strain energy density near the vertex is larger than those near the base corners. The magnitude of strain energy density increases roughly from 2.15 to 2.35 (10^9 kg/ms^2) as the base angle varies from 30° to 75° .

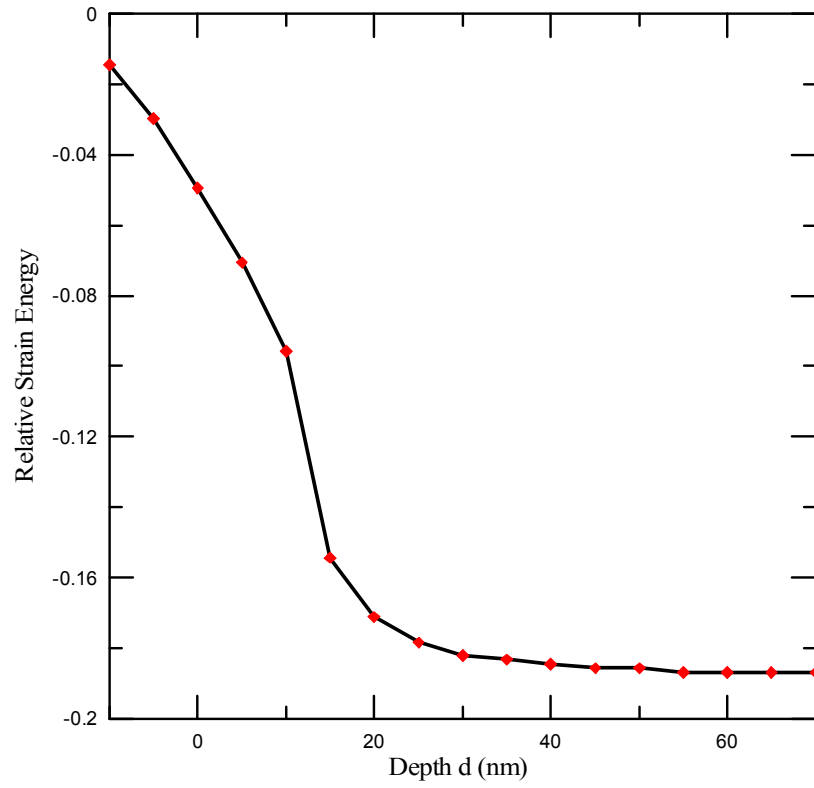


Figure 10.3: Variation of relative strain energy with depth of a square QWR.

Base angle (degree)	Relative strain energy ($\times 10^3$)
30	-5.88
37	-6.91
45	-7.90
52	-8.70
60	-9.76
67	-11.1
75	-14.3

Table 10.1: Variation of relative strain energy with base angle of the isosceles triangle of InAs (111) QWR, which is free-standing on the GaAs (111) substrate.

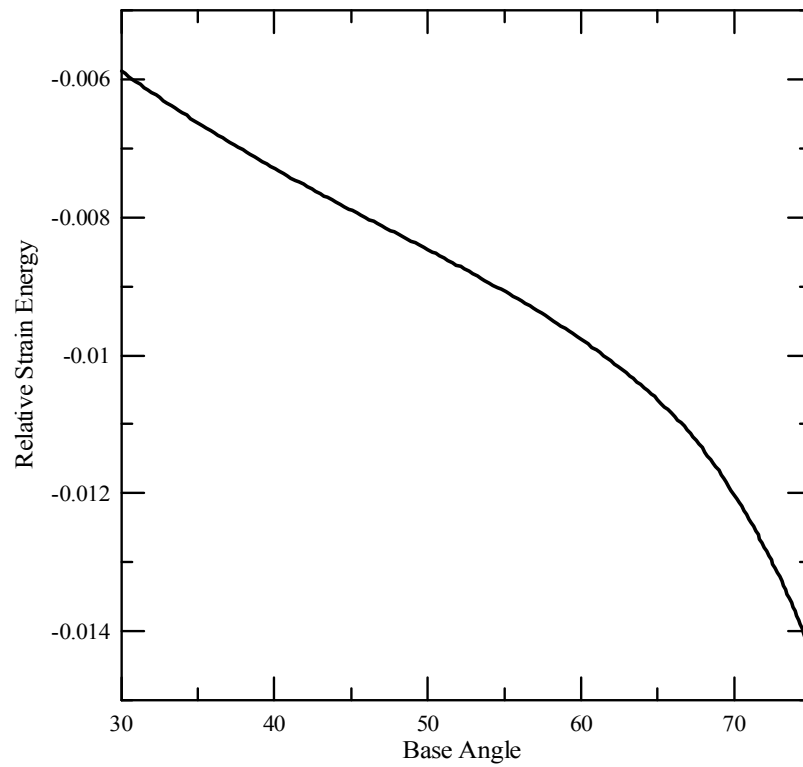
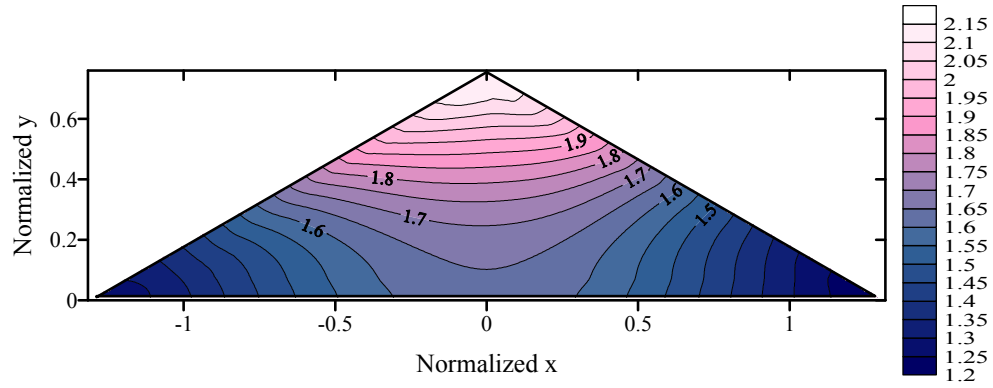
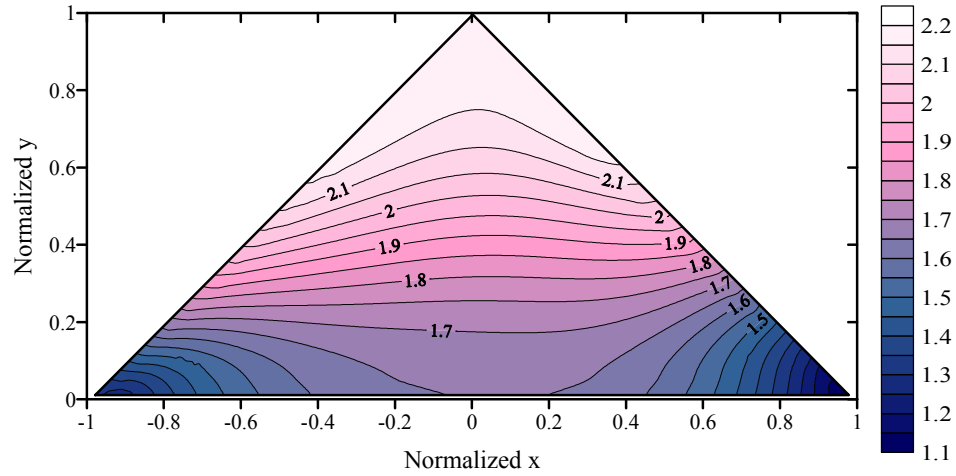


Figure 10.4: Variation of relative strain energy with base angle of isosceles triangle of InAs (111) QWR, which is free-standing on the GaAs (111) substrate.



(a)



(b)

Figure 10.5: Contours of strain energy density (10^9 kg/ms^2) in isosceles triangle of InAs (111) QWR with base angle 30° (a) or 45° (b)

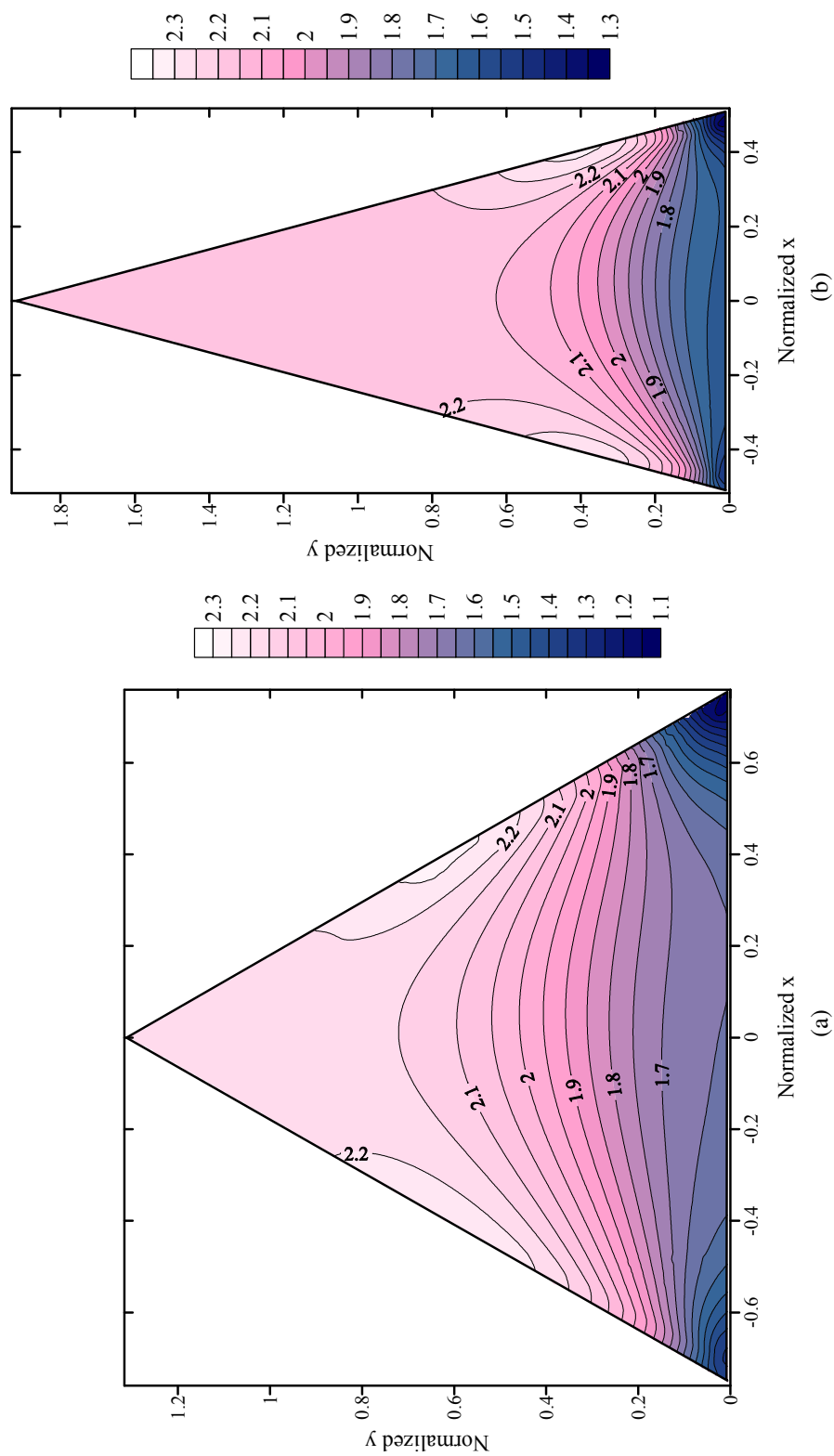


Figure 10.6: Contours of strain energy density (10^9 kg/ms²) in isosceles triangle of InAs (111) QWR with base angle 60° (a) or 75° (b).

10.3 Conclusions

In the chapter, we first derive the bimaterial Green's functions in anisotropic elastic media in terms of the elegant Stroh formalism. The corresponding BEM formulation is then presented. Since the involved Green's functions are in exact closed forms, the kernel integration can be analytically carried out for the constant element discretization. After testing our bimaterial BEM program for various reduced simple cases, we then apply our program to calculate the strain energy density and the relative strain energy in InAs (111) QWR free-standing on or embedded in GaAs (111) substrate. Our numerical results showed that, for the case of an isosceles triangle of InAs (111) QWR on the substrate, the strain energy density within the QWR strongly depends on the base angle of the triangle. We also observed that the magnitude of the relative strain energy for this case increases with increasing base angle. For a square QWR either free standing on or embedded in the substrate, we found that the magnitude of the relative strain energy increases with increasing depth of the QWR in the substrate, which represents the competition between the surface and bulk energies. Our numerical examples also demonstrate the significant influence of the QWR shape and location on both the strain energy density and the relative strain energy in the QWR, which should be particularly useful to the successful growth of QWRs via epitaxial approach.

Chapter 11

Strain Energy On The Surface Of Half-Plane Substrate Induced By An Isolated QD

In this chapter, we present an analytical method for the QD-induced strain field in half-space semiconductor substrates under the assumption of continuum elasticity. Furthermore, under the epitaxial growth, the misfit strain within the QD could be gradient, instead of uniform distribution [189], and as such, the material property in the QD could be difficult to calibrate [190]. Thus, the well-known inclusion model will be adopted in this chapter. It was verified recently that the inclusion model could predict slightly different results as compared to the inhomogeneity model using the bulk property of the QD (about 10% within the strained quantum structures, see, e.g., [24, 33]). Under these assumptions, we derive our solution based on the Green's function method in terms of the Stroh formalism with the corresponding exact integration of the Green's functions over the QD surface (composed piecewise of flat triangles).

This chapter is organized as follows: In section 11.1, the strained QD system is described. In section 11.2, the surface of the QD is approximated by a number of flat triangles over which the area integration is carried out exactly so that the induced elastic fields can be expressed in terms of a simple line integral over $[0, \pi]$. If the QD is a point source, then the QD-induced elastic fields can be analytically expressed by point-force Green's functions in the half-space. In section 11.3, numerical examples are carried out for buried cubic, pyramidal, truncated pyramidal, and point QDs in half-spaces. The effects of QD shape and depth on the strain energy are discussed. Conclusions are drawn in section 11.4.

11.1 Problem description for QD Embedded in Anisotropic Half-space Substrate

We now assume that the 3D point-force Green's functions are given for the half-space substrate, then for the general eigenstrain γ_{ij}^* at $\mathbf{x} = (x_1, x_2, x_3)$ within the QD domain V , the induced displacement at $\mathbf{d} = (d_1, d_2, d_3)$ can be found using the superposition method.

That is, the response is an integral, over V , of the equivalent body force defined by equation (2.10), multiplied by the point-force Green's functions, as

$$u_k(\mathbf{d}) = - \int_V U_j^k(\mathbf{x}; \mathbf{d}) [C_{ijlm} \gamma_{lm}^*(\mathbf{x})]_{,i} dV(\mathbf{x}) \quad (11.1)$$

where $U_j^k(\mathbf{x}; \mathbf{d})$ is the j^{th} Green's elastic displacement at \mathbf{x} due to a point force in the k^{th} direction applied at \mathbf{d} . Integrating by parts and noting that the eigenstrain is nonzero only in the QD domain V , Eq. (11.1) can be expressed alternatively as

$$u_k(\mathbf{d}) = \int_V U_{j,x_i}^k(\mathbf{x}; \mathbf{d}) C_{ijlm} \gamma_{lm}^*(\mathbf{x}) dV(\mathbf{x}) \quad (11.2)$$

If we further assume that the eigenstrain is constant within the QD domain V , then the domain integration can be transformed to the boundary integration, that is

$$u_k(\mathbf{d}) = C_{ijlm} \gamma_{lm}^* \int_{\partial V} U_j^k(\mathbf{x}; \mathbf{d}) n_i(\mathbf{x}) dS(\mathbf{x}) \quad (11.3)$$

where $n_i(\mathbf{x})$ is the outward normal on the boundary ∂V of the QD.

In order to find the elastic strain, we take the derivatives of Eq. (11.3) with respect to the observation point \mathbf{d} (i.e., the source point of the point-force Green's function), which yields (for $k, p = 1, 2, 3$)

$$\gamma_{kp}(\mathbf{d}) = \frac{1}{2} \gamma_{lm}^* C_{ijlm} \int_{\partial V} [U_{j,d_p}^k(\mathbf{x}; \mathbf{d}) + U_{j,d_k}^p(\mathbf{x}; \mathbf{d})] n_i(\mathbf{x}) dS(\mathbf{x}) \quad (11.4)$$

The stresses inside and outside the QD are obtained from Eq. (2.4).

It is obvious that in order to solve the QD-induced elastic field, the key is to carry out the surface integration involved in equations (11.3) and (11.4). This requires the integral of the corresponding half-space Green's functions, which are discussed below.

11.2 Integration of Half-space Green's Functions over QD Surfaces

We assume that the boundary of the QD can be approximated by a number of flat triangles. We want to analytically integrate the half-space Green's functions over one of the flat triangles. To do so, we first briefly review the half-space Green's functions in general anisotropic semiconductors.

The half-space point-force Green's function with source point at \mathbf{d} and field point at \mathbf{x} can be expressed as a sum of an explicit infinite-space solution and a complementary part in terms of a line integral over $[0, \pi]$ [2]

$$\mathbf{U}(\mathbf{x}; \mathbf{d}) = \mathbf{U}^\infty(\mathbf{x}; \mathbf{d}) + \frac{1}{2\pi^2} \int_0^\pi \bar{\mathbf{A}} \mathbf{G}_1 \mathbf{A}^T d\theta \quad (11.5)$$

where overbar means complex conjugate, superscript T denotes matrix transpose, and

$$(\mathbf{G}_1)_{ij} = \frac{(\bar{\mathbf{B}}^{-1}\mathbf{B})_{ij}}{-\bar{p}_i x_3 + p_j d_3 - [(x_1 - d_1) \cos \theta + (x_2 - d_2) \sin \theta]} \quad (11.6)$$

We point out that, on the right-hand side of Eq. (11.5), the first term corresponds to the Green's displacement tensor in an anisotropic infinite space. Its integration over a flat triangle was presented by Wang et al. [191]. Also in Eqs. (11.5) and (11.6), the Stroh eigenvalues p_j , and matrices of eigenvectors \mathbf{A} and \mathbf{B} are all functions of θ as well as of the elastic stiffness tensor of the semiconductor material.

In order to find the misfit strain-induced elastic fields, we also need the derivatives of the Green's displacement tensor with respect to the field point (x_1, x_2, x_3) of the Green's function [64, 117]. They are found to be (where $j = 1, 2, 3$)

$$\frac{\partial \mathbf{U}(\mathbf{x}; \mathbf{d})}{\partial x_j} = \frac{\partial \mathbf{U}^\infty(\mathbf{x}; \mathbf{d})}{\partial x_j} - \frac{1}{2\pi^2} \int_0^\pi \bar{\mathbf{A}} \mathbf{G}_2 \langle g_j \rangle \mathbf{A}^T d\theta \quad (11.7)$$

where

$$(\mathbf{G}_2)_{ij} = \frac{(\bar{\mathbf{B}}^{-1}\mathbf{B})_{ij}}{\{-\bar{p}_i x_3 + p_j d_3 - [(x_1 - d_1) \cos \theta + (x_2 - d_2) \sin \theta]\}^2} \quad (11.8)$$

$$\begin{aligned} \langle g_1 \rangle &= \text{diag}[\cos \theta, \cos \theta, \cos \theta] & \langle g_2 \rangle &= \text{diag}[\sin \theta, \sin \theta, \sin \theta] \\ \langle g_3 \rangle &= \text{diag}[\bar{p}_1, \bar{p}_2, \bar{p}_3] \end{aligned} \quad (11.9)$$

Again, since the integration on a flat triangle has already been presented for the infinite part of the half-space Green's function [191], we only need to present the integration of the complementary part of the Green's function, i.e., the integration of the second term on the right-hand side of Eq. (11.7).

We consider first the integration of the Green's displacement tensor. Again, we assume that the QD surface can be effectively approximated by a number of flat triangles. Therefore, the integral expression Eq. (11.3) over a flat triangle, Δ , is

$$u_k(\mathbf{d}) = C_{ijlm} \gamma_{lm}^* n_i \int_{\Delta} U_j^k(\mathbf{x}; \mathbf{d}) dA(\mathbf{x}) \quad (11.10)$$

where n_i is the outward normal to Δ . Substituting Eq. (11.5) into (11.10) and changing the integration orders, the contribution from the complementary part can be expressed as

$$u_k(\mathbf{d}) = \frac{1}{2\pi^2} C_{ijlm} \gamma_{lm}^* n_i \int_0^\pi \bar{\mathbf{A}} \left[\int_{\Delta} \mathbf{G}_1 d\Delta(\mathbf{x}) \right] \mathbf{A}^T d\theta \quad (11.11)$$

While the outside line integration can be easily carried out by employing Gaussian quadrature, we discuss the area integration over the flat triangle, which can be done analytically as will be shown below. Actually, since in the expression for \mathbf{G}_1 in Eq. (11.6), its numerator is a function of θ only, the integration over the flat triangle Δ needs to be carried out for the following expression only.

$$F_1(d_j, \theta) = \int_{\Delta} \frac{d\Delta(\mathbf{x})}{-\bar{p}_i x_3 + p_j d_3 - [(x_1 - d_1) \cos \theta + (x_2 - d_2) \sin \theta]} \quad (11.12)$$

Similarly, in order to find the QD-induced strain field, (Eqs. (11.4) and (11.7)), one needs only to carry out the following area integration over the flat triangle.

$$F_2(d_j, \theta) = \int_{\Delta} \frac{d\Delta(\mathbf{x})}{\{-\bar{p}_i x_3 + p_j d_3 - [(x_1 - d_1) \cos \theta + (x_2 - d_2) \sin \theta]\}^2} \quad (11.13)$$

The area integration over a flat triangle in Eqs. (11.12) and (11.13) can be carried out exactly. To do so, we introduce the following transformation between the global coordinate system $\mathbf{x} = (x_1, x_2, x_3)$ and local coordinate system $\xi = (\xi_1, \xi_2, \xi_3)$ associated with the flat triangle (Figure 11.1)

$$\begin{bmatrix} x_1 - x_{01} \\ x_2 - x_{02} \\ x_3 - x_{03} \end{bmatrix} = \begin{bmatrix} a_{11} & a_{12} & a_{13} \\ a_{21} & a_{22} & a_{23} \\ a_{31} & a_{32} & a_{33} \end{bmatrix} \begin{bmatrix} \xi_1 \\ \xi_2 \\ \xi_3 \end{bmatrix} \quad (11.14)$$

Then, the integration becomes ($n = 1, 2$)

$$F_n(d_j, \theta) = \int_0^h d\xi_2 \int_{-l_1 + l_1 \xi_2/h}^{l_2 - l_2 \xi_2/h} d\xi_1 \frac{1}{[f_1(d_j, \theta) \xi_1 + f_2(d_j, \theta) \xi_2 + f_3(d_j, \theta)]^n} \quad (11.15)$$

where

$$f_1(d_j, \theta) = -(\bar{p}_i a_{31} + a_{11} \cos \theta + a_{21} \sin \theta) \quad (11.16)$$

$$f_2(d_j, \theta) = -(\bar{p}_i a_{32} + a_{12} \cos \theta + a_{22} \sin \theta) \quad (11.17)$$

$$f_3(d_j, \theta) = -\bar{p}_i(x_{03} + a_{33} \xi_3) + p_j d_3 + d_1 \cos \theta + d_2 \sin \theta - (x_{01} + a_{13} \xi_3) \cos \theta - (x_{02} + a_{23} \xi_3) \sin \theta \quad (11.18)$$

The integration can now be carried out, and the results are

$$F_1(d_j, \theta) = \frac{1}{f_1} \left[\frac{f_1 l_2 + f_3}{f_2 - f_1 l_2/h} \ln \left(\frac{f_2 h + f_3}{f_1 l_2 + f_3} \right) - \frac{-f_1 l_1 + f_3}{f_2 + f_1 l_1/h} \ln \left(\frac{f_2 h + f_3}{-f_1 l_1 + f_3} \right) \right] \quad (11.19)$$

$$F_2(d_j, \theta) = \frac{1}{f_1} \left[\frac{1}{f_2 + f_1 l_1/h} \ln \left(\frac{f_2 h + f_3}{-f_1 l_1 + f_3} \right) - \frac{1}{f_2 - f_1 l_2/h} \ln \left(\frac{f_2 h + f_3}{f_1 l_2 + f_3} \right) \right] \quad (11.20)$$

With these exact expressions, the QD-induced displacement and strain fields can be finally expressed in terms of the line integration over $[0, \pi]$ (e.g., Eq. (11.11) for the induced displacements). Again the line integration can be carried out numerically using 8-point Gaussian quadrature.

11.3 Numerical Examples

We now apply our analytical solutions to calculate the strain energy induced by a buried QD within the GaAs half-space substrate. The surface of the substrate is traction free. The QD is located at depth d below the surface (Figure 11.2) and the misfit strain is hydrostatic, i.e. $\gamma_{xx}^* = \gamma_{yy}^* = \gamma_{zz}^* = 0.07$. We point out that this misfit strain is relatively large and

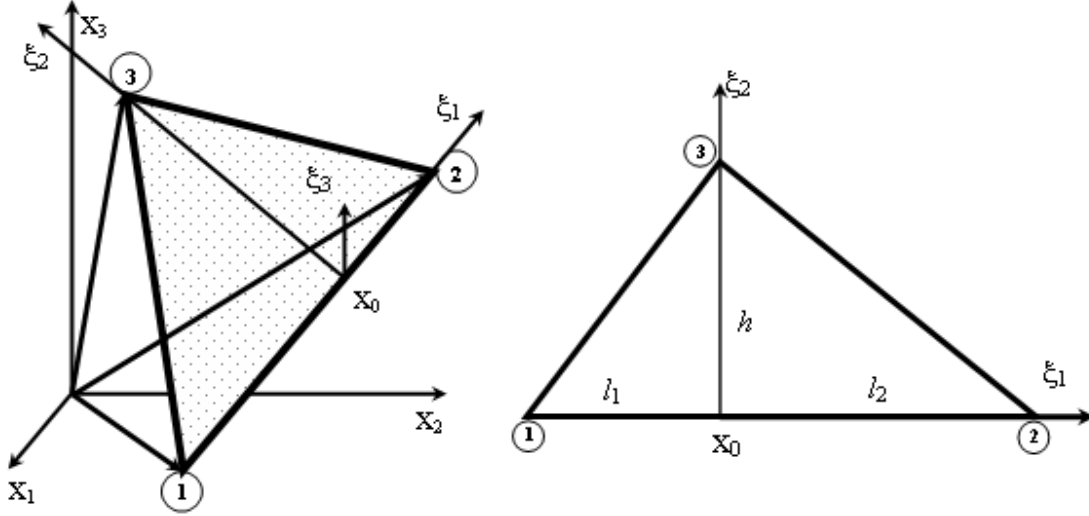


Figure 11.1: Geometry of the flat triangle Δ (with corners 1,2,3), and transformation from the global (x_1, x_2, x_3) to local (ξ_1, ξ_2, ξ_3) coordinates where ξ_3 is along the outward normal direction of the flat triangle.

the corresponding nonlinear influence will be pursued using other methods, such as the multiscale meshless method [192]. As for the QD shape, we assume it to be either cubic, pyramidal, truncated pyramidal, or point type. The QDs have the same height h ($= 4$ nm, except for point QD). To make all the QDs (including the point QD) have the same volume, we have the base length $2.155h$ for cubic QD, upper length $1.79h$ and lower length $2.5h$ for truncated pyramid QD, base length $3.732h$ for pyramid QD (Figure 11.2). For the point QD case, it is located at the middle height of the cubic QD (i.e., its vertical distance to the surface is $d + h/2$). We studied the effect of the QD shape and depth on the strain energy on the surface.

Shown in Figures 11.3a–d are, respectively, contours of the normalized strain energy on the surface of GaAs (001) (top row) and GaAs (111) (bottom row), induced by a buried cubic, truncated pyramidal, pyramidal or point type QD. In this example, the depth $d = 2$ nm, height $h = 4$ nm, and the strain energy is normalized by 118.8×10^{15} N · m. (This normalization factor is also used for the strain energies in Table 11.1). It is clear that different QD shapes (including point QD) induce different strain energy distributions on the surface of the substrate. Besides the difference on the contour shape, the strain energy values are also different. For example, the contours with value 0.3, 0.6 and 0.9 (corresponding, respectively, to the heavy blue, red and black curves) move towards the center when the QD shape changes from left to right (i.e., cubic, truncated pyramid, pyramid, and point type). Table 11.1 lists the maximum strain energy values corresponding to different QD shapes at different depths within the GaAs substrate with both (001) and (111) orientations. It is clear from Table 11.1 that while the induced maximum strain energy value decreases with increasing depth, its value on the substrate GaAs (001) is always larger than that of the corresponding inclined substrate GaAs (111). Furthermore, the effect of the QD shapes (cubic, truncated pyramid, pyramid, and point QD) on the strain energy is complicated, as can be seen from Figures 11.3a–d. Also from Figures 11.3a–d, it is observed, by comparing

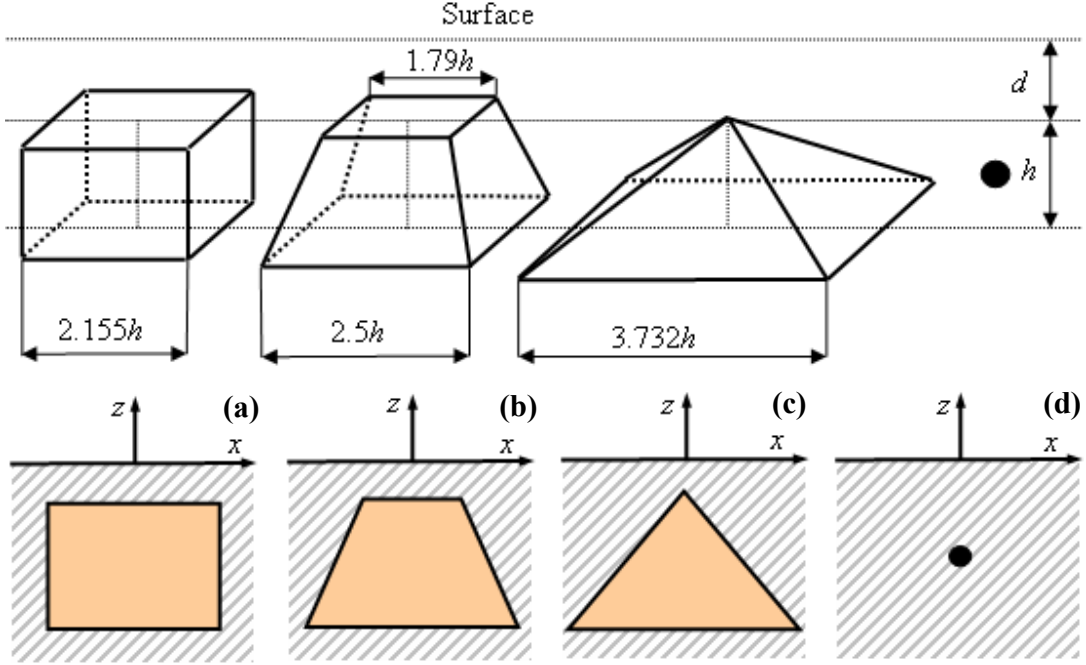


Figure 11.2: Geometry for (a) a cubic QD, (b) a truncated pyramid QD, (c) a pyramid QD, and (d) a point QD. Top row is the 3D view and bottom row is the vertical x - z plan view. All these QDs have the same volume.

the top row to the bottom row, that the strain energy contour lines of equal value all move towards the center, and that the contours shapes of the strain energy over GaAs (001) are sharply different to those over GaAs (111).

We now study the effect of QD depth on the strain energy distribution on the surface. The top row of Figure 11.4 shows the depths of cubic QD within the substrate where d equals 1 nm, 2 nm, or 3 nm, while the strain energy distributions on the surface of GaAs (001) and (111) are shown, respectively, in the middle and bottom rows. Again, the heavy blue, red and black contour lines correspond, respectively, to the strain energy values of 0.3, 0.6, and 0.9. It is apparent from Figure 11.4 that as the QD moves away from the surface, the strain energy contours approach to those due to a point QD with equal volume. Similar numerical results are shown in Figures 11.5 and 11.6, respectively, for the truncated pyramidal and pyramidal QDs. While the strain energy distributions induced by the pyramidal QD are similar to those by an equivalent-volume QD, those by cubic and truncated pyramidal QD are different. These again demonstrate the effect of the QD shape and depth on the strain energy.

11.4 Conclusions

In this chapter, we presented an analytical method for calculating the QD-induced strain fields in half-space semiconductor substrates. The QD is assumed to be of any polyhedral shape which can be efficiently approximated by a number of flat triangles. We studied

Depth			Cubic	Truncated pyramid	Pyramid
$d = 1 \text{ nm}$	(001)	E_{max}	2.54	2.93	2.71
		(x,y)	$(\pm 1, \pm 1)$	$(\pm 1, \pm 1)$	$(0,0)$
	(111)	E_{max}	2.55	2.75	2.05
		(x,y)	$(1,0)$	$(1,0)$	$(0,0)$
$d = 2 \text{ nm}$	(001)	E_{max}	1.77	1.99	0.96
		(x,y)	$(0,0)$	$(0,0)$	$(0,0)$
	(111)	E_{max}	1.31	1.34	0.75
		(x,y)	$(0,0)$	$(0,0)$	$(0,0)$
$d = 3 \text{ nm}$	(001)	E_{max}	1.03	1.09	0.41
		(x,y)	$(0,0)$	$(0,0)$	$(0,0)$
	(111)	E_{max}	0.70	0.70	0.36
		(x,y)	$(0,0)$	$(0,0)$	$(0,0)$

Table 11.1: Maximum strain energy E_{max} on the surface of the substrate GaAs for different QD shapes with different depths (unit of energy = $118.8 \times 10^{15} \text{ N} \cdot \text{m}$).

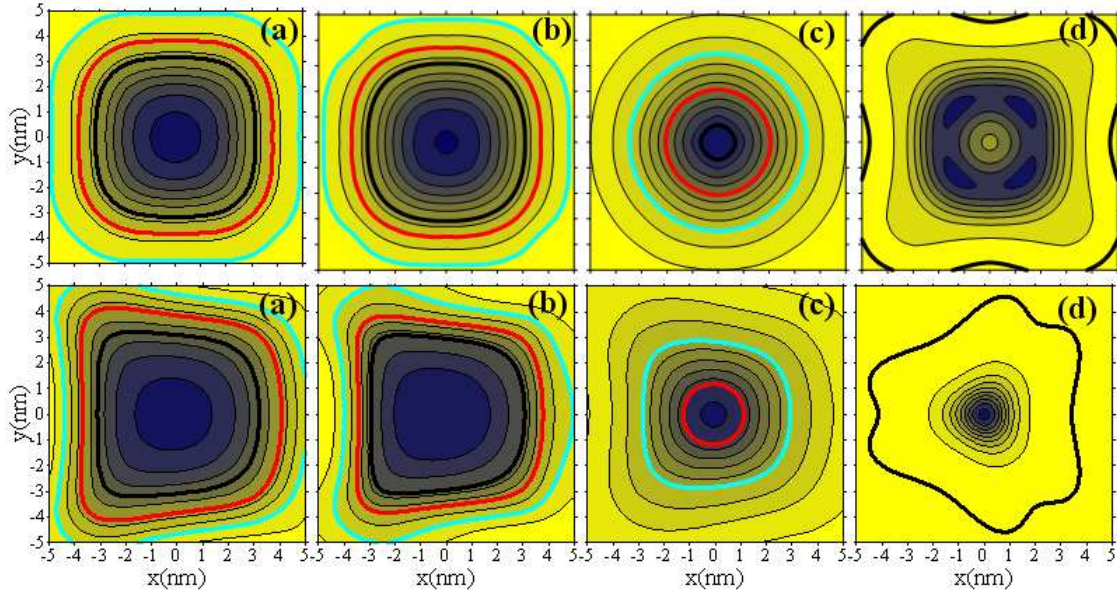


Figure 11.3: Normalized strain energy on the surface of the half-space substrate of GaAs (001) (top row) and GaAs (111) (bottom row) induced by (a) a cubic, (b) a truncated pyramid, (c) a pyramid, and (d) a point QD, where the heavy blue, red and black lines correspond to normalized strain energy of 0.3, 0.6 and 0.9 respectively. The QD is embedded within the substrate with its top side at a depth $d = 2 \text{ nm}$ from the surface.

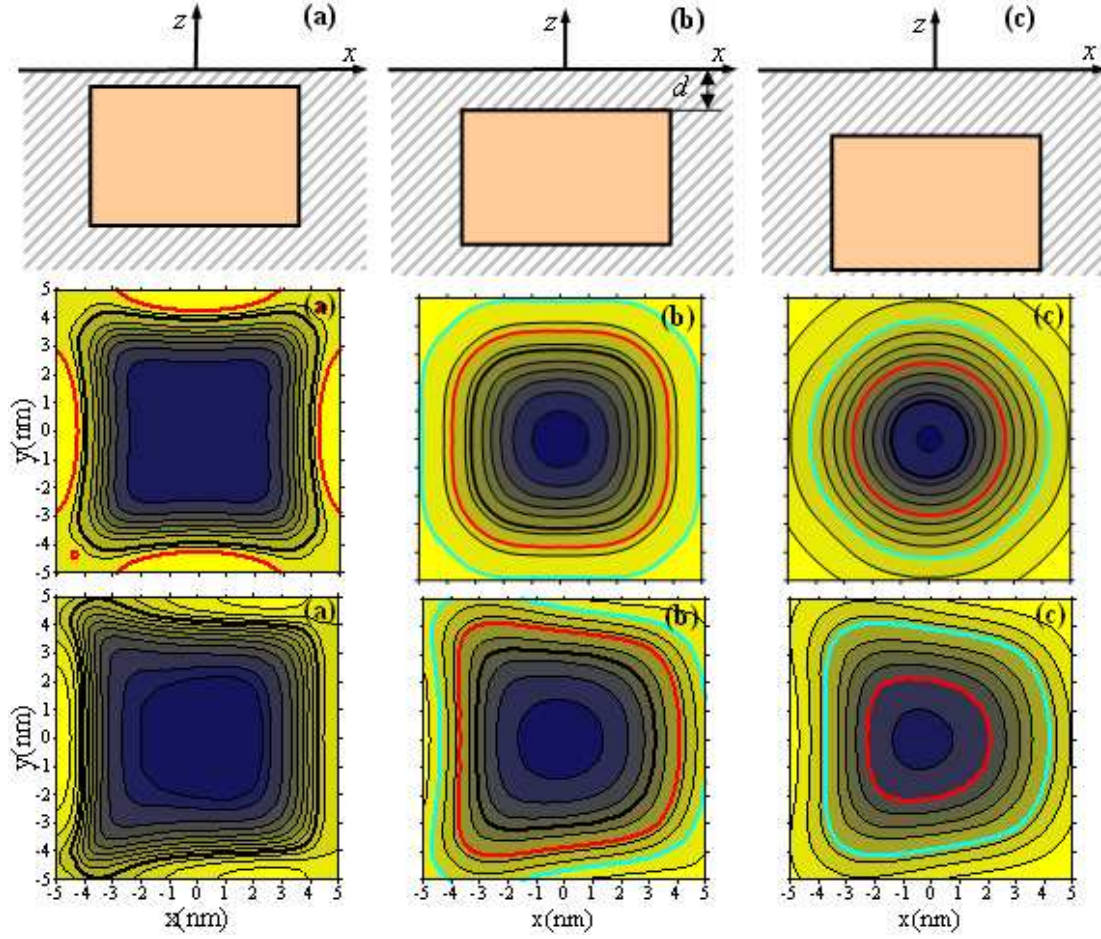


Figure 11.4: Geometry of a cubic QD within a half-space substrate with different depth d : the vertical x - z plan view (top row), and the strain energy induced by the cubic QD in substrate GaAs(001) (middle row) and GaAs (111) (bottom row): (a) $d = 1$, (b) $d = 2$, and (c) $d = 3$. The heavy blue, red and black lines correspond to normalized strain energy of 0.3, 0.6 and 0.9 respectively.

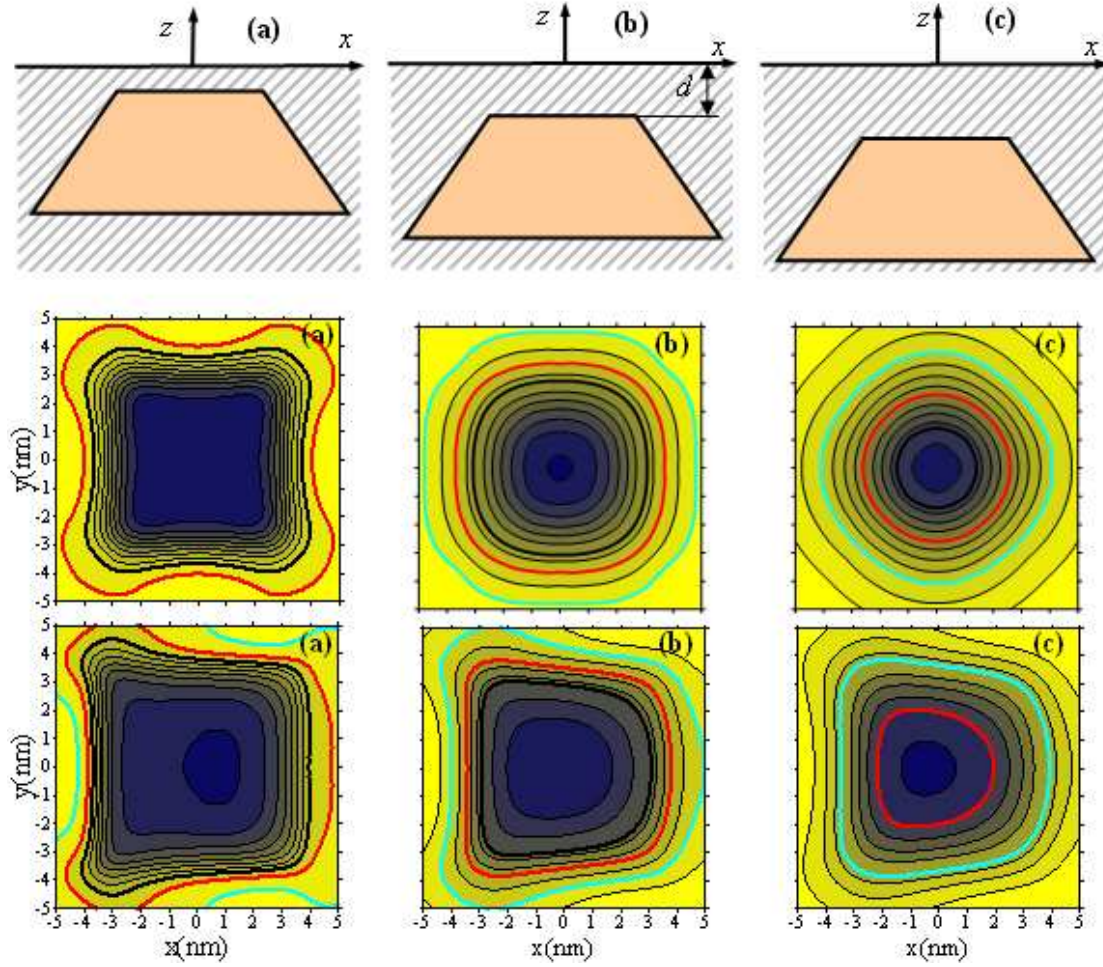


Figure 11.5: Geometry of a truncated pyramid QD within a half-space substrate with different depth d : the vertical x - z plan view (top row), and the strain energy induced by the truncated pyramid QD in substrate GaAs(001) (middle row) and GaAs (111) (bottom row): (a) $d = 1$, (b) $d = 2$, and (c) $d = 3$. The heavy blue, red and black lines correspond to normalized strain energy of 0.3, 0.6 and 0.9 respectively.

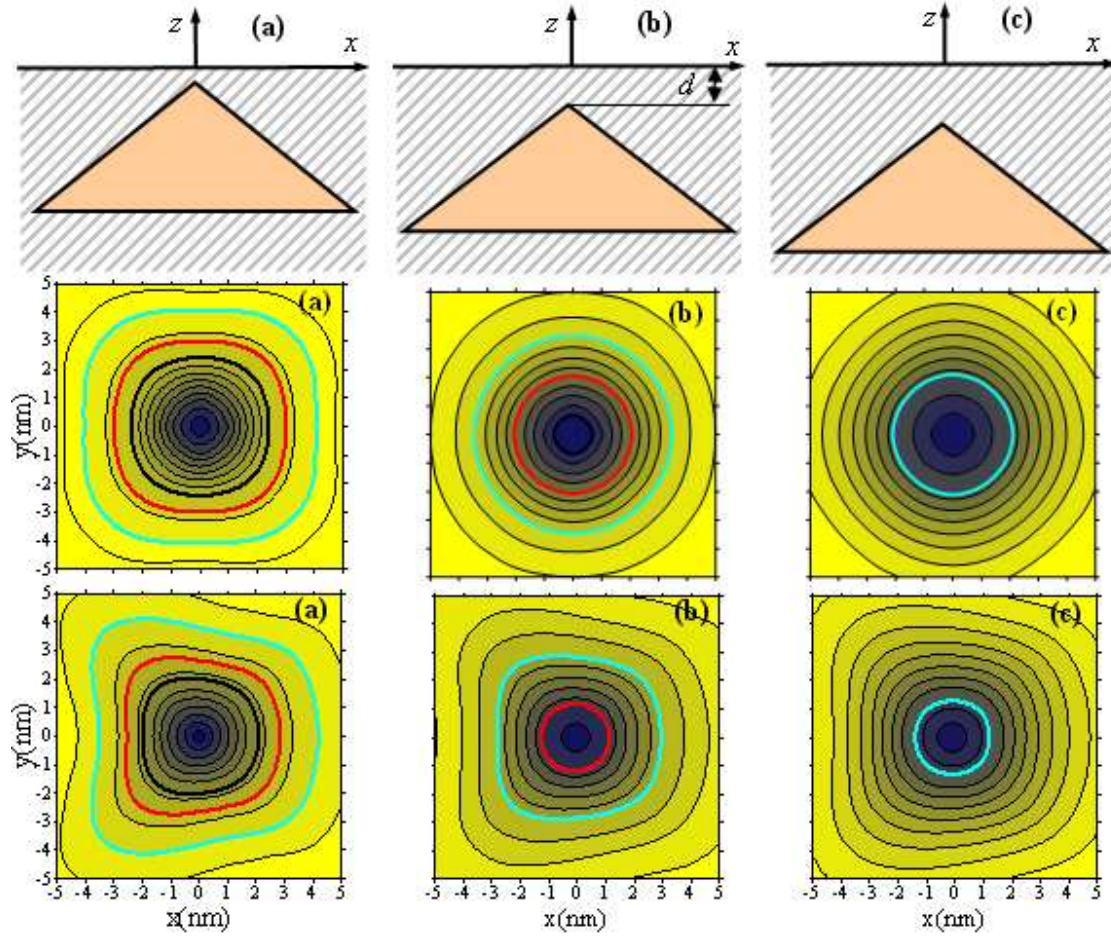


Figure 11.6: Geometry of a pyramid QD within a half-space substrate with different depth d : the vertical x - z plan view (top row), and the strain energy induced by the pyramid QD in substrate GaAs(001) (middle row) and GaAs (111) (bottom row): (a) $d = 1$, (b) $d = 2$, and (c) $d = 3$. The heavy blue, red and black lines correspond to normalized strain energy of 0.3, 0.6 and 0.9 respectively.

cubic, pyramidal, truncated pyramidal and point QDs within the GaAs (001) and GaAs (111) half-space substrates. The numerical results illustrate that the shape of the QDs has apparent influence on the strain energy distribution on the surface, so is the depth of the QDs. These results should be interesting to the overgrowth of QDs on the substrate where the long-range strain energy on the surface plays an important role in controlling the new QD patterns and shapes.

Chapter 12

Elastic And Electric Fields Distribution In AlN QDs Structures

In the previous reports, we used an analytical method based on Green's functions and the Stroh formalism to calculate the induced elastic fields in and around GaAs quantum dot (QD) heterostructures embedded in anisotropic half-space [193]. In this chapter, we extend the analytical solution to nitride-based QDs structures which have a strong built-in electric field.

We consider in detail the case of AlN QDs in the shape of hexagonal truncated-pyramids. Two different growth orientations are studied: one is AlN (0001) growing along the (0001) axis and the other is AlN (1000) growing along the polar direction. A schematic 3D view of an AlN QD is shown in Figure 12.1a with cross section in x - y plane shown in Figure 12.1b. The QD size is determined by the top and base diameters of the pyramid, $R_b = 8.5$ nm and $R_t = 4$ nm. $h = 4.1$ nm is the QD height and $d = 6.9$ nm is the distance between top of QD and half space surface. The size of the QD is used to close to the experimental values [194].

Before looking at multiple dots, a single isolated hexagonal truncated-pyramidal dot is studied to facilitate comparison with simplified model in which the QD is assumed to be a point [2]. The calculated electric potential distributions induced by a single QD are presented at the free surface (Figure 12.2). The strain distributions along a line scan A (Figure 12.1a) are shown in Figure 12.3. The results are compared to those of previously published calculations for a single point dot. Very similar trends are observed. We also investigated the electric potential distribution on the surface due to two hexagonal truncated-pyramidal QDs when the distance D_x (Figure 12.1c) between two QDs is equal to 25 nm (Figure 12.4). These results provide a very useful framework to analyze the properties of nitride-based QDs structures.

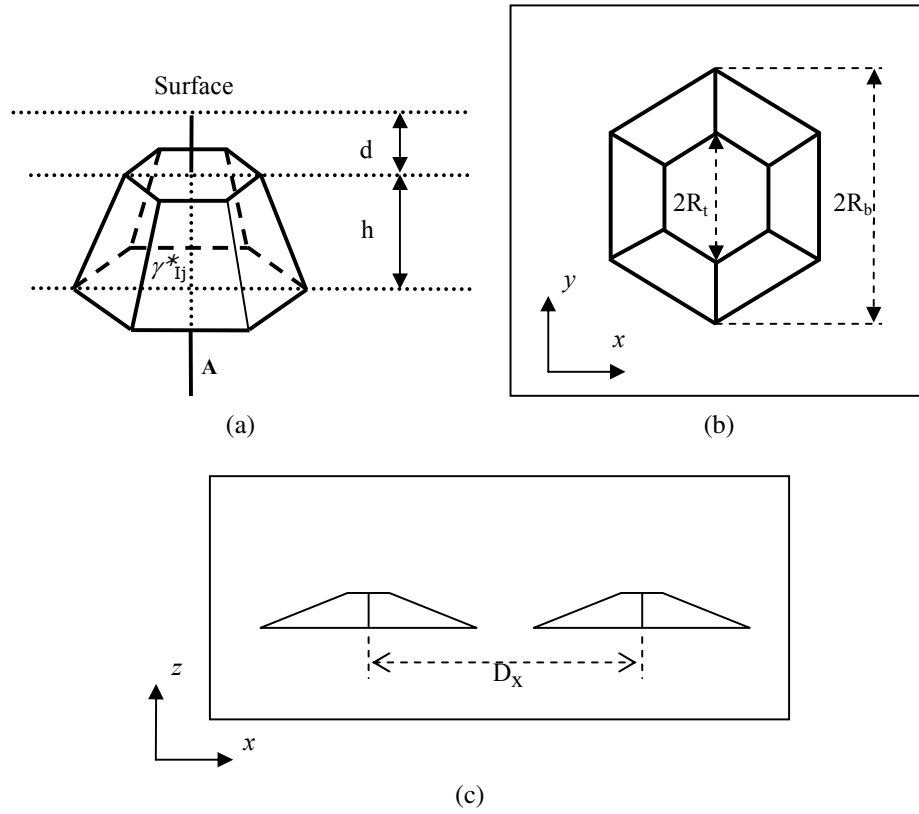


Figure 12.1: Schematic diagrams of hexagonal truncated-pyramidal QD showing dot shape and geometrical parameters. (a) 3D view of a single QD buried under half space substrate. Line A is parallel to the z -axis; (b) View of the QD structure in x - y plane; (c) View of two QDs in x - z plane.

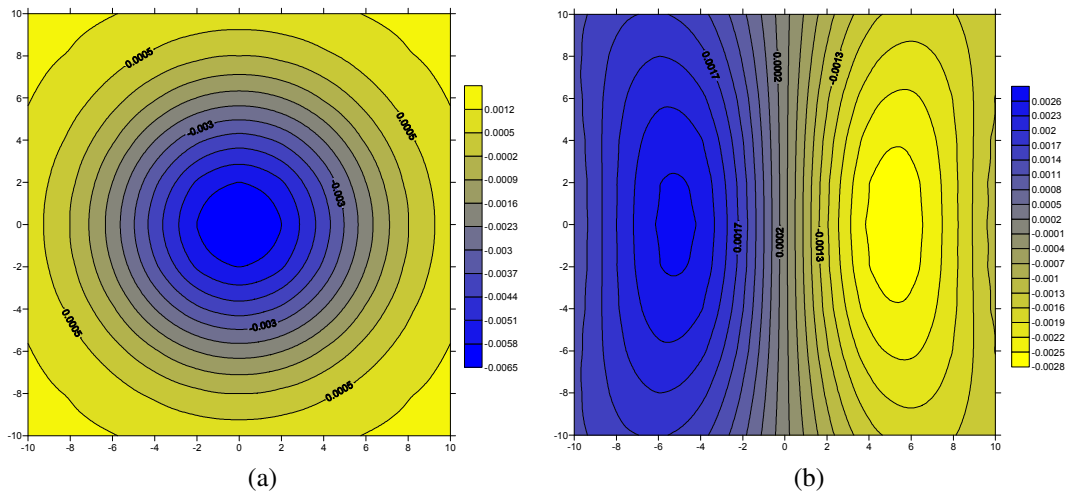


Figure 12.2: (a) Contours of the electric potential Φ on the surface of AlN (0001) due to a hexagonal truncated-pyramidal QD. (b) Contours of the electric potential Φ on the surface of AlN (1000) due to a hexagonal truncated-pyramidal QD.

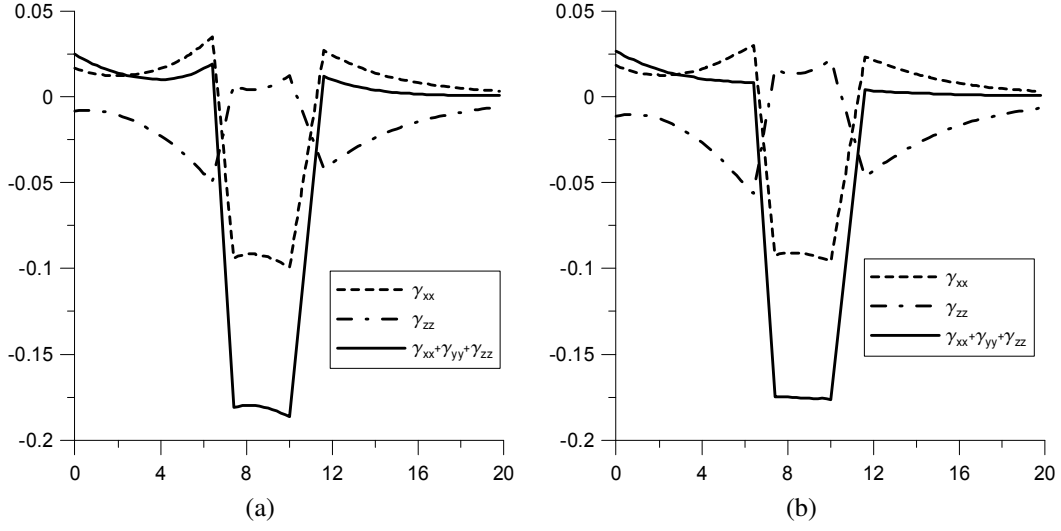


Figure 12.3: Strain distributions along line A of the QD embedded in a matrix of (a) AlN (0001) or (b) AlN (1000). The dashed line denotes γ_{xx} , the dot-dashed line γ_{zz} , and the solid line hydrostatic strain $\gamma_{xx} + \gamma_{yy} + \gamma_{zz}$.

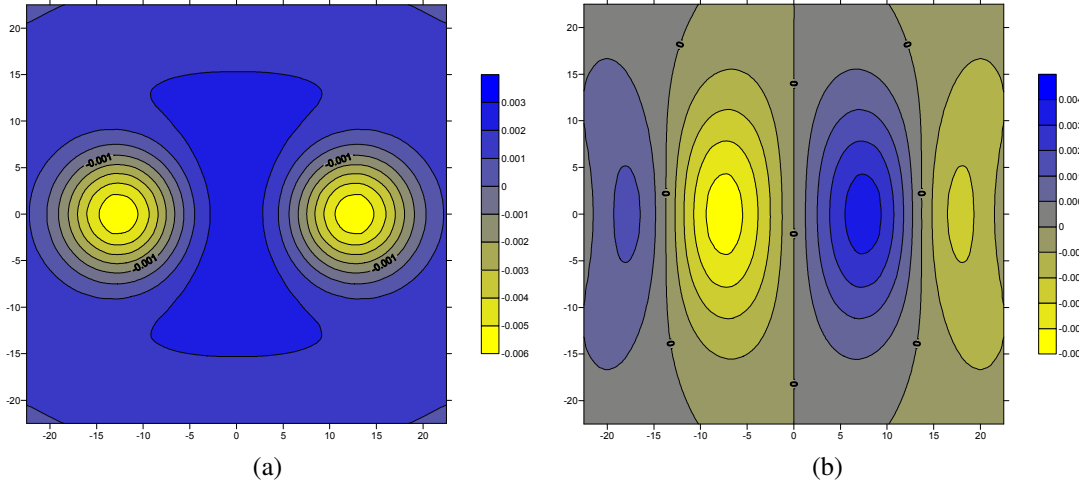


Figure 12.4: (a) Contours of the electric potential Φ on the surface of AlN (0001) due to two hexagonal truncated-pyramidal QDs. (b) Contours of the electric potential Φ on the surface of AlN (1000) due to two hexagonal truncated-pyramidal QDs. The distance D_x between the two QDs is 25 nm.

Chapter 13

Ab initio calculation on magnetic and magnetoelectric coupling effect on a series of perovskite compounds

Oxides with perovskite or perovskite-related structures display a large variety of intriguing physical properties and raise several important fundamental issues in solid-state chemistry and physics. The research of these materials is also of great interest because of their promising technological applications. For example, simple perovskite oxides such as SrTiO_3 and BaTiO_3 have been studied extensively and are already widely used in electronic devices. Some of the intriguing physical properties found recently in perovskite oxides and perovskite-related oxides are the high- T_c superconductivity of cupric oxides, the colossal magnetoresistance (MR) of manganese oxides, and multiferroicity of BiFeO_3 . These properties will be useful in future electronics and spintronics.

The general formula of the perovskite oxide structure is ABO_3 , in which A represents relatively large cations such as alkaline metal, alkaline-earth metal, and lanthanide ions, while B generally represents transition-metal ions. The structure is described as a framework of corner-sharing BO_6 octahedra that contains A cations in 12-fold-coordinated sites. By introduction of additional elements into the A or B sites, ordered superstructures are often stabilized, and the special-ordered arrangements of the A or B cations in the perovskite structures open up possibilities for making compounds with new properties. Large numbers of B-site ordered compounds have been obtained, such as $\text{Sr}_2\text{FeMoO}_6$, $\text{La}_2\text{NiMnO}_6$, etc. In this project, a series of calculations has been carried out on the A-site-ordered perovskites, that is, $\text{TbCu}_3\text{Mn}_4\text{O}_{12}$, $\text{CaFe}_3\text{Ti}_4\text{O}_{12}$ and $\text{CaFeTi}_2\text{O}_6$.

For $\text{TbCu}_3\text{Mn}_4\text{O}_{12}$, the electronic and magnetic properties of the three-magnetic-sublattice double perovskite $\text{TbCu}_3\text{Mn}_4\text{O}_{12}$ are investigated by performing density functional theory calculations along with the analysis of the spin-orbit coupling (SOC) effect on Tb^{3+} ($4f^8$) ions at A sites. The electronic structure calculations show that $\text{TbCu}_3\text{Mn}_4\text{O}_{12}$ is half-metallic and its half-metallicity can only be correctly described when the electron correlation on Tb^{3+} $4f^8$ electrons is considered. The energies of different magnetic configurations among the three magnetic sublattices are also calculated, revealing that the magnetic configuration with Mn and Cu spins in the antiparallel arrangement and with the Tb magnetic moments ferromagnetically/antiferromagnetically (FM/AFM) coupled to Cu/Mn

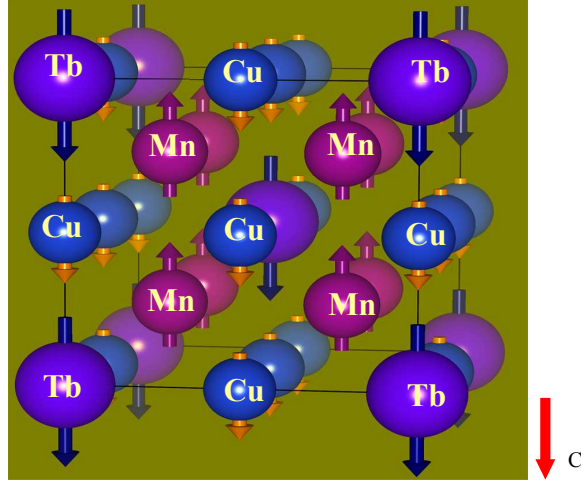


Figure 13.1: The GGA predicted ground state magnetic configuration-**AF2**. (The arrow directions represent the spin arrangement)

spins (that is $\text{Tb}^{\downarrow}\text{Cu}_3^{\downarrow}\text{Mn}_4^{\uparrow}\text{O}_{12}$) is the lowest energetic magnetic state, which is consistent with recent experimental results. The magnetic anisotropy is further calculated for the [111], [110], and [001] spin quantization directions. It is found that the [111]-direction is more stable than the [110]- and [001]-directions by 123 meV and 135 meV per formula unit, respectively, indicating a significant magnetic anisotropy. Our detailed projected partial density of states analysis finally shows that Tb is expected to interact ferromagnetically with A-site Cu and antiferromagnetically with B-site Mn sublattices by way of $4f$ - $2p$ - $3d$.

Figure 13.1 in the follow shows the lowest energy magnetic configuration of $\text{TbCu}_3\text{Mn}_4\text{O}_{12}$. Based on this magnetic configuration, its electronic structures obtained at different calculating levels are analyzed in detail, as seen in Figure 13.2, which shows that at the lower symmetry due to the spin-orbit coupling, Tb $4f$ electronic configuration is correctly described using GGA+U method. $\text{TbCu}_3\text{Mn}_4\text{O}_{12}$ is half-metallic. As to the magnetic coupling between Tb- $4f$ and Cu- $3d$ as well as Mn- $3d$, the calculations reveal that it is by way of $4f$ -O $2p$ - $3d$, which is shown in Figures 13.3a and 13.3b.

The electronic and magnetic properties of $\text{CaFe}_3\text{Ti}_4\text{O}_{12}$ and $\text{CaFeTi}_2\text{O}_6$ were also investigated using density functional theory. The calculations predict that $\text{CaFe}_3\text{Ti}_4\text{O}_{12}$ is an insulator with its Fe^{2+} ions preferably being antiferromagnetically coupled by the Fe-O-Ti-O-Fe path. Such electronic and magnetic properties are similar to its isostructural perovskite $\text{CaCu}_3\text{Ti}_4\text{O}_{12}$. On the other hand, the calculations indicate $\text{CaFeTi}_2\text{O}_6$ is half metallic and its Fe^{2+} ions are inclined to be ferromagnetically coupled. The different magnetic interactions in $\text{CaFe}_3\text{Ti}_4\text{O}_{12}$ and $\text{CaFeTi}_2\text{O}_6$ are ascribed to their different orbital occupations since orbital ordering and magnetic ordering are closely correlated in transition metal perovskites. This theoretical investigation suggests that altering coordination of A-site transition metal ions (Fe^{2+} in the investigated system) in $\text{A}'\text{A}_3\text{Ti}_4\text{O}_{12}$ double perovskites is another way to control their magnetic properties. Figure 13.4 present the different crystal structures for these two compounds and the different coordination of Fe^{2+} ions. Figure 13.5 shows the different orbital occupation within these two compounds. Figure 13.6 shows that $\text{CaFe}_3\text{Ti}_4\text{O}_{12}$ is semiconductor while $\text{CaFeTi}_2\text{O}_6$ is half-metallic.

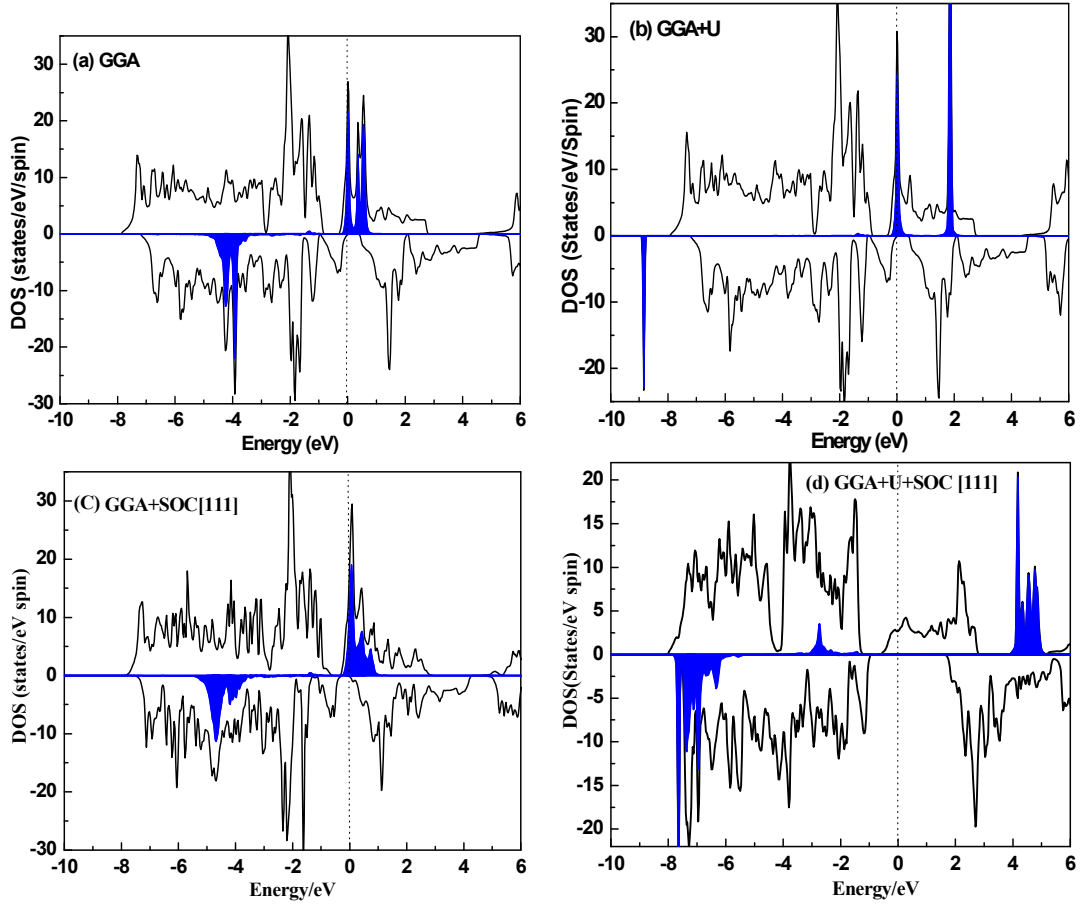


Figure 13.2: Total density of states (TDOS) along with partial density of states (PDOS) of $4f$ orbitals calculated for $\text{TbCu}_3\text{Mn}_4\text{O}_{12}$ in the **AF2** magnetic state using different methods. (a) GGA, (b) GGA+U with U_f 6.0 eV, (c) GGA+SOC [111], and (e) GGA+ U_f [111] with $U_f = 6.0$ eV at lower symmetry. The Fermi energy is indicated by the dotted line. The positive and negative values indicate spin up and spin down, respectively.

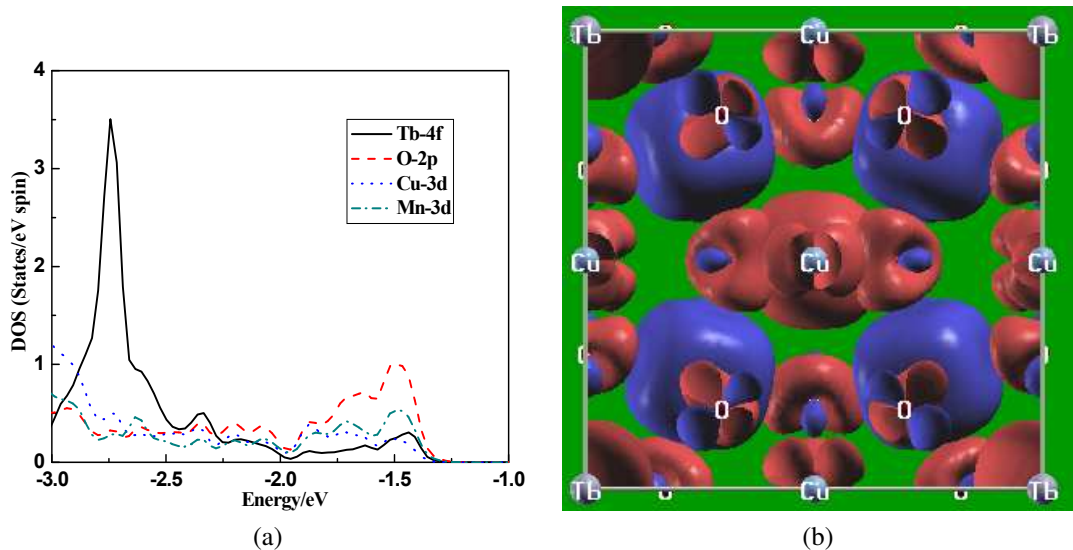


Figure 13.3: (a) Density of states (DOS) versus electronic energy for electrons of orbitals Tb-4f, O-2p, Cu-3d, and Mn-3d. (b) Electronic density distributions for electrons with energies in the range of -2.0 to -1.5 eV. Distributions colored red are for electrons with spin down (\downarrow), and distributions colored blue are for electrons with spin up (\uparrow).

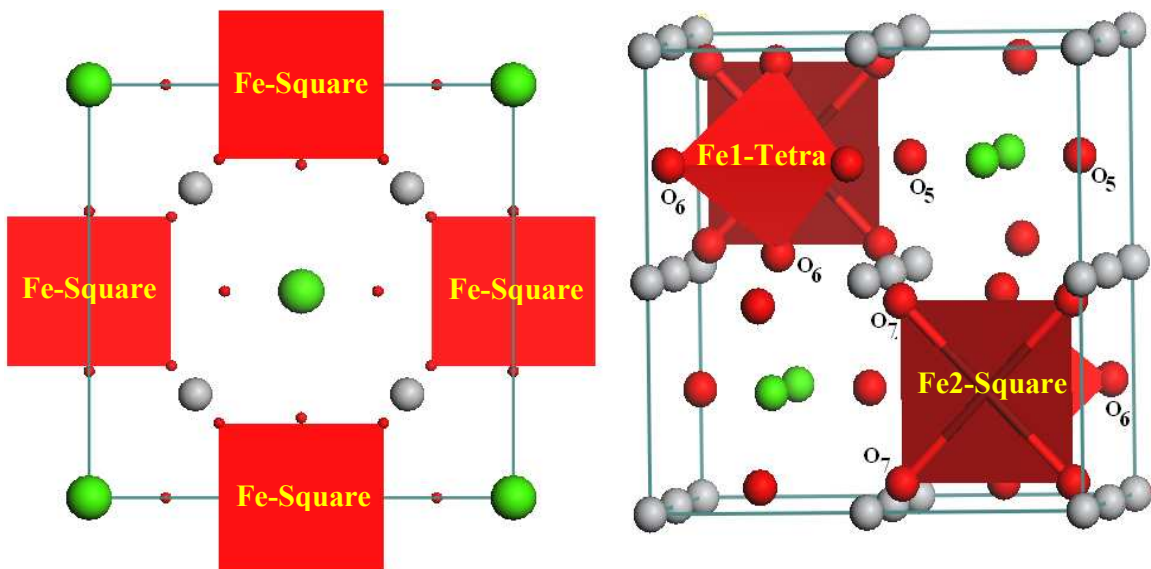


Figure 13.4: Crystal structures and the coordination environment of Fe ions of CaFe₃Ti₄O₁₂ in the left and CaFeTi₂O₆ in the right.

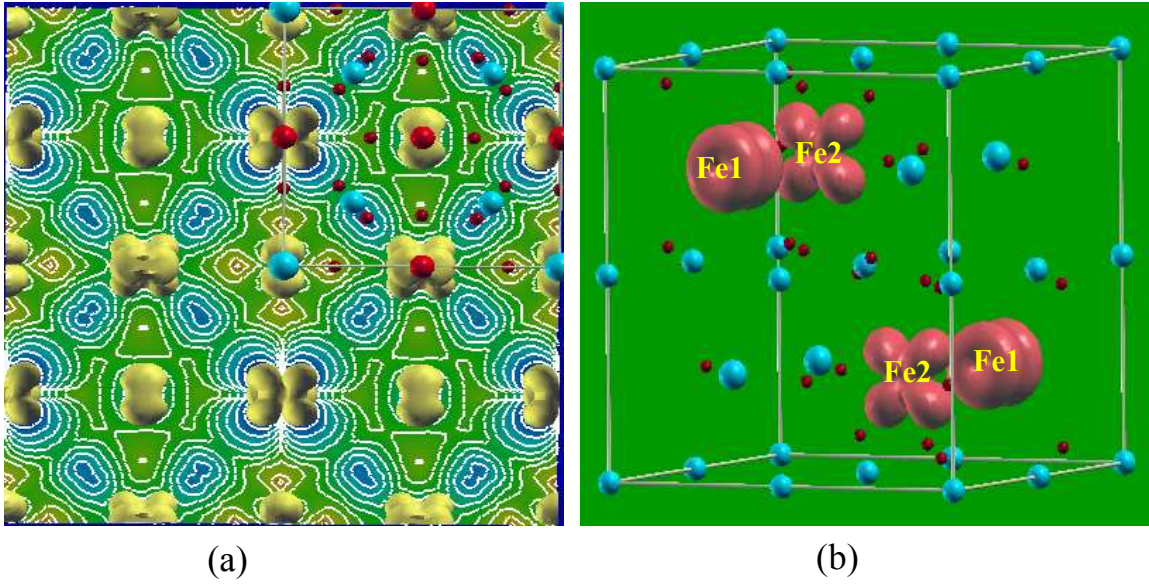


Figure 13.5: Electron density plots around Fermi level for (a) AFM $\text{CaFe}_3\text{Ti}_4\text{O}_{12}$ (d_{xy} , d_{xz} and d_{yz} orbitals are the same due to its $m-3$ point group symmetry in this perovskite) and (b) FM $\text{CaFeTi}_2\text{O}_6$ (isosurface at $0.1 \text{ e}/\text{\AA}^3$ produced using XCRYSDEN).

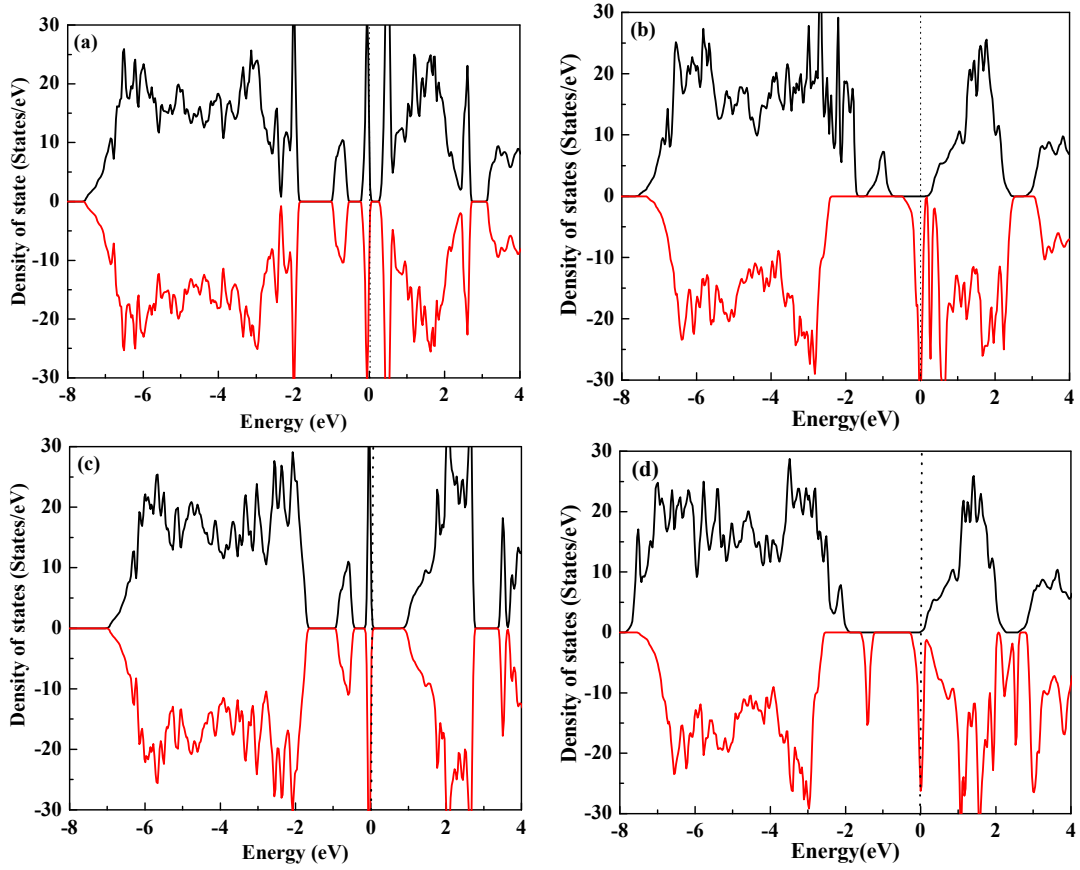


Figure 13.6: GGA calculated total density of states for (a) $\text{CaFe}_3\text{Ti}_4\text{O}_{12}$ in AFM and (b) $\text{CaFeTi}_2\text{O}_6$ in FM; and GGA+ U_{eff} ($U_{\text{eff}} = 4.0$ eV) calculated results for (c) $\text{CaFe}_3\text{Ti}_4\text{O}_{12}$ in AFM and (d) $\text{CaFeTi}_2\text{O}_6$ in FM.

References

- [1] E. Pan. Elastic and piezoelectric fields around a quantum dot: Fully coupled or semicoupled model? *Journal of Applied Physics*, 91:3785–3796, 2002.
- [2] E. Pan. Elastic and piezoelectric fields in substrates GaAs (001) and GaAs (111) due to a buried quantum dot. *Journal of Applied Physics*, 91:6379–6387, 2002.
- [3] R. Bonnet. Elasticity theory of straight dislocations in a multilayer. *Physical Review B*, 53:10978–10982, 1996.
- [4] M. E. Levinshtein, S. L. Rumyantsev, and M. S. Shur, editors. *Properties of Advanced Semiconductor Materials GaN, AlN, InN, BN, SiC, SiGe*. John Wiley & Sons, 2001.
- [5] I. Vurgaftman, J. R. Meyer, and L. R. Ram-Mohan. Band parameters for III–V compound semiconductors and their alloys. *Journal of Applied Physics*, 89:5815–5875, 2001.
- [6] Qun Shen and Stefan Kycia. Determination of interfacial strain distribution in quantum-wire structures by synchrotron x-ray scattering. *Physical Review B*, 55:15791–15797, 1997.
- [7] E. S. Tentarelli, J. D. Reed, Y.-P. Chen, W. J. Schaff, and L. F. Eastman. Strain-induced shift in photoluminescence energy in $\text{In}_{0.2}\text{Ga}_{0.8}\text{As}/\text{GaAs}$ quantum wires. *Journal of Applied Physics*, 78:4031–4034, 1995.
- [8] A. Ulyanenko, N. Darowski, J. Grenzer, U. Pietsch, K. H. Wang, and A. Forchel. Evaluation of strain distribution in freestanding and buried lateral nanostructures. *Physical Review B*, 60:16701–16714, 1999.
- [9] A. Freundlich, A. Alemu, and S. Bailey. Quantum wire solar cell. In *Conference Record of the Thirty-first IEEE Photovoltaic Specialists Conference*, pages 137–140, 2005.
- [10] R. Maranganti and P. Sharma. A review of strain field calculations in embedded quantum dots and wires. In Michael Reith and Wolfram Schommers, editors, *Handbook of Theoretical and Computational Nanotechnology*, chapter 118. American Scientific, 2005.

- [11] David A. Faux, James R. Downes, and Eoin P. O'Reilly. Analytic solutions for strain distributions in quantum-wire structures. *Journal of Applied Physics*, 82:3754–3762, 1997.
- [12] H. T. Johnson and L. B. Freund. The influence of strain on confined electronic states in semiconductor quantum structures. *International Journal of Solids and Structures*, 38:1045–1062, 2001.
- [13] F. Glas. Analytical calculation of the strain field of single and periodic misfitting polygonal wires in a half-space. *Philosophical Magazine A*, 82:2591–2608, 2002.
- [14] X. Zhang and P. Sharma. Size dependency of strain in arbitrary shaped anisotropic embedded quantum dots due to nonlocal dispersive effects. *Physical Review B*, 72:195345, 2005.
- [15] H. J. Chu and J. Wang. Strain distribution in arbitrarily shaped quantum dots with nonuniform composition. *Journal of Applied Physics*, 98:034315, 2005.
- [16] D. L. Smith. Strain-generated electric fields in [111] growth axis strained-layer superlattices. *Solid State Communications*, 57:919–921, 1986.
- [17] S. N. Mohammad and H. Morkoç. Progress and prospects of group-III nitride semiconductors. *Progress in Quantum Electronics*, 20:361 – 525, 1996.
- [18] John H. Davies. Elastic and piezoelectric fields around a buried quantum dot: A simple picture. *Journal of Applied Physics*, 84:1358–1365, 1998.
- [19] Seoung-Hwan Park and Shun-Lien Chuang. Piezoelectric effects on electrical and optical properties of wurtzite GaN/AlGaIn quantum well lasers. *Applied Physics Letters*, 72:3103–3105, 1998.
- [20] B. Jogai, J. D. Albrecht, and E. Pan. Energy levels in polarization superlattices: a comparison of continuum strain models. *Semiconductor Science and Technology*, 19:733–741, 2004.
- [21] B. Jogai, J. D. Albrecht, and E. Pan. Effect of electromechanical coupling on the strain in AlGaIn/GaN heterojunction field effect transistors. *Journal of Applied Physics*, 94:3984–3989, 2003.
- [22] B. Jogai, J. D. Albrecht, and E. Pan. Electromechanical coupling in free-standing AlGaIn/GaN planar structures. *Journal of Applied Physics*, 94:6566–6573, 2003.
- [23] E. Pan. Eshelby problem of polygonal inclusions in anisotropic piezoelectric full- and half-planes. *Journal of the Mechanics and Physics of Solids*, 52:567–589, 2004.
- [24] E. Pan, F. Han, and J. D. Albrecht. Strain fields in InAs/GaAs quantum wire structures: Inclusion versus inhomogeneity. *Journal of Applied Physics*, 98:013534, 2005.

- [25] E. Pan. Mindlin's problem for an anisotropic piezoelectric half-space with general boundary conditions. *Proceedings of the Royal Society of London A*, 458:181–208, 2002.
- [26] M. Grundmann, O. Stier, and D. Bimberg. InAs/GaAs pyramidal quantum dots: Strain distribution, optical phonons, and electronic structure. *Physical Review B*, 52:11969–11981, 1995.
- [27] J. D. Eshelby. Elastic inclusions and inhomogeneities. In I. N. Sneddon and R. Hill, editors, *Progress in solid mechanics*, volume 2, pages 89–140. North-Holland, 1961.
- [28] J. D. Eshelby. The determination of the elastic field of an ellipsoidal inclusion, and related problems. *Proceedings of the Royal Society of London A*, 241:376–396, 1957.
- [29] T. Mura. *Micromechanics of Defects in Solids*. Kluwer Academic Publishers, 2nd edition, 1987.
- [30] David A. Faux, James R. Downes, and Eoin P. O'Reilly. A simple method for calculating strain distributions in quantum-wire structures. *Journal of Applied Physics*, 80:2515–2517, 1996.
- [31] C. Q. Ru. Eshelby's problem for two-dimensional piezoelectric inclusions of arbitrary shape. *Proceedings of the Royal Society of London A*, 456:1051–1068, 2000.
- [32] Frank Glas. Elastic relaxation of a truncated circular cylinder with uniform dilational eigenstrain in a half space. *physica status solidi (b)*, 237:599–610, 2003.
- [33] B. Yang and E. Pan. Elastic analysis of an inhomogeneous quantum dot in multilayered semiconductors using a boundary element method. *Journal of Applied Physics*, 92:3084–3088, 2002.
- [34] C. A. Brebbia and J. Dominguez. *Boundary Elements: An Introductory Course*. Computational Mechanics Publications, 1992.
- [35] T. C. T. Ting. *Anisotropic Elasticity: Theory and Applications*. Oxford University Press, 1996.
- [36] E. Pan and X. Jiang. Singularity analysis at the vertex of polygonal quantum wire inclusions. *Mechanics Research Communications*, 33:1–8, 2006.
- [37] Ursula M. E. Christmas, A. D. Andreev, and D. A. Faux. Calculation of electric field and optical transitions in InGaN/GaN quantum wells. *Journal of Applied Physics*, 98:073522, 2005.
- [38] J. Wang, J. B. Neaton, H. Zheng, V. Nagarajan, S. B. Ogale, B. Liu, D. Viehland, V. Vaithyanathan, D. G. Schlom, U. V. Waghmare, N. A. Spaldin, K. M. Rabe, M. Wuttig, and R. Ramesh. Epitaxial BiFeO₃ multiferroic thin film heterostructures. *Science*, 299:1719–1722, 2003.

- [39] W. Eerenstein, N. D. Mathur, and J. F. Scott. Multiferroic and magnetoelectric materials. *Nature*, 442:759–765, 2006.
- [40] Martin Gajek, Manuel Bibes, Stephane Fusil, Karim Bouzehouane, Josep Fontcuberta, Agnes Barthelemy, and Albert Fert. Tunnel junctions with multiferroic barriers. *Nature Materials*, 6:296–302, 2007.
- [41] Ce Wen Nan, Ming Li, and Jin H. Huang. Calculations of giant magnetoelectric effects in ferroic composites of rare-earth–iron alloys and ferroelectric polymers. *Physical Review B*, 63:144415, 2001.
- [42] M. I. Bichurin, I. A. Kornev, V. M. Petrov, A. S. Tatarenko, Yu. V. Kiliba, and G. Srinivasan. Theory of magnetoelectric effects at microwave frequencies in a piezoelectric/magnetostrictive multilayer composite. *Physical Review B*, 64:094409, 2001.
- [43] G. Srinivasan, E. T. Rasmussen, J. Gallegos, R. Srinivasan, Yu. I. Bokhan, and V. M. Laletin. Magnetoelectric bilayer and multilayer structures of magnetostrictive and piezoelectric oxides. *Physical Review B*, 64:214408, 2001.
- [44] M. I. Bichurin, V. M. Petrov, and G. Srinivasan. Theory of low-frequency magnetoelectric effects in ferromagnetic-ferroelectric layered composites. *Journal of Applied Physics*, 92:7681–7683, 2002.
- [45] E. Pan. Three-dimensional Green’s functions in anisotropic magneto-electro-elastic bimetals. *Zeitschrift für Angewandte Mathematik und Physik (ZAMP)*, 53:815–838, 2002.
- [46] Shashidhar Srinivas and Jiang Yu Li. The effective magnetoelectric coefficients of polycrystalline multiferroic composites. *Acta Materialia*, 53:4135–4142, 2005.
- [47] X. Wang and E. Pan. Electromagnetic fields induced by a point source in a uniaxial multiferroic full-space, half-space, and bimaterial space. *Journal of Materials Research*, 22:2144–2155, 2007.
- [48] X. Wang and E. Pan. Electromagnetic fields induced by a cuboidal inclusion with uniform spontaneous polarization and magnetization. *Journal of Applied Physics*, 101:103524, 2007.
- [49] S. Doniach and E. H. Sondheimer. *Green’s Functions for Solid State Physics*. World Scientific Publishing, 1999.
- [50] Liang Jun Li and Jiang Yu Li. Electromagnetic fields induced in a uniaxial multiferroic material by a point source or an ellipsoidal inclusion. *Physical Review B*, 73:184416, 2006.
- [51] L. Dong, G. Q. Gu, and K. W. Yu. First-principles approach to dielectric response of graded spherical particles. *Physical Review B*, 67:224205, 2003.

- [52] S. Suresh. Graded materials for resistance to contact deformation and damage. *Science*, 292:2447–2451, 2001.
- [53] K.-S. Chang, M. A. Aronova, C.-L. Lin, M. Murakami, M.-H. Yu, J. Hattrick-Simpers, O. O. Famodu, S. Y. Lee, R. Ramesh, M. Wuttig, I. Takeuchi, C. Gao, and L. A. Bendersky. Exploration of artificial multiferroic thin-film heterostructures using composition spreads. *Applied Physics Letters*, 84:3091–3093, 2004.
- [54] M. Murakami, K.-S. Chang, M. A. Aronova, C.-L. Lin, Ming H. Yu, J. Hattrick-Simpers, M. Wuttig, I. Takeuchi, C. Gao, B. Hu, S. E. Lofland, L. A. Knauss, and L. A. Bendersky. Tunable multiferroic properties in nanocomposite PbTiO_3 – CoFe_2O_4 epitaxial thin films. *Applied Physics Letters*, 87:112901, 2005.
- [55] S. Fujino, M. Murakami, S.-H. Lim, L. G. Salamanca-Riba, M. Wuttig, and I. Takeuchi. Multiphase growth in Bi-Mn-O thin films. *Journal of Applied Physics*, 101:013903, 2007.
- [56] Z.-G. Ban, S. P. Alpay, and J. V. Mantese. Fundamentals of graded ferroic materials and devices. *Physical Review B*, 67:184104, 2003.
- [57] L. J. Gray, T. Kaplan, J. D. Richardson, and G. H. Paulino. Green’s functions and boundary integral analysis for exponentially graded materials: Heat conduction. *Journal of Applied Mechanics*, 70:543–549, 2003.
- [58] J. D. Richardson L. J. Gray J. R. Berger P. A. Martin. On Green’s function for a three-dimensional exponentially graded elastic solid. *Proceedings of the Royal Society of London A*, 458:1931–1947, 2002.
- [59] Youn-Sha Chan, L. J. Gray, T. Kaplan, and Glaucio H. Paulino. Green’s function for a two-dimensional exponentially graded elastic medium. *Proceedings of the Royal Society of London A*, 460:1689–1706, 2004.
- [60] E. Pan and F. Han. Green’s functions for transversely isotropic piezoelectric functionally graded multilayered half spaces. *International Journal of Solids and Structures*, 42:3207–3233, 2005.
- [61] B. U. Felderhof. Fluctuations of polarization and magnetization in dielectric and magnetic media. *The Journal of Chemical Physics*, 67:493–500, 1977.
- [62] James Baker-Jarvis and Pavel Kabos. Dynamic constitutive relations for polarization and magnetization. *Physical Review E*, 64:056127, 2001.
- [63] M. Bornatici and O. Maj. The effective polarization and magnetization fields in terms of charge-current densities. *Physica Scripta*, 73:160–163, 2006.
- [64] Ernian Pan. A BEM analysis of fracture mechanics in 2D anisotropic piezoelectric solids. *Engineering Analysis with Boundary Elements*, 23:67–76, 1999.

- [65] Ernian Pan and Bernard Amadei. A 3-D boundary element formulation of anisotropic elasticity with gravity. *Applied Mathematical Modelling*, 20:114–120, 1996.
- [66] L. Sorba, G. Bratina, A. Franciosi, L. Tapfer, G. Scamarcio, V. Spagnolo, and E. Molinari. Si-GaAs(001) superlattices. *Applied Physics Letters*, 61:1570–1572, 1992.
- [67] G. Scamarcio, V. Spagnolo, E. Molinari, L. Tapfer, L. Sorba, G. Bratina, and A. Franciosi. Phonons in Si/GaAs superlattices. *Physical Review B*, 46:7296–7299, 1992.
- [68] M. Alexe and U. Goesele, editors. *Wafer Bonding: Applications and Technology*. Springer-Verlag, 2004.
- [69] J. S. Koehler. Attempt to design a strong solid. *Physical Review B*, 2:547–551, 1970.
- [70] Peter Anderson, I. H. Lin, and Robb Thomson. Fracture in multilayers. *Scripta Metallurgica et Materialia*, 27:687–692, 1992.
- [71] D. S. Lashmore and R. Thomson. Cracks and dislocations in face-centered cubic metallic multilayers. *Journal of Materials Research*, 7:2379–2386, 1992.
- [72] X.G. Ning, David S. Wilkinson, Jian Fu Mao, J. H. Li, Heng Qiang Ye, Z. J. Pu, and D. X. Zou. High resolution transmission electron microscope investigations of phases, domains and interfaces in $\text{Ti}_{50.5}\text{Al}_{46.5}\text{Cr}_3/\text{TiB}_2$ composites. In A.C. Ferro, J.P. Conde, and M.A. Fortes, editors, *Intergranular and Interphase Boundaries in Materials*, volume 207–209 of *Materials Science Forum*, pages 313–316. Trans Tech Publications, 1996.
- [73] Wei Cai, Vasily V. Bulatov, Jinpeng Chang, Ju Li, and Sidney Yip. Anisotropic elastic interactions of a periodic dislocation array. *Physical Review Letters*, 86:5727–5730, 2001.
- [74] Wei Cai, Vasily V. Bulatov, Jinpeng Chang, Ju Li, and Sidney Yip. Periodic image effects in dislocation modelling. *Philosophical Magazine*, 83:539–567, 2003.
- [75] Ju Li, Cai-Zhuang Wang, Jin-Peng Chang, Wei Cai, Vasily V. Bulatov, Kai-Ming Ho, and Sidney Yip. Core energy and peierls stress of a screw dislocation in bcc molybdenum: A periodic-cell tight-binding study. *Physical Review B*, 70:104113, 2004.
- [76] H. Bougrab, K. Inal, H. Sabar, and M. Berveiller. Periodic dislocation configuration analysis by lattice distortion evaluation: micromechanical approach and x-ray diffraction line broadening. *Journal of Applied Crystallography*, 37:270–278, 2004.
- [77] R. Bonnet. Misfit dislocations in limited inhomogeneous media: A review. *Interface Science*, 4:169–179, 1997.

- [78] R. Bonnet. A biperiodic network of misfit dislocations in a thin bicrystalline foil. *physica status solidi (a)*, 180:487–497, 2000.
- [79] T. Outtas, L. Adami, A. Derardja, S. Madani, and R. Bonnet. Anisotropic elastic field of a thin bicrystal deformed by a biperiodic network of misfit dislocations. *physica status solidi (a)*, 188:1041–1045, 2001.
- [80] Toufik Outtas, Lahbib Adami, and Roland Bonnet. A biperiodic interfacial pattern of misfit dislocation interacting with both free surfaces of a thin bicrystalline sandwich. *Solid State Sciences*, 4:161–166, 2002.
- [81] Rachid Benbouda, Abdelkader Mihi, Mourad Brioua, Salah Madani, and Lahbib Adami. The stress field of a dislocation array in an ultra thin anisotropic heterogeneous bicrystal. *physica status solidi (a)*, 202:2462–2466, 2005.
- [82] D. M. Barnett and J. Lothe. Line force loading on anisotropic half-spaces and wedges. *Physica Norvegica*, 8:13–22, 1975.
- [83] Ernian Pan. Static Green’s functions in multilayered half spaces. *Applied Mathematical Modelling*, 21:509–521, 1997.
- [84] B. Yang and E. Pan. Efficient evaluation of three-dimensional Green’s functions in anisotropic elastostatic multilayered composites. *Engineering Analysis with Boundary Elements*, 26:355–366, 2002.
- [85] E. Pan. Three-dimensional fundamental solutions in multilayered piezoelectric solids. *The Chinese Journal of Mechanics*, 19:127–132, 2003.
- [86] E. Pan, B. Yang, G. Cai, and F. G. Yuan. Stress analyses around holes in composite laminates using boundary element method. *Engineering Analysis with Boundary Elements*, 25:31–40, 2001.
- [87] Roland Stalder, Henning Sirringhaus, Nico Onda, and Hans von Känel. Observation of misfit dislocations in epitaxial CoSi_2/Si (111) layers by scanning tunneling microscopy. *Applied Physics Letters*, 59:1960–1962, 1991.
- [88] J. G. Belk, D. W. Pashley, B. A. Joyce, and T. S. Jones. Dislocation displacement field at the surface of InAs thin films grown on GaAs(110). *Physical Review B*, 58:16194–16201, 1998.
- [89] Toby D. Young, Joseph Kioseoglou, George P. Dimitrakopoulos, Paweł Dłużewski, and Philomela Komninou. 3D modelling of misfit networks in the interface region of heterostructures. *Journal of Physics D: Applied Physics*, 40:4084–4091, 2007.
- [90] James L. Klemm and Robert Wm. Little. The semi-infinite elastic cylinder under self-equilibrated end loading. *SIAM Journal on Applied Mathematics*, 19:712–729, 1970.

- [91] A. E. H. Love. *A Treatise on the Mathematical Theory of Elasticity*. Dover Publications, 4th edition, 1944.
- [92] R. W. Little and S. B. Childs. Elastostatic boundary region problems on solid cylinders. *Quarterly of Applied Mathematics*, 25:261–274, 1967.
- [93] N. G. Stephen and M. Z. Wang. Decay rates for the hollow circular cylinder. *Journal of Applied Mechanics*, 59:747–753, 1992.
- [94] N. G. Stephen. Decay rates for the compound circular cylinder. *Journal of Strain Analysis*, 26:215–220, 1991.
- [95] Jian Qiao Ye. Edge effects in angle-ply laminated hollow cylinders. *Composite Structures*, 52:247–253, 2001.
- [96] Jianqiao Ye. Decay rate of edge effects in cross-ply-laminated hollow cylinders. *International Journal of Mechanical Sciences*, 43:455–470, 2001.
- [97] R. C. Batra and J. S. Yang. Saint-Venant’s principle in linear piezoelectricity. *Journal of Elasticity*, 38:209–218, 1995.
- [98] Alessandra Borrelli, Cornelius Horgan, and M. Patria. Saint-Venant end effects in anti-plane shear for classes of linear piezoelectric materials. *Journal of Elasticity*, 64:217–236, 2001.
- [99] Hui Fan. Decay rates in a piezoelectric strip. *International Journal of Engineering Science*, 33:1095–1103, 1995.
- [100] Alessandra Borrelli, Cornelius O. Horgan, and M. Cristina Patria. Saint-Venant end effects for plane deformations of linear piezoelectric solids. *International Journal of Solids and Structures*, 43:943–956, 2006.
- [101] Horng-Shyang Chen, Dong-Ming Yeh, Yen-Cheng Lu, Cheng-Yen Chen, Chi-Feng Huang, Tsung-Yi Tang, C. C. Yang, Cen-Shawn Wu, and Chii-Dong Chen. Strain relaxation and quantum confinement in InGaN/GaN nanoposts. *Nanotechnology*, 17:1454–1458, 2006.
- [102] J. E. Van Nostrand, K. L. Averett, R. Cortez, J. Boeckl, C. E. Stutz, N. A. Sanford, A. V. Davydov, and J. D. Albrecht. Molecular beam epitaxial growth of high-quality GaN nanocolumns. *Journal of Crystal Growth*, 287:500–503, 2006. The 16th American Conference on Crystal Growth and Epitaxy - ACCGE 16.
- [103] Nicolas Thillozen, Kathrin Sebald, Hilde Hardtdegen, Ralph Meijers, Raffaella Calarco, Simone Montanari, Nicoleta Kaluza, Jurgen Gutowski, and Hans Luth. The state of strain in single GaN nanocolumns as derived from micro-photoluminescence measurements. *Nano Letters*, 6:704–708, 2006.
- [104] H. J. Ding, B. Chen, and J. Liang. General solutions for coupled equations for piezoelectric media. *International Journal of Solids and Structures*, 33:2283–2298, 1996.

- [105] X. Wang. An electric point charge moving along the poling direction of a transversely isotropic piezoelectric solid. *Archive of Applied Mechanics*, 74:509–516, 2005.
- [106] H. Zheng, J. Wang, S. E. Lofland, Z. Ma, L. Mohaddes-Ardabili, T. Zhao, L. Salamanca-Riba, S. R. Shinde, S. B. Ogale, F. Bai, D. Viehland, Y. Jia, D. G. Schlom, M. Wuttig, A. Roytburd, and R. Ramesh. Multiferroic $\text{BaTiO}_3 - \text{CoFe}_2\text{O}_4$ nanostructures. *Science*, 303:661–663, 2004.
- [107] N. Hur, S. Park, P. A. Sharma, J. S. Ahn, S. Guha, and S. W. Cheong. Electric polarization reversal and memory in a multiferroic material induced by magnetic fields. *Nature*, 429:392–395, 2004.
- [108] Ce-Wen Nan, Gang Liu, and Yuanhua Lin. Influence of interfacial bonding on giant magnetoelectric response of multiferroic laminated composites of $\text{Tb}_{1-x}\text{Dy}_x\text{Fe}_2$ and $\text{PbZr}_x\text{Ti}_{1-x}\text{O}_3$. *Applied Physics Letters*, 83:4366–4368, 2003.
- [109] X. Wang, E. Pan, and J. D. Albrecht. Exact closed-form electromagnetic Green’s functions for graded uniaxial multiferroic materials. *Journal of Applied Physics*, 103:113511, 2008.
- [110] Yachin Ivry, Vera Lyahovitskaya, Ilya Zon, Igor Lubomirsky, Ellen Wachtel, and Alexander L. Roytburd. Enhanced pyroelectric effect in self-supported films of BaTiO_3 with polycrystalline macrodomains. *Applied Physics Letters*, 90:172905, 2007.
- [111] G. L. Yuan and Siu Wing Or. Enhanced piezoelectric and pyroelectric effects in single-phase multiferroic $\text{Bi}_{1-x}\text{Nd}_x\text{FeO}_3$ ($x = 0-0.15$) ceramics. *Applied Physics Letters*, 88:062905, 2006.
- [112] A. Hadni. Applications of the pyroelectric effect. *Journal of Physics E: Scientific Instruments*, 14:1233–1240, 1981.
- [113] T. Yoshida, H. Osada, S. Chiba, T. Kikuchi, N. Tayama, K. Seki, and H. Matsuki. Construction of magnetic infrared sensor utilizing ferrimagnetic film. *IEEE Transactions on Magnetics*, 35:3637–3639, 1999.
- [114] Cun-Fa Gao and Naotake Noda. Thermal Green’s functions for a heat source in a piezoelectric solid with a parabolic boundary. *Journal of Thermal Stresses*, 29:1019–1030, 2006.
- [115] Qing-Hua Qin. 2D Green’s functions of defective magnetoelectroelastic solids under thermal loading. *Engineering Analysis with Boundary Elements*, 29:577–585, 2005.
- [116] R. Sabadini, M. Bonafede, and E. Boschi. A thermomagnetoelastic model of the earthquake source mechanism. *Il Nuovo Cimento C*, 1:523–538, 1978.
- [117] Ernian Pan. A general boundary element analysis of 2-D linear elastic fracture mechanics. *International Journal of Fracture*, 88:41–59, 1997.

- [118] Trung-Kien Nguyen, Karam Sab, and Guy Bonnet. First-order shear deformation plate models for functionally graded materials. *Composite Structures*, 83:25–36, 2008.
- [119] K. J. Sohn and J. H. Kim. Structural stability of functionally graded panels subjected to aero-thermal loads. *Composite Structures*, 82:317–325, 2008.
- [120] M. Darabi, M. Darvizeh, and A. Darvizeh. Non-linear analysis of dynamic stability for functionally graded cylindrical shells under periodic axial loading. *Composite Structures*, 83:201–211, 2008.
- [121] W. Q. Chen, H. M. Wang, and R. H. Bao. On calculating dispersion curves of waves in a functionally graded elastic plate. *Composite Structures*, 81:233–242, 2007.
- [122] J. Yang and Y. Chen. Free vibration and buckling analyses of functionally graded beams with edge cracks. *Composite Structures*, 83:48–60, 2008.
- [123] Yoshihiro Ootao and Yoshinobu Tanigawa. Transient piezothermoelastic analysis for a functionally graded thermopiezoelectric hollow sphere. *Composite Structures*, 81:540–549, 2007.
- [124] Manfred Fiebig. Revival of the magnetoelectric effect. *Journal of Physics D: Applied Physics*, 38:R123–R152, 2005.
- [125] V. J. Folen, G. T. Rado, and E. W. Stalder. Anisotropy of the magnetoelectric effect in Cr_2O_3 . *Physical Review Letters*, 6:607–608, 1961.
- [126] A. M. J. G. Run, D. R. Terrell, and J. H. Scholing. An in situ grown eutectic magnetoelectric composite material. *Journal of Materials Science*, 9:1710–1714, 1974.
- [127] Jungho Ryu, Alfredo Vázquez Carazo, Kenji Uchino, and Hyoun-Ee Kim. Magnetoelectric properties in piezoelectric and magnetostrictive laminate composites. *Japanese Journal of Applied Physics*, 40:4948–4951, 2001.
- [128] Jiang Yu Li and Martin L. Dunn. Micromechanics of magneto-electro-elastic composite materials: Average fields and effective behavior. *Journal of Intelligent Material Systems and Structures*, 9:404–416, 1998.
- [129] Zuorong Chen, Shouwen Yu, Lu Meng, and Ye Lin. Effective properties of layered magneto-electro-elastic composites. *Composite Structures*, 57:177–182, 2002.
- [130] Ce-Wen Nan, Gang Liu, Yuanhua Lin, and Haydn Chen. Magnetic-field-induced electric polarization in multiferroic nanostructures. *Physical Review Letters*, 94:197203, 2005.
- [131] Mordehai Milgrom and S. Shtrikman. Linear response of two-phase composites with cross moduli: Exact universal relations. *Physical Review A*, 40:1568–1575, 1989.
- [132] Y. Benveniste. Magnetoelectric effect in fibrous composites with piezoelectric and piezomagnetic phases. *Physical Review B*, 51:16424–16427, 1995.

- [133] G. Harshé, J. P. Dougherty, and R. E. Newnham. Theoretical modelling of multilayer magnetoelectric composites. *International journal of applied electromagnetics in materials*, 4:145–149, 1993.
- [134] G. Harshé. *Magnetoelectric effect in piezoelectric magnetostrictive composites*. PhD thesis, Pennsylvania State University, 1991.
- [135] Z. Huang. Theoretical modeling on the magnetization by electric field through product property. *Journal of Applied Physics*, 100:114104, 2006.
- [136] Shuxiang Dong, Jie-Fang Li, and D. Viehland. Longitudinal and transverse magnetoelectric voltage coefficients of magnetostrictive/piezoelectric laminate composite: theory. *IEEE Transactions on Ultrasonics, Ferroelectrics and Frequency Control*, 50:1253–1261, 2003.
- [137] F. Yang, Y. M. Wen, P. Li, M. Zheng, and L. X. Bian. The resonant magnetoelectric response of magnetostrictive/piezoelectric laminated composite under the consideration of losses. *Acta Physica Sinica*, 56:3539–3549, 2007.
- [138] J. M. Qu and M. Cherkaoui. *Fundamentals of Micromechanics of Solids*. John Wiley & Sons, Inc, 2006.
- [139] V. M. Petrov, G. Srinivasan, M. I. Bichurin, and A. Gupta. Theory of magnetoelectric effects in ferrite piezoelectric nanocomposites. *Physical Review B*, 75:224407, 2007.
- [140] E. Pan. Exact solution for simply supported and multilayered magneto-electro-elastic plates. *Journal of Applied Mechanics*, 68:608–618, 2001.
- [141] M. I. Bichurin, V. M. Petrov, and G. Srinivasan. Theory of low-frequency magnetoelectric coupling in magnetostrictive-piezoelectric bilayers. *Physical Review B*, 68:054402, 2003.
- [142] X. Wang and E. Pan. Magnetoelectric effects in multiferroic fibrous composite with imperfect interface. *Physical Review B*, 76:214107, 2007.
- [143] W. Q. Chen and Kang Yong Lee. Time-dependent behaviors of angle-ply laminates with viscous interfaces in cylindrical bending. *European Journal of Mechanics - A/Solids*, 23:235–245, 2004.
- [144] M. F. Ashby. Boundary defects, and atomistic aspects of boundary sliding and diffusional creep. *Surface Science*, 31:498–542, 1972.
- [145] R. Raj and M. Ashby. On grain boundary sliding and diffusional creep. *Metallurgical and Materials Transactions B*, 2:1113–1127, 1971.
- [146] Z. Suo. Motions of microscopic surfaces in materials. *Advances in Applied Mechanics*, 33:193–294, 1997.
- [147] J. V. Funn and I. Dutta. Creep behavior of interfaces in fiber reinforced metal-matrix composites. *Acta Materialia*, 47:149–164, 1998.

- [148] L. H. He and C. W. Lim. Time-dependent interfacial sliding in fiber composites under longitudinal shear. *Composites Science and Technology*, 61:579–584, 2001.
- [149] L. H. He and C. W. Lim. Electromechanical responses of piezoelectric fiber composites with sliding interface under anti-plane deformations. *Composites Part B: Engineering*, 34:373–381, 2003.
- [150] Huajian Gao, Lin Zhang, and Shefford P. Baker. Dislocation core spreading at interfaces between metal films and amorphous substrates. *Journal of the Mechanics and Physics of Solids*, 50:2169–2202, 2002.
- [151] H. Fan and G. F. Wang. Interaction between a screw dislocation and viscoelastic interfaces. *International Journal of Solids and Structures*, 40:763–776, 2003.
- [152] L. H. He and J. Jiang. Transient mechanical response of laminated elastic strips with viscous interfaces in cylindrical bending. *Composites Science and Technology*, 63:821–828, 2003.
- [153] X. Wang, E. Pan, and W. J. Feng. Time-dependent Green’s functions for an anisotropic bimaterial with viscous interface. *European Journal of Mechanics - A/Solids*, 26:901–908, 2007.
- [154] D. L. Clements. A crack between dissimilar anisotropic media. *International Journal of Engineering Science*, 9:257–265, 1971.
- [155] Zhigang Suo. Singularities, interfaces and cracks in dissimilar anisotropic media. *Proceedings of the Royal Society of London A*, 427:331–358, 1990.
- [156] X. Jiang and E. Pan. Exact solution for 2D polygonal inclusion problem in anisotropic magneto-electroelastic full-, half-, and bimaterial-planes. *International Journal of Solids and Structures*, 41:4361–4382, 2004.
- [157] T. C. T. Ting. Image singularities of Green’s functions for anisotropic elastic half-spaces and bimaterials. *Quarterly Journal of Mechanics and Applied Mathematics*, 45:119–139, 1992.
- [158] J. Dundurs. Elastic interaction of dislocations with inhomogeneities. In T. Mura, editor, *Mathematical Theory of Dislocations*, pages 70–115. ASME, 1969.
- [159] Chien-Ching Ma and Ru-Li Lin. Image singularities of Green’s functions for an isotropic elastic half-plane subjected to forces and dislocations. *Mathematics and Mechanics of Solids*, 6:503–524, 2001.
- [160] Kang Yong Lee, Won Gyu Lee, and Y. Eugene Pak. Interaction between a semi-infinite crack and a screw dislocation in a piezoelectric material. *Journal of Applied Mechanics*, 67:165–170, 2000.
- [161] X. Wang and E. Pan. Interaction between a screw dislocation and a viscoelastic piezoelectric bimaterial interface. *International Journal of Solids and Structures*, 45:245–257, 2008.

- [162] J. Dundurs and G. P. Sendeckyj. Behavior of an edge dislocation near a bimetallic interface. *Journal of Applied Physics*, 36:3353–3354, 1965.
- [163] B. T. Chen, C. T. Hu, and Sanboh Lee. Dislocations near a sliding interface. *International Journal of Engineering Science*, 36:1011–1034, 1998.
- [164] Changsong Dongye and T. C. T. Ting. Explicit expressions of Barnett-Lothe tensors and their associated tensors for orthotropic materials. *Quarterly of Applied Mathematics*, 47:723–734, 1989.
- [165] T. C. T. Ting and D. M. Barnett. Image force on line dislocations in anisotropic elastic half-spaces with a fixed boundary. *International Journal of Solids and Structures*, 30:313–323, 1993.
- [166] X. Wang, Y. P. Shen, and J. K. Du. Green’s function for the anisotropic piezoelectric bimaterials with a slipping interface. *Acta Mechanica Sinica*, 14:189–194, 2001.
- [167] Peter B. Nagy and Adnan H. Nayfeh. On the thermoelectric magnetic field of spherical and cylindrical inclusions. *Journal of Applied Physics*, 87:7481–7490, 2000.
- [168] Adnan H. Nayfeh, Hector Carreon, and Peter B. Nagy. Role of anisotropy in non-contacting thermoelectric materials characterization. *Journal of Applied Physics*, 91:225–231, 2002.
- [169] Hector Carreon, Balachander Lakshminarayan, Waseem I. Faidi, Adnan H. Nayfeh, and Peter B. Nagy. On the role of material property gradients in noncontacting thermoelectric nde. *NDT & E International*, 36:339–348, 2003.
- [170] W. E. Bies, R. J. Radtke, H. Ehrenreich, and E. Runge. Thermoelectric properties of anisotropic semiconductors. *Physical Review B*, 65:085208, 2002.
- [171] Kuei Fang Hsu, Sim Loo, Fu Guo, Wei Chen, Jeffrey S. Dyck, Ctirad Uher, Tim Hogan, E. K. Polychroniadis, and Mercouri G. Kanatzidis. Cubic $\text{AgPb}_m\text{SbTe}_{2+m}$: Bulk thermoelectric materials with high figure of merit. *Science*, 303:818–821, 2004.
- [172] Eric Quarez, Kuei-Fang Hsu, Robert Pcionek, N. Frangis, E. K. Polychroniadis, and Mercouri G. Kanatzidis. Nanostructuring, compositional fluctuations, and atomic ordering in the thermoelectric materials $\text{AgPb}_m\text{SbTe}_{2+m}$: The myth of solid solutions. *Journal of the American Chemical Society*, 127:9177–9190, 2005.
- [173] M. S. Dresselhaus, G. Chen, M. Y. Tang, R. G. Yang, H. Lee, D. Z. Wang, Z. F. Ren, J.-P. Fleurial, and P. Gogna. New directions for low-dimensional thermoelectric materials. *Advanced Materials*, 19:1043–1053, 2007.
- [174] Akram I. Boukai, Yuri Bunimovich, Jamil Tahir-Kheli, Jen-Kan Yu, William A. Goddard III, and James R. Heath. Silicon nanowires as efficient thermoelectric materials. *Nature*, 451:168–171, 2008.

- [175] Allon I. Hochbaum, Renkun Chen, Raul Diaz Delgado, Wenjie Liang, Erik C. Garnett, Mark Najarian, Arun Majumdar, and Peidong Yang. Enhanced thermoelectric performance of rough silicon nanowires. *Nature*, 451:163–167, 2008.
- [176] G. Jeffrey Snyder and Eric S. Toberer. Complex thermoelectric materials. *Nature Materials*, 7:105–114, 2008.
- [177] Johann H. Hinken and Yury Tavrín. Thermoelectric squid method for the detection of segregations. In Sarah Kallsen, Connie Nessa, Donald O. Thompson, Dale E. Chimenti, and Linda Poore, editors, *Review of Progress in Quantitative Nondestructive Evaluation*, volume 19, pages 2085–2092. AIP, 2000.
- [178] K.I. Maslov and V.K. Kinra. Non-contact thermoelectric NDE for alloy microstructural analysis. *Materials Evaluation*, 59:1081–1084, 2001.
- [179] Alok Sutradhar and Glaucio H. Paulino. A simple boundary element method for problems of potential in non-homogeneous media. *International Journal for Numerical Methods in Engineering*, 60:2203–2230, 2004.
- [180] Bernard Collet, Michel Destrade, and Gérard A. Maugin. Bleustein-Gulyaev waves in some functionally graded materials. *European Journal of Mechanics - A/Solids*, 25:695–706, 2006.
- [181] E. Pan and X. Jiang. Effect of qwr shape on the induced elastic and piezoelectric fields. *Computer Modeling in Engineering and Science*, 6:77–90, 2004.
- [182] V. Holý, G. Springholz, M. Pinczolits, and G. Bauer. Strain induced vertical and lateral correlations in quantum dot superlattices. *Physical Review Letters*, 83:356–359, 1999.
- [183] J. Stangl, V. Holý, and G. Bauer. Structural properties of self-organized semiconductor nanostructures. *Reviews of Modern Physics*, 76:725–783, 2004.
- [184] R. Phillips. *Crystals, Defects, and Microstructures: Modeling Across Scales*. Cambridge University Press, 2001.
- [185] B. Yang and V. K. Tewary. Formation of a surface quantum dot near laterally and vertically neighboring dots. *Physical Review B*, 68:035301, 2003.
- [186] E. Pan, J. D. Albrecht, and Y. Zhang. Elastic and piezoelectric fields in quantum wire semiconductor structures – a boundary integral equation analysis. *physica status solidi (b)*, 244:1925–1939, 2007.
- [187] Chun-Wei Pao and David J. Srolovitz. Stress and morphology evolution during island growth. *Physical Review Letters*, 96:186103, 2006.
- [188] Chun-Wei Pao and David J. Srolovitz. Atomistic simulation of stress evolution during island growth. *Journal of the Mechanics and Physics of Solids*, 54:2527–2543, 2006.

- [189] A. Malachias, S. Kycia, G. Medeiros-Ribeiro, R. Magalhães Paniago, T. I. Kamins, and R. Stanley Williams. 3d composition of epitaxial nanocrystals by anomalous X-ray diffraction: Observation of a Si-rich core in Ge domes on Si(100). *Physical Review Letters*, 91:176101, 2003.
- [190] R. Zhu, E. Pan, P. W. Chung, X. Cai, K. M. Liew, and A. Buldum. Atomistic calculation of elastic moduli in strained silicon. *Semiconductor Science and Technology*, 21:906–911, 2006.
- [191] C. Y. Wang, M. Denda, and E. Pan. Analysis of quantum-dot-induced strain and electric fields in piezoelectric semiconductors of general anisotropy. *International Journal of Solids and Structures*, 43:7593–7608, 2006.
- [192] S. P. Shen and S. N. Atluri. Multiscale simulation based on the meshless local Petrov-Galerkin (MLPG) method. *Computer Modeling in Engineering and Science*, 5:235–255, 2004.
- [193] E. Pan, Y. Zhang, P. W. Chung, and M. Denda. Strain energy on the surface of an anisotropic half-space substrate: effect of quantum-dot shape and depth. *Computer Modeling in Engineering and Science*, 24:157–168, 2008.
- [194] M. Arlery, J. L. Rouvière, F. Widmann, B. Daudin, G. Feuillet, and H. Mariette. Quantitative characterization of GaN quantum-dot structures in AlN by high-resolution transmission electron microscopy. *Applied Physics Letters*, 74:3287–3289, 1999.